Aalborg Universitet

Harmonic Modelling, Propagation and Mitigation for Large Wind Power Plants Connected via Extra Long HVAC Cables

With special focus on harmonic stability

Dowlatabadi, Mohammadkazem Bakhshizadeh

HARMONIC MODELLING, PROPAGATION AND MITIGATION FOR LARGE WIND POWER PLANTS CONNECTED VIA EXTRA LONG HVAC CABLES

WITH SPECIAL FOCUS ON HARMONIC STABILITY

BY
MOHAMMADKAZEM B. DOWLATABADI

DISSERTATION SUBMITTED 2018

AALBORG UNIVERSITY
DENMARK

HARMONIC MODELLING, PROPAGATION AND MITIGATION FOR LARGE WIND POWER PLANTS CONNECTED VIA EXTRA LONG HVAC CABLES

With special focus on harmonic stability

by

Mohammadkazem B. Dowlatabadi

AALBORG UNIVERSITY
DENMARK

Dissertation submitted 2018

.

…to my family for their encouragement and their exceptional love

ENGLISH SUMMARY

The wind power industry is rapidly growing and is gradually replacing conventional power plants. Therefore, the effects of wind power plants cannot be neglected any longer and the grid codes and requirements are becoming more complex and challenging. Power electronic devices such as STATCOMs and wind turbines can help the wind power plant developers to meet some of the requirements; however, it also brings some new challenges in terms of power quality and stability.

Larger offshore wind power plants are being placed farther from shore. Longer and longer cables, bigger and bigger transformers as well as other passive components within the wind power plant electrical infrastructure (e.g. shunt reactors, harmonic filters, capacitor banks, etc.) can potentially create phenomena not seen before such as resonances within the lower frequency range. This PhD project is focused on investigating and addressing the system/level harmonic analysis in offshore wind power plants taking into consideration the interaction between active components (e.g. wind turbines and STATCOMs), resonances in the external system, offshore electrical infrastructure as well as HVAC transmission assets. The specific aim is to improve existing and to develop new analysis methods as well as implement state-of-the-art models to ensure reliability, availability and robustness of offshore wind power plants as large power generation units in the electrical power system.

This project is an industrial PhD project; therefore, the challenges that are considered have more industry-oriented perspective. For instance, a big portion of the thesis is about processing, analysis and interpretation of numerical data delivered by the suppliers of different components such as wind turbines, STATCOMs and cables. How can these data be used for the harmonic studies? and what should additionally be delivered for future projects to ensure stable operation of the wind power plant? These are the questions answered by this research project.

An analysis tool has also been developed during this project, which loads all the necessary data from the models already developed in the power system analysis software, and evaluates the stability of the entire system. The tool has also some useful add-ons for the sensitivity analysis of large systems and the participation factor analysis. The participation factor analysis is an important tool to quantify the contribution of different components (i.e. active and passive) to a potential stability problem, since there are usually different parties involved in an offshore wind power plant, such as different wind turbines and STATCOM suppliers. Furthermore, the sensitivity analysis enables the user to see how a change in the system can improve or worsen the stability.

DANSK RESUME

Vindmølleindustrien udvikler sig hurtigt, og erstatter gradvist den konventionelle energi produktion. Grundet denne udvikling kan vindkraft ikke negligeres og kompleksiteten af tekniske forskrifter og kravene til vindkraftanlæg er som følge deraf blevet modificeret og blevet mere udfordrende. Effektelektroniske enheder som STATCOM og vindmøller (WT) kan hjælpe projektudvikleren til at imødekomme disse krav; også selvom dette også betyder nye udfordringer ift. spændingskvalitet og stabilitet.

Større havvindmølleparker bliver placeret længere fra kysten. Længere kabler, og større transformere såvel som passive komponenter (f.eks. reaktorer, harmoniske filtre, kondensatorbatterier osv.) kan potentielt resultere i ukendte fænomener som resonans i det lavfrekvente område. Denne Ph.d. afhandling fokuserer på at undersøge og adressere harmoniske studier i havvindmølleparker på system niveau hvor der tages højde for interaktion mellem de aktive komponenter (f.eks. vindturbiner og STATCOMS), eksterne resonanskilder, offshore elektrisk infrastruktur såvel som HVAC transmissionsudstyr. Det specifikke formål er at forbedre eksisterende- og udvikle nye analysemetoder, og implementere de nyeste modeller for at sikre pålidelighed og tilgængelighed i havvindmølleparker, som værende store el-producerende enheder på el-nettet.

Dette er et industrielt ph.d. studie, derfor er problemstillingerne behandlet i et industrielt perspektiv. F.eks. er størstedelen af afhandlingen vedrørende de numeriske data opgivet af leverandører af de pågældende komponenter såsom vindmøller, STATCOM og kabler. Hvordan kan disse data benyttes til harmoniske studier? Og hvad skal yderligere leveres til fremtidige studier for at sikre en stabil drift af vindmølleparker? Disse spørgsmål er forsøgt besvaret i afhandlingen.

Et værktøj er blevet udviklet gennem dette studie, som henter den nødvendige data fra allerede udviklede modeller i det elektrotekniske analyse værktøj, og evaluerer stabiliteten af hele vindmøllen systemet. Værktøjet har yderligere brugbare tilføjelsesprogrammer til sensitivitetsanalyse og bidragsanalyse af større systemer. Bidragsanalyse er et vigtigt værktøj til at kvantificere bidraget fra forskellige komponenter, da der som regel er flere parter involveret i en havvindmøllepark, såsom vindturbine- og STATCOM-leverandører. Sensitivitetsanalysen tillader brugeren at observerer, hvordan ændringer kan forbedre eller forværre stabiliteten.

ACKNOWLEDGEMENTS

Mohammadkazem Bakhshizadeh Dowlatabadi

March 2018, Copenhagen, Denmark

TABLE OF CONTENTS

LIST OF FIGURES

LIST OF TABLES

LIST OF ABBREVIATIONS

AC	Alternating current
AFE	Active front end
CCM	Component connection method
DC	direct current
DDSRF	Decoupled double SRF
DQ	Direct-quadrature
GNC	Generalized Nyquist criterion
HTF	Harmonic transfer function
HV	High voltage
IBSA	Impedance based stability analysis
LHP	Left half plane
LTI	Linear time invariant
LTP	Linear time periodic
LV	Low voltage
MF	Matrix fitting
MIMO	Multi Input Multi Output
MV	Medium voltage
ODE	Ordinary differential equation
OWPP	Offshore wind power plant
PCC	Point of common coupling
PF	Participation factor
PI	Proportional integrator
PLL	Phase locked loop
PoC	Point of connection
PR	Proportional resonant
RHP	Right half plane
SCF	Signal conditioning filter
SEB	Sequence extraction block
SISO	Single Input Single Output
SRF	Synchronous reference frame
SS	State space
TIP	Transmission interface point

VF	Vector fitting
VSC	Voltage source converter
VSI	Voltage source inverter
WPP	Wind power plant

LIST OF PRINCIPAL SYMBOLS

Y	Admittance
Z	Impedance
s	Laplace operator
θ	Phase angle of a rotating frame
ω	Angular frequency
G_c	Transfer function of a current controller
k_p	Proportional gain of a PI current regulator
k_i	Integrator gain of a PI current regulator
G_{cv}	Transfer function of a dc link voltage controller
k_{pv}	Proportional gain of a dc link voltage regulator
k_{iv}	Integrator gain of a dc link voltage regulator
k_{ppll}	Proportional gain of an SRF PLL
k_{ipll}	Integrator gain of an SRF PLL
I	Identity matrix
δ	Phase difference between two rotating frames
T_d	Amount of a time delay
x	State variable
u	Input of a state space model
y	Output of a state space model
λ	Eigenvalue
ζ	Damping of an eigenvalue
P	Participation factor
Φ	Right eigenvector
Ψ	Left eigenvector
M	Modulation index
Z_0	Characteristic impedance of a line/cable
γ	Propagation constant of a line/cable
R_d	Damping resistor in an LCL filter
r_{Lg}, L_g	Equivalent resistance and inductance of the grid side inductor of an LCL filter
r_{Lf}, L_f	Equivalent resistance and inductance of the converter side inductor of an LCL filter
r_{Cf}, C_f	Equivalent resistance and capacitance of the capacitor in an LCL filter
R_s, L_s	Equivalent resistance and inductance of a source

CHAPTER 1. INTRODUCTION AND PROBLEM DEFINITION

"Don't be satisfied with stories, how things have gone with others. Unfold your own myth."

Rumi

1.1. BACKGROUND

Renewable energy sources are replacing conventional power plants, and offshore wind power plays steadily more important role [1]. Figure 1-1 shows the total installed capacity of wind power all around the world until 2017 [2], [3]. Therefore, there is a need to modify the grid codes, which are mainly designed for conventional power plants, to consider the large wind power generation capacity as shown in Figure 1-1 and to accommodate different characteristics of wind power plants (WPPs) [4].
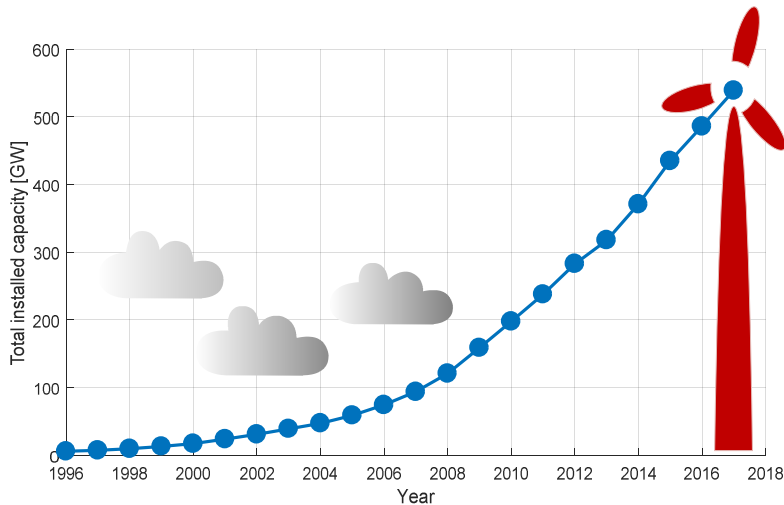
Figure 1-1 Total installed capacity of wind power plants in the world.

Power electronic converters offer many advantages to the power system. For instance, a Type 4 wind turbine (WT) generator with a back-to-back converter [5] as shown in Figure 1-2 ideally decouples the grid from the generator. Thereby, not only the generator can operate in the variable speed mode, but it can also support the grid by injecting reactive power. The other advantages are higher efficiency and reduced

loading on the gearbox [5]. However, the power electronic converters have a large drawback that is "Harmonics". Harmonics are generated by the power electronic equipment (switching harmonics) or nonlinear loads and components in the electrical system (known as characteristic harmonics) as well as due to potential controller instability as shown in Figure 1-3, where WTs are connected to an MV network (array network), and to reduce the losses and voltage drop, the voltage is stepped up and the power is transmitted to the grid by means of submarine export cables. An onshore STATCOM can improve the reactive power requirements at the grid interface point.
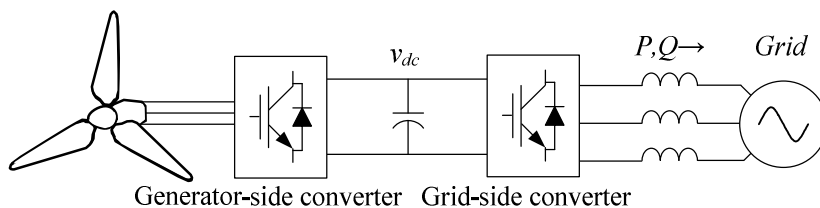
Figure 1-2 A full power back-to-back converter in a Type 4 wind turbine [5].
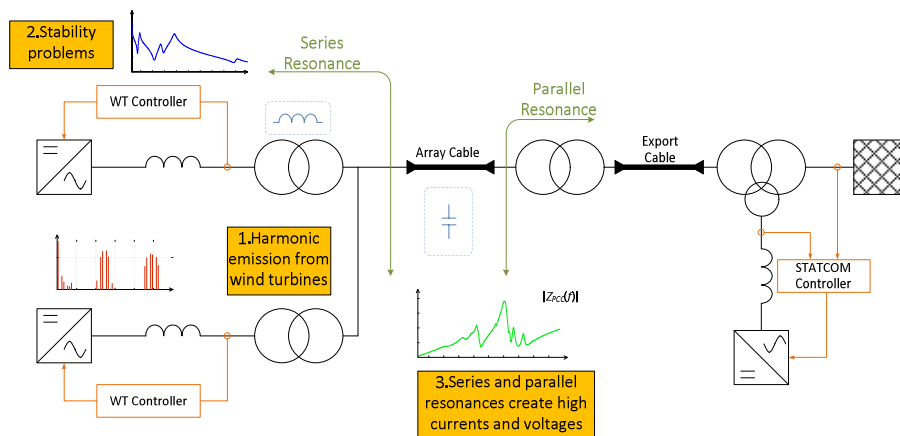
Figure 1-3 Harmonic problems in an offshore wind power plant [6]*.*

The negative effects of harmonics can be counted as [7]

1) Reduction of efficiency in generation, transmission and utilization of electric power.
2) Risk of harmonic amplification due to possible series and parallel resonances, highlighted as number 3 in Figure 1-3.
3) Insulation aging caused by voltage or temperature stresses.
4) Error in measurement devices.

5) Malfunction of protection devices.
6) Vibration of power system components.

A power electronic converter can also be considered as a high bandwidth controller, which may interact with other converters or with the resonances in the system. Consequently, as shown in Figure 1-4, it can produce excessive amounts of harmonic voltages and currents due to instability (highlighted as the second item in Figure 1-3) [8]–[10]. For instance, in the BorWin 1 project, which is the first HVDC connection of an offshore wind power plant (OWPP), harmonic stability problems caused a long shut down of the project [11], [12]. The characteristic harmonics in the power system have been investigated extensively [7]. However, there are still many open questions for the stability-related harmonics, such as the challenges in detailed modelling of the WPP elements, methodologies for large scale analysis, controller tuning and mitigation techniques of the harmonics.
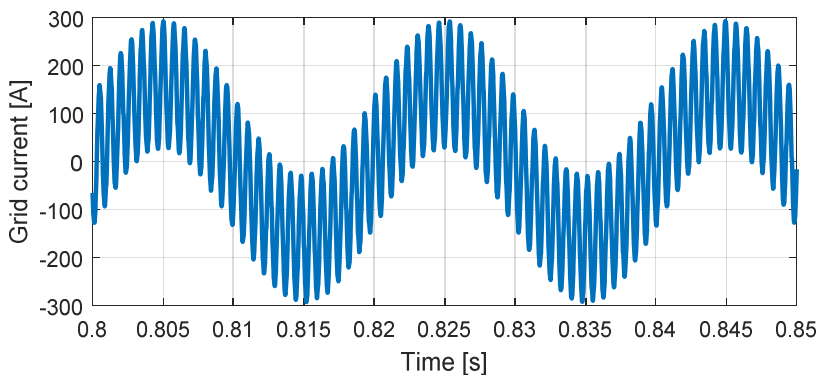
Figure 1-4 Power quality problems generated due to an instability.

The impedance-based stability analysis [13] and the eigenvalue-based stability analysis [14] are two typical methods to evaluate the small signal stability of a power-electronic-based power system. In the impedance based stability analysis of an active element (e.g. a WT as shown in Figure 1-5), the ratio of the external impedance (load impedance) to the internal impedance (source impedance) is used to evaluate the stability, while in the eigenvalue based stability analysis, as it can be guessed from the name, the stability is evaluated by looking at the eigenvalues of the entire system, which can be obtained from state-space matrices. Complexity-wise, the impedance based method is advantageous, due to the fact that it only needs impedances, which can be numerical tables from simulations or experiments. In contrast, the eigenvalue based method needs state-space definitions for each element. However, the impedance based method is a local method and it only evaluates the system from the point under study. If the point under study is changed then the result could be a less-, more- or even unstable system. This method is useful

for small systems where a few converters are connected, and for larger system the process cannot be repeated for all nodes in the system. In multi-vendor and large projects it is crucial to identify the origin of the problem and ask the corresponding supplier to do the fine tuning. This can be done by the participation factor analysis, which is a well-known method in power system analysis [15]. Participation factors can easily be obtained from the state space representation of the system. As discussed, both of these methods have advantages and disadvantages, and therefore, it is very interesting to improve the methods, to extend them and even to combine them.
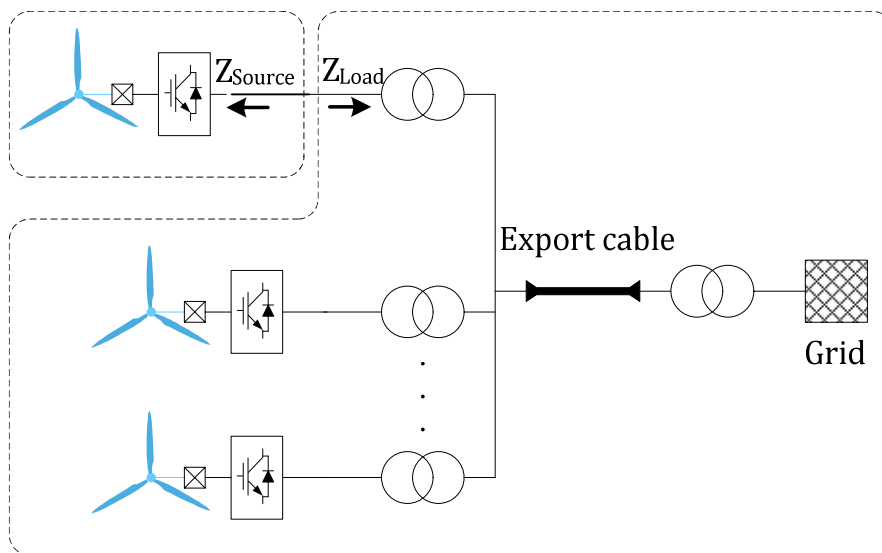
Figure 1-5 Source and load impedances in a multi-converter system like a windfarm.

As it is highlighted in the title, this PhD project focuses on large OWPP located far from shore. Thus, as it can be seen in Figure 1-6 the longer the cable is, the lower the resonance frequencies are. It could even be between the second and third harmonic of the grid frequency. Therefore, all components should correctly be modelled in the low frequency range to assess such system. In harmonic stability studies the current control loop is normally considered and the synchronization loop is neglected. However, if the low frequency behavior is of interest it cannot be neglected according to Figure 1-7 (f_1 is the fundamental frequency and f_s is the switching frequency).
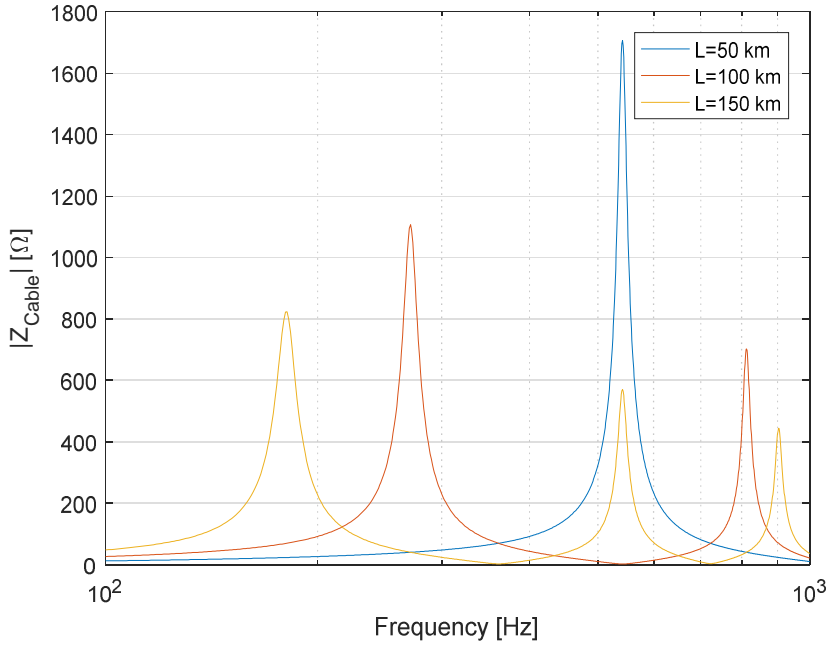
Figure 1-6 Impedance characteristic of a long submarine cable as a function of frequency [16].
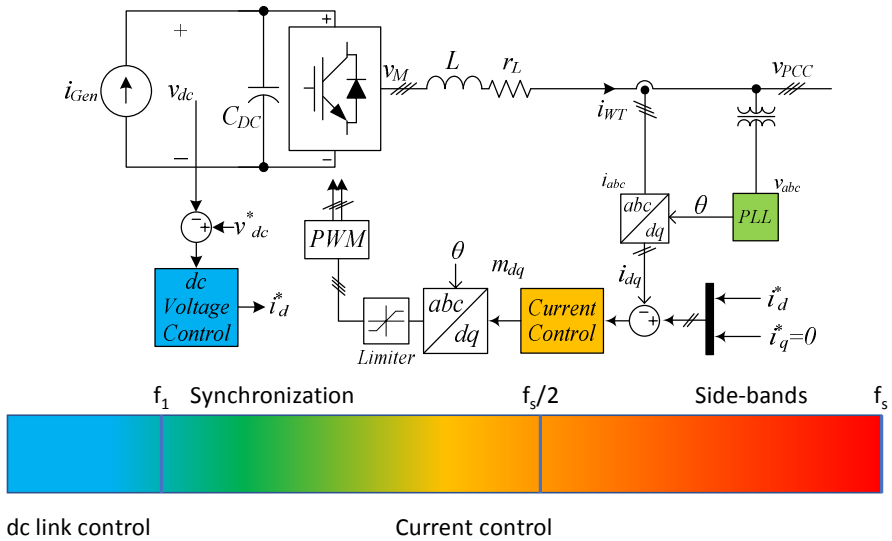
Figure 1-7 Multi-time scale stability investigation of a voltage source converter [17].

The same also holds true for the cable modelling. The proximity effect mainly affects the low frequency characteristics of a power cable [18]. The non-uniform current distribution in Figure 1-8 is mainly due to the proximity and skin effects. Therefore, a more detailed cable modelling should be done to reflect the harmonic losses and cable resonance characteristics. Figure 1-9 shows the frequency dependent resistance and inductance of a power cable. It should be noted that in this thesis cable modelling is not discussed. Instead methods to consider the detailed cable models in the stability studies are investigated.
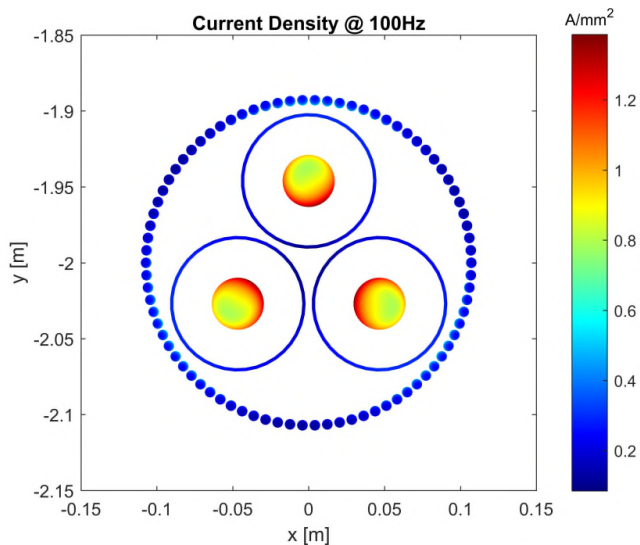
Figure 1-8 Non-uniform current distribution in a submarine cable due to the proximity and skin effects (simulated at 100 Hz).
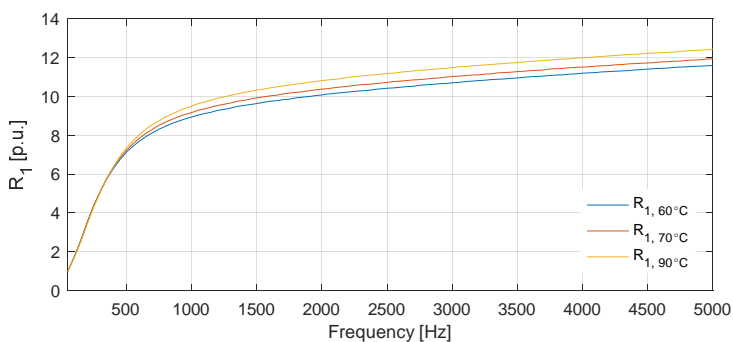
(a)
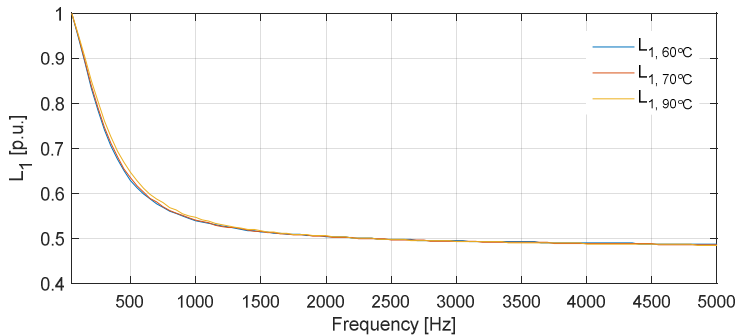
(b)

Figure 1-9 Effects of frequency and temperature on (a) cable resistance (b) cable inductance (positive sequence).

However, this brings new challenges such as how the numerical data can be imported into the stability studies. For the impedance based stability analysis it is a straightforward approach due to the fact that numerical impedances can be used to plot the final diagrams [19]. Whereas, in the eigenvalue based stability analysis, this data should be converted to state space matrices, which need an analytical definition of the frequency dependent characteristics. For third-party products such as WTs all control loops and parameters are needed for analytical modelling. However, due to the confidentiality these data are not always available.

Most of the literature regarding the harmonic stability use small scale systems for the presentation of the cases [20]–[22]. However, in author's view, it is necessary to define a framework, which is able easily to model new elements, to address the above-mentioned challenges and to provide reliable results for large scale systems. Figure 1-10 gives an illustration of such a stability analysis platform. Part of the tool uses an identification technique to obtain analytical state space models for cables, transformers and black-box models. Then, analytical models are fed into the calculation core of the tool. It uses a modular method to build up the state space matrices of the entire system. The eigenvalues and eigenvectors of the system afterwards are calculated and the most critical dynamics of the system are identified. Finally, an optimized sensitivity tool is utilized to investigate how a change in a parameter will affect the stability of the system. Figure 1-11 shows an example of the sensitivity analysis performed by the mentioned platform to see how the size of the dc link capacitor affects the eigenvalues of the system.
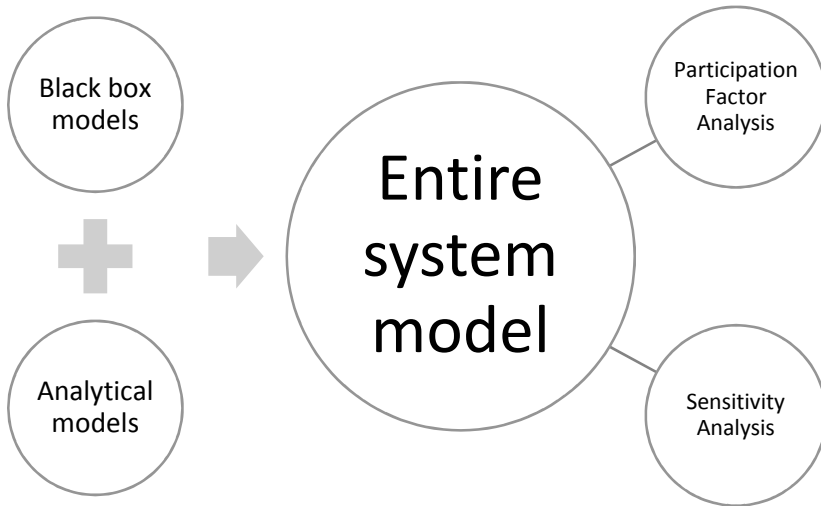
Figure 1-10 Different modules of the proposed stability analysis platform.
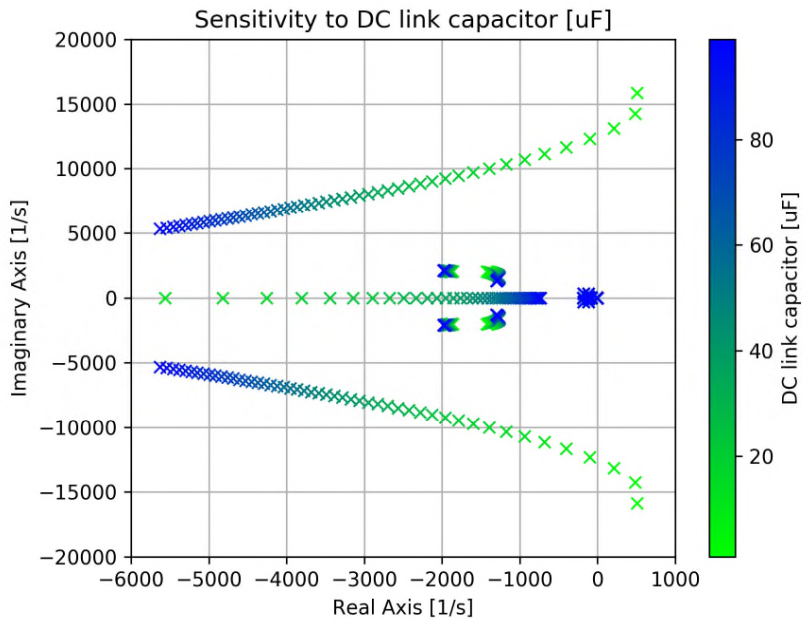
Figure 1-11 Sensitivity analysis performed by the stability analysis platform.

1.2. MOTIVATION AND OBJECTIVES

This Industrial PhD project is focusing on investigating and addressing the harmonic studies in OWPPs on a system level taking into consideration the interaction between the active components (e.g. WTs and STATCOMs), resonances in the external system, offshore electrical infrastructure as well as HVAC transmission assets. The specific aim is to improve existing and to develop new analysis methods and implement state-of-the-art models in order to ensure reliability and availability of OWPPs as large power generation units in the electrical power system.

The PhD project also leads to computational effective models and necessary tools for determination of the stability margins during the design phase OWPPs as well as adaptive or flexible solutions possibly to be implemented even during the execution phase of a project. The PhD project shall provide proposals for new standards, recommendations and guidance related to harmonics and resonances analysis in OWPPs connected via long and very long[1] (e.g. >160 km) HVAC cables (e.g. 220 kV).

Ørsted Wind Power expects through this project to meet a necessary need to develop and strengthen in-house competencies regarding modelling and design of OWPPs with long HVAC grid connection systems employing power electronic devices in such components as WTs, STATCOMs, etc. With regards to on-going commercial projects, the PhD project is highly relevant to the Hornsea Project one OWPP (UK), which is the first OWPP to be built by Ørsted Wind Power using a 175 km 220 kV HVAC grid connection, which is a much longer grid connection system compared to what has so far been considered feasible with HVAC cables.

The project is a continuation of the industrial PhD projects "Harmonics in Large Offshore Wind Farms" [1] finalized in 2011 and ,"Harmonics in Large Offshore Wind Farms Employing Power Electronics in Transmission System", [23] finalized in 2015. The first project was mainly focused on the WTs as a source of harmonic emission where in the second project the main focus was on the modelling of the voltage source converter (VSC) HVDC systems connection OWPPs to power grid on land. This project uses the knowledge obtained in those projects and focuses on the interaction between the OWPP and the power electronics in the wind power systems using long HVAC cables.

In order to achieve the above-mentioned goals, the following main objectives are defined as:

---

[1] A long cable by definition is a cable that the capacitive current needs to be considered in the design (e.g. longer than 20 km for 220 kV). However, in this thesis, the focus is on the low frequency resonances that are created by the long cables.

- Develop and validate appropriate models of different WPP elements focusing on the low frequency behavior.
- Investigate the challenges in the stability analysis of large-scale systems by:
  - o Comparing stability evaluation methods
  - o Identifying the main contributors to an instability
  - o Dealing with black-box models
  - o Accelerating the analysis of large-systems
- Identify the main challenges when long cables are used.
- Propose solutions for mitigating the harmonic problems

In order to meet the above-mentioned objectives, the following research questions have been formulated:

1. What is the state-of-the-art in the modelling of elements of an OWPP?
   a. What details are important?
   b. How should the models be validated?
   c. Are these methods applicable to the large-scale systems?
2. What is the state-of-the-art in the stability analysis?
   a. What are the advantages and disadvantages of each method?
   b. Are they applicable to large-scale systems?
   c. Which domain should be used for the three-phase analysis?
   d. Which method should be chosen for this thesis?
   e. Is there a modular way to simply use different models in the analysis?
3. What are the challenges in using black-box models?
4. Can we use the small-signal stability analysis as in power systems for power electronic based power systems?
5. What is the state-of-the-art in mitigating the harmonics and stability problems?
   a. What is the origin of high frequency problems?
   b. What is the origin of low frequency problems?
   c. What are the possible solutions?

1.2.1. COMMERCIAL PERSPECTIVES

Ørsted Wind Power develops a number of OWPPs far from shore and connected to the power systems in the UK, DE, DK and elsewhere. Therefore, research and collaboration with the academia is needed in order to optimize the overall electrical infrastructure, reduce the risks and consequently reduce the cost of electricity.

The commercial goal for Ørsted Wind Power is to gain a better understanding of HVAC cable connected OWPPs, in order to ensure reliability and availability of OWPPs. This will reduce the cost of electricity, as the risk of costly delays and modifications after the project has been commissioned can be reduced and

operational availability and the reliability can be improved. The project is an important part of Ørsted's continuous development of electrical system simulation competences. This is required by the transmission system operators and is necessary in order to meet the new challenges associated with grid connection OWPPs with long HVAC cable systems.

The commercial goal for Aalborg University is to broaden its research areas, improve academic core competences and thereby attract more new students and research projects in the field of HVAC cable based transmission technology, wind power plants, harmonics and power electronic devices in modern transmission systems and power systems.

1.2.2. DISTRIBUTION OF ROLES IN THE PHD PROJECT

Ørsted Wind Power

- Contribute with application knowledge and experience in hosting an Industrial PhD in an industrial research and development environment.
- Deliver relevant technical data and available harmonic measurement data.
- Contribute to supervision with industrial guidance.

Department of Energy Technology, Aalborg University

- Contribute with academic guidance supervision and course activities in Doctoral School.
- Contribute to knowledge related to OWPP grid connection with main emphasis on OWPP connected via a very long HVAC transmission system.
- Contribute with knowledge related to power electronics in wind turbines and their control
- Contribute with harmonic modelling methods and mitigation techniques in power electronic based power systems from the ERC Advanced Grant project Harmony, where around twenty researchers have been active (www.harmony.et.aau.dk)

1.3. APPROACH AND METHODOLOGY

The following is the proposed methodology to address the main goals of this PhD project.

- **Literature review and theoretical analysis**
  In the recent years many projects and papers on wind power plant studies have been published. A review on the challenges and the recent achievements on this topic (e.g. on the modelling of different elements of an OWPP) enables the PhD student to identify the gaps and propose an

appropriate study plan. Moreover, the lessons learnt in the previous studies leads to a better resource management of the project.

- **Component modelling and validation**
  After obtaining the basic knowledge about the problem and establishing the basis for modelling, new models and methods can be proposed. These methods should be validated either by experiments or computer simulations using the full detailed models. Differences in the results should be highlighted and it should be concluded whether the models have enough accuracy and performance.

- **Investigating the applicability of previous methods and improving them**
  Well-known methods for the analysis of the problem can be investigated to see whether they can be used for the current problem. For instance, there are methods and softwares for dealing with small signal stability analysis of classical power systems, and therefore, it is appealing to see if the user can benefit from them.

- **Defining a large scale offshore wind power plant**
  Finally, all the proposed methods and models should be tested in a realistic OWPP. An OWPP should be defined, where the identified critical challenges are present. It must be noted that this model cannot use project specific data and will only be based on public data.

1.4. LIMITATIONS

The following list is the limitations and assumptions of this research.

1) The zero sequence is not considered in this project. Normally a delta-star step-up transformer is used for the WTs. Therefore, the zero-sequence components cannot be observed by the controllers. However, if the system is heavily unbalanced then the couplings with all sequences should be considered in the harmonic analysis of the network. This is not the case in transmission systems.

2) The tap changer of a transformer is not modelled. Considering the limited tap changing capability of the transformer, it seems the results would not be too different. However, it is suggested to investigate to what extent a tap position can change the final results as a future work. The network modelling would need further changes as explained in Chapter 3.

3) The system is assumed to be a radial network; therefore, the phase displacements of the transformers are neglected. Similar to the previous point, considering the phase shifts needs the network modelling part to be updated. However, this is a valid assumption, since in offshore applications; to reduce the cost, the radial networks are preferable.

4) The dynamics of the generator side converter as well as the mechanical modes of the turbine are neglected. This is just a matter of complexity in the modelling. The methodology used in this thesis is a modular approach and new models can easily be used.

5) It is assumed in the identification that the measurements are noise-free. There are methods to identify the systems with the noisy measurements. However, in this thesis these methods are not investigated.

1.5. THESIS OUTLINE

In Chapter 2 the frequency domain modelling techniques are introduced and power converters are modelled, especially in the low frequency range. Impedance based stability analysis and the eigenvalue based stability analysis are introduced and the models are improved to consider the effects of the synchronization and dc link control loops. The derived models are also verified by perturbing the detailed models in time domain circuit simulators. Eigenvalue based stability analysis is more complicated compared to the impedance based stability analysis but it has a useful feature "participation factor analysis", which specifies the contribution of different elements on a specific dynamic. This is very important in multi-vendor projects.

In Chapter 3, the stability analysis platform is discussed in detail. The interconnection of different state space models is described and a method is used to directly obtain the state space model of the network.

In Chapter 4, the challenges with the numerical data delivery of suppliers are discussed. The suppliers of power electronic converters are reluctant to share the control structure of their products due to the confidentiality. The stability analysis is reviewed using numerical and black-box models for linear and nonlinear system as well as in impedance based stability analysis and eigenvalue based stability analysis.

In Chapter 5, a sensitivity analysis tool in the stability analysis is introduced and different mitigation measures such as passive and active damping are investigated for a 35-WT OWPP. The low frequency behavior of the system is also investigated and it is shown that the phase locked loop (PLL) can interact with the long cable.

Chapter 6 summarizes the work and discusses some possible future work.

1.6. PUBLICATIONS

Journal publications

[J.1]   M. K. Bakhshizadeh, X. Wang, F. Blaabjerg, J. Hjerrild, **Ł.** Kocewiak, C. L. Bak, and B. Hesselbæk, "Couplings in Phase Domain Impedance Modelling of Grid-Connected Converters," *IEEE Trans. Power Electron.*, vol. 31, no. 10, pp. 6792–6796, 2016.

[J.2]   M. K. Bakhshizadeh, C. Yoon, J. Hjerrild, C. L. Bak, Ł. Kocewiak, F. Blaabjerg, and B. Hesselbæk, "The Application of Vector Fitting to Eigenvalue-Based Harmonic Stability Analysis," *IEEE J. Emerg. Sel. Top. Power Electron.*, vol. 5, no. 4, pp. 1487–1498, Dec. 2017.

[J.3]   M. K. Bakhshizadeh, F. Blaabjerg, J. Hjerrild, X. Wang, Ł. Kocewiak, and C. L. Bak, "A Numerical Matrix-Based Method for Stability and Power Quality Studies Based on Harmonic Transfer Functions," *IEEE J. Emerg. Sel. Top. Power Electron.*, vol. 5, no. 4, pp. 1542–1552, Dec. 2017.

[J.4]   M. K. Bakhshizadeh, F. Blaabjerg, J. Hjerrild, Ł. Kocewiak, and C. Leth Bak, "Improving the Impedance Based Stability Criterion by Using the Vector Fitting Method," *IEEE Trans. Energy Convers.,* to be published.

[J.5]   M. K. Bakhshizadeh, J. Hjerrild, Ł. Kocewiak, C. L. Bak, F. Blaabjerg, X. Wang, "The Method to Speed up Harmonic Stability Studies in Large Wind Power Plants," to be submitted.

Conference publications

[C.1]   M. K. Bakhshizadeh, F. Blaabjerg, C. L. Bak, F. Faria da Silva, J. Hjerrild, Ł. Kocewiak, B. Hesselbæk, and T. Sørensen, "Harmonic Modelling, Propagation and Mitigation for Large Wind Power Plants Connected via Long HVAC Cables: Review and Outlook of Current Research," *in IEEE ENERGYCON 2016*, 2016, pp. 1–5

[C.2]   M. K. Bakhshizadeh, J. Hjerrild, Ł. Kocewiak, B. Hesselbæk, X. Wang, F. Blaabjerg, and C. L. Bak, "Small-signal model of a decoupled double synchronous reference frame current controller," in *2016 IEEE 17th Workshop on Control and Modeling for Power Electronics (COMPEL)*, 2016, pp. 1–6.

[C.3]   M. K. Bakhshizadeh, J. Hjerrild, Ł. Kocewiak, F. Blaabjerg, C. L. Bak, X. Wang, F. M. F. da Silva, and B. Hesselbæk, "A Numerical Matrix-Based method in Harmonic Studies in Wind Power Plants," in *15th Wind*

Integration Workshop, 2016, pp. 335–339.

[C.4]   M. K. Bakhshizadeh, J. Hjerrild, Ł. Kocewiak, F. Blaabjerg, C. L. Bak, "On Aggregation Requirements for Harmonic Stability Analysis in Wind Power Plants," in *16th Wind Integration Workshop*, 2017, pp. 424-427.

CHAPTER 2. MODELLING AND STABILITY ANALYSIS

"...all models are approximations. Essentially, all models are wrong, but some are useful."

George E. P. Box

2.1. INTRODUCTION

Harmonics is a frequency domain concept; therefore, the first step would be to find the frequency domain models of all components in a system. In this chapter, two methods for the modelling in the frequency domain are presented.

The first method models a component (e.g. a power converter) as an impedance/admittance including all the controllers and passive elements, and by doing this, the stability of the system can be evaluated by the impedance based stability analysis. The harmonic propagation in a system can also be analyzed by using a harmonic load flow analysis, if all elements are modelled as frequency dependent impedances.

The second method considers a power electronic based power system as an interconnected control system, and then by finding the state space model of the system, the stability can be evaluated.

In this chapter, these methods are reviewed with a special focus on the low frequency range. Then, the developed models are used and verified by stability evaluation of different test cases, where the validation results are also used in the next chapters.

Last but not least, the impedance based stability analysis is used in a large scale OWPP, and a method is proposed to accelerate such studies.

2.2. IMPEDANCE BASED STABILITY ANALYSIS

2.2.1. THEORITICAL BACKGROUND

Figure 2-1 shows the Norton equivalent circuit of a current controlled inverter connected to a grid. The terminal voltage can be obtained as

$$V(s) = \frac{I_s(s)}{Y_l(s) + Y_s(s)} \qquad (2\text{-}1)$$

which can be rewritten in the following form:

$$V(s) = \frac{I_s(s)}{Y_l(s)} \cdot \frac{1}{1 + Y_s(s)/Y_l(s)} \qquad (2\text{-}2)$$

The objective of the impedance based stability analysis is to evaluate the interactions between the converter and the grid. Therefore, it is a valid assumption to say that both the grid and the power converter are stable while connected to ideal sources/loads. This means that $I_s(s)$ and $1/Y_l(s)$ have no unstable poles and the stability of the system can be evaluated by the second term on the right-hand side of (2-2):

$$H(s) = \frac{1}{1 + Y_s(s)/Y_l(s)} \qquad (2\text{-}3)$$

which resembles a closed loop system, whose loop gain is $Y_s(s)/Y_l(s)$ [24]. In the literature the loop gain is also called as minor feedback loop gain [24]. Therefore, stability evaluation methods for open loop transfer function such as the Nyquist stability criterion and the Bode diagram can be used.
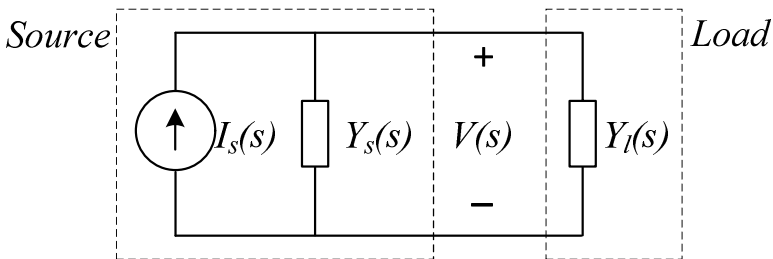
Figure 2-1 Norton equivalent circuit of a current controlled converter connected to a load, where source and load impedances are highlighted [24].

2.2.2. SINGLE-PHASE SYSTEMS

In this part the Norton equivalent of a single phase current controlled converter is derived. Figure 2-2 shows a current controlled converter with an LCL filter where the grid side current is controlled. In this section, the effects of the outer loop control such as the synchronization loop and the power control loops are neglected. A proportional resonant controller is used to control the grid ac current i_g.
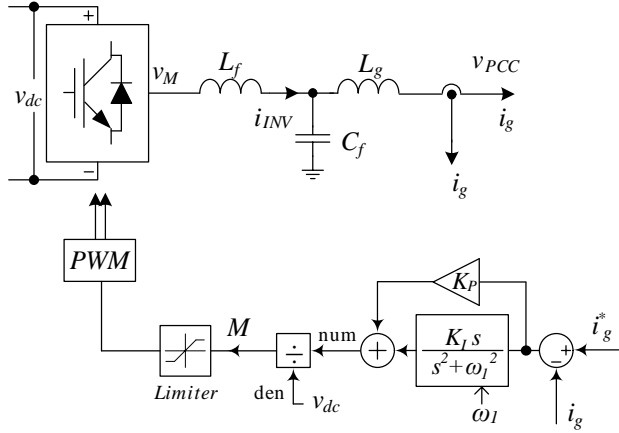
Figure 2-2 A single phase current controlled converter.

Figure 2-3 shows the control block diagram of Figure 2-2. The output current can be derived as a function of the current set point and the PCC voltage V_{pcc} as

$$i_g(s) = G_{cl}(s)i_g^*(s) - Y_{oi}(s)V_{pcc}(s) \qquad (2\text{-}4)$$

where

$$G_{cl}(s) = \frac{T_c(s)}{1 + T_c(s)} \qquad (2\text{-}5)$$

$$Y_{oi}(s) = \frac{Y_o(s)}{1 + T_c(s)} \qquad (2\text{-}6)$$

$$T_c(s) = G_c(s)G_{PWM}(s)Y_g(s) \qquad (2\text{-}7)$$

and $Y_g(s)$ and $Y_m(s)$ are the transfer functions of the LCL filter as follows

$$Y_g(s) = \frac{i_g(s)}{V_{PWM}(s)}\bigg|_{V_{PCC}=0} = \frac{Z_{Cf}}{Z_{Cf}Z_{Lf} + Z_{Lg}Z_{Lf} + Z_{Lg}Z_{Cf}} \qquad (2\text{-}8)$$

$$Y_o(s) = \frac{i_g(s)}{V_{PCC}(s)}\bigg|_{V_{PWM}=0} = \frac{Z_{Cf} + Z_{Lf}}{Z_{Cf}Z_{Lf} + Z_{Lg}Z_{Lf} + Z_{Lg}Z_{Cf}} \tag{2-9}$$

and

$$G_c(s) = \frac{1}{V_{dc}}\left(K_p + \frac{K_i s}{s^2 + \omega_1^2}\right) \tag{2-10}$$

is a proportional resonant controller and

$$G_{PWM}(s) = V_{dc}e^{-1.5sT_s} \tag{2-11}$$

is the PWM model with the time delay of the digital computation and the PWM delay (T_s is the sampling period) [25]. Hence, the modulation index M must be in the range [-0.5 , 0.5] in order to avoid over-modulation.
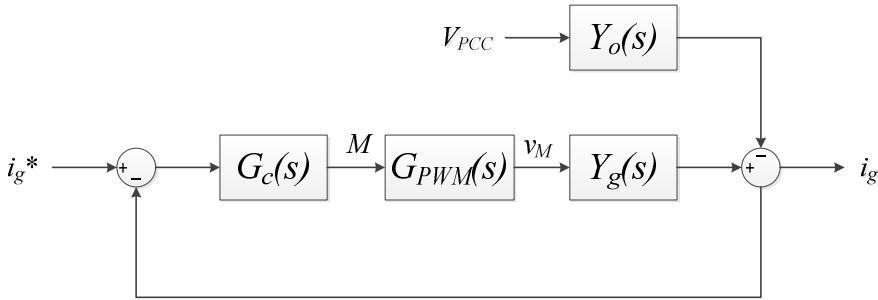
Figure 2-3 Control block diagram of the converter shown in Figure 2-2 [21].

2.2.3. THREE-PHASE SYSTEM

There are different domains to study a three-phase system like the stationary reference frame, the rotating frame, the sequence domain [26]. In this part, different domains and their advantages are briefly reviewed.

2.2.3.1 Impedance modelling in the stationary frame

If the current control is implemented in the stationary frame (i.e. PR controllers), then the impedances should be expressed in the stationary frame. It can be seen in Figure 2-4 the controllers in *αβ* frame or *abc* domain are fully decoupled. Therefore, the impedance model is not different from the single-phase model, which was shown in §2.2.2.
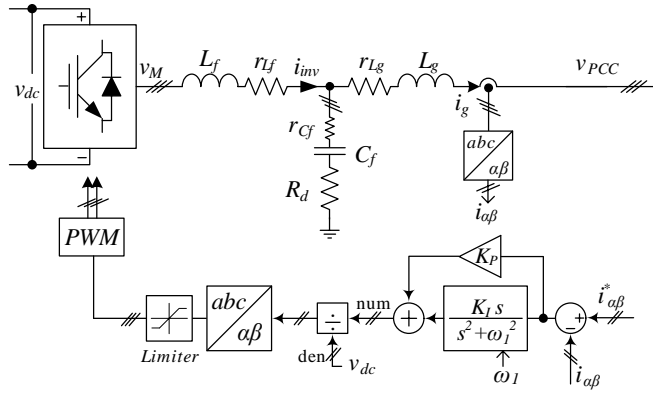
Figure 2-4 Current control in the stationary frame for a three-phase system.

2.2.3.2 Impedance modelling in the rotating frame

Park transformation is an effective method in studying electrical machines, since it converts the time varying mutual inductances between the stator and the rotor into the time-invariant parameters [27]. In this thesis, amplitude-invariant *dq* transformation as given in (2-12) is used, where the *q* axis is leading the *d* axis. It is also assumed that the system is balanced; therefore, the zero component of the *dq* transformation is dropped.

$$
\begin{bmatrix} I_d \\ I_q \end{bmatrix} = \frac{2}{3} \begin{bmatrix} \cos\theta & \cos\left(\theta - \frac{2\pi}{3}\right) & \cos\left(\theta + \frac{2\pi}{3}\right) \\ -\sin\theta & -\sin\left(\theta - \frac{2\pi}{3}\right) & -\sin\left(\theta + \frac{2\pi}{3}\right) \end{bmatrix} \begin{bmatrix} I_a \\ I_b \\ I_c \end{bmatrix} = T_{dq} I_{abc} \qquad (2\text{-}12)
$$

Figure 2-5 shows the grid side converter of a Type 4 WT. The machine (generator) side converter controls the power and the grid side converter controls the dc link voltage, and thereby, the power produced by the WT is injected to the grid. The reactive power can also be set independently by the grid side converter; however, in this work, it is considered as zero. In Figure 2-5, the current source i_{Gen} is the produced power from the WT, and the SCF block stands for the signal conditioning filter, which includes hardware anti-aliasing filters. For deriving the impedance model, first the PLL and the dc link controller are neglected, and their effects will be considered in the models later on. The converter side current is controlled, and therefore, other parts of the filter can be considered in the load/grid impedance.

Figure 2-5 Grid side converter of a back-to-back Type 4 wind turbine.

It is important to correctly transform the transfer functions from the *abc* domain to the *dq* domain. If one assumes that (2-13) is a balanced transfer function matrix in the *abc* domain, then the equivalent *dq* domain representation, considering the transformation matrix as (2-12), can be written as (2-14) [28].

$$F_{abc} = \begin{bmatrix} F(s) & 0 & 0 \\ 0 & F(s) & 0 \\ 0 & 0 & F(s) \end{bmatrix} \tag{2-13}$$

$$F_{dq} = \frac{1}{2} \begin{bmatrix} F(s - j\omega_1) + F(s + j\omega_1) & -j\big(F(s - j\omega_1) - F(s + j\omega_1)\big) \\ j\big(F(s - j\omega_1) - F(s + j\omega_1)\big) & F(s - j\omega_1) + F(s + j\omega_1) \end{bmatrix} \tag{2-14}$$

where ω_1 is the fundamental angular frequency of the system. For instance, the *dq* domain model of the impedance of an inductance is

$$\begin{bmatrix} Ls + r_L & -\omega_1 L \\ \omega_1 L & Ls + r_L \end{bmatrix} \tag{2-15}$$

and similarly, the admittance of a capacitor is

$$\begin{bmatrix} Cs & -\omega_1 C \\ \omega_1 C & Cs \end{bmatrix} \tag{2-16}$$

Figure 2-6 shows the equivalent circuit of Figure 2-5 in the *dq* domain, where a stiff dc link is considered.

Figure 2-6 Equivalent circuit of Figure 2-5 in the dq domain (the PLL and dc link controller are neglected).
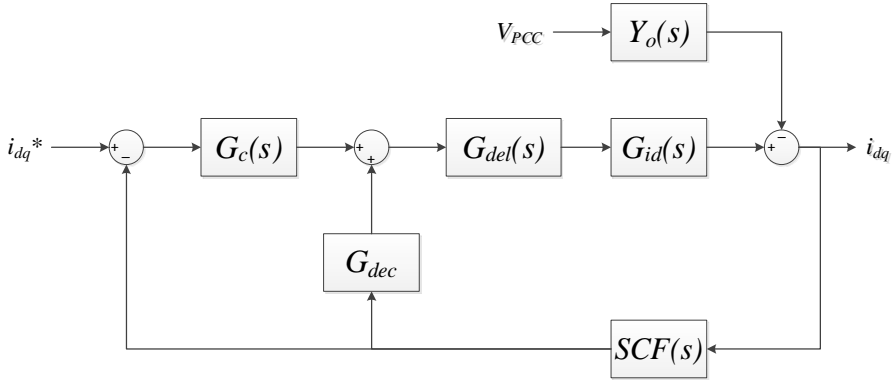
Figure 2-7 Block diagram of Figure 2-5, where the PLL and the dc link controller are neglected.

The control block diagram is shown in Figure 2-7, where the electrical equations as (2-17) can be expressed by Y_o and G_{id} blocks (Note matrices are denoted by bold symbols).

$$\begin{bmatrix} v_d \\ v_q \end{bmatrix} = \begin{bmatrix} Ls + r_L & -\omega_1 L \\ \omega_1 L & Ls + r_L \end{bmatrix} \begin{bmatrix} -i_d \\ -i_q \end{bmatrix} + \begin{bmatrix} vc_d \\ vc_q \end{bmatrix} \tag{2-17}$$

$$\boldsymbol{Y_o} = -\begin{bmatrix} Ls + r_L & -\omega_1 L \\ \omega_1 L & Ls + r_L \end{bmatrix}^{-1} \tag{2-18}$$

$$\boldsymbol{G_{id}} = \begin{bmatrix} Ls + r_L & -\omega_1 L \\ \omega_1 L & Ls + r_L \end{bmatrix}^{-1} \tag{2-19}$$

It should be noted that G_{del} is the PWM delay model in the dq domain, which can be obtained from (2-14) by having the abc domain model as

$$G_{del_{abc}}(s) = \begin{bmatrix} 1 & 0 & 0 \\ 0 & 1 & 0 \\ 0 & 0 & 1 \end{bmatrix} e^{-1.5sT_s} \tag{2-20}$$

SCF is similarly the signal conditioning filter in the dq domain, whose abc domain representation is

$$SCF_{abc}(s) = \begin{bmatrix} 1 & 0 & 0 \\ 0 & 1 & 0 \\ 0 & 0 & 1 \end{bmatrix} \frac{\omega_n^2}{s^2 + 2\xi\omega_n s + \omega_n^2} \tag{2-21}$$

which is a second order low-pass filter, where ω_n is the cutoff frequency and ξ is the damping of the filter.

$G_c(s)$ is the current controller, which is implemented in the dq domain as two PI controllers:

$$\boldsymbol{G_c}(s) = \begin{bmatrix} k_p + \dfrac{k_i}{s} & 0 \\ 0 & k_p + \dfrac{k_i}{s} \end{bmatrix} \tag{2-22}$$

and G_{dec} is the decoupling term which is used to improve the performance and decouple d and q signals.

$$\boldsymbol{G_{dec}}(s) = \begin{bmatrix} 0 & -k_d \\ k_d & 0 \end{bmatrix} \tag{2-23}$$

The output admittance of the converter assuming $i_{dq}*=0$ is indeed the transfer function from the terminal voltage to the current inward the converter (mind the direction shown in Figure 2-6).

$$\boldsymbol{Y_{out}} = \begin{bmatrix} Y_{dd} & Y_{dq} \\ Y_{qd} & Y_{qq} \end{bmatrix} = -\left(\boldsymbol{Y_g} \boldsymbol{G_{PWM}} (\boldsymbol{G_c} - \boldsymbol{G_{dec}}) \boldsymbol{SCF} + \boldsymbol{I_{2\times2}} \right)^{-1} \boldsymbol{Y_o} \tag{2-24}$$

If the PLL is considered then the system becomes nonlinear due to the dynamics of the detected angle, which is a trigonometric function and should also be considered in the model. Small-signal linearization can be used to simplify the analysis. Figure 2-8 shows the small signal model of Figure 2-6 in the dq domain.
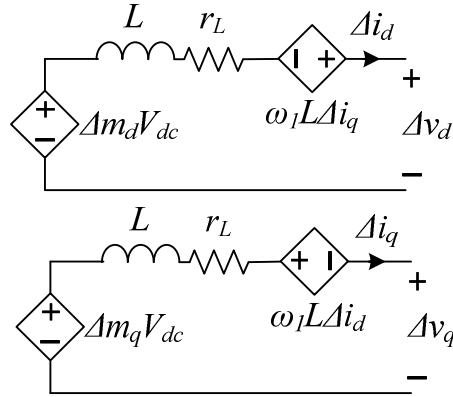
Figure 2-8 Small signal equivalent circuit of Figure 2-5 in the dq domain.

The rotating frame is a virtual frame that is calculated by the PLL, and if there is a small signal perturbation at the terminal voltage, the rotating frame would also be perturbed. In other words, the *dq* domain quantities, which are calculated by the controller, are now slightly different from what they would be without the perturbation. Therefore, it is beneficial here to define two frames, one is the system frame, which is aligned with the fundamental frequency and would not be affected by the perturbation and the other frame is the controller rotating frame, which is aligned with the PLL. Superscript "s" stands for system frame and superscript "c" stands for the controller frame [20].

$$\begin{bmatrix} V_d^c + \Delta v_d^c \\ 0 + \Delta v_q^c \end{bmatrix} = \begin{bmatrix} \cos\Delta\theta & \sin\Delta\theta \\ -\sin\Delta\theta & \cos\Delta\theta \end{bmatrix} \begin{bmatrix} V_d^s + \Delta v_d^s \\ 0 + \Delta v_q^s \end{bmatrix} \qquad (2\text{-}25)$$

where *Δθ* is the phase difference between the two frames. Equation (2-25) can easily be simplified by assuming *Δθ≈0* to

$$\begin{bmatrix} \Delta v_d^c \\ \Delta v_q^c \end{bmatrix} = \begin{bmatrix} \Delta v_d^s \\ \Delta v_q^s - V_d^s \Delta\theta \end{bmatrix} \qquad (2\text{-}26)$$

Figure 2-9 shows the block diagram of a synchronous reference frame (SRF)-PLL, where the small signal model is given by

$$\Delta\theta = \Delta v_q^c \left(kp_{pll} + \frac{ki_{pll}}{s} \right) \cdot \frac{1}{s} \qquad (2\text{-}27)$$

Then, if (2-26) is combined with (2-27), the relationship of the detected angle with the voltage in the system coordinates can be obtained as (2-28).

$$\Delta\theta = \frac{kp_{pll}s + ki_{pll}}{s^2 + V_d^s kp_{pll}s + V_d^s ki_{pll}}\Delta v_q^s = G_{PLL}(s)\Delta v_q^s \tag{2-28}$$
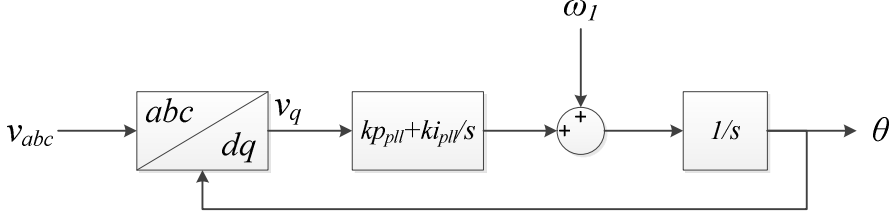
Figure 2-9 Block diagram of an synchronous reference frame-PLL.

It is worth to study how the currents in the controller reference frame are affected by the perturbation:

$$\begin{bmatrix} \Delta i_d^c \\ \Delta i_q^c \end{bmatrix} = \begin{bmatrix} \Delta i_d^s \\ \Delta i_q^s \end{bmatrix} + \begin{bmatrix} I_q^s G_{PLL}(s) \\ -I_d^s G_{PLL}(s) \end{bmatrix} v_q^s = \begin{bmatrix} \Delta i_d^s \\ \Delta i_q^s \end{bmatrix} + \boldsymbol{G}_{PLL}^I \begin{bmatrix} \Delta v_d^s \\ \Delta v_q^s \end{bmatrix} \tag{2-29}$$

The modulation indices are the outcome of the controller, and therefore, during the reverse *dq* transformation, they are affected by the perturbation

$$\begin{bmatrix} \Delta m_d^s \\ \Delta m_q^s \end{bmatrix} = \begin{bmatrix} \Delta m_d^c \\ \Delta m_q^c \end{bmatrix} + \begin{bmatrix} 0 & -M_q^s G_{PLL}(s) \\ 0 & M_d^s G_{PLL}(s) \end{bmatrix} \begin{bmatrix} \Delta v_d^s \\ \Delta v_q^s \end{bmatrix} = \begin{bmatrix} \Delta m_d^c \\ \Delta m_q^c \end{bmatrix} + \boldsymbol{G}_{PLL}^d \begin{bmatrix} \Delta v_d^s \\ \Delta v_q^s \end{bmatrix} \tag{2-30}$$

Therefore, the block diagram of the current controller can be updated as shown in Figure 2-10. Notice the highlighted coordinates and additional blocks introduced by the PLL. Thus, the output admittance can be updated as

$$\boldsymbol{Y}_{out} = -(\boldsymbol{G}_{id}\boldsymbol{G}_{del}(\boldsymbol{G}_c - \boldsymbol{G}_{dec})\boldsymbol{SCF} + \boldsymbol{I}_{2\times2})^{-1}\Big(\boldsymbol{Y}_o$$
$$+ \boldsymbol{G}_{id}\boldsymbol{G}_{del}\big((\boldsymbol{G}_{dec} - \boldsymbol{G}_c)\boldsymbol{G}_{PLL}^i + \boldsymbol{G}_{PLL}^d\big)\boldsymbol{SCF}\Big) \tag{2-31}$$
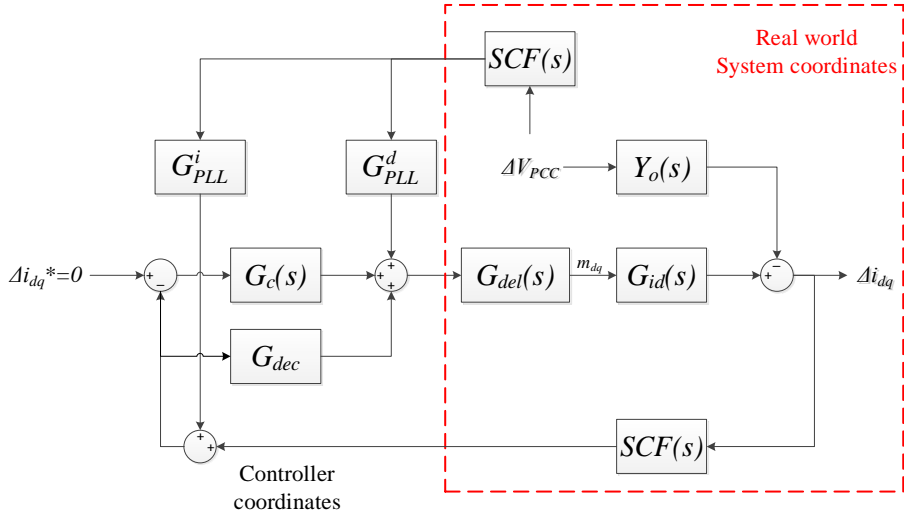
Figure 2-10 Block diagram of Figure 2-5 including the PLL.

To model the dc link controller, the dynamics of the dc side should also be considered. Assuming lossless power switches in the converter, the dc side and ac side active powers are equal.

$$P = v_{dc}i_{dc} = \frac{3}{2}\left(v_d i_d + v_q i_q\right) \Rightarrow i_{dc} = \frac{3}{2}\left(d_d i_d + d_q i_q\right) \tag{2-32}$$

$$v_{dc} = -Z_{dc}i_{dc} \tag{2-33}$$

$$\Delta v_{dc} = -\frac{3}{2}Z_{dc}\left(\Delta i_d^s D_d^s + I_d^s \Delta d_d^s + \Delta i_q^s D_q^s + I_q^s \Delta d_q^s\right) \tag{2-34}$$

The modulation in the ac side can also be linearized as

$$v_c = m_{dq}v_{dc} \Rightarrow \Delta v_c = M_{dq}\Delta v_{dc} + \Delta m_{dq}V_{dc} \tag{2-35}$$

Therefore, the equivalent circuit in the *dq* domain and the control block diagram can be updated as shown in Figure 2-11, where

$$G_{cv}(s) = \begin{bmatrix} -\left(k_{p_{dc}} + \frac{k_{i_{dc}}}{s}\right) \\ 0 \end{bmatrix} \tag{2-36}$$

$$Z_{dc} = \frac{1}{C_{dc}s} \tag{2-37}$$

From the dc side

$$\Delta v_{dc} = -\frac{3}{2}Z_{dc}[I_d^s \quad I_q^s]\begin{bmatrix}\Delta d_d^s \\ \Delta d_q^s\end{bmatrix} - \frac{3}{2}Z_{dc}[D_d^s \quad D_q^s]\begin{bmatrix}\Delta i_d^s \\ \Delta i_q^s\end{bmatrix}$$
$$= \boldsymbol{G_{dv}}\begin{bmatrix}\Delta d_d^s \\ \Delta d_q^s\end{bmatrix} + \boldsymbol{G_{iv}}\begin{bmatrix}\Delta i_d^s \\ \Delta i_q^s\end{bmatrix} \tag{2-38}$$

and from the ac side

$$\begin{bmatrix}\Delta i_d^s \\ \Delta i_q^s\end{bmatrix}\Bigg|_{\Delta d_{dq}=0 \& \Delta v_{dq}=0} = \begin{bmatrix}Ls + r_L & -\omega_1 L \\ \omega_1 L & Ls + r_L\end{bmatrix}^{-1}\begin{bmatrix}D_d^s \\ D_q^s\end{bmatrix}\Delta v_{dc} = \boldsymbol{G_{vi}}\Delta v_{dc} \tag{2-39}$$

Therefore,

$$\boldsymbol{Y_{out}} = -(\boldsymbol{I}_{2\times2} - \boldsymbol{G_{vi}G_{iv}} - (\boldsymbol{G_{vi}G_{vd}} + \boldsymbol{G_{id}})\boldsymbol{\Gamma_i})^{-1}(\boldsymbol{Y_o} + \boldsymbol{G_{id}\Gamma_v}) \tag{2-40}$$

where

$$\boldsymbol{\Gamma_i} = -(\boldsymbol{I}_{2\times2} + \boldsymbol{G_{del}G_{ci}G_{cv}}SCF_{dc}\boldsymbol{G_{vd}})^{-1}\boldsymbol{G_{del}G_{ci}}(\boldsymbol{G_{cv}}SCF_{dc}\boldsymbol{G_{iv}} + SCF) \tag{2-41}$$

$$\boldsymbol{\Gamma_v} = (\boldsymbol{I}_{2\times2} + \boldsymbol{G_{del}G_{ci}G_{cv}}SCF_{dc}\boldsymbol{G_{vd}})^{-1}\boldsymbol{G_{del}}(\boldsymbol{G_{PLL}^d} - \boldsymbol{G_{ci}G_{PLL}^i})SCF \tag{2-42}$$
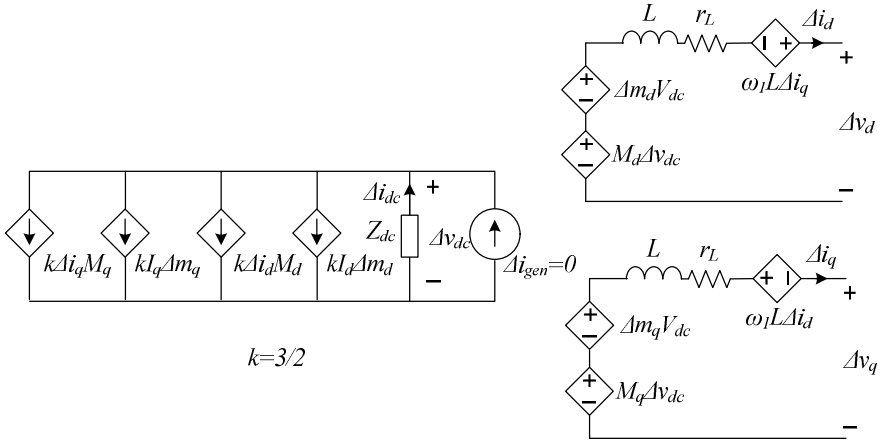
(a)
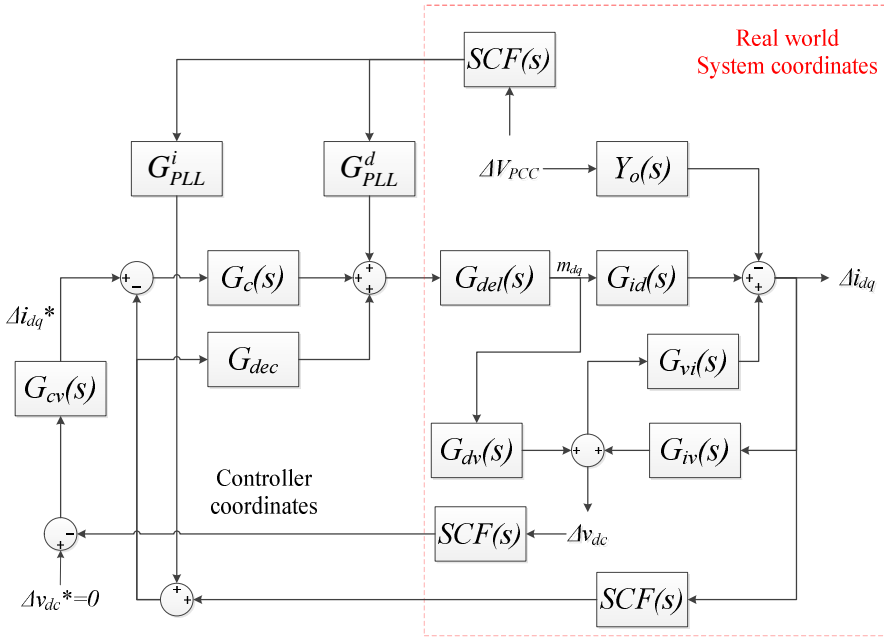
(b)

Figure 2-11 Effects of considering the dc link controller on (a) equivalent circuit (b) control block diagram.

In [29] G_{vi} is not considered but it is a main contribution of the developed model in this thesis. Assume if G_{vi} is not considered and if the dc link controller gains are zero, then the perturbation on the dc link voltage cannot be seen anywhere in the model of Figure 2-11 (b), but in reality it obviously affects the output current. To validate the developed admittance matrix the method shown in Figure 2-12 can be used in a circuit simulator like PLECS [30]. The perturbations must be applied in the *dq* domain (v_d and v_q blocks), and the observations must be read in the same *dq* frame (i_d and i_q blocks) [31], [32]. The necessary angle of the *dq* transformation is a ramp signal, whose slope is ω_1. It must be noted that the measurement is carried out in the system coordinates; therefore, no PLL is needed. By using the frequency sweep feature in PLECS, the admittance matrices can be found as shown in Figure 2-13, which shows a perfect correlation with the developed model (the parameters of the Active Front End can be found in §2.4.3). It must be noted that the full detailed switching models are employed in this model. Figure 2-14 shows how neglecting G_{vi} affects the impedances. To see how this assumption affects the stability evaluation refer to §2.4.3.
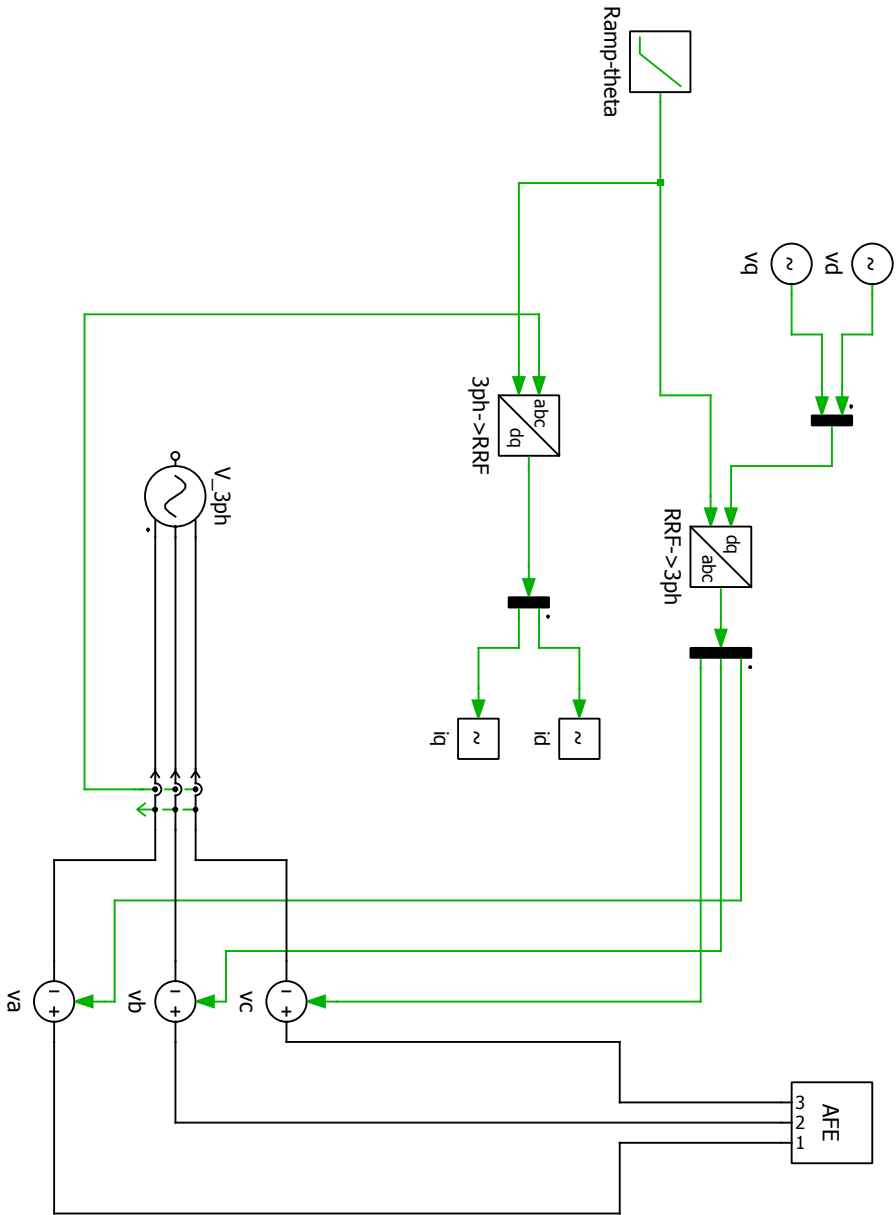
Figure 2-12 How to measure the dq admittances using a circuit simulator (e.g. PLECS).
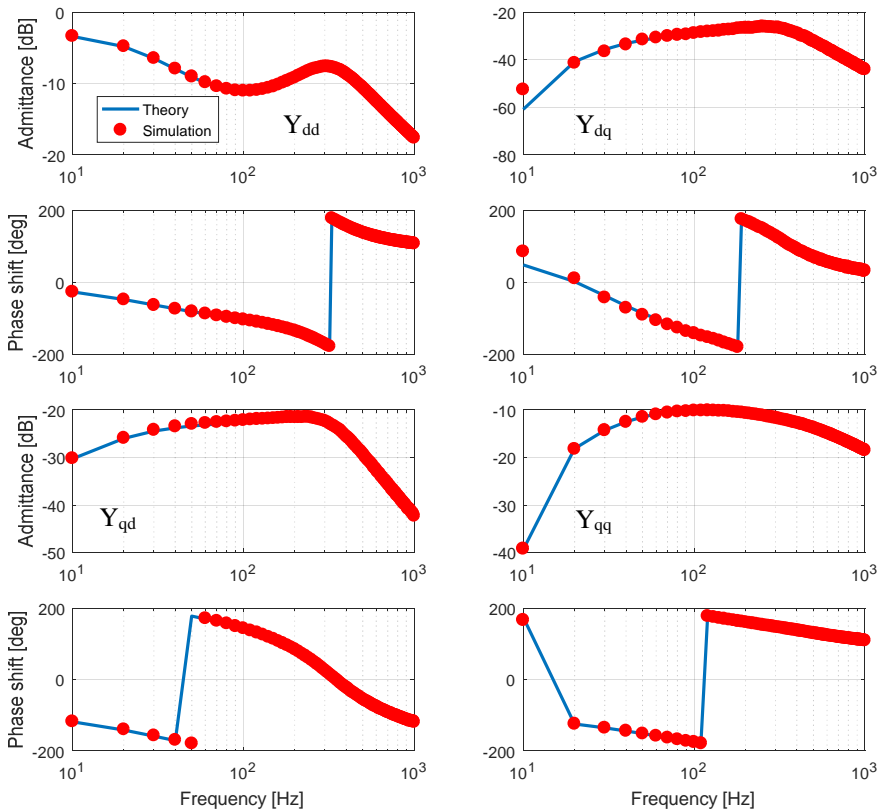
Figure 2-13 Validation of the converter admittance (derived theoretically) by time domain simulation.
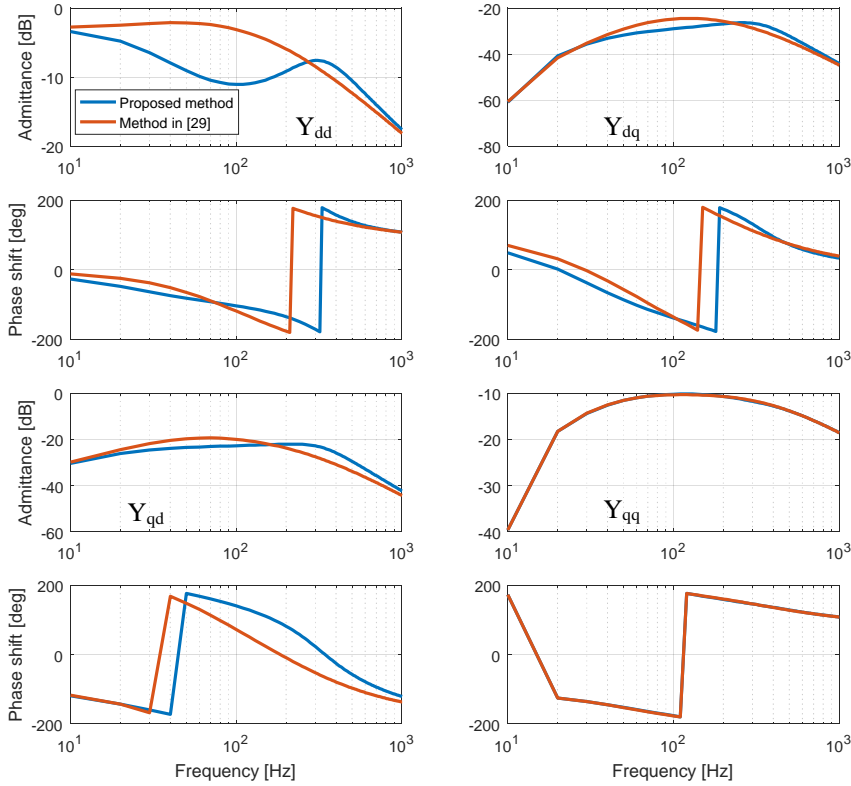
Figure 2-14 Comparison of the calculated dq admittance by the developed model and the model presented in [29].

2.2.3.3 Impedance modelling in the sequence domain

In this method small signal perturbations are imposed to the three-phase voltages/currents and by observing the three phase phasors of the response in currents/voltages, the admittance/impedance at a given frequency and sequence can be obtained. For instance, in time domain the Phase A voltage in Figure 2-15 can be represented as [33]

$$v_a(t) = V_1 \cos \omega_1 t + V_p \cos(\omega_p t) + V_n \cos(\omega_n t) \tag{2-43}$$

where ω_1 is the system base frequency, V_1 is the fundamental voltage at PCC, V_p and V_n are the positive- and negative-sequence perturbations, which are much smaller than V_1. In the frequency domain, the voltage of phase A is given by (2-44).

$$\mathbf{V_a}(f) = \begin{cases} \mathbf{V_1} = V_1/2, & f = \pm f_1 \\ \mathbf{V_p} = V_p/2 & f = \pm f_p \\ \mathbf{V_n} = V_n/2 & f = \pm f_n \end{cases} \tag{2-44}$$

where $\mathbf{V_p}$ and $\mathbf{V_n}$ are complex vectors rotating with the specified frequency and in this example their angles are zero. The electrical relationships using an average model of the converter in the frequency domain can be written as it follows

$$LsI_{abc} = M_{abc}(s)G_{PWM}(s) - V_{abc} \tag{2-45}$$

where M_{abc} is the modulation signal, and $G_{PWM}(s)$ as discussed before models the gain and delay of the converter, which in the frequency domain can be considered as

$$G_{PWM}(s) = V_{dc}e^{-1.5sT_s} \tag{2-46}$$

and T_s is the sampling period.

(a)

(b)
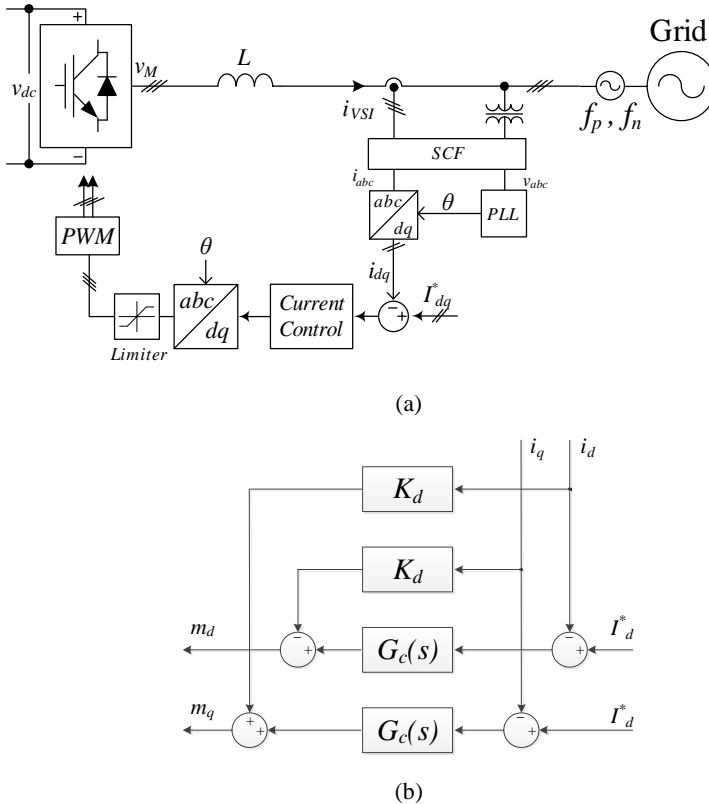
Figure 2-15 Considered voltage source converter for the sequence domain impedance derivation (a) the circuit layout (b) the current controller.

Without PLL

First, the effects of the PLL are neglected. Therefore, the detected angle of the PLL is free of any perturbation. The actual currents in the *dq* frame can be written as

$$\begin{bmatrix} I_d \\ I_q \end{bmatrix} = \frac{2}{3} \begin{bmatrix} \cos\theta & \cos\left(\theta - \frac{2\pi}{3}\right) & \cos\left(\theta + \frac{2\pi}{3}\right) \\ -\sin\theta & -\sin\left(\theta - \frac{2\pi}{3}\right) & -\sin\left(\theta + \frac{2\pi}{3}\right) \end{bmatrix} \begin{bmatrix} I_a \\ I_b \\ I_c \end{bmatrix} = T_{dq} I_{abc} \qquad (2\text{-}47)$$

where $\theta(t)$ is the detected angle obtained by a PLL. The frequency domain representation of the dq currents is

$$I_d(f) = \begin{cases} I_d^* & f = dc \\ SCF\left(s = \pm j\omega_p\right)\mathbf{I_p} & f = \pm(f_p - f_1) \\ SCF\left(s = \pm j\omega_n\right)\mathbf{I_n} & f = \pm(f_n + f_1) \end{cases} \qquad (2\text{-}48)$$

$$I_q(f) = \begin{cases} I_q^* & f = dc \\ \mp jSCF\left(s = \pm j\omega_p\right)\mathbf{I_p} & f = \pm(f_p - f_1) \\ \pm jSCF(s = \pm j\omega_n)\mathbf{I_n} & f = \pm(f_n + f_1) \end{cases} \qquad (2\text{-}49)$$

where $\mathbf{I_p}$ and $\mathbf{I_n}$ are the currents in the positive- and negative-sequence domain, respectively and they will be calculated later. M_d and M_q can according to Figure 2-15 (b) in the dq domain be found by

$$\begin{bmatrix} M_d \\ M_q \end{bmatrix} = \begin{bmatrix} -G_c(f) & -K_d \\ K_d & -G_c(f) \end{bmatrix} \begin{bmatrix} I_d \\ I_q \end{bmatrix} \qquad (2\text{-}50)$$

Assuming the fundamental current control is fulfilled, the modulation signals affected by the perturbations are

$$M_d(f) = \begin{cases} \left(-G_C\left(s = \pm j(\omega_p - \omega_1)\right) \pm jK_d\right)SCF\left(s = \pm j\omega_p\right)\mathbf{I_p} & f = \pm(f_p - f_1) \\ \left(-G_C\left(s = \pm j(\omega_n + \omega_1)\right) \mp jK_d\right)SCF\left(s = \pm j\omega_n\right)\mathbf{I_n} & f = \pm(f_n + f_1) \end{cases}$$

$$(2\text{-}51)$$

$$M_q(f) = \begin{cases} \left(\pm jG_C\left(s = \pm j(\omega_p - \omega_1)\right) + K_d\right)SCF\left(s = \pm j\omega_p\right)\mathbf{I_p} & f = \pm(f_p - f_1) \\ \left(\mp jG_C\left(s = \pm j(\omega_n + \omega_1)\right) + K_d\right)SCF\left(s = \pm j\omega_n\right)\mathbf{I_n} & f = \pm(f_n + f_1) \end{cases}$$

$$(2\text{-}52)$$

The modulation signal of phase A after the inverse dq transformation is

$$M_a(f)$$
$$= \begin{cases} M_d^0 \pm jM_q^0 & f = \pm f_1 \\ \left(-G_C\left(s = \pm j(\omega_p - \omega_1)\right) \pm jK_d\right)SCF(s = \pm j\omega_p)\mathbf{I_p} & f = \pm f_p \\ \left(-G_C(s = \pm j(\omega_n + \omega_1)) \mp jK_d\right)SCF(s = \pm j\omega_n)\mathbf{I_n} & f = \pm f_n \end{cases} \qquad (2\text{-}53)$$

where M_d^0 and M_q^0 are the modulation indices at the fundamental frequency, which can be obtained after a load flow analysis. By using (2-45) the admittance of the converter can be found as [33]

$$Y_p(s) = \frac{I_p}{V_p} = \frac{1}{G_{PWM}(G_c(s - j\omega_1) - jK_d)SCF(s) + sL} \qquad (2\text{-}54)$$

$$Y_n(s) = \frac{I_n}{V_n} = \frac{1}{G_{PWM}(G_c(s + j\omega_1) + jK_d)SCF(s) + sL} \qquad (2\text{-}55)$$

With PLL

An SRF-PLL as shown in Figure 2-9 is also considered in this part. Similarly the relationship between the detected angle and the perturbation can be described by [33], [34]

$$\Delta\theta(f)$$
$$= \begin{cases} \mp jG_{PLL}\left(s = \pm j(\omega_p - \omega_1)\right)SCF(s = \pm j\omega_p)\mathbf{V_p} & f = \pm(f_p - f_1) \\ \pm jG_{PLL}(s = \pm j(\omega_n + \omega_1))SCF(s = \pm j\omega_n)\mathbf{V_n} & f = \pm(f_n + f_1) \end{cases} \qquad (2\text{-}56)$$

where G_{PLL} is the same as given in (2-28) .

The small signal model of the dq and inverse dq transformations can be written as:

$$T_{dq_{PLL}} = \begin{bmatrix} \cos\Delta\theta & \sin\Delta\theta \\ -\sin\Delta\theta & \cos\Delta\theta \end{bmatrix} T_{dq} \approx \begin{bmatrix} 1 & \Delta\theta \\ -\Delta\theta & 1 \end{bmatrix} T_{dq} \qquad (2\text{-}57)$$

$$T_{dq_{PLL}}^{-1} \approx T_{dq}^{-1} \begin{bmatrix} 1 & -\Delta\theta \\ \Delta\theta & 1 \end{bmatrix} \qquad (2\text{-}58)$$

Therefore, by considering the PLL effect, (2-48) and (2-49) can be updated. It is worth noting that as discussed in [34] the PLL creates additional frequency couplings in the currents. These additional components are considered as $\mathbf{I_{p2}}$ and $\mathbf{I_{n2}}$ analytically and will be eliminated in the end.

$$I_a(f) = \begin{cases} \mathbf{I_1} & f = \pm f_1 \\ \mathbf{I_p} & f = \pm f_p \\ \mathbf{I_n} & f = \pm f_n \\ \mathbf{I_{p2}} & f = \pm(f_p - 2f1) \\ \mathbf{I_{n2}} & f = \pm(f_n + 2f1) \end{cases} \tag{2-59}$$

Then, the currents in the dq frame are

$$I_d(f) = \begin{cases} I_d^* & f = dc \\ SCF\left(s = \pm j(\omega_p - 2\omega_1)\right)\mathbf{I_{p2}} + & f = \pm(f_p - f_1) \\ \quad SCF(s = \pm j\omega_p)\mathbf{I_p} + \Delta\theta I_q^* \\ SCF(s = \pm j(\omega_n + 2\omega_1))\mathbf{I_{n2}} + & f = \pm(f_n + f_1) \\ \quad SCF(s = \pm j\omega_n)\mathbf{I_n} + \Delta\theta I_q^* \end{cases} \tag{2-60}$$

$$I_q(f) = \begin{cases} I_q^* & f = dc \\ \pm jSCF\left(s = \pm j(\omega_p - 2\omega_1)\right)\mathbf{I_{p2}} & f = \pm(f_p - f_1) \\ \quad \mp jSCF(s = \pm j\omega_p)\mathbf{I_p} - \Delta\theta I_d^* \\ \mp jSCF(s = \pm j(\omega_n + 2\omega_1))\mathbf{I_{n2}} & f = \pm(f_n + f_1) \\ \quad \pm jSCF(s = \pm j\omega_n)\mathbf{I_n} - \Delta\theta I_d^* \end{cases} \tag{2-61}$$

Similar to (2-53), the modulation index of the phase A can be found by

$$\begin{bmatrix} M_a \\ M_b \\ M_c \end{bmatrix} = T_{dq}^{-1}\begin{bmatrix} 1 & -\Delta\theta \\ \Delta\theta & 1 \end{bmatrix}\begin{bmatrix} M_d \\ M_q \end{bmatrix} = T_{dq}^{-1}\begin{bmatrix} M_d - \Delta\theta M_q \\ M_d\Delta\theta + M_q \end{bmatrix} = T_{dq}^{-1}\begin{bmatrix} M_{d1} \\ M_{q1} \end{bmatrix} \tag{2-62}$$

$$M_a(f) = \begin{cases} M_d^0 \pm jM_q^0 & f = \pm f_1 \\ \left.(M_{d1} \pm jM_{q1})\right|_{f\pm(f_p-f_1)} & f = \pm f_p \\ \left.(M_{d1} \mp jM_{q1})\right|_{f\pm(f_n+f_1)} & f = \pm f_n \\ \left.(M_{d1} \mp jM_{q1})\right|_{f\pm(f_p-f_1)} & f = \pm(f_p - 2f1) \\ \left.(M_{d1} \pm jM_{q1})\right|_{f\pm(f_n+f_1)} & f = \pm(f_n + 2f1) \end{cases} \tag{2-63}$$

No additional frequency components are generated in the modulation signal. Therefore, assuming those frequency couplings was a valid assumption. The current response by using (2-45) is

$$
I_a(f) = \begin{cases} Y_{pp}V_p & f = f_p & Pos.\,Seq. \\ Y_{np}V_p & f = f_p - 2f_1 & Neg.\,Seq. \\ Y_{nn}V_n & f = f_n & Neg.\,Seq. \\ Y_{pn}V_n & f = f_n + 2f_1 & Pos.\,Seq \end{cases} \tag{2-64}
$$

where

$$
Y_{pp} = \frac{1 - G_{PWM}(s)SCF(s)G_{PLL}(s - j\omega_1)\left(\dfrac{M_{dq}^0}{2} + \dfrac{I_{dq}^0}{2}G_c(s - j\omega_1)\right)}{sL + G_{PWM}(s)SCF(s)G_c(s - j\omega_1)} \tag{2-65}
$$

$Y_{pn}(s)$

$$
= \frac{G_{PWM}(s + 2j\omega_1)SCF(s)G_{PLL}(s + j\omega_1)\left(\dfrac{M_{dq}^0}{2} + \dfrac{I_{dq}^0}{2}G_c(s + j\omega_1)\right)}{L(s + 2j\omega_1) + G_{PWM}(s + 2j\omega_1)SCF(s + 2j\omega_1)G_c(s + j\omega_1)} \tag{2-66}
$$

$$
Y_{nn}(s) = \mathrm{conj}\left(Y_{pp}(s)\right) \tag{2-67}
$$

$$
Y_{np}(s) = \mathrm{conj}\left(Y_{pn}(s)\right) \tag{2-68}
$$

where $M_{dq}^0 = M_d^0 + jM_q^0$ and $I_{dq}^0 = I_d^0 + jI_q^0$ are the complex modulation signal (fundamental frequency) and the complex current references.

Similar to the *dq* admittances, the derived admittance can be verified by time domain simulations in PLECS as shown in Figure 2-16. The perturbations are three voltages sources, which have the same amplitude and frequency but the phase angles are set according to the sequence. In steady state the currents are read and after an FFT all frequency components can be obtained. The positive frequencies in Figure 2-17 represent the positive sequence and the negative frequencies represent the negative sequence. That is the reason in the legend both positive and negative sequence components can be seen. It can be seen that both the direct components (Y_{pp} and Y_{nn}) and the frequency couplings (Y_{np} and Y_{pn}) are in good agreement with the simulations. In §2.4.1, the effects of the frequency couplings on the stability studies are studied as a test case.
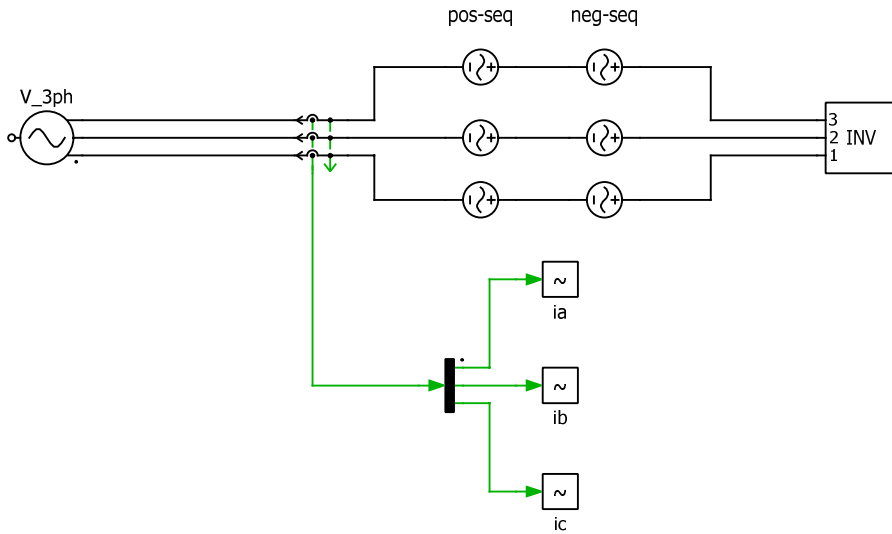
Figure 2-16 How to measure the positive- and negative-sequence admittances using a circuit simulator.
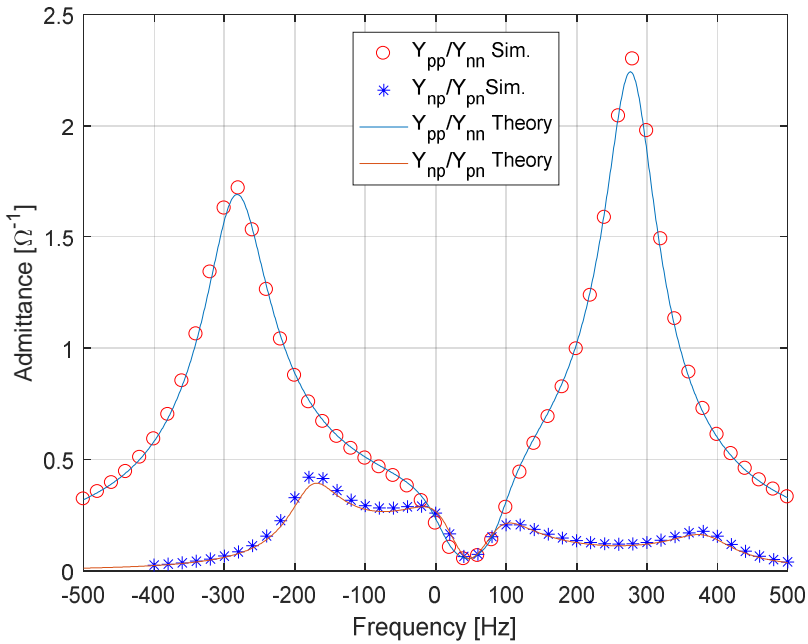
Figure 2-17 Validation of the sequence admittances by time domain simulation, for the system shown in Figure 2-15.

2.2.3.4 Comparing different domains and methods for stability analysis

In [26], [33], it has been stated that sequence domain modelling is more advantageous to the *dq* domain, since it results in scalar impedances not 2×2 matrices. However, in this chapter it is shown that the PLL creates a coupling term in the sequence domain impedances, and therefore, the final impedances are also 2×2 matrices. Moreover, the sequence domain impedance in this situation has a big drawback, which is the frequency coupling that makes the analysis much more complicated than the *dq* domain models. The *dq* domain transfer function matrices can easily be analyzed by the classical control theory, since there is no frequency coupling (multi-frequency response). Therefore, the *dq* domain is used for the rest of the studies in this thesis as long as the system is balanced. For unbalanced systems, there are more frequency couplings, and the theory of Linear Time Periodic systems should be used for both domains; however, the analysis in the sequence domain is more intuitive in this case (see §4.2.2). The measurements in the sequence domain are easier than in the *dq* domain, since in the *dq* domain the perturbation should be synchronized with the fundamental frequency of the system, which is not exactly known. Table 2-1 summarizes the differences between the two domains.

Table 2-1 Comparison of different domains for modelling of three-phase systems.

Feature	Modelling domain	
	Sequence domain	*dq* domain
Measurements	Easy	Difficult
Importance of Fundamental frequency	Not important	Important
Complexity of high frequency models	1×1 impedances	2×2 impedances
Complexity of the low frequency models	2×2 impedances	2×2 impedances
Unbalanced systems	Medium	Difficult
Applicability of classical control theory	Difficult due to complex-coefficient transfer functions	Medium as MIMO transfer functions are used

2.3. EIGENVALUE BASED STABILITY ANALYSIS

2.3.1. NONLINEAR STATE SPACE EQUATIONS OF THE SYSTEM

In this part the dynamical equations of an active front end (AFE) as shown in Figure 2-18 are obtained and no linearization is used. For the sake of simplicity, the signal conditioning filters are neglected. The ac side equations in the system coordinates can be written as

$$\frac{d}{dt} i_d^s = \frac{1}{L}\left(-v_d^s - r i_d^s + \omega_b L i_q^s - m_d^s v_{dc}\right) \tag{2-69}$$

$$\frac{d}{dt} i_q^s = \frac{1}{L}\left(-v_q^s - r i_q^s - \omega_b L i_d^s - m_q^s v_{dc}\right) \tag{2-70}$$
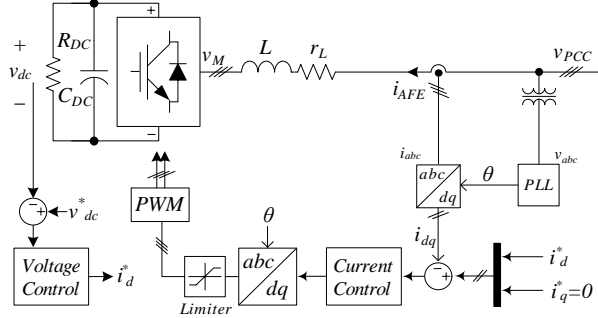
Figure 2-18 An active front end, where the signal conditioning filters are neglected.

Similarly the dc side equations can be written as

$$\frac{d}{dt} v_{dc} = \frac{1}{C_{dc}}\left(-i_{dc} - \frac{v_{dc}}{R_{dc}}\right) \tag{2-71}$$

$$i_{dc} = \frac{3}{2}\left(m_d^s i_d^s + m_q^s i_q^s\right) \tag{2-72}$$

The dc link controller is a proportional integrator controller as shown in Figure 2-19. The differential equation of the dc link controller can be written as

$$i_d^* = -\left((v_{dc}^* - v_{dc})k_{p_v} + k_{i_v} x_{dc}\right) \tag{2-73}$$

$$\frac{d}{dt} x_{dc} = v_{dc}^* - v_{dc} \tag{2-74}$$
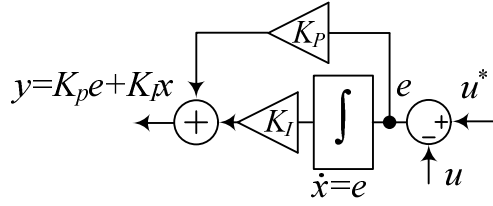
Figure 2-19 Differential algebraic equations of a PI controller.

Similarly, the current controller can be modelled. Note the controller acts on the currents in the controller frame as it follows

$$m_d^c = (i_d^* - i_d^c)k_p + k_i x_{i_d^c} \tag{2-75}$$

$$\frac{d}{dt}x_{i_d^c} = i_d^* - i_d^c - K_d i_q^c \tag{2-76}$$

$$m_q^c = (i_q^* - i_q^c)k_p + k_i x_{i_q^c} \tag{2-77}$$

$$\frac{d}{dt}x_{i_q^c} = i_q^* - i_q^c + K_d i_d^c \tag{2-78}$$

The effects of the frame rotation between the controller and the system coordinates can be summarized as

$$\begin{bmatrix} v_d^c \\ v_q^c \end{bmatrix} = \begin{bmatrix} \cos\delta & \sin\delta \\ -\sin\delta & \cos\delta \end{bmatrix} \begin{bmatrix} v_d^s \\ v_q^s \end{bmatrix} \tag{2-79}$$

$$\begin{bmatrix} i_d^c \\ i_q^c \end{bmatrix} = \begin{bmatrix} \cos\delta & \sin\delta \\ -\sin\delta & \cos\delta \end{bmatrix} \begin{bmatrix} i_d^s \\ i_q^s \end{bmatrix} \tag{2-80}$$

$$\begin{bmatrix} c_d^s \\ c_q^s \end{bmatrix} = \begin{bmatrix} \cos\delta & -\sin\delta \\ \sin\delta & \cos\delta \end{bmatrix} \begin{bmatrix} m_d^c \\ m_q^c \end{bmatrix} \tag{2-81}$$

where c_{dq}^s is the modulation index in the system coordinates before modelling the delay. The large signal model of the PLL can easily be obtained from Figure 2-9 as

$$\frac{d}{dt}x_{PLL} = v_q^c \tag{2-82}$$

$$\frac{d}{dt}\delta = k_{p_{pll}}v_q^c + k_{i_{pll}}x_{PLL} \tag{2-83}$$

The delay in the converter can be modelled by a Padé approximant. For the sake of simplicity, a first order approximation is used.

$$e^{-sT_d} \approx \frac{1 - sT_d/2}{1 + sT_d/2} \tag{2-84}$$

This can be easily transformed to the state space equations as

$$A = -\frac{2}{T_d}, \qquad B = 1 \tag{2-85}$$

$$C = \frac{4}{T_d}, \qquad D = -1 \tag{2-86}$$

It must be noted that (2-84) is valid in the *abc* domain. The *dq* model can be obtained by using (2-87) and (2-88) [35], which is discussed in more details in §3.4.1.

$$A_{dq} = \begin{bmatrix} A & \omega_1 \\ -\omega_1 & A \end{bmatrix}, \qquad B_{dq} = \begin{bmatrix} B & 0 \\ 0 & B \end{bmatrix} \tag{2-87}$$

$$C_{dq} = \begin{bmatrix} C & 0 \\ 0 & C \end{bmatrix}, \qquad D_{dq} = \begin{bmatrix} D & 0 \\ 0 & D \end{bmatrix} \tag{2-88}$$

Therefore, the modulation indices in the system coordinates after the delays are

$$\begin{bmatrix} m_d^s \\ m_q^s \end{bmatrix} = C_{dq} \begin{bmatrix} x_{delay}^d \\ x_{delay}^q \end{bmatrix} + D_{dq} \begin{bmatrix} c_d^s \\ c_q^s \end{bmatrix} \tag{2-89}$$

$$\frac{d}{dt} \begin{bmatrix} x_{delay}^d \\ x_{delay}^q \end{bmatrix} = A_{dq} \begin{bmatrix} x_{delay}^d \\ x_{delay}^q \end{bmatrix} + B_{dq} \begin{bmatrix} c_d^s \\ c_q^s \end{bmatrix} \tag{2-90}$$

The final nonlinear state space model can be represented as

$$\frac{d}{dt} x_T = f(x_T, u_T) \tag{2-91}$$

$$y_T = g(x_T, u_T) \tag{2-92}$$

where

$$x_T = \begin{bmatrix} v_{dc} & i_d^s & i_q^s & x_{dc} & x_{i_d^c} & x_{i_q^c} & x_{PLL} & \delta & x_{delay}^d & x_{delay}^q \end{bmatrix}^T \tag{2-93}$$

$$u_T = \begin{bmatrix} v_d^s & v_q^s & v_{dc}^* & \cdots \end{bmatrix}^T \qquad\qquad (2\text{-}94)$$

$$y_T = \begin{bmatrix} i_d^s & i_q^s & \delta & \cdots \end{bmatrix}^T \qquad\qquad (2\text{-}95)$$

As seen in (2-94) and (2-95), the inputs and outputs can be defined arbitrarily.

Figure 2-20 compares the large signal transients of the detailed model in the circuit simulator and the solution of the ordinary differential equations of (2-91), where there is a good agreement between the two methods. ODE stands for the solution of the ordinary differential equations described by (2-91).

(a)

(b)

(c)
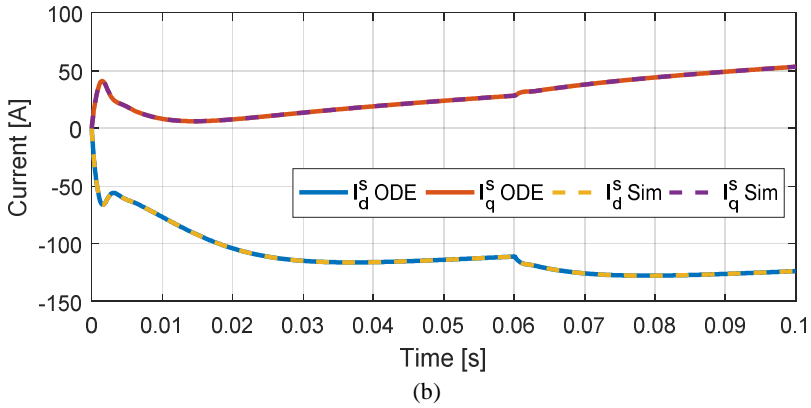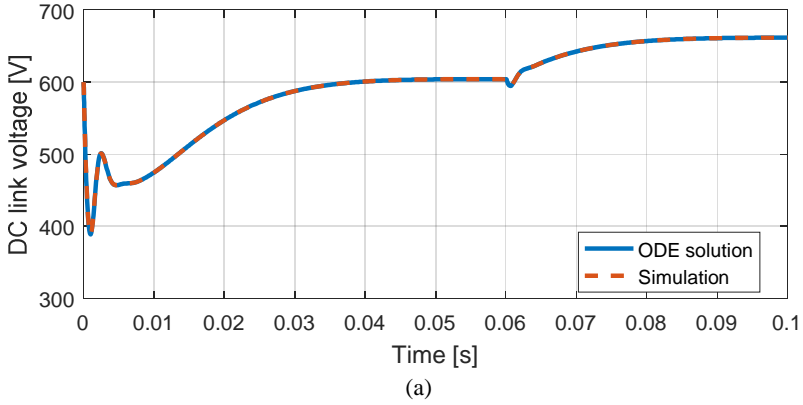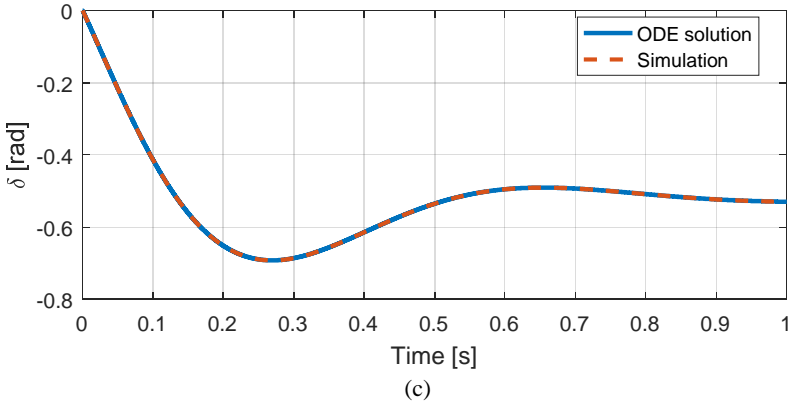
Figure 2-20 Comparing the time domain results with the nonlinear state space model of the AFE in Figure 2-18 (a) DC link voltage (b) dq currents in the system coordinates (c) the angle between the system and controller coordinates.

2.3.2. LINEARIZED STATE SPACE MODEL

Classical design techniques for controllers and analysis methods such as Bode plots and root locus design work well for linear systems. A nonlinear model can be approximated by a linear model around its equilibrium point (steady state operating point). The linearization process in (2-96) and (2-97) is based on the first order Taylor series expansion. It should be noted that the approximated model is valid for a small region around the equilibrium point.

$$\frac{d}{dt}\Delta x_T = \left[\frac{\partial f}{\partial x_T}\right]\Delta x_T + \left[\frac{\partial f}{\partial u_T}\right]\Delta u_T = A\Delta x_T + B\Delta u_T \tag{2-96}$$

$$\Delta y_T = \left[\frac{\partial g}{\partial x_T}\right]\Delta x_T + \left[\frac{\partial g}{\partial u_T}\right]\Delta u_T = C\Delta x_T + D\Delta u_T \tag{2-97}$$

In Figure 2-21 the set point of the dc link voltage is increased by 1%, which can be considered as a small signal change. It can be seen that the linearized and nonlinear models are almost the same. However, if the change in the dc link is increased, then an error can be seen in the linearized model in Figure 2-22.

It should be noted in harmonic emission studies the harmonics are much smaller than the fundamental component; therefore, the linearized models can typically be used for the analysis. For stability studies, it is also a valid assumption to use linearized models, because based on the Lyapunov's indirect method, if a linearized model around an operating point is unstable then the original nonlinear model is unstable at that operating point [36].
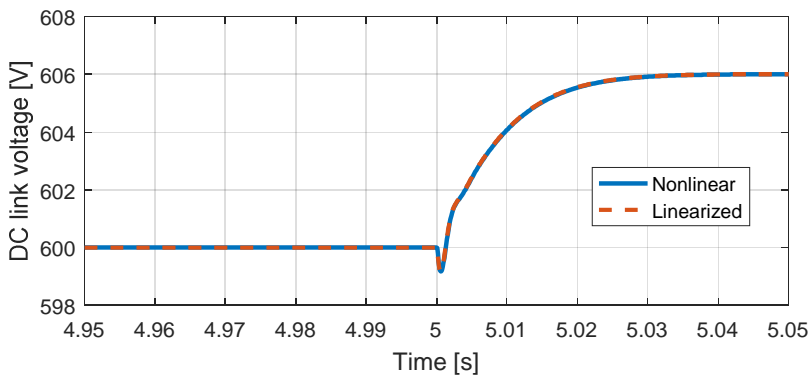
(a)
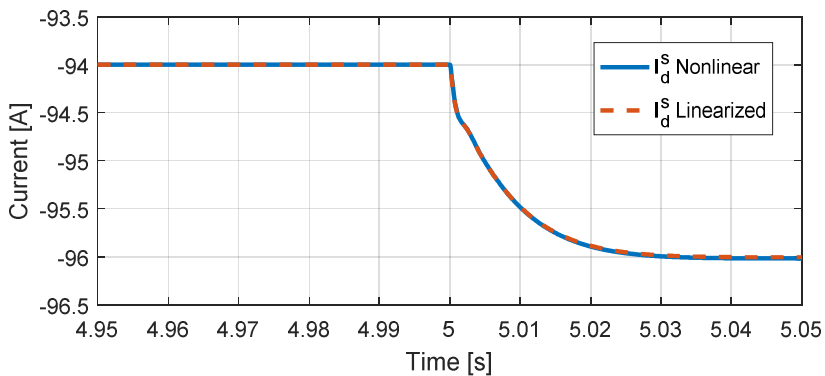
(b)

Figure 2-21 A one-percent step is applied to the dc voltage set point (a) dc voltage (b) direct current in the system coordinates.
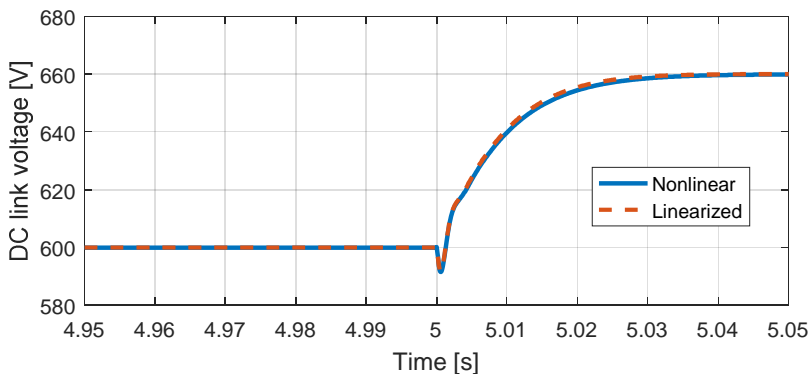
(a)
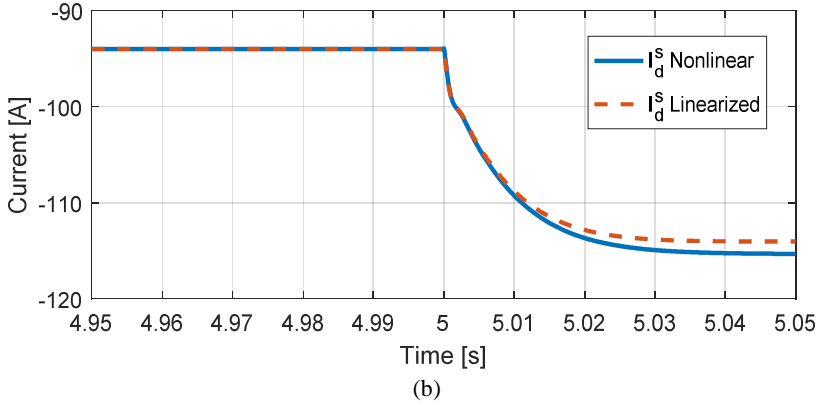
Figure 2-22 A ten-percent step is applied to the dc voltage set point (a) dc voltage (b) direct current in the system coordinates.

The eigenvalues of matrix *A* (also called system or state matrix) are the same as the poles of the equivalent transfer function [37]. Therefore, the stability of the system can be evaluated by the sign of their real part. The *i*th eigenvalue can be a complex number like

$$\lambda_i = \sigma_i + j\omega_i \tag{2-98}$$

where ω_i is the oscillation frequency of this particular eigenvalue and $1/\sigma_i$ is the time constant of this transient dynamic [15]. The damping ratio is defined as

$$\xi_i = -\frac{\sigma_i}{\sqrt{\sigma_i^2 + \omega_i^2}} \tag{2-99}$$

"In other words, the transient response of the system to a perturbation includes this frequency, which will decay with the specified time constant/damping. A negative damping by definition indicates an unstable case, where instead of damping, amplifying happens. Therefore, not only the stability of the system can be assessed using the sign of the real parts, but also the minimum damping of the system can be found. The latter can be considered as a measure that states how stable a system is." [38].

The Participation Factor (PF) analysis can be done by some simple matrix operations [15], [38], [39]. For the *i*th eigenvalue, the participation index can be calculated by

$$P_{ki} = \frac{\partial \lambda_i}{\partial a_{kk}} = \Phi_{ki} \Psi_{ik} \tag{2-100}$$

where Φ_i is the right eigenvector of the ith eigenvalue, Ψ_i is the left eigenvector of the ith eigenvalue as given in (2-101) and (2-102), and P_{ki} indicates the contribution of the kth state on the ith eigenvalue. It should be noted a participation index is unitless.

$$A\Phi_i = \lambda_i \Phi_i \qquad (2\text{-}101)$$

$$\Psi_i A = \Psi_i \lambda_i \qquad (2\text{-}102)$$

2.4. TEST CASES FOR THE STABILITY EVALUATION

In this part the developed models are used for stability evaluations in a few test cases. In the first case the sequence domain impedances are used for stability evaluation and it is shown that the cross couplings between the sequences and frequencies must be considered to assess the stability correctly. The second case uses the impedance based stability analysis and the eigenvalue based stability analysis for a linear multi-converter system. The results are validated by time domain simulations and a Prony analysis is used to find the damping of an oscillatory signal [40]. In the third case, a nonlinear multi-converter system is investigated in the *dq* domain and the results are validated by time domain simulations. The last case is a different study, which investigates the problems that might occur if aggregation is used in the stability analysis.

2.4.1. IMPORTANCE OF THE FREQUENCY COUPLINGS

In §2.2.3.3 it was shown that an additional frequency exists in response to a perturbation (f_p in Figure 2-23), and as it can be seen in Figure 2-17, the magnitude of this coupling term could even be higher in the low frequency range. In this part the importance of considering the coupling terms in the stability evaluation are investigated. Figure 2-23 shows a three-phase current controlled voltage source converter connected to an inductive grid, where the parameters are listed in Table 2-2.

If the couplings are neglected (as it is assumed in [33]), then the Nyquist diagrams of the minor loop gains of the positive and negative sequence system are as plotted in Figure 2-24. The system is stable even with very high bandwidth PLLs; however, as it is shown in Figure 2-25, the system will be unstable for BW_{PLL}=70 Hz. It is worth noting that since the coefficients of (2-65)-(2-68) are complex the Nyquist plot is not symmetrical [41]. Figure 2-26 shows the generalized Nyquist criterion (GNC) plot of the impedance ratios in the *dq* domain based on [20], where it is clear for BW_{PLL}=70 Hz the Nyquist plot encircles the critical point.
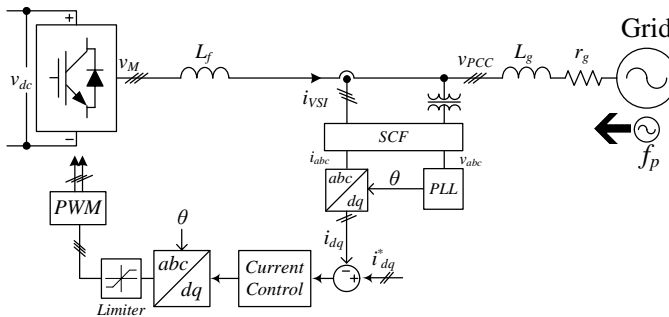
*Figure 2-23 A system for sequence domain modelling, where a current controlled voltage
source converter is connected to the grid* [34].

Table 2-2 Parameters of grid-connected inverter for simulation [34].

Symbol	Description	Value
V_g	Grid line-ground peak voltage	90 V
f_1	Grid frequency	50 Hz
L_g	Grid inductance	3 mH
R_g	Grid equivalent resistance	0.5 Ω
L_f	Filter inductance	1.5 mH
V_{dc}	Inverter dc voltage	300 V
I_{dr}	d channel current reference	7 A
I_{qr}	q channel current reference	0 A
K_p	Proportional gain of the current controller	0.01
K_i	Integrator gain of current controller	3
BW_{PLL}	Bandwidth of PLL (Stable)	50 Hz
	(Unstable)	70 Hz
K_d	Decoupling term	0
f_s	Sampling frequency	5 kHz
f_{sw}	Switching frequency	5 kHz
SCF	Signal conditioning filter for both voltages and current	$1/(0.00044s + 1)$

(a)

(b)
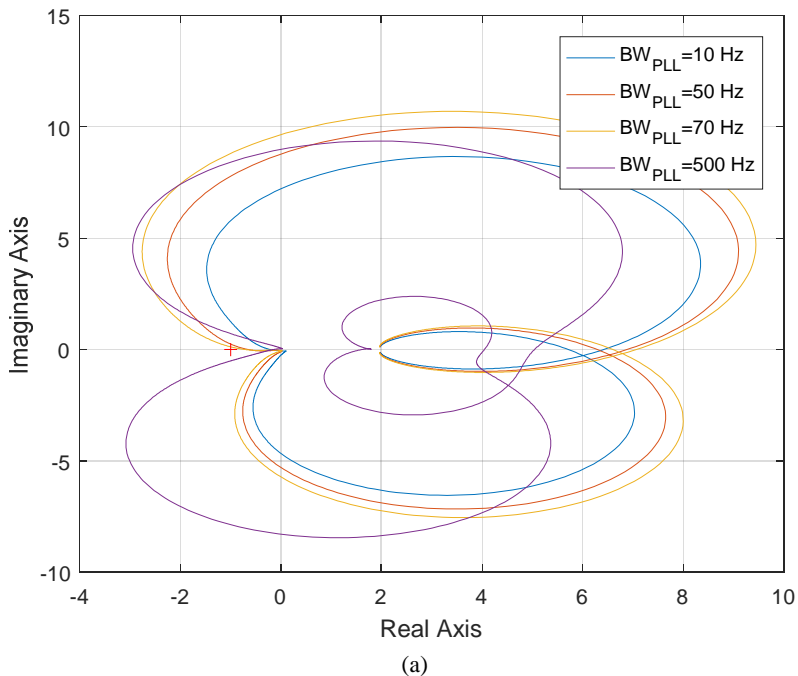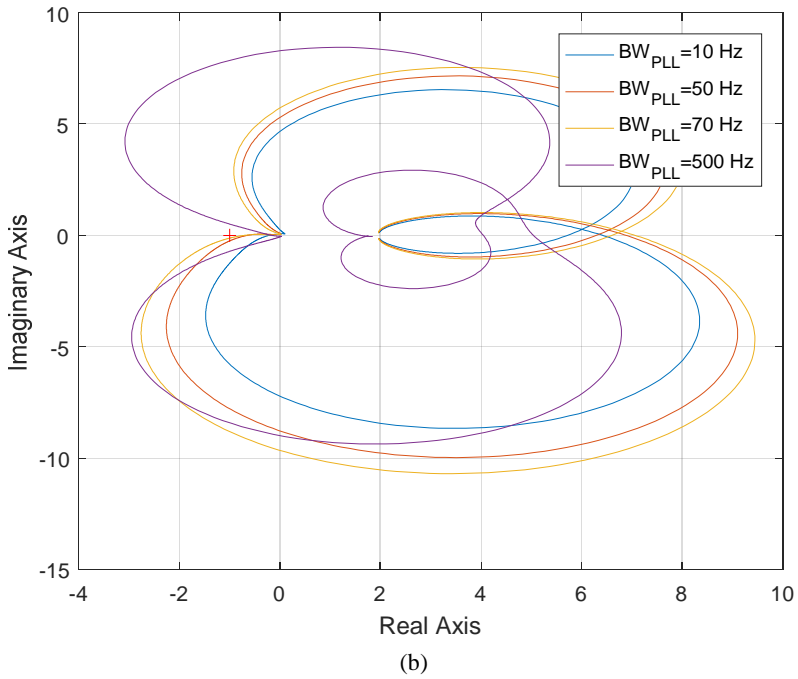
Figure 2-24 Nyquist plots of the minor loop gain using different PLL bandwidths neglecting the sequence coupling (a) positive-sequence impedances (b) negative-sequence impedances .
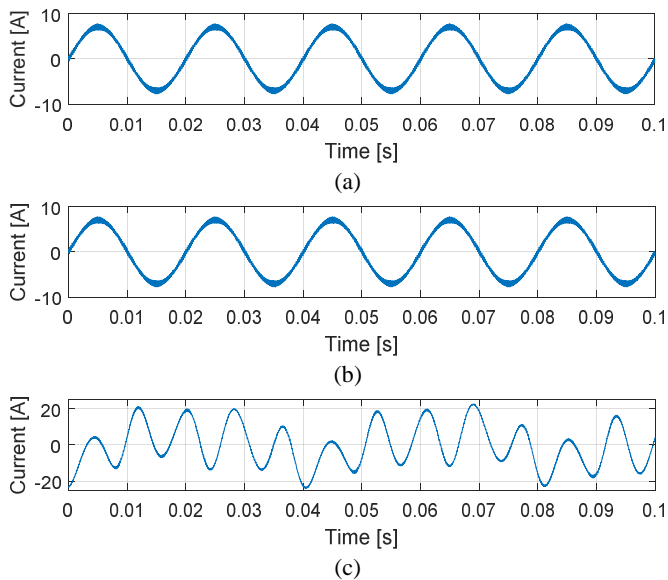
Figure 2-25 Simulation results of the output current of the converter in Figure 2-23 for (a) BW_PLL=10 Hz (b) BW_PLL=50 Hz (c) BW_PLL=70 Hz [34].
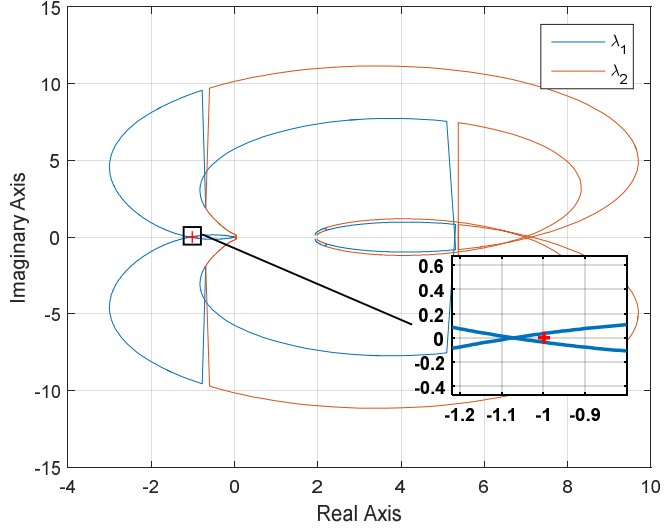
Figure 2-26 Generalized Nyquist plot in dq domain using the approach proposed in [20] *(BW$_{PLL}$=70 Hz)* [34].

The coupling terms in (2-69) not only couple the positive-sequence with the negative-sequence, but also couple two different frequencies. In [34], it has been proposed to define the admittance matrix of the converter as

$$Y = \begin{bmatrix} Y_{pp}(s) & Y_{pn}(s - 2j\omega_1) \\ Y_{np}(s) & Y_{nn}(s - 2j\omega_1) \end{bmatrix}$$
(2-103)

It is worth noting that the frequency coupling is modelled by the frequency shift $s-2j\omega_1$. Therefore, the frequency shift should also be considered in the grid impedance and consequently in the minor loop gain.

$$L = \begin{bmatrix} Z_g(s) & 0 \\ 0 & Z_g(s - 2j\omega_1) \end{bmatrix} \times Y$$
(2-104)

where $Z_g(s)=sL_g+R_g$ is the grid impedance.

Figure 2-27 shows the generalized Nyquist plot of *L* in (2-104), which is almost the same as the *dq* domain GNC in Figure 2-26. A hardware prototype is used to validate the result experimentally. The parameters are similar to the simulation case. Figure 2-28 shows output current of the converter, where the PLL bandwidth is changed from 50 Hz to 70 Hz.
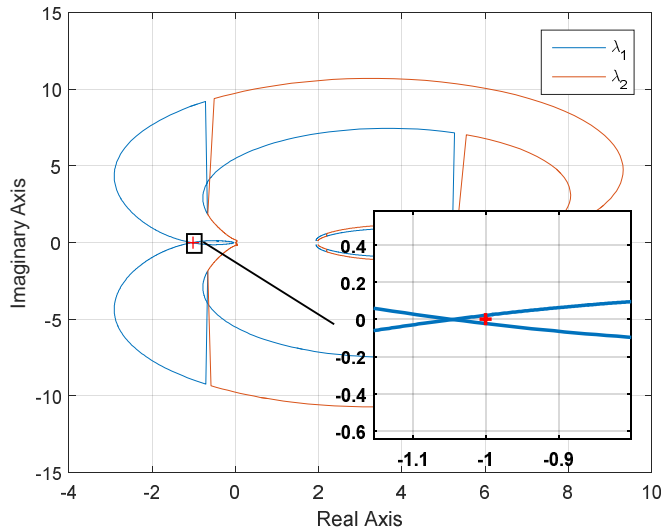
Figure 2-27 Generalized Nyquist plot using (2-104)in the sequence domain (BW$_{PLL}$=70 Hz)
[34].
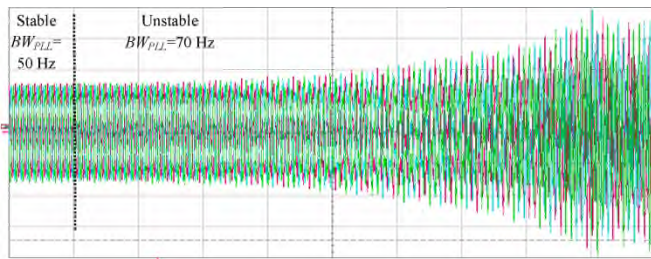
Figure 2-28 Experimental results of the output currents of the inverter. Instability is due to the change of the PLL bandwidth (BW$_{PLL}$) from 50 Hz to 70 Hz (5 A/div and 10 ms/div) [34].

2.4.2. A LINEAR FIVE-CONVERTER SYSTEM

The objective of this test case is to investigate the stability analysis methods in multi-converter systems. This system, which is based on Cigré LV benchmark, has first been introduced in [22] for stability studies. Figure 2-29 show the system layout and the current controllers used in this example. Since the PLL is neglected the system is a linear system, and single phase impedances are enough for the stability evaluation due the fact the controller is implemented in the $\alpha\beta$ domain.
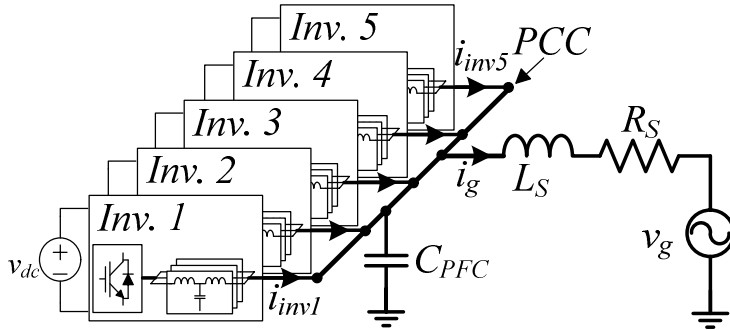
(a)
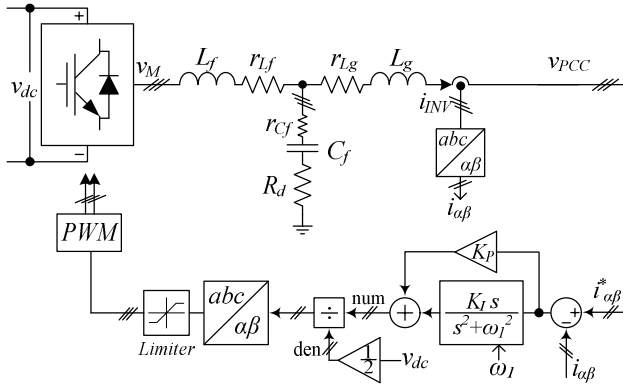
(b)

Figure 2-29 Considered power system, which is based on Cigré LV benchmark system [22]: *a) the overall power scheme. (b) the converter internal control structure* [38].

The parameters of the system are listed in Table 2-3. In [22] it has been shown that depending on how many converters are connected, there are different stable and unstable cases. Figure 2-30 shows the grid current for the defined cases in Table 2-4.

Table 2-3 Parameters of the considered system in Figure 2-29 [38].

Symbol	Description	Inverters				
		1	2	3	4	5
f_{sw}	Switching/Sampling frequency [kHz]	10		16		10
V_{dc}	DC-link voltage [V]	750				
L_f	Inverter side inductor of the filter [mH]	0.87	1.2	5.1	3.8	0.8
C_f	Filter capacitor [µF]	22	15	2	3	15
L_g	Grid side inductor of the filter [mH]	0.22	0.3	1.7	1.3	0.2
r_{Lf}	Parasitic resistance of L_f [mΩ]	11.4	15.7	66.8	49.7	10
r_{Cf}	Parasitic resistance of C_f [mΩ]	7.5	11	21.5	14.5	11
r_{Lg}	Parasitic resistance of L_g [mΩ]	2.9	3.9	22.3	17	2.5
R_d	Damping resistance [Ω]	0.2	1.4	7	4.2	0.9
K_p	Proportional gain of the controller	5.6	8.05	28.8	16.6	6.5
K_i	Integrator gain of the controller	1000		1500		1000
L_s	Grid inductance [mH]	0.4				
R_s	Grid resistance [Ω]	0.1				
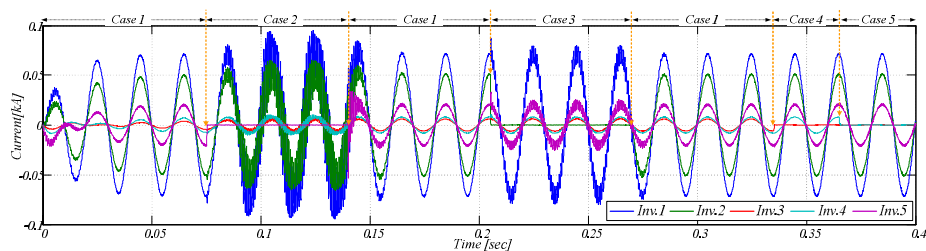
Figure 2-30 Time domain simulations for different cases shown in Table 2-4 [38].

Table 2-4 Different configurations of Figure 2-29 and the corresponding results [38].

Case No.	Description	Result
1	All are connected	Stable
2	Inverter 5 is disconnected	Unstable
3	Inverter 2 is disconnected	Unstable
4	Inverter 3 is disconnected	Stable
5	Inverters 3 and 4 are disconnected	Stable

Figure 2-31 shows the results of the impedance based stability analysis, where Inverter 1 is the source impedance for all cases. It can be seen that the Nyquist plot only encircles the critical point for Case 2 and Case 3, which is verified by time domain simulations in Figure 2-30.
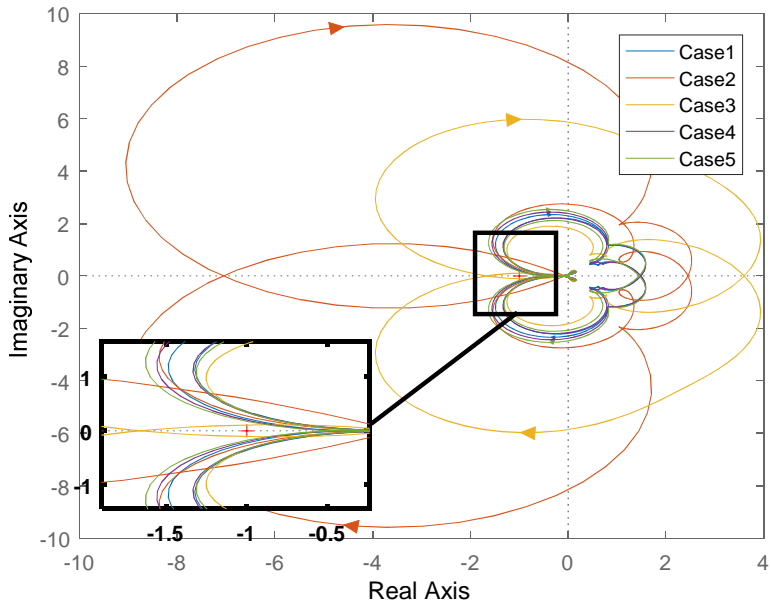
Figure 2-31 Impedance based stability analysis for the system in Figure 2-29 and the arrangements of Table 2-4 .

The results of the eigenvalue-based stability analysis for Cases 2, 4 and 5 are shown in Figure 2-32, where the dominant eigenvalues of the systems in these cases are highlighted.

(a)

(b)

(c)
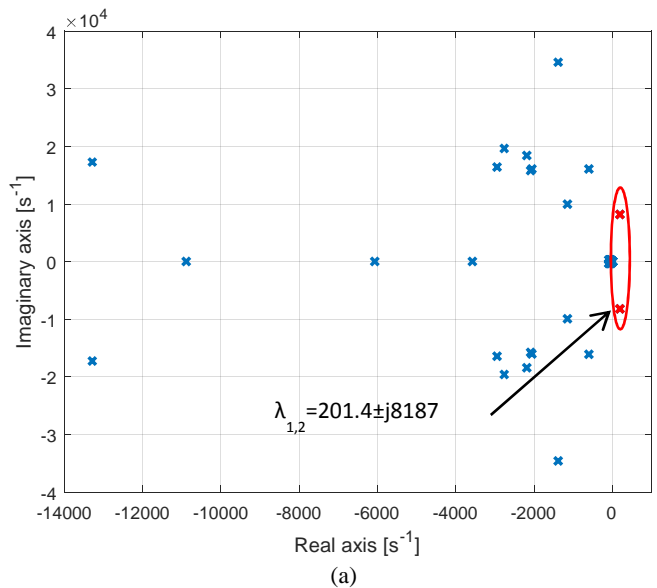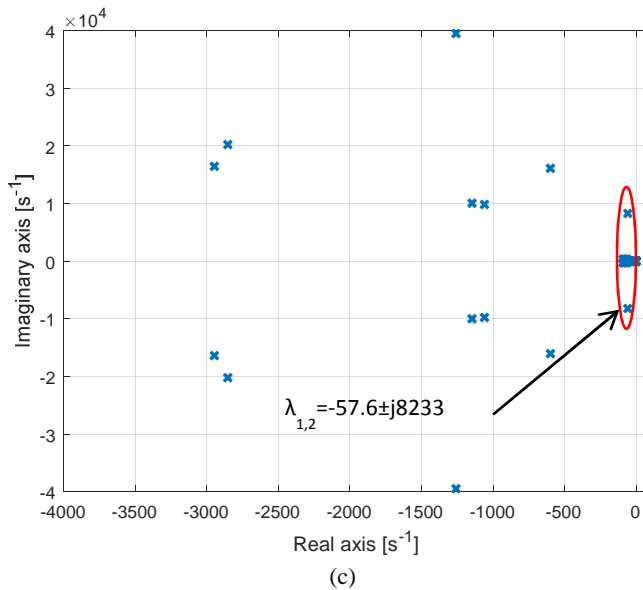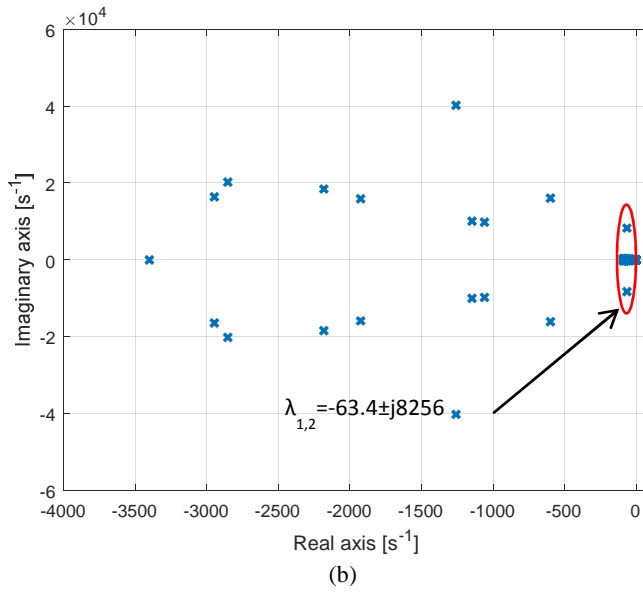
Figure 2-32 Eigenvalue-based stability analysis for the system in Figure 2-29 (a) Case 2 (b)
Case 4 (c) Case 5 (see Table 2-4).

It is worth to see how the dominant eigenvalues affect the transient response. In
Figure 2-33, a perturbation is applied to Cases 2, 4 and 5, and the transient response
is logged. It is difficult to measure the oscillation frequency and the time constant
due to the large fundamental component. Prony analysis is a strong method to find

the sinusoidal decaying components similar to the Fourier analysis that identifies frequency components in a waveform. The results of the Prony analysis (real and imaginary parts of an oscillatory eigenvalue) as shown in Table 2-5 are in good agreement with the dominant eigenvalues highlighted in Figure 2-32. Since the Prony analysis is a numerical method with a limited data, the damping of the fundamental frequency components are not zero.

(a)

(b)

(c)
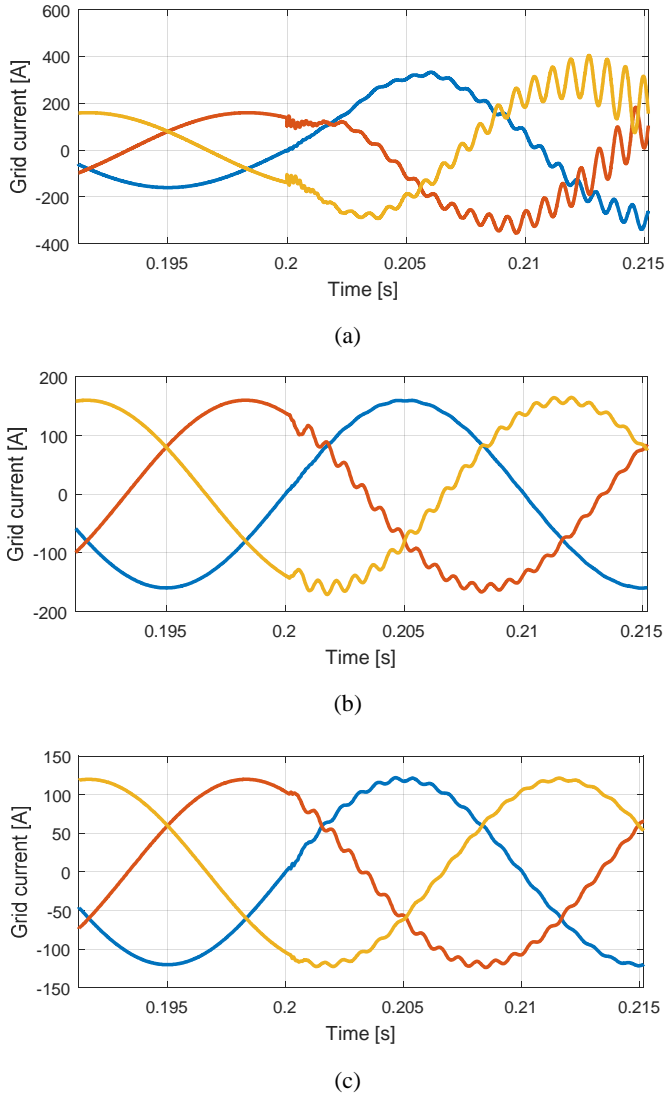
Figure 2-33 Time domain results of (a) Case 2 (b) Case 4 and (c) Case 5 (see Table 2-4).

Table 2-5 Results of the Prony analysis for Cases 2, 4 and 5 (see Table 2-4).

Case	No.	Real part (σ) [1/s]	Frequency (ω) [rad/s]
Case 2	1	-0.15	314.159
	2	226.8	8200
Case 4	1	-0.13	314.159
	2	-74.2	8277
Case 5	1	-0.015	314.159
	2	-62.9	8229

2.4.3. A NONLINEAR TWO-CONVERTER SYSTEM

In this test case, a nonlinear two-converter system is investigated. A voltage source inverter (VSI) and a grid are feeding an active front end (AFE) and a local capacitive-resistive load as depicted in Figure 2-34.
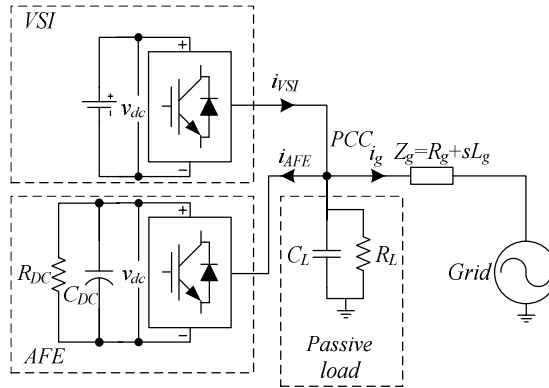
Figure 2-34 Considered nonlinear power system with a voltage source inverter and an active front end [29], [38].

The synchronization and dc link control loops are the main nonlinearities that are investigated in this case. Figure 2-35 shows the control structure of the converter and the system parameters are listed in Table 2-6 and Table 2-7.

(a)

(b)
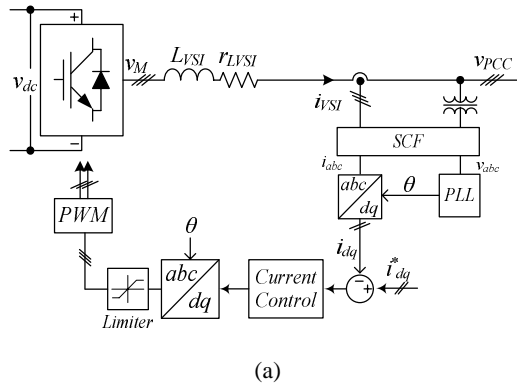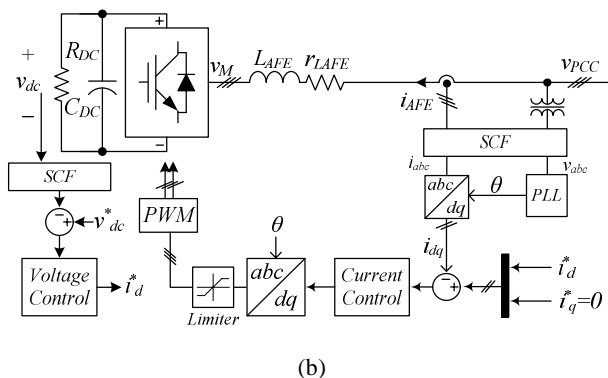
Figure 2-35 Power circuit and control structure of (a) the voltage source inverter (b) the active front end [38].

Table 2-6 Parameters of the system in Figure 2-34 [38].

Symbol	Description	Value
System Parameters		
V_g	Grid voltage (phase voltage rms) [V]	120
f_g	Grid frequency [Hz]	60
R_L	Resistance of local passive load [Ω]	10
C_L	Capacitance of local passive load [μF]	250
L_g	Grid inductance [mH]	0.2
R_g	Grid resistance [Ω]	1.1
Parameters of the VSI		
L_{VSI}	Inductance of the inverter [mH]	1.0
r_{LVSI}	Self-resistance of L_{VSI} [mΩ]	120
V_{dc}	DC link voltage [V]	600
$i^*_{d\text{-}vsi}$	d channel current reference [A]	140
$i^*_{q\text{-}vsi}$	q channel current reference [A]	0
k_{piVSI}	Proportional gain of current controller	0.0105
k_{iiVSI}	Integrator gain of current controller	1.1519
k_{pllVSI}	Proportional gain of PLL	0.1
$k_{ipllVSI}$	Integrator gain of PLL	0.32 (stable)
		5.2 (unstable)
Parameters of the AFE		
L_{AFE}	Inductance of the AFE [mH]	0.5
r_{LAFE}	Self-resistance of L_{AFE} [mΩ]	90
C_{dcAFE}	Dc link capacitor [μF]	100
R_{dc}	Dc load resistance [Ω]	13.825
V^*_{dc}	DC link voltage reference [V]	600
$i^*_{q\text{-}vsi}$	q channel current reference [A]	0
k_{piAFE}	Proportional gain of current controller	0.0052
k_{iiAFE}	Integrator gain of current controller	1.152
k_{pvAFE}	Proportional gain of dc link voltage controller	0.0628
k_{ivAFE}	Integrator gain of dc link voltage controller	45.45
k_{pllAFE}	Proportional gain of PLL	0.05
$k_{ipllAFE}$	Integrator gain of PLL	0.5

Table 2-7 Additional parameters of the converters in Figure 2-34 [38].

Symbol	Description	Value
SCF	Signal Conditioning Filter	$\dfrac{\omega_n^2}{s^2 + 2\xi\omega_n + \omega_n^2}$
ω_n	Natural frequency of SCF [rad/s]	1.23e6
ξ	Damping factor of SCF [rad/s]	4.74e-13
f_{sw}	Switching/sampling frequency [kHz]	20
T_{del}	Time delay due to the digital control and PWM	$1.5/f_{sw}$

To eliminate the nonlinearities in the system, small signal linearization can be used. As discussed before this method needs the steady state operating points. The results of the load flow analysis are listed in Table 2-8 (note the current direction in Figure 2-34).

Table 2-8 Load flow results of the system in Figure 2-34.

Symbol	Description	Value
V_d^s	PCC voltage (d channel)	204.25
V_q^s	PCC voltage (q channel)	0
I_{d-VSI}^s	Output current of VSI (d channel)	140
I_{q-VSI}^s	Output current of VSI (q channel)	0
I_{d-AFE}^s	Output current of AFE (d channel)	85.18
I_{q-AFE}^s	Output current of AFE (q channel)	0
M_{d-VSI}^s	Modulation index of VSI (d channel)	0.37
M_{q-VSI}^s	Modulation index of VSI (q channel)	0.08
M_{d-AFE}^s	Modulation index of AFE (d channel)	0.33
M_{q-AFE}^s	Modulation index of AFE (q channel)	-0.01

The linearized admittances are plotted in Figure 2-36, where it can be seen that a change in the PLL of the VSI affects the low frequency behavior.
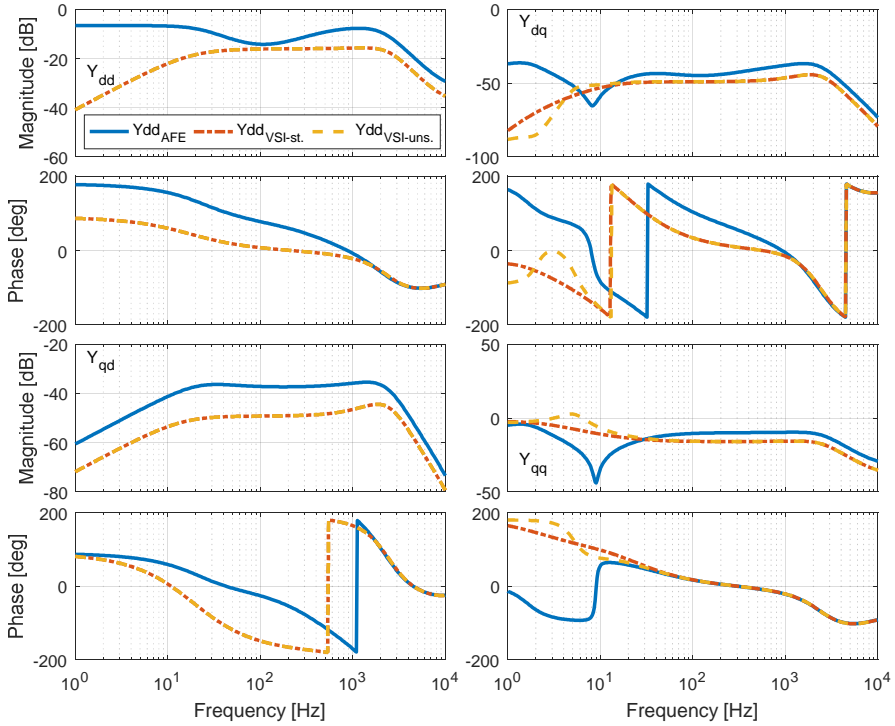
Figure 2-36 Admittances of the AFE and the VSI for stable and unstable designs (see Table 2-6) in the dq domain [38].

The impedance based stability analysis is used with the *dq* domain admittance, and it can be seen from Figure 2-37 that the method correctly predicts the stable and unstable operations.

The dominant poles of the system are found by the eigenvalue based stability analysis and they are shown in Figure 2-38, where the instability is predicted correctly.
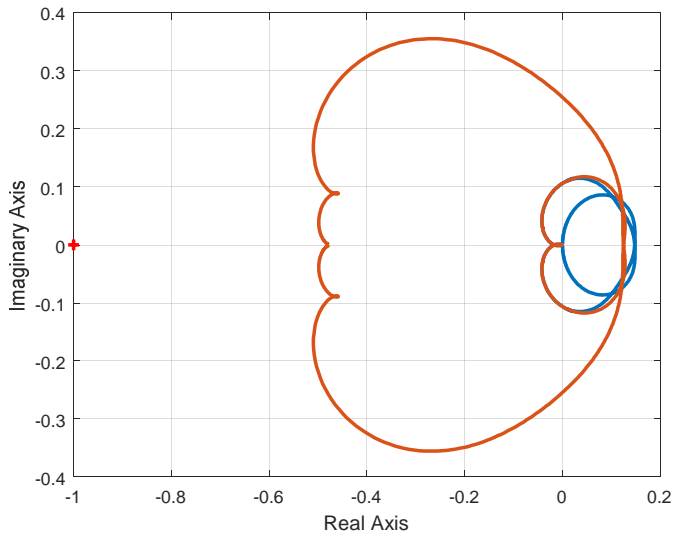
(a)
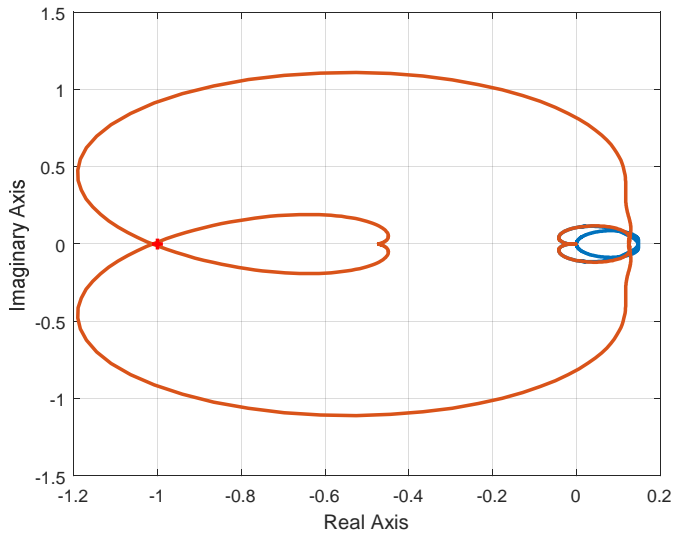
(b)

*Figure 2-37 Impedance based stability analysis for the system shown in Figure 2-34 (a)
Stable system (b) unstable system as defined in Table 2-6* [38]*.*
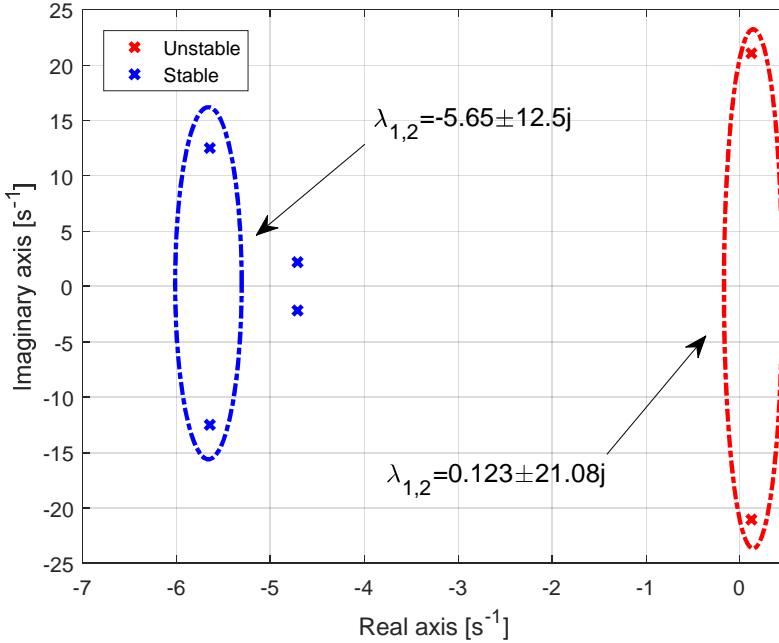
Figure 2-38 Eigenvalue based stability analysis for stable and unstable system (low frequency poles are shown) as defined in Table 2-6 [38].

To validate the damping and the oscillation frequency of the dominant poles shown in Figure 2-38 ($\lambda_{1,2}$), a perturbation can be applied in the simulations and the transient response can be investigated. Since in the *dq* domain, the fundamental frequency signals are converted to dc signals, the time constant and oscillation frequency can be measured directly.

The dashed orange curves in Figure 2-39 are the exponential curves like

$$Ae^{t/\tau} \tag{2-105}$$

where *A* is the initial magnitude and τ is the time constant (inverse of the real part of an eigenvalue and could be positive or negative). It can be seen that the exponential curves are the envelopes of the oscillatory transients.
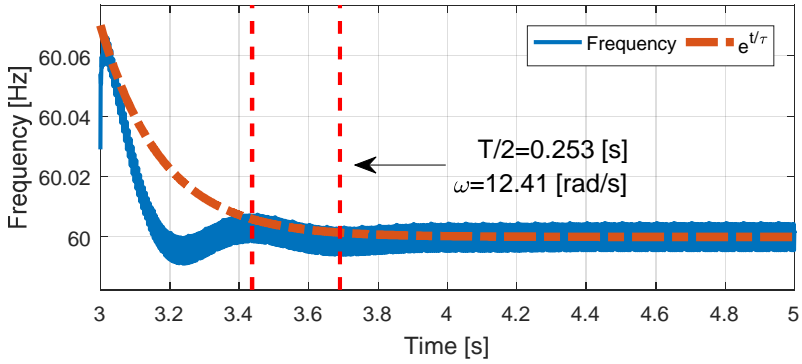
(a)
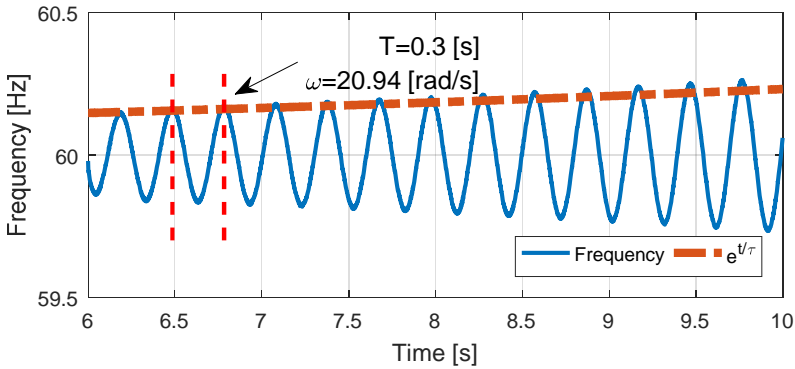
(b)

*Figure 2-39 Time domain simulations of the nonlinear system in Figure 2-34 for (a) stable
case (b) unstable case. The damping and oscillation frequency are estimated* [38].

Participation factor analysis as discussed in §2.3.2 and (2-100) can be performed for
the unstable case to find the root cause of this instability. As expected the PLL of the
VSI is the most important state variable that is contributing to this instability, and
since this is a low frequency instability, high frequency loops have no contribution.

Table 2-9 Largest contributors to the instability.

State name	Contribution [%]
VSI.PLL2	37.25
VSI.PLL1	34.51
AFE.PLL2	16.96
AFE.PLL1	7.25

Figure 2-14 compares the admittance of the AFE, which is modelled by the
proposed method and the method developed in [29]. It is interesting to see whether
this difference in the modelling affects the stability evaluation or not. Therefore the
system is intentionally made unstable by reducing the dc link capacitor to 5 µF as it

can be seen in Figure 2-40. The results of the eigenvalue based analysis using the two methods as shown in Figure 2-41, verifies the effectiveness of the proposed method.
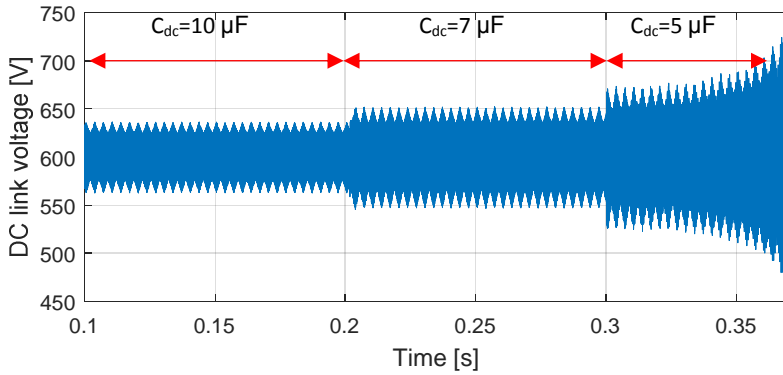
Figure 2-40 DC link voltage for different DC link capacitor values.
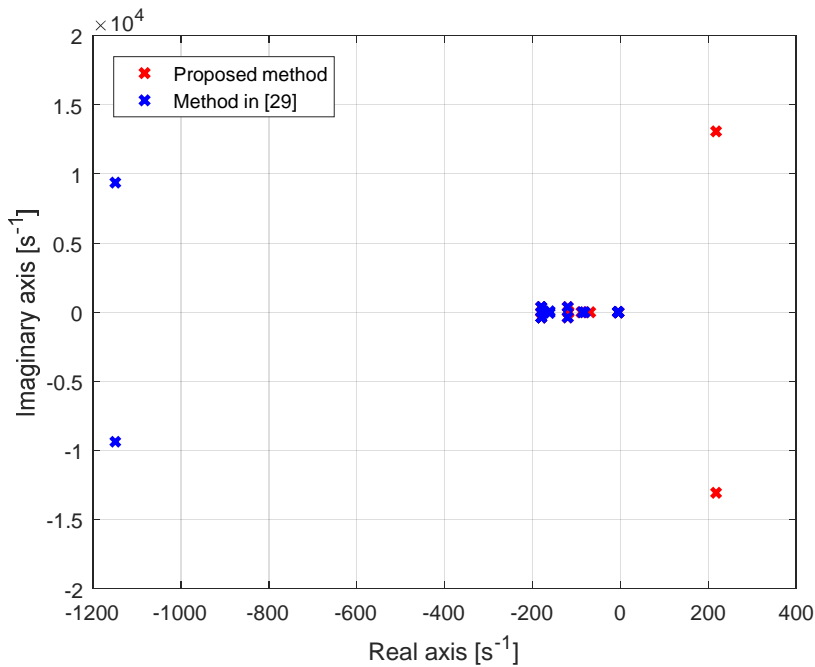
Figure 2-41 Eigenvalues of the system of Figure 2-34 when the dc link capacitor is 5 μF using the proposed method in (2-40) and in [29].

2.4.4. AGGREGATION OF THE CONVERTERS AND THE ASSOCIATED PROBLEMS

Aggregation can be used to group a number of converters into a scaled-up converter, and therefore, the order of the final transfer function/state matrices can significantly be reduced [19]. Figure 2-42 (a) shows two similar converters that are connected to the PCC by similar impedances. Figure 2-42 (b) illustrates how aggregation can be used to reduce the complexity. The equivalent electrical parameters are as follows

$$Z_l = Z_{l1} \parallel Z_{l2} = Z_{l1}/2 \qquad (2\text{-}106)$$

$$Y_c = Y_{c1} + Y_{c2} = 2Y_{c1} \qquad (2\text{-}107)$$

where Y_c is the equivalent admittance of the converter, which includes all passive and active components, and Z_l is the cable impedance.

(a)

(b)
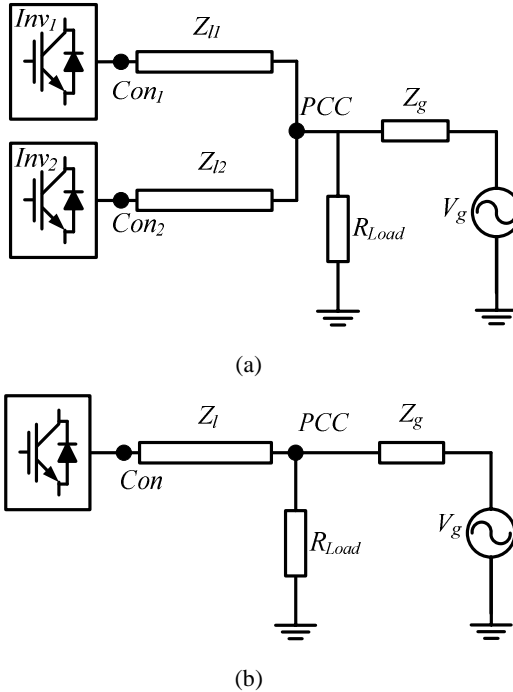
Figure 2-42 Considered power system for aggregation studies: (a) full detailed representation (b) simplified (aggregated) representation [42].

In this part a case study is presented, where the problems of aggregation are highlighted. The inverters are the same as *Inverter 1* in Table 2-3 and the parameters of the passive system are listed in Table 2-10.

Table 2-10 Passive parameters of the system in Figure 2-42 [42].

Symbol	Description	Value
V_g	Grid voltage (phase-ground) rms [V]	220
R_g	Grid equivalent resistance [Ω]	0.1
L_g	Grid equivalent inductance [mH]	3
L_1	Inductance of Cable 1[mH]	0.3
L_2	Inductance of Cable 2[mH]	0.3
R_{Load}	Load resistance [Ω]	40

Figure 2-43 shows the eigenvalue plot of the considered case study for both the full and the aggregated models. It can be seen that there are two unstable eigenvalues in the full system that are not observable in the aggregated model. In other words, the system is predicted to be stable when an aggregated model is used. Therefore, it is interesting to see these results by means of time domain simulations. Figure 2-44 shows that when the aggregated model is used the system is stable, while the full model simulation is unstable.
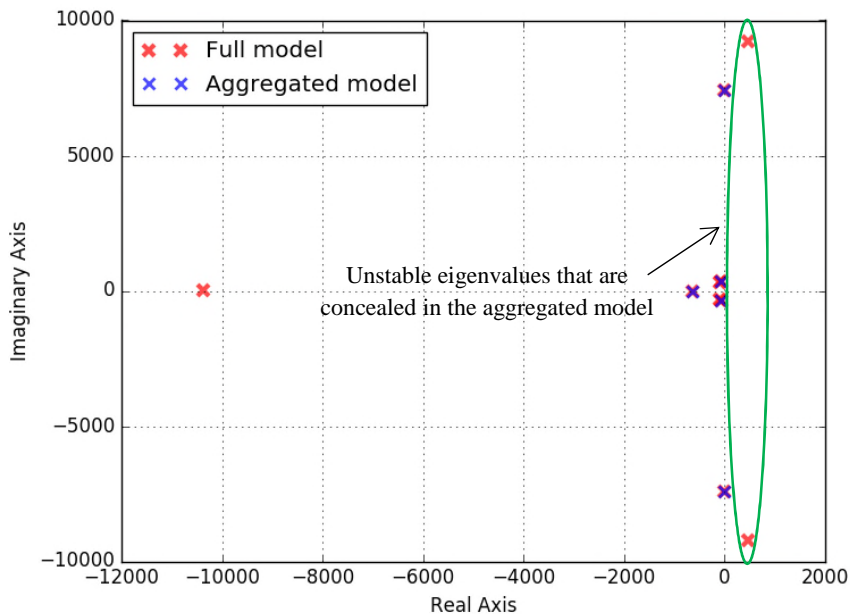
Figure 2-43 Eigenvalues of the considered system in Figure 2-42 [42].
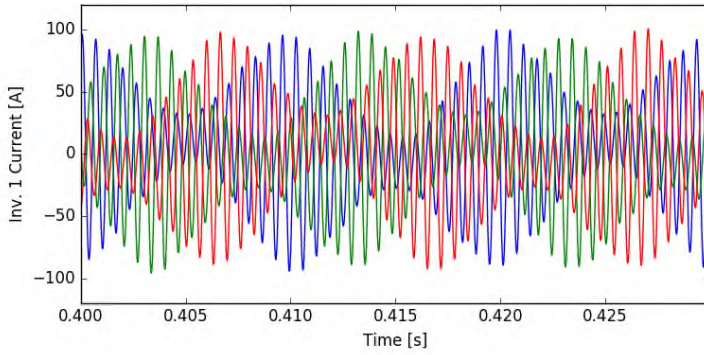
(a)
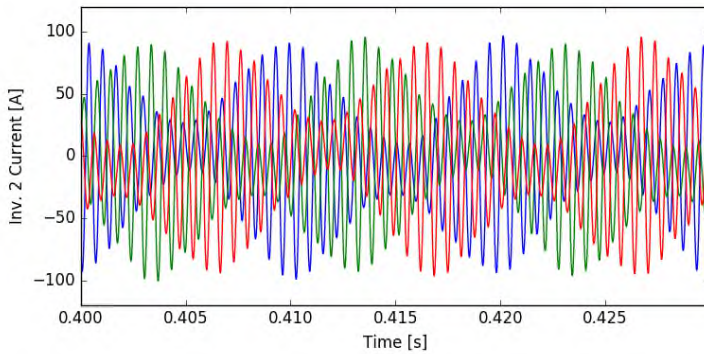
(b)
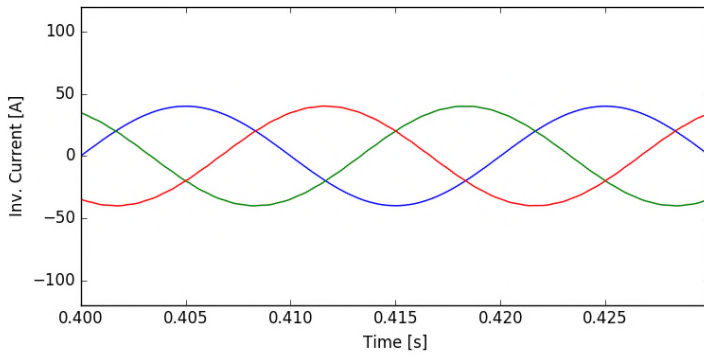
(c)

*Figure 2-44 Output currents of (a) Inverter 1 in full model (b) Inverter 2 in full model (c)
aggregated inverter* [42].

Again a participation factor analysis is done in order to confirm that the source of this instability is a part of the aggregated model [15]. Table 2-11 shows participation factor analysis results for the full detailed and the aggregated models. It is evident that the external grid does not have any effect on the unstable poles. In other words, the origin of this instability is inside the aggregated models, and this is the reason it is not observable by the simplified aggregated models.

Table 2-11 Contributors to the most critical poles shown in Figure 2-43 that are found using the participation factor analysis [42].

Poles / Contributors		470.9±9225j	-11±7421j
Full model	Inverter 1	46%	49%
	Inverter 2	46%	49%
	Grid	0	1.5%
	Cable 1	4%	0.05%
	Cable 2	4%	0.05%
Aggregated model	Inverter		0.98
	Grid		0.015
	Cable		0.001

Based on the results of this study, the internal dynamics may be concealed, when the aggregation is used, while the external dynamics of both models are the same. Therefore, the aggregation can be used safely if it is ensured that there is no internal instability inside the equivalent model. The network shown in Figure 2-45 is a typical example of a radial network, where Y_i and Z_i represent a converter and a connection branch, respectively. Aggregated models can significantly reduce the complexity of the stability analysis of Figure 2-45. However, at each step of simplification, the internal behavior of the equivalent subsystems must be investigated. Since, this is an internal analysis; the external network can be replaced by an ideal source. Hence, first the red circle in Figure 2-45 can be aggregated and afterwards, the black and yellow ovals can be replaced by equivalent aggregated circuits.
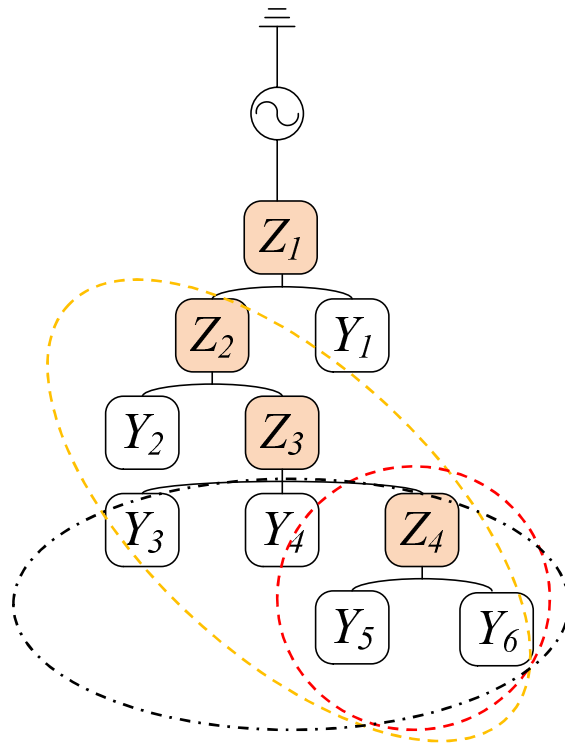
Figure 2-45 Equivalent subsystems must be stable internally during aggregation process.

2.5. LARGE SCALE STABILITY ANALYSIS

The Impedance-Based Stability Analysis (IBSA) is a powerful method for the stability analysis in power-electronic-based power systems such as WPPs [21], [24]. In this method the network is divided into two sub-networks, one is the equivalent impedance of the power converter, and the other one is the external impedance seen from the terminals of the power converter. The open loop system frequency response is defined as the ratio of the load impedance over the source impedance, here the external network impedance and the WT equivalent impedance, respectively. By plotting the Nyquist diagram of the open loop gain, the stability of the closed loop system can be evaluated. The relative stability indices such as phase margin and gain margin can also be obtained from the Nyquist diagram. The internal impedance of the WT can easily be obtained from the analytical model or based on frequency sweep by measurements or in simulations and it is not dependent in the network topology (assuming a linear system). However, the external load impedance is dependent on the topology and the frequency dependent characteristics of the other passive and possibly active elements.

In many commercial power system analysis tools, there is a feature to measure the driving point impedance (self-impedance seen from a node) as a function of frequency (the frequency scan). This impedance can then be used in the IBSA. However, in large WPPs, the complexity of electrical infrastructure leads to time consuming (and sometimes even not feasible) impedance calculations. Moreover, the study must also be repeated for different internal WPP contingencies, e.g. export cable, offshore transformer or harmonic filter outage.

It has also been shown in [22] that connecting/disconnecting power converters can affect the stability significantly (see §2.4.2). Therefore, the stability evaluation must be repeated for different number of WTs in operation.

The grid is also a time varying impedance and some large loads/generators can influence the grid impedance significantly. Therefore, the harmonic stability studies should be repeated for a number of probable grid scenarios. The exemplary grid impedances in Figure 2-46 show that the resonance profile of the network can vary significantly.
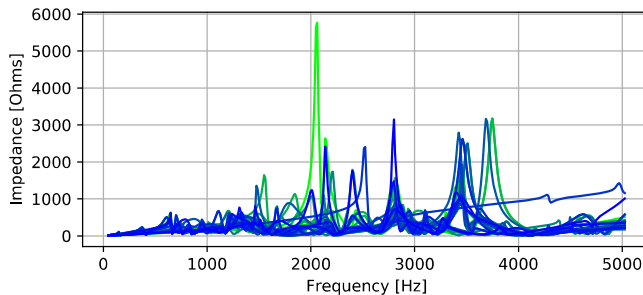
Figure 2-46 Examples of grid impedance.

A normal frequency scan (from 100 Hz to 2500 Hz with 1 Hz resolution) in an exemplary OWPP takes typically around two minutes on an average PC. Therefore, it can be seen that for an OWPP with 200 WTs and for possible 8 internal contingency scenarios as well as for 400 different grid profiles, the study takes more than two years ($200 \times 8 \times 400 \times 2$ min)!

In this part, some simple techniques are used to partition the network into a few sub-networks. This leads to significant simplification of the analyzed system. Then, by using some circuit theory operations, the study time can be reduced significantly.

2.5.1. THE PROPOSED METHOD

Using a simplified model of the system is also another approach to speed up the studies. For instance, one can assume that all WTs are connected in parallel via symmetrical electrical circuit and have the same operating point [9], [19]. However, the focus of this part is not how to choose simplified models or what are the advantages and disadvantages. Instead, this section discusses methods that can speed up both methodologies.

Figure 2-47 shows a schematic OWPP layout and how the IBSA can be applied. Z_{load} is obviously dependent on the number of WTs in operation, the grid impedance and the internal contingency cases that will affect the interconnection of the elements (e.g. an export cable failure will result in reconfiguration of the entire OWPP). If the highlighted area in Figure 2-47 is considered as a two-port network (see Appendix A) as shown in Figure 2-48, it can be seen that its behavior is independent of the grid and only includes the contingency cases inside the WPP and the number of WTs in operation. Therefore, the impedance measurements of such a large system are needed for much less cases and the effects of the grid can be considered afterwards in a numerical computing software such as MATLAB®[43]. The remaining part of the study is simple impedance calculations in a very small system (a two-port system), which can be done much faster than calculating the impedances of the entire system.
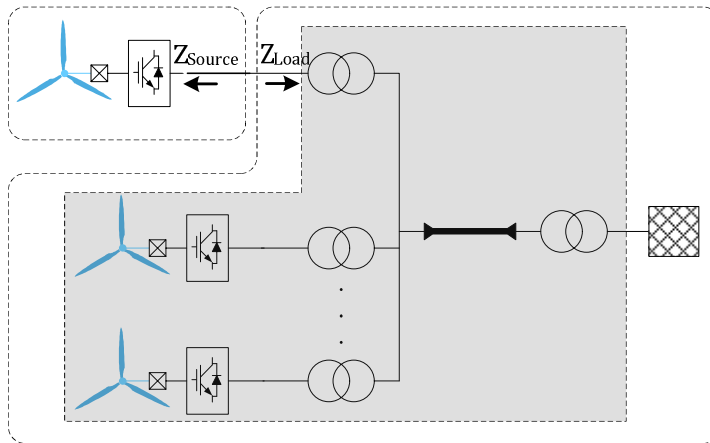
Figure 2-47 How to use impedance based stability analysis in a wind power plant.
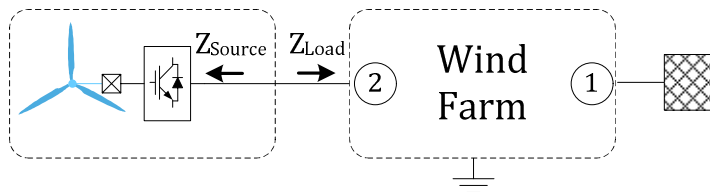
Figure 2-48 Use of two-port networks to simplify the impedance based stability analysis for the system shown in Figure 2-47 .

The main challenge in finding the parameters of the highlighted two-port network is the mutual impedances between the connection point of the OWPP to the grid and the terminals of the WT under study. Some power system softwares such as DIgSILENT PowerFactory [44] are able to calculate both the driving point impedance and the mutual impedance (i.e. diagonal and off diagonal elements of the impedance matrix). Therefore, by disconnecting the grid and the WT under study, a 2×2 impedance matrix can be obtained as shown in Figure 2-49 (for parameters see Appendix B). It should be noted that the abovementioned frequency scans must still be performed for all WTs and all contingency cases, which will take 200×8×2 min ≈ 2 days.
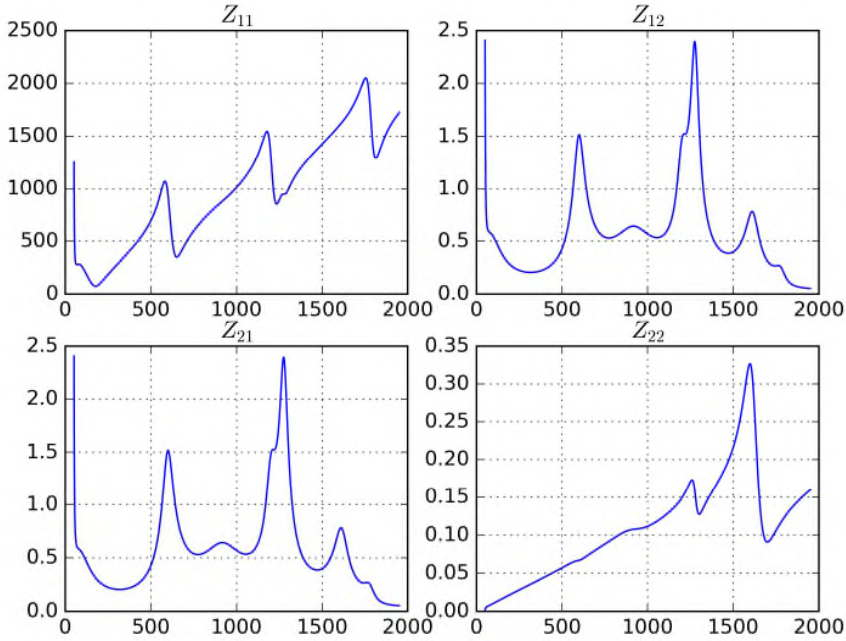
Figure 2-49 Elements of the impedance matrix of the highlighted two-port network in Figure 2-47 and Figure 2-48.

The grid impedance is shunt connected to the first port of two-port WPP representation. Therefore, the driving point impedance of second port (Z_{Load}) can be calculated by

$$Z_{load} = \frac{Z_{wf_{11}}Z_{wf_{22}} - Z_{wf_{12}}Z_{wf_{21}} + Z_{wf_{22}}Z_g}{Z_{wf_{11}} + Z_g}$$ (2-108)

Equation (2-108) can quickly be calculated for all the grid impedances, since all the parameters are numerical vectors. It should be noted that this task together with calculating the stability margins takes five milliseconds for each case on an average PC. The total number of cases is now 1600 (of the previous part) times 400 grid cases which takes 1600×400×5 ms ≈ 50 min.

Figure 2-50 shows Z_{Load} as a function of number of WTs in operation for the intact operation of an OWPP presented in Appendix B and a given grid profile. Furthermore, Figure 2-51 shows the Nyquist diagram of the mentioned case, where the number of WTs in operation is varied. It can be seen from Figure 2-52 that the phase margin is dependent on the number of WTs in operation. The periodical behavior observed in Figure 2-52 is due to the symmetry in the OWPP layout, i.e. there are seven WT strings, and therefore, the characteristics are almost repeated seven times.
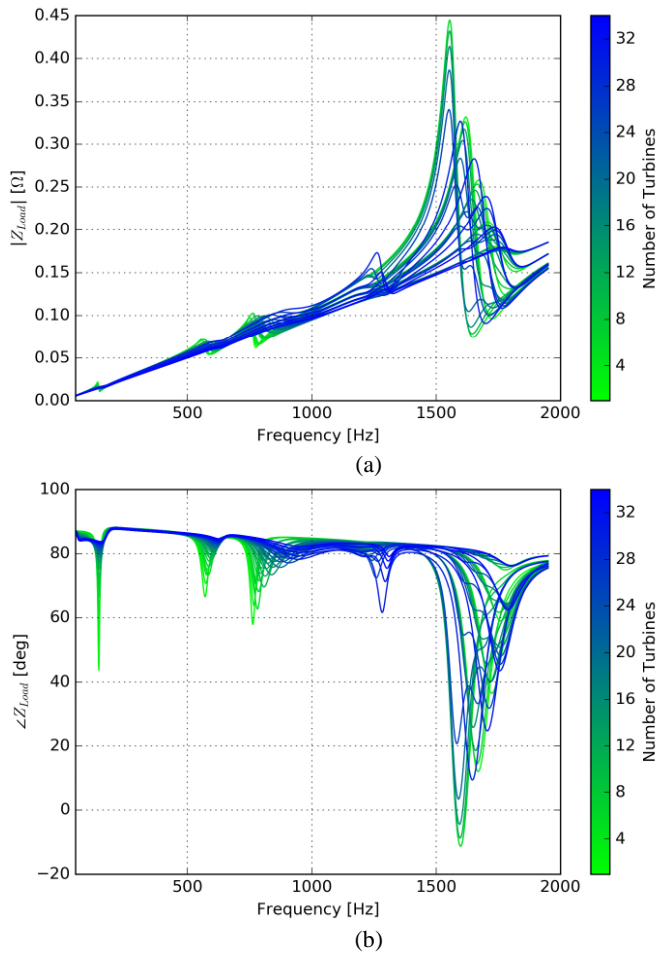
Figure 2-50 Driving point impedance at the wind turbine terminals (Z_{Load}) as a function of number of wind turbines in operation. (a) Magnitude (b) Phase.
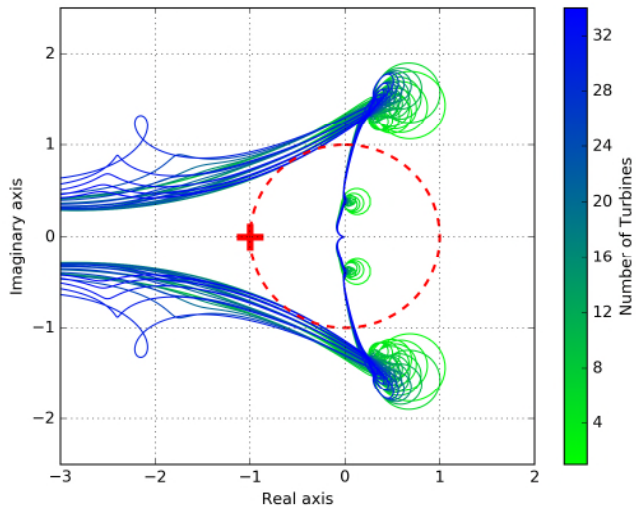
Figure 2-51 Nyquist diagram of the full detailed analysis for different number of wind turbines in operation.
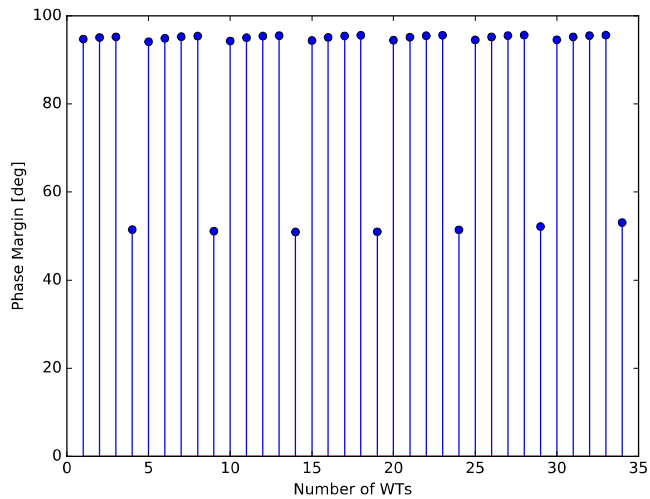
Figure 2-52 Phase margin as a function of number of wind turbines in operation for the full detailed analysis.

2.6. SUMMARY

In this chapter different modelling techniques such as impedance representation and state space representation have been reviewed. The impedance modelling in different domains has been presented, where a contribution of this work has been to show that there also exists a frequency and sequence coupling in the sequence domain impedance modelling, which affects the harmonics significantly. In the *dq* domain modelling the low frequency models have been improved for converters with the dc link controllers. The developed models have also been used in analysis of a few test cases, which have covered linear and nonlinear multi-converter systems. Another contribution of this thesis reported in this chapter is the instability inside the aggregated models, which may provide misleading results regarding the stability analysis. The impedance stability analysis is further used for stability analysis of a large OWPP. Some practical difficulties in the analysis have been reviewed and a method has been proposed to accelerate the studies. It should be noted that the low frequency range is neglected in order to enable the user to use the current software and tools. In the next chapter, a systematic approach for state space modelling of large systems is presented, which enables the user also to investigate the low frequency behavior of the system.

CHAPTER 3. STABILITY ANALYSIS PLATFORM

"The hidden harmony is better than the obvious."

Heraclitus

3.1. INTRODUCTION

Recent versions of commercial power system softwares support scripting in Python. Python is a free, open-source and high-level programming language [45], which has a lot of free and useful libraries such as advanced plotting modules and mathematical calculations. DIgSILENT PowerFactory [44] is widely used in Europe for power system analysis and it has a nice toolbox for small signal stability analysis of large power systems. However, the main objective in small signal stability studies is the electromechanical interactions of synchronous generators (rotor angle stability), and since this phenomenon happens very close to the fundamental frequency (due to the large masses in a power system), the dynamics of the network can be neglected (phasors can be used to represent network elements) and the system can be studied only by dynamical equations of the generators. However, this is not the case for stability studies in power electronic based power systems, where the instability frequency can be at several kHz. Therefore, there is a need for additional methods/tools, preferably combined with PowerFactory because:

1) Some networks have already been implemented in PowerFactory, and therefore by doing the stability analysis in PowerFactory the possible human errors in exporting the necessary information to other softwares can be avoided.
2) The user can benefit from the nice data handling and the user interface.
3) Some routines are already implemented in the software such as load flow analysis which is really useful in calculating the initial conditions in linearizing nonlinear systems.

Based on the abovementioned reasons, a stability analysis platform, which is discussed in this chapter, has been implemented in PowerFactory using Python. It extracts all information from the electrical network model, such as the connection graph, electrical characteristics and then, the rest of the study is done in mathematical libraries of Python such as NumPy [46] and SciPy [47] (see Figure 3-1).
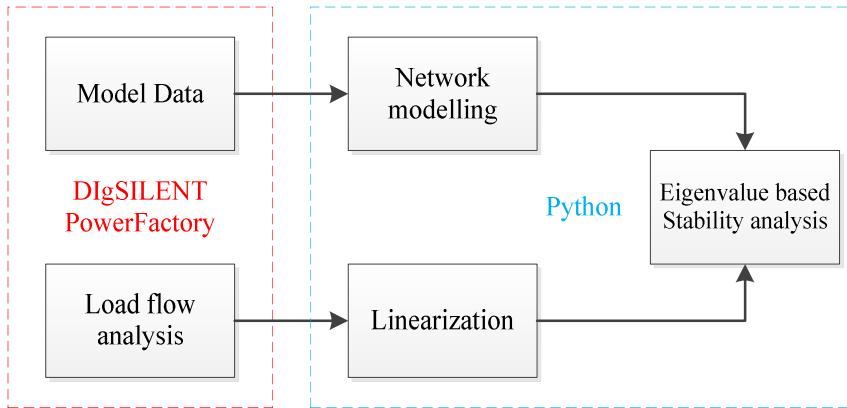
Figure 3-1 Stability analysis platform uses the features of DIgSILENT PowerFactory.

3.2. MODELLING FRAMEWORK

It has been shown in Chapter 2 that modelling of a converter in the *dq* domain is more straightforward as long as the system is balanced. Considering the very negligible impedance imbalance in the generation and transmission levels (i.e. a WPP and transmission assets), *dq* domain is chosen for stability studies in this work. To eliminate the mutual impedances in a three-phase system, the positive sequence representation can be used. For static elements such as cables and transformers, the positive sequence impedance is equal to the negative sequence impedance since the component behavior does not depend on the voltage sequence. However, for rotating machines or active elements such as WTs the sequence is important. To illustrate how the positive sequence can be used for calculating the *dq* impedances, a coupled inductive and three-phase branch as shown in Figure 3-2 is considered.
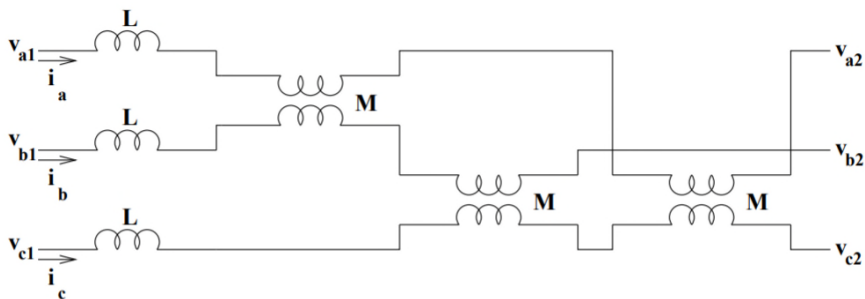
Figure 3-2 A coupled inductive three phase branch.

The impedance of a coupled inductance as shown in Figure 3-2 in the *abc* domain is

$$z_{abc} = s \begin{bmatrix} L & M & M \\ M & L & M \\ M & M & L \end{bmatrix} \tag{3-1}$$

where L is the self-inductance and M is the mutual inductance as shown in Figure 3-2. In can easily be transformed to the sequence domain as

$$z_{seq} = s \begin{bmatrix} L - M & 0 & 0 \\ 0 & L - M & 0 \\ 0 & 0 & L + 2M \end{bmatrix} \tag{3-2}$$

It is also worth noting how (3-1) can be transformed into the *dq* domain

$$z_{dq0} = \begin{bmatrix} (L - M)s & -(L - M)\omega & 0 \\ (L - M)\omega & (L - M)s & 0 \\ 0 & 0 & (L + 2M)s \end{bmatrix} \tag{3-3}$$

It can be seen that the *dq* domain impedance is actually the transformation of the positive sequence impedance into the *dq* domain, if the zero sequence is not of interest. Therefore, in this chapter by assuming a symmetrical system, a single line representation of the circuit based on the positive sequence parameters is created, and afterwards it is transformed to the *dq* domain.

3.3. COMBINING ALL MODELS INTO A SINGLE STATE SPACE MODEL

In the stability analysis platform, each component is modelled separately and in the end the Component Connection Method (CCM) is used to calculate the overall state matrices [48].

3.3.1. COMPONENT CONNECTION METHOD.

If an interconnected system is formed of n subsystems, then on the first step, the dynamical state space matrices of each subsystem as written in (3-4) can simply be appended to create block diagonal state matrices. It should be noted that (3-5)-(3-8) are nothing but just rewritten in the matrix form.

$$\begin{aligned} \dot{x}_i &= A_i x_i + B_i u_i \\ y_i &= C_i x_i + D_i u_i \end{aligned} \tag{3-4}$$

$$A_{app} = \begin{bmatrix} A_1 & 0 & \cdots & 0 \\ 0 & A_2 & \cdots & \vdots \\ \vdots & \vdots & \ddots & 0 \\ 0 & \cdots & 0 & A_n \end{bmatrix}, \ x_{app} = \begin{bmatrix} x_1 \\ x_2 \\ \vdots \\ x_n \end{bmatrix} \tag{3-5}$$

$$B_{app} = \begin{bmatrix} B_1 & 0 & \cdots & 0 \\ 0 & B_2 & \cdots & \vdots \\ \vdots & \vdots & \ddots & 0 \\ 0 & \cdots & 0 & B_n \end{bmatrix}, \ u_{cmp} = \begin{bmatrix} u_1 \\ u_2 \\ \vdots \\ u_n \end{bmatrix} \tag{3-6}$$

$$C_{app} = \begin{bmatrix} C_1 & 0 & \cdots & 0 \\ 0 & C_2 & \cdots & \vdots \\ \vdots & \vdots & \ddots & 0 \\ 0 & \cdots & 0 & C_n \end{bmatrix}, \ y_{cmp} = \begin{bmatrix} y_1 \\ y_2 \\ \vdots \\ y_n \end{bmatrix} \tag{3-7}$$

$$D_{app} = \begin{bmatrix} D_1 & 0 & \cdots & 0 \\ 0 & D_2 & \cdots & \vdots \\ \vdots & \vdots & \ddots & 0 \\ 0 & \cdots & 0 & D_n \end{bmatrix} \tag{3-8}$$

Then, the interconnection between the inputs and outputs can be defined as

$$u_{app} = L_1 y_{cmp} + L_2 u_{sys}$$
$$y_{sys} = L_3 y_{cmp} + L_4 u_{sys} \tag{3-9}$$

where L_1 to L_4, which are called the interconnection matrices, define the relationship between the inputs and outputs of the individual components (u_{cmp} and y_{cmp}) and the inputs and outputs of the total system (u_{sys} and y_{sys}). The total state space model is described by

$$\dot{x}_{app} = A_T x_{app} + B_T u_{sys}$$
$$y_{sys} = C_T x_{app} + D_T u_{sys} \tag{3-10}$$

where,

$$A_T = A_{app} + B_{app} L_1 \left(I - D_{app} L_1 \right)^{-1} C_{app}$$

$$B_T = B_{app} L_1 \left(I - D_{app} L_1 \right)^{-1} D_{app} L_2 + B_{app} L_2$$

$$C_T = L_3 \left(I - D_{app} L_1 \right)^{-1} C_{app}$$

$$D_T = L_3 \left(I - D_{app} L_1 \right)^{-1} D_{app} L_2 + L_4 \tag{3-11}$$

and I is the identity matrix.

3.3.2. HOW TO CONVERT AN ELECTRICAL NETWORK TO A CONTROL SYSTEM

An electrical network (a physical system in general) is totally different from a control system. In a control system signals are unidirectional signals but in an electrical system in addition to the control signals, the electrical quantities are tied to each other by algebraic equations. Therefore, an electrical network formed of different converters can be converted to a control system with some feedback loops to consider the algebraic equations. To enlighten this, consider the power system shown in Figure 3-3. The system has a current-controlled converter (shown as a current source) and a voltage-controlled converter (shown as a voltage source), which also has an input for the reference signal.
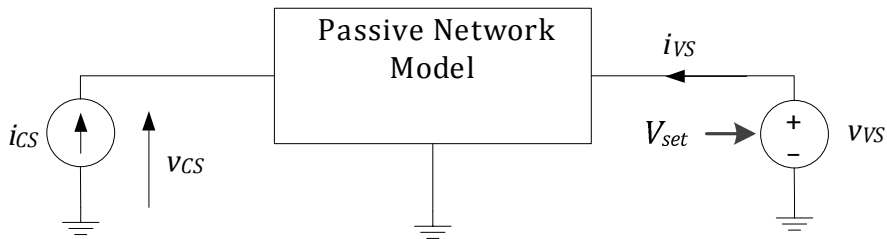
Figure 3-3 An electrical system formed of two converters.

The current source can be considered as a control subsystem, whose output and input are the terminal current and voltage, respectively. Similarly, the outputs and inputs of the voltage source can be considered as its set point and voltage and current, respectively. It must be noted that the voltages and currents also have some relations defined by the passive network. Therefore, if the network itself is considered as a subsystem, it should complement the inputs and outputs of other subsystems. Figure 3-4 shows how the entire system looks like as an interconnected control system. The CCM can now be used because all the subsystems and interconnections are known. The inputs and outputs are highlighted with red and blue signals, respectively. The elements of u_{cmp} and y_{cmp} vectors are also highlighted in Figure 3-4. Any signal can be considered as the system input and output. As an example, the voltage set point v_{set} is considered as the input to the overall system and v_{cs} is considered as the output. L_1, L_2, L_3 and L_4 are the interconnection matrices of (3-9) and (3-11), which are given as (3-12).
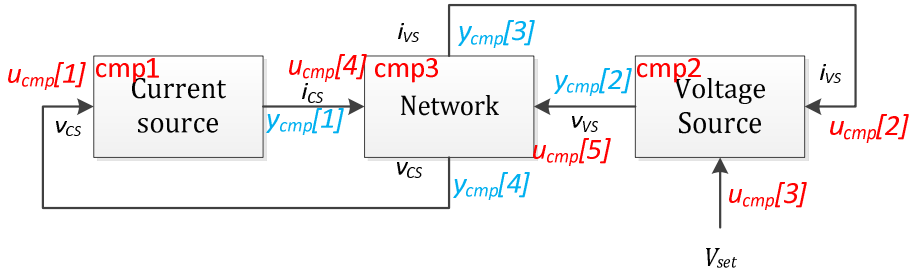
Figure 3-4 Electrical system considered in Figure 3-3 as a control system.

$$L_1 = \begin{bmatrix} 0 & 0 & 0 & 1 \\ 0 & 0 & 1 & 0 \\ 0 & 0 & 0 & 0 \\ 1 & 0 & 0 & 0 \\ 0 & 1 & 0 & 0 \end{bmatrix}, L_2 = \begin{bmatrix} 0 \\ 0 \\ 1 \\ 0 \\ 0 \end{bmatrix} \tag{3-12}$$

$$L_3 = \begin{bmatrix} 0 & 0 & 0 & 1 \end{bmatrix}, L_4 = \begin{bmatrix} 0 \end{bmatrix}$$

3.3.2.1 Improper transfer functions

A transfer function is called improper, if the order of the numerator polynomial is more than the order of the denominator polynomial. The state space model of an improper transfer function could not be described by only *A, B, C* and *D* matrices and another matrix *E* is needed to model the extra order.

$$\dot{x} = Ax + Bu$$
$$y = Cx + Du + E\dot{u} \tag{3-13}$$

This case is not uncommon in electrical systems, for instance the impedance/admittance of an inductor/capacitor is improper. The CCM is not able to deal with improper subsystems, and therefore, it should be changed slightly. Figure 3-5 shows a simple example where a current controlled converter is in series with an inductor. The converter admittance is proper; however, the grid impedance is not.
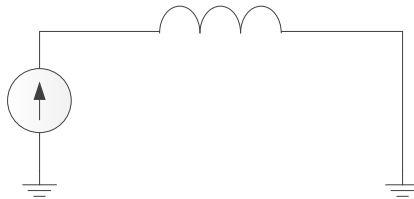
Figure 3-5 Example of an improper network, where a current source is in series with an inductor.

The workaround proposed in this work is to feed the input's derivative to the improper transfer function in addition to the original input. Figure 3-6 (a) shows the original model and Figure 3-6 (b) is how this problem can be solved by providing the current derivative. By doing this the improper transfer function becomes a proper transfer function, which has two inputs. This derivative must be delivered by the subsystem, whose output was connected to the input of the improper subsystem. This can easily be done if the admittance model of the converter is strictly proper ($D==0$). Equation (3-14) shows how the derivative can be calculated. $Y(s)$ is the admittance model of a converter. The additional output is the derivative of the original output.
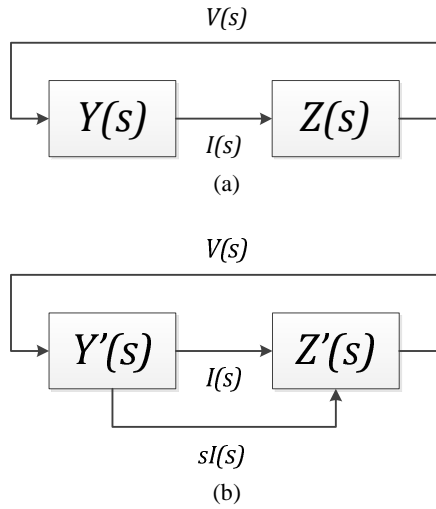
Figure 3-6 Control representation of the network shown in Figure 3-5. (a) Original block diagram (b) The improper transfer function can be avoided by introducing an extra input which is the derivative of the original input.

The output derivative can easily be calculated if its model is strictly proper ($D==0$).

$$y = Cx \Rightarrow \dot{y} = C\dot{x} = C(Ax + Bu) \tag{3-14}$$

Then the new state space matrices are

$$C_{new} = \begin{bmatrix} C \\ CA \end{bmatrix}, D_{new} = \begin{bmatrix} [0] \\ CB \end{bmatrix} \tag{3-15}$$

3.3.3. A GLOBAL REFERENCE SYSTEM

If a per unit system is used, then an ideal transformers can be eliminated from the studies [15], and the passive system is simplified to only RLC elements. Therefore, it is necessary to change a per unit model, when it is defined in another base. For instance, the parameters of a transformer are normalized based on its nominal power, which could differ from the base power of the system. This can easily be done by changing B, C and D matrices, which define the input output characteristics of a dynamical model. For instance, for an admittance model, whose input is the voltage and the output is current, the adjustment can be done by using

$$B_{new} = B \frac{v_{base_{old}}}{v_{base_{new}}}$$

$$C_{new} = C \frac{i_{base_{old}}}{i_{base_{new}}} \qquad (3\text{-}16)$$

$$D_{new} = C \frac{Z_{base_{old}}}{Z_{base_{new}}}$$

It must be noted that in this chapter, time and frequency are not normalized. For more information see §3.4.1.

In this stability analysis platform, all subsystems are modelled in dq domain, and each converter has its own reference frame and therefore, it is necessary to define a global reference frame and the inputs and outputs must be transformed accordingly. DQ axes in Figure 3-7 is the system global reference frame and dq_i is the reference frame of the ith component and δ_i is the phase difference between the two frames.
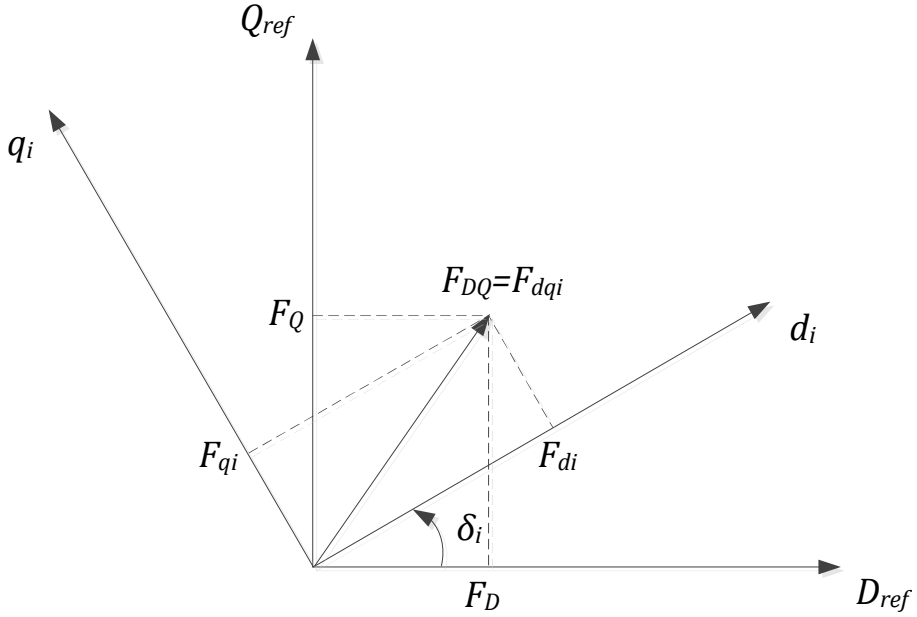
Figure 3-7 How to transform from one rotating frame to another frame.

The inputs to the subsystem must be transformed to the subsystem's reference frame and the outputs must be returned in the global reference frame. Therefore,

$$B_{new} = B \begin{bmatrix} \cos\delta & \sin\delta \\ -\sin\delta & \cos\delta \end{bmatrix}$$

$$C_{new} = \begin{bmatrix} \cos\delta & -\sin\delta \\ \sin\delta & \cos\delta \end{bmatrix} C \qquad (3\text{-}17)$$

$$D_{new} = \begin{bmatrix} \cos\delta & -\sin\delta \\ \sin\delta & \cos\delta \end{bmatrix} D \begin{bmatrix} \cos\delta & \sin\delta \\ -\sin\delta & \cos\delta \end{bmatrix}$$

3.4. MODELS OF DIFFERENT ELEMENTS

3.4.1. NETWORK MODELLING

For small networks, a direct transformation from the transfer function form to the state space form using (3-18) and (3-19) is doable.

$$G(s) = \frac{b_0 s^n + b_1 s^{n-1} + b_2 s^{n-2} + \cdots + b_{n-1}s + b_n}{a_0 s^n + a_1 s^{n-1} + a_2 s^{n-2} + \cdots + a_{n-1}s + a_n} \qquad (3\text{-}18)$$

$$A = \begin{bmatrix} 0 & 1 & 0 & 0 & \cdots & 0 \\ 0 & 0 & 1 & 0 & \cdots & 0 \\ 0 & 0 & 0 & 1 & \cdots & 0 \\ \vdots & \vdots & \vdots & \vdots & \ddots & \vdots \\ 0 & 0 & 0 & 0 & \cdots & 1 \\ -\dfrac{a_n}{a_0} & -\dfrac{a_{n-1}}{a_0} & -\dfrac{a_{n-2}}{a_0} & -\dfrac{a_{n-3}}{a_0} & \cdots & -\dfrac{a_1}{a_0} \end{bmatrix}$$

$$B = \begin{bmatrix} 0 \\ 0 \\ 0 \\ \vdots \\ 0 \\ 1 \end{bmatrix}$$

(3-19)

$$C = \begin{bmatrix} \dfrac{b_n}{a_0} - \dfrac{a_n}{a_0^2} b_0 & \dfrac{b_{n-1}}{a_0} - \dfrac{a_{n-1}}{a_0^2} b_0 & \dfrac{b_{n-2}}{a_0} - \dfrac{a_{n-2}}{a_0^2} b_0 & \cdots & \dfrac{b_1}{a_0} - \dfrac{a_1}{a_0^2} b_0 \end{bmatrix}$$

$$D = \frac{b_0}{a_0}$$

For instance, the network model of Figure 3-8 in the Laplace domain is given as

$$V_{PCC}(s) = \frac{R_s + sL_s}{sC_{PFC}(R_s + sL_s) + 1} I_{inv1}(s) \\ + \frac{1}{(sC_{PFC}(R_s + sL_s) + 1)} V_G(s)$$

(3-20)
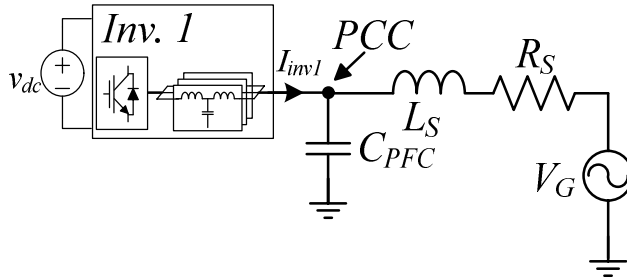
Figure 3-8 An electrical network including a voltage source inverter connected to a grid.

and it can easily be transformed into the state space form (if i_{inv} is considered as the only input) by using

$$A = \begin{bmatrix} 0 & 1 \\ \dfrac{-1}{C_{PFC}L_s} & \dfrac{-R_s}{L_s} \end{bmatrix}, B = \begin{bmatrix} 0 \\ 1 \end{bmatrix},$$

(3-21)

$$C = \begin{bmatrix} R_s/C_{PFC}L_s & 1/C_{PFC} \end{bmatrix}, D = [0]$$

However, this method fails for larger system, since it needs the inversion of large symbolic matrices. The method, which is used here as a solution, is a well-established method, which directly yields the state space equations of a network. The complete method can be found in [49]; therefore, in here it is introduced briefly. The method works perfectly for systems with RLC elements and ideal voltage/current sources. As discussed previously, the converters and other dynamical models are modelled separately and therefore, they are represented as current/voltage sources in finding the state space model of the network.

The first step is to represent the electrical network by a directed graph, whose vertices/nodes are the nodes of the electrical system and the edges are the components. Then, the normal tree[2] of this graph must be found, which contains all voltage sources as twigs[3] and all current sources as links[4]. Then as many capacitors as possible must be placed in the twigs and as many inductors as possible in the links. This can be done by assigning a weight as shown in Table 3-1 to each edge, and then the minimum spanning tree of the system gives the normal tree. There are different methods to find the minimum spanning tree of large graphs and in in here Kruskal's algorithm [50] is used. It must be noted that there are cases where an inductor must inevitably be placed in a twig or a capacitor must be placed in a link. These cases make the model of the electrical system improper; however, the systematic approach that is presented here is able to handle them correctly.

Table 3-1 Weight factors for different elements in an electrical network.

Element	Weight
Voltage sources	0
Capacitors	100
Resistors	1000
Inductors	100000
Current sources	5000000

Then the second step is to write KVL equations for the fundamental loops and KCL equations for the fundamental cutsets.

---

[2] In graph theory, a tree is a graph, in which any two nodes are connected by exactly one path. In other words, there is no loop in a tree.

[3] A twig is a branch of a tree.

[4] A link is an edge of a graph that is not a twig of its tree.

$$i_{twig} = -Q_l i_{link}$$

$$v_{link} = Q_l' v_{twig}$$

(3-22)

where Q_l is a sub matrix of the fundamental cutset matrix Q as

$$Q = \begin{bmatrix} I_{n_{twigs} \times n_{twigs}} & Q_{l_{n_{twigs} \times n_{links}}} \end{bmatrix}$$

(3-23)

where I is the unity matrix. If one sorts the columns and rows of Q_l based on the order mentioned for twigs and links, then it would be

$$Q_l = \begin{matrix} links \rightarrow \\ twigs \downarrow \\ \\ E \\ C \\ R \\ L \end{matrix} \quad \begin{matrix} C & R & L & J \end{matrix} \\ \begin{bmatrix} Q_{EC} & Q_{ER} & Q_{EL} & Q_{EJ} \\ Q_{CC} & Q_{CR} & Q_{CL} & Q_{CJ} \\ 0 & Q_{RR} & Q_{RL} & Q_{RJ} \\ 0 & 0 & Q_{LL} & Q_{LJ} \end{bmatrix}$$

(3-24)

It should be noted that the fundamental cut set matrix defines the topology of the system and only contains ones, zeros and minus ones. The differential algebraic equation of the electrical network can then be written as

$$\begin{bmatrix} i_{Ct} \\ i_{Cl} \end{bmatrix} = \frac{d}{dt} \begin{bmatrix} C_t & 0 \\ 0 & C_l \end{bmatrix} \begin{bmatrix} v_{Ct} \\ v_{Cl} \end{bmatrix}$$

$$\begin{bmatrix} v_{Lt} \\ v_{Ll} \end{bmatrix} = \frac{d}{dt} \begin{bmatrix} L_t & 0 \\ 0 & L_l \end{bmatrix} \begin{bmatrix} i_{Lt} \\ i_{Ll} \end{bmatrix}$$

(3-25)

$$\begin{bmatrix} i_{Rt} \\ v_{Rl} \end{bmatrix} = \begin{bmatrix} R_t & 0 \\ 0 & R_l^{-1} \end{bmatrix} \begin{bmatrix} v_{Rt} \\ i_{Rl} \end{bmatrix}$$

where C_t is a matrix that contains the values of the capacitors in the twigs (notice subscript t) as its diagonal elements, C_l is the matrix of the capacitors in the links, L_t and L_l define the matrices of inductor in the twigs and the links, respectively, and finally R_t and R_l are the similar matrices for resistors in the twigs and the links.

By eliminating some variables and considering the ideal voltage/current sources as the inputs to the control system, the state variable equations can be written as

$$\dot{x} = Ax + B_1 u + B_2 \dot{u} \tag{3-26}$$

where

$$x = \begin{bmatrix} v_{Ct} \\ i_{Ll} \end{bmatrix} \tag{3-27}$$

$$u = \begin{bmatrix} v_E \\ i_J \end{bmatrix} \tag{3-28}$$

$$A = \begin{bmatrix} \mathbb{C}^{-1} & 0 \\ 0 & \mathbb{L}^{-1} \end{bmatrix} \begin{bmatrix} -\mathbb{Y} & \mathbb{H} \\ \mathbb{G} & -\mathbb{Z} \end{bmatrix} \tag{3-29}$$

$$B_1 = \begin{bmatrix} \mathbb{C}^{-1} & 0 \\ 0 & \mathbb{L}^{-1} \end{bmatrix} \begin{bmatrix} -\widetilde{\mathbb{Y}} & \widetilde{\mathbb{H}} \\ \widetilde{\mathbb{G}} & -\widetilde{\mathbb{Z}} \end{bmatrix} \tag{3-30}$$

$$B_2 = \begin{bmatrix} \mathbb{C}^{-1} & 0 \\ 0 & \mathbb{L}^{-1} \end{bmatrix} \begin{bmatrix} \widetilde{\mathbb{C}} & 0 \\ 0 & \widetilde{\mathbb{L}} \end{bmatrix} \tag{3-31}$$

$$\mathbb{C} = C_t + Q_{CC} C_l Q'_{CC} \tag{3-32}$$

$$\widetilde{\mathbb{C}} = -Q_{CC} C_l Q'_{EC} \tag{3-33}$$

$$\mathbb{L} = L_l + Q'_{LL} L_t Q_{LL} \tag{3-34}$$

$$\widetilde{\mathbb{L}} = -Q'_{LL} L_t Q_{LJ} \tag{3-35}$$

$$\mathcal{R} = R_l + Q'_{RR} R_t Q_{RR} \tag{3-36}$$

$$\mathcal{G} = R_t^{-1} + Q_{RR} R_l^{-1} Q'_{RR} \tag{3-37}$$

$$\mathbb{Y} = Q_{CR} \mathcal{R}^{-1} Q'_{CR} \tag{3-38}$$

$$\mathbb{H} = -Q_{CL} + Q_{CR} \mathcal{R}^{-1} Q'_{RR} R_t Q_{RL} \tag{3-39}$$

$$\mathbb{Z} = Q'_{RL} \mathcal{G}^{-1} Q_{RL} \tag{3-40}$$

$$\mathbb{G} = -\mathbb{H}' \tag{3-41}$$

$$\widetilde{\mathbb{Y}} = Q_{CR} \mathcal{R}^{-1} Q'_{ER} \tag{3-42}$$

$$\mathbb{H} = -Q_{CJ} + Q_{CR} \mathcal{R}^{-1} Q'_{RR} R_t Q_{RJ} \tag{3-43}$$

$$\widetilde{\mathbb{Z}} = Q'_{RL} \mathcal{G}^{-1} Q_{Rj} \tag{3-44}$$

$$\mathbb{G} = Q'_{EL} - Q'_{RL}G^{-1}Q_{RR}R_l^{-1}Q'_{ER} \tag{3-45}$$

The outputs must be chosen as the voltage/currents of the current/voltage sources. By doing this the necessary impedance/admittance models described in §3.3.2 can be obtained.

$$y = Cx + D_1u + D_2\dot{u} \tag{3-46}$$

where

$$y = \begin{bmatrix} i_E \\ v_J \end{bmatrix} \tag{3-47}$$

$$C = \begin{bmatrix} -Q_{EC}C_lQ'_{CC}\mathbb{C}^{-1}[-\mathbb{Y} & \mathbb{H}] \\ -Q'_{LJ}L_tQ_{LL}\mathbb{L}^{-1}[\mathbb{G} & -\mathbb{Z}] \end{bmatrix} + \begin{bmatrix} -Q_{ER}[R^{-1}Q'_{CR} & -R^{-1}Q'_{RR}R_tQ_{RL}] \\ Q'_{RJ}[-G^{-1}Q_{RR}G_lQ'_{CR} & -G^{-1}Q_{RL}] \end{bmatrix} \\ + \begin{bmatrix} 0 & -Q_{EL} \\ Q'_{CJ} & 0 \end{bmatrix} \tag{3-48}$$

$$D_1 = \begin{bmatrix} -Q_{EC}C_lQ'_{CC}\mathbb{C}^{-1}[-\widehat{\mathbb{Y}} & \widehat{\mathbb{H}}] \\ -Q'_{LJ}L_tQ_{LL}\mathbb{L}^{-1}[\widehat{\mathbb{G}} & -\widehat{\mathbb{Z}}] \end{bmatrix} + \begin{bmatrix} -Q_{ER}[R^{-1}Q'_{ER} & -R^{-1}Q'_{RR}R_tQ_{RJ}] \\ Q'_{RJ}[-G^{-1}Q_{RR}G_lQ'_{ER} & -G^{-1}Q_{RJ}] \end{bmatrix} \\ + \begin{bmatrix} 0 & -Q_{EJ} \\ Q'_{EJ} & 0 \end{bmatrix} \tag{3-49}$$

$$D_2 = \begin{bmatrix} -Q'_{EC}(C_lQ'_{CC}\mathbb{C}^{-1}[\widehat{\mathbb{C}} & 0] + C_l[Q'_{EC} & 0]) \\ -Q'_{LJ}(L_tQ_{LL}\mathbb{L}^{-1}[0 & \widehat{\mathbb{L}}] + L_t[0 & Q_{LJ}]) \end{bmatrix} \tag{3-50}$$

Considering the discussion in §3.3.2.1 in respect to the improper networks, and the suggested idea, which requires the derivatives of inputs as a new input, the state space equations are

$$\dot{x} = Ax + [B_1 \quad B_2]\begin{bmatrix} u \\ \dot{u} \end{bmatrix}$$

$$y = Cx + [D_1 \quad D_2]\begin{bmatrix} u \\ \dot{u} \end{bmatrix} \tag{3-51}$$

As discussed earlier the network parameters are normalized in order to eliminate the ideal transformers, and therefore, the network can be modelled by only RLC elements plus ideal sources. Therefore, all parameters in the system such as resistances, inductances and capacitances are normalized. This also implies that the time is also normalized. However, it is preferred to express the time in seconds. Therefore, the above equations must be changed slightly. The time derivative terms must be updated by

$$\frac{d}{dt_{pu}}x = \frac{1}{\omega_b}\frac{d}{dt}x \tag{3-52}$$

Where, ω_b is the nominal (base) frequency of the system. Therefore, the state equations become

$$\dot{x} = \omega_b A x + \begin{bmatrix} \omega_b B_1 & B_2 \end{bmatrix}\begin{bmatrix} u \\ \dot{u} \end{bmatrix}$$

$$y = Cx + \begin{bmatrix} D_1 & \dfrac{1}{\omega_b}D_2 \end{bmatrix}\begin{bmatrix} u \\ \dot{u} \end{bmatrix} \tag{3-53}$$

Equation (3-53) describe a single phase system (only positive sequence), therefore they must be transformed into the *dq* domain. As discussed in Chapter 2, the *abc* to *dq* transformation matrix is

$$\begin{aligned}
\begin{bmatrix} f_{dq} \end{bmatrix} &= [T(\theta)][f_{abc}] \\
&= \frac{2}{3}\begin{bmatrix} \cos\theta & \cos\left(\theta - \dfrac{2\pi}{3}\right) & \cos\left(\theta + \dfrac{2\pi}{3}\right) \\ -\sin\theta & -\sin\left(\theta - \dfrac{2\pi}{3}\right) & -\sin\left(\theta + \dfrac{2\pi}{3}\right) \end{bmatrix}[f_{abc}]
\end{aligned} \tag{3-54}$$

$$[f_{abc}] = [T_n(\theta)][f_{dq}] = \begin{bmatrix} \cos\theta & -\sin\theta \\ \cos\left(\theta - \dfrac{2\pi}{3}\right) & -\sin\left(\theta - \dfrac{2\pi}{3}\right) \\ \cos\left(\theta + \dfrac{2\pi}{3}\right) & -\sin\left(\theta + \dfrac{2\pi}{3}\right) \end{bmatrix}[f_{dq}] \tag{3-55}$$

The three-phase network dynamics are

$$\begin{aligned}
\frac{d}{dt}\begin{bmatrix} x_a \\ x_b \\ x_c \end{bmatrix} &= \begin{bmatrix} A & 0 & 0 \\ 0 & A & 0 \\ 0 & 0 & A \end{bmatrix}\begin{bmatrix} x_a \\ x_b \\ x_c \end{bmatrix} + \begin{bmatrix} B_1 & 0 & 0 \\ 0 & B_1 & 0 \\ 0 & 0 & B_1 \end{bmatrix}\begin{bmatrix} u_a \\ u_b \\ u_c \end{bmatrix} \\
&\quad + \begin{bmatrix} B_2 & 0 & 0 \\ 0 & B_2 & 0 \\ 0 & 0 & B_2 \end{bmatrix}\frac{d}{dt}\begin{bmatrix} u_a \\ u_b \\ u_c \end{bmatrix}
\end{aligned} \tag{3-56}$$

$$\begin{bmatrix} y_a \\ y_b \\ y_c \end{bmatrix} = \begin{bmatrix} C & 0 & 0 \\ 0 & C & 0 \\ 0 & 0 & C \end{bmatrix}\begin{bmatrix} x_a \\ x_b \\ x_c \end{bmatrix} + \begin{bmatrix} D_1 & 0 & 0 \\ 0 & D_1 & 0 \\ 0 & 0 & D_1 \end{bmatrix}\begin{bmatrix} u_a \\ u_b \\ u_c \end{bmatrix} + \begin{bmatrix} D_2 & 0 & 0 \\ 0 & D_2 & 0 \\ 0 & 0 & D_2 \end{bmatrix}\frac{d}{dt}\begin{bmatrix} u_a \\ u_b \\ u_c \end{bmatrix}$$

By using the following properties one can express (3-56) in the *dq* domain as (3-59).

$$[T(\theta)]\begin{bmatrix} F & 0 & 0 \\ 0 & F & 0 \\ 0 & 0 & F \end{bmatrix}[T_n(\theta)] = \begin{bmatrix} F & 0 \\ 0 & F \end{bmatrix} \tag{3-57}$$

$$[T(\theta)]\begin{bmatrix} F & 0 & 0 \\ 0 & F & 0 \\ 0 & 0 & F \end{bmatrix}\frac{d}{dt}[T_n(\theta)] = \begin{bmatrix} 0 & -F\omega_b \\ F\omega_b & 0 \end{bmatrix} \tag{3-58}$$

$$\frac{d}{dt}[x_{dq}] = \begin{bmatrix} A & \omega_b \times I \\ -\omega_b \times I & A \end{bmatrix}[x_{dq}] + \begin{bmatrix} B_1 & -B_2\omega_b \\ B_2\omega_b & B_1 \end{bmatrix}[u_{dq}]$$
$$+ \begin{bmatrix} B_2 & 0 \\ 0 & B_2 \end{bmatrix}\frac{d}{dt}[u_{dq}] \tag{3-59}$$

$$[y_{dq}] = \begin{bmatrix} C & 0 \\ 0 & C \end{bmatrix}[x_{dq}] + \begin{bmatrix} D_1 & -D_2\omega_b \\ D_2\omega_b & D_1 \end{bmatrix}[u_{dq}] + \begin{bmatrix} D_2 & 0 \\ 0 & D_2 \end{bmatrix}\frac{d}{dt}[u_{dq}]$$

It should be noted that the network uses the global reference frame. Thus, no further adjustments are needed for the frame transformation.

3.4.2. CABLE MODELLING

In this chapter, it is assumed that a nominal π-model is sufficient for modeling a cable. However, this is not the case when the cable is too long or the behavior in a wide frequency range is of interest. A more detailed approach will be presented in Chapter 4, which covers the frequency dependent characteristics such as skin effect and proximity effect.

A cable can be modelled by nominal π-section(s), whose parameters are obtained from the per unit length characteristics that can be found in the cable catalog.
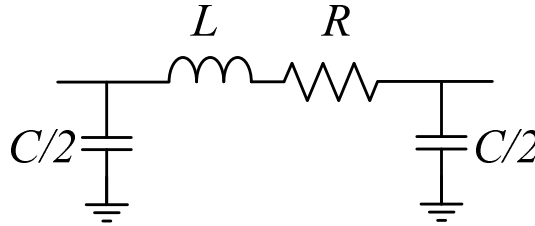
Figure 3-9 Modelling a cable using the nominal π-model.

It can be seen that the final model is indeed a passive RLC model, where the systematic network modelling approach explained in §3.4.1 is able to easily transform to the state space representation, no matter how many sections are used. It

is also worth to note that usually the cable parameters are given in the sequence domain, which is perfect for the systematic approach.

3.4.3. TRANSFORMER MODELLING

The same as the previous part, the frequency dependency such as skin effect is neglected in the transformer modelling. A more detailed modelling approach is presented in Chapter 4. Figure 3-10 shows an equivalent positive sequence model of a two-winding transformer.
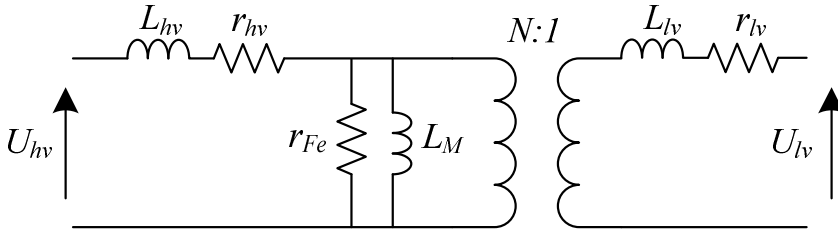
Figure 3-10 Two-winding transformer model used for harmonic studies.

The parameters of Figure 3-10 are normally not stated in the catalog (or in PowerFactory), instead the short circuit impedance and losses are available. The equations below can be used to obtain the necessary values. It must be noted that the base power of the transformer might be different from the system's base. Therefore, necessary adjustments must be done afterwards.

The short circuit (leakage) impedance is:

$$z_{sc} = \frac{uk}{100} \tag{3-60}$$

The resistive part of the leakage impedance can be calculated from the copper losses.

$$r_{sc} = \frac{P_{cu}/1000}{S_{base}} \tag{3-61}$$

where P_{cu} is the copper losses in kW and S_{base} is the rated power of the transformer in MVA. Consequently, the leakage reactance can be defined as

$$x_{sc} = \sqrt{z_{sc}^2 - r_{sc}^2} \tag{3-62}$$

In this thesis, it is assumed that the per unit leakage impedance is equally distributed in the HV and LV sides of the transformer. However, they can easily be adjusted if the exact distribution is known.

$$z_{hv} = 0.5r_{sc} + j0.5x_{sc}$$

$$z_{lv} = 0.5r_{sc} + j0.5x_{sc}$$

(3-63)

The magnetizing impedance can be found from the no load current as

$$z_m = \frac{1}{I_0/100}$$

(3-64)

where, I_0 is the no-load current in percent. Similarly, the resistive model of the core can be found from the no-load losses as:

$$r_{Fe} = \frac{S_{base}}{P_{Fe}/1000}$$

(3-65)

where P_{FE} is the iron losses in kW.

Finally, the magnetizing inductance can be found by

$$x_M = \frac{1}{\sqrt{\frac{1}{z_M^2} - \frac{1}{r_{Fe}^2}}}$$

(3-66)

As stated before, the frequency dependent characteristics are neglected; therefore, fixed parameters are used in here. One important thing in the transformer modelling is the phase difference between the HV and LV sides of the transformer, which affects the model in the frequency domain. However, the voltages and currents at each side are shifted with the same angle and therefore, one can disregard this phase difference in the modelling. It must be noted that this only holds for radial networks such as wind power plants.

3.4.4. POWER ELECTRONIC CONVERTERS

In Chapter 2, the converter model is derived in the *dq* domain. Figure 3-11shows how a converter is modelled in PowerFactory. The library based approach used in the software lets the user to define new controllers and to easily use them. After a load flow analysis the software also calculates the steady state values of the internal signals such as the currents, voltages and modulation indices in the *dq* domain,

which are needed for the linearization of a nonlinear power converter as shown in Table 2-8.
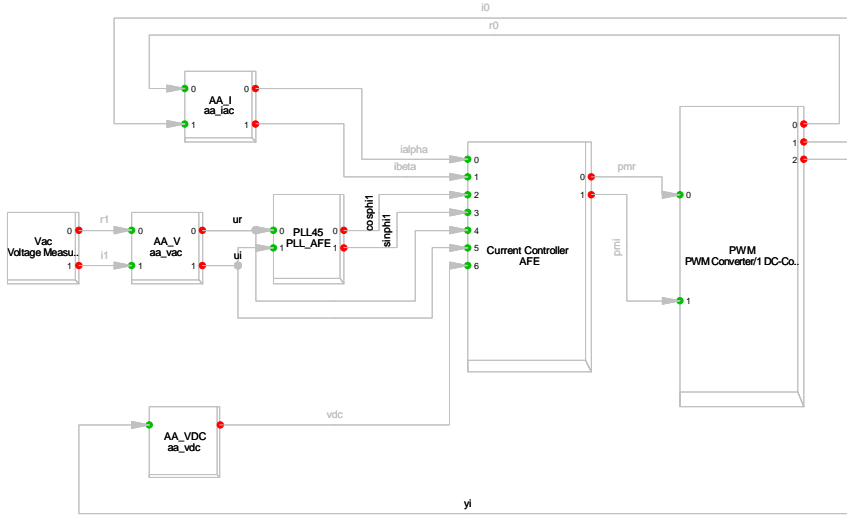
Figure 3-11 Implementation of a power converter in PowerFactory.

3.4.5. SYNCHRONOUS MACHINE MODEL

The stability analysis platform can be used to study the interactions with a synchronous generator, such as sub synchronous resonance or control interactions. The CCM in the core of this stability platform enables the user to add different elements easily. Only the impedance or admittance models of a component are needed. Equation (3-67) shows a generic 8th order model of a synchronous machine, in which the rotor is modelled by one field winding and one damper winding in the d-axis and two damper windings in the q-axis [51].

$$\frac{d}{dt}\begin{bmatrix} \psi_d \\ \psi_F \\ \psi_D \\ \psi_q \\ \psi_G \\ \psi_Q \\ \omega \\ \delta \end{bmatrix} = [A]\begin{bmatrix} \psi_d \\ \psi_F \\ \psi_D \\ \psi_q \\ \psi_G \\ \psi_Q \\ \omega \\ \delta \end{bmatrix} + [B]\begin{bmatrix} v_{ds} \\ v_{qs} \\ p_t \\ E_f \end{bmatrix} \tag{3-67}$$

$$\begin{bmatrix} i_{ds} \\ i_{qs} \\ \omega \end{bmatrix} = [C] \begin{bmatrix} \psi_d \\ \psi_F \\ \psi_D \\ \psi_q \\ \psi_G \\ \psi_Q \\ \omega \\ \delta \end{bmatrix} + [D] \begin{bmatrix} v_{ds} \\ v_{qs} \\ p_t \\ E_f \end{bmatrix}$$

where ψ_d is the flux linkage in the stator d-axis, ψ_q is the flux linkage in the stator q-axis, ψ_F is the flux linkage of the field winding, ψ_D, ψ_G and ψ_Q are the flux linkages in the rotor damping winding D, G and Q. v_{ds} and v_{qs} are the voltages at the machine terminals in the global reference frame of the system. i_{ds} and i_{qs} are the stator currents in the global reference frame of the system. p_t is the mechanical power of the prime mover and E_f is the field voltage.

The excitation system (AVR) and the turbine shaft model can easily be embedded into the above model by using the CCM. Figure 3-12 shows how this can be done. It is also worth noting that additional controllers such as governor and PSS can also be implemented similarly.
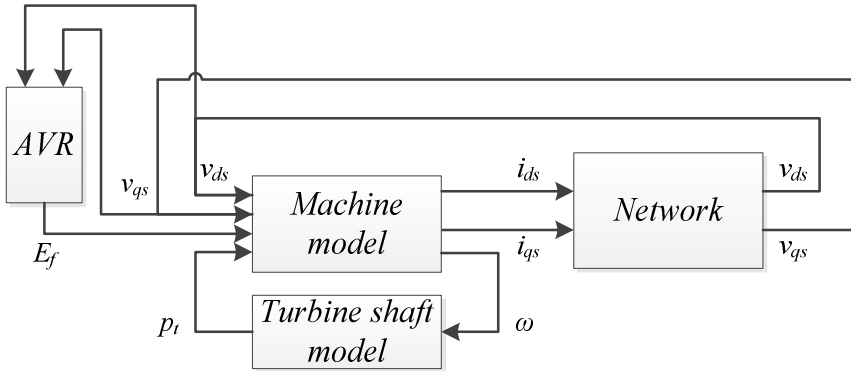
Figure 3-12 Interconnected synchronous machine model.

3.5. VALIDATION AND ANALYSIS

The resultant matrices are of large size and therefore it is necessary to somehow validate the results before doing any analysis based on them. The validation can be done in different ways such as

1) Time domain simulations: as shown in Chapter 2, the time domain results can be used to validate the dominant poles of the system. However, for a

large system, it takes a long time to simulate a perturbation in a large system.

2) Commercial power system softwares are able to analyze the small signal stability of a large system. However, it should be noted that those methods are mainly designed for analysis of electromechanical oscillations and they neglect the dynamics in the grid. Therefore, the results are valid for the low frequency oscillations (e.g. less than 5 Hz). Therefore, they are not helpful in validating the medium to high frequency range dynamics. However, they can be used to validate the low frequency poles of the system.

3) In commercial power system tools, the impedance frequency scan can be performed from different points. The same information can also be obtained from the state-space matrices created by the stability analysis platform. Therefore, if the frequency responses are the same from different viewpoints, then the results are validated.

3.5.1. KUNDUR'S 4-MACHINE 2-AREA SYSTEM

In this example a test system, which has been introduced in [15], is investigated. The system is formed of two areas, which are connected by a weak connection. Each area has 2 synchronous machines. Figure 3-13 shows the schematic of this system and the parameters can be found in [15]. The results of the small signal stability analysis calculated by DIgSILENT PowerFactory are valid for the low frequency range, and therefore, they can be used to validate the low frequency dynamics calculated by the developed stability analysis platform. Figure 3-14 shows a good agreement between the two methods ("Code" refers to the developed tool and "PF" stands for PowerFactory).
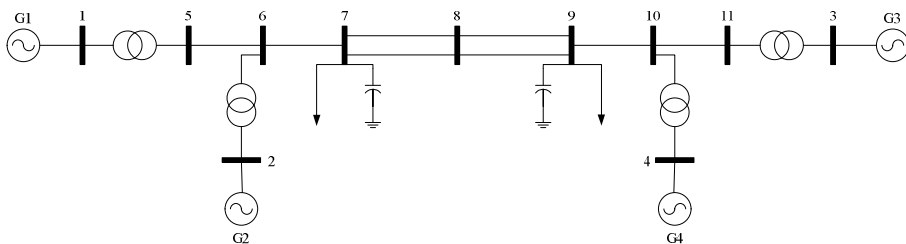
Figure 3-13 Kundur's 4-Machine 2-Area System [15].
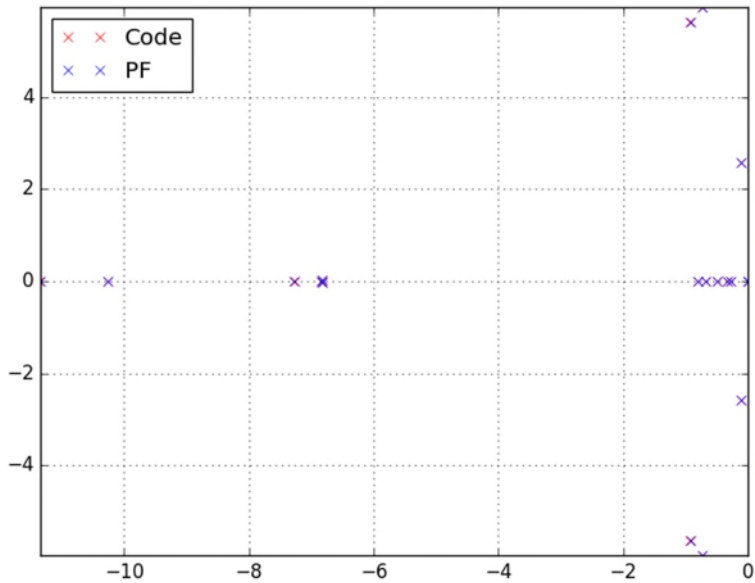
Figure 3-14 Comparing the identified eigenvalues by the Modal Analysis Toolbox in PowerFactory and the developed tool for the Kundur's system.

3.5.2. 35-WT OFFSHORE WIND POWER PLANT

In this part, the developed stability analysis platform is validated for a large scale system shown in Appendix B. The third approach of validation, which is based on the frequency scan results, is used. The driving point impedance is measured from the highlighted bus bars in Figure 3-15 using the impedance frequency scan in PowerFactory. It should be noted PowerFactory measures the impedance of the passive elements only in the sequence domain. Therefore, the WTs are modelled by a frequency dependent cable (see §4.3.3.2), which replicates the high frequency behavior of a power converter. Similarly the impedance in the sequence domain is calculated by the developed tool for those bus bars and the results are shown in Figure 3-16, where a good agreement between the two tools can be seen. It is worth to mention that the final model includes 627 RLC elements and around 300 state variables.
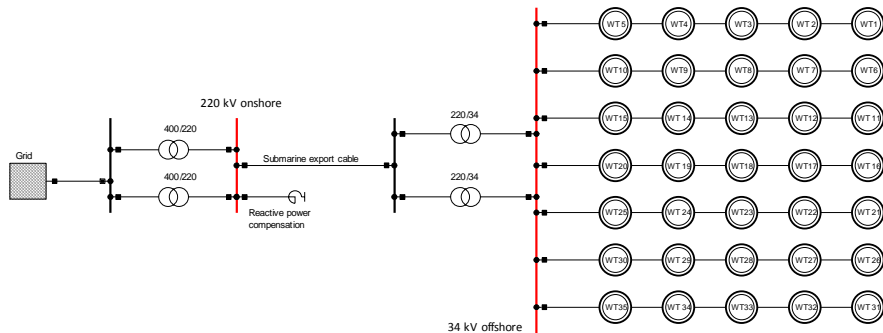
(a)
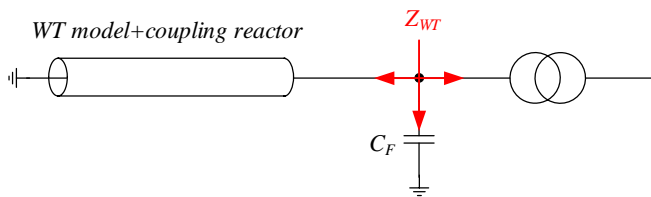
(b)

Figure 3-15 Impedance frequency scan at the (a) 34 kV offshore and 220 kV onshore busbars (b) Wind turbine terminals (the WT is modeled as a frequency dependent impedance).
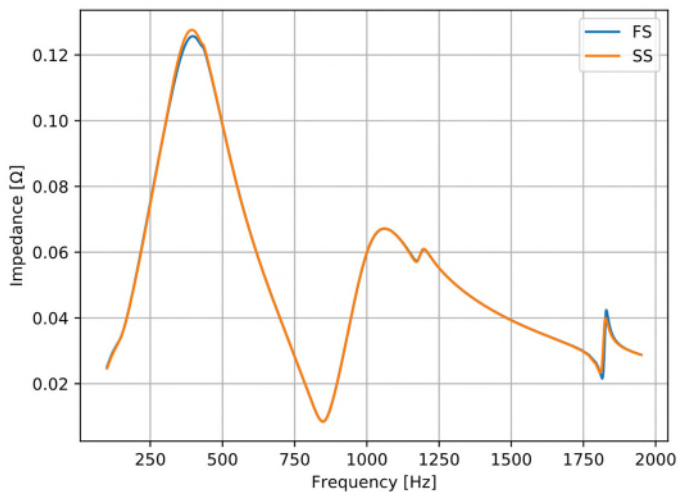
(a)
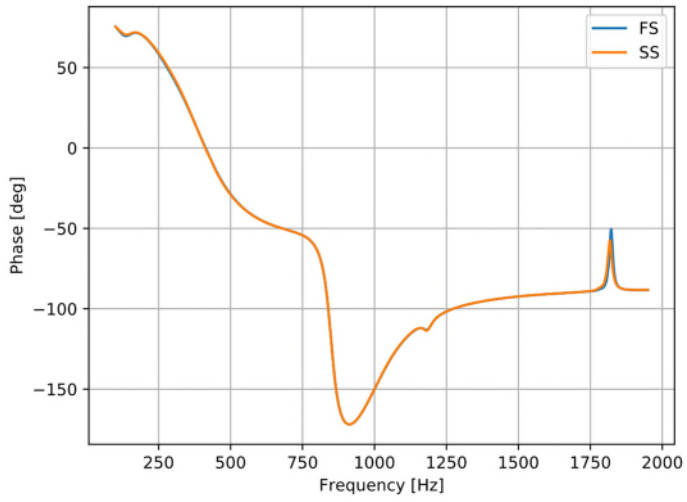
(b)
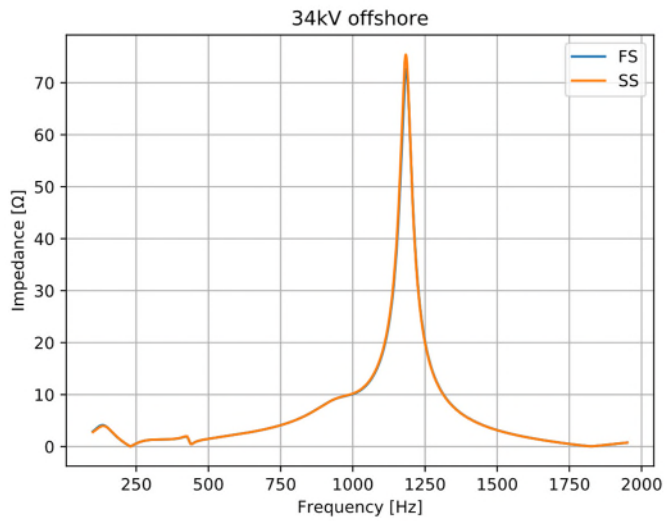
(c)
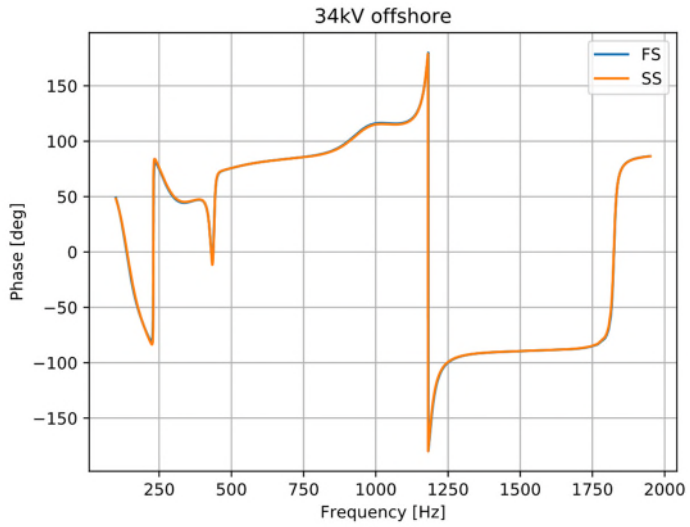
(d)
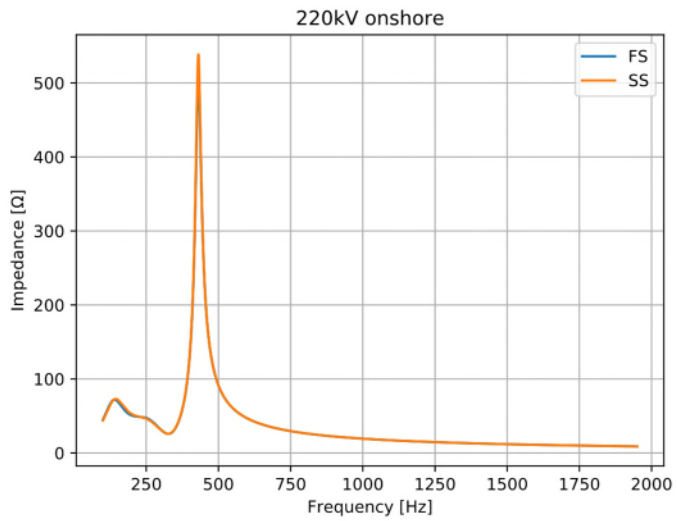
(e)
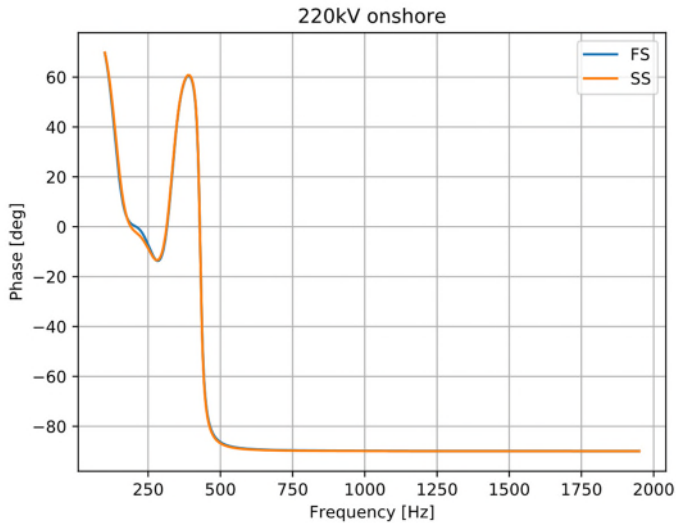
(f)

Figure 3-16 Comparing the impedance frequency scans calculated by PowerFactory (FS) and the tool (SS) for (a),(b) Wind turbine terminal (c),(d) 34 kV offshore bus bar (e),(f) 220 kV onshore bus bar for the system shown in Figure 3-15.

3.6. SUMMARY

In this chapter, a tool is presented, which is able to perform the eigenvalue based stability analysis in a large system. First it is shown how to consider an electrical network as a control system and how CCM can be used to model this large and interconnected system. The state space modelling of the system is divided into different parts:

1) Passive element modelling such as cables and transformers.
2) Network modelling
3) Converter modelling
4) Synchronous machine modelling

In this chapter the frequency dependency in cables and transformers are neglected for the sake of a clearer presentation. These challenges will be discussed in the next chapter.

Finally the results of this tool are validated by different methods. The low frequency eigenvalues can be verified by the modal analysis toolbox in PowerFactory. For the high frequency eigenvalues, the impedance frequency scans are suggested.

CHAPTER 4. NUMERICAL DATA AND BLACK-BOX MODELS

"Number rules the universe."

Pythagoras

4.1. INTRODUCTION

Nowadays, manufacturers of different elements of a power system use more advanced techniques to optimize the design and achieve better performance. For instance, a WT supplier uses different control loops to improve the dynamics and performance of a WT. Therefore, the suppliers try not to disclose the software, parameters and codes of their products and try to deliver black-box models, which contain the minimum amount of information. For instance, for a power converter, as discussed in the previous chapters, the terminal characteristics is of importance and if it is delivered as a numerical lookup table such as shown in Figure 4-1, then the internal characteristics such as controller structure and parameters are difficult to obtain.
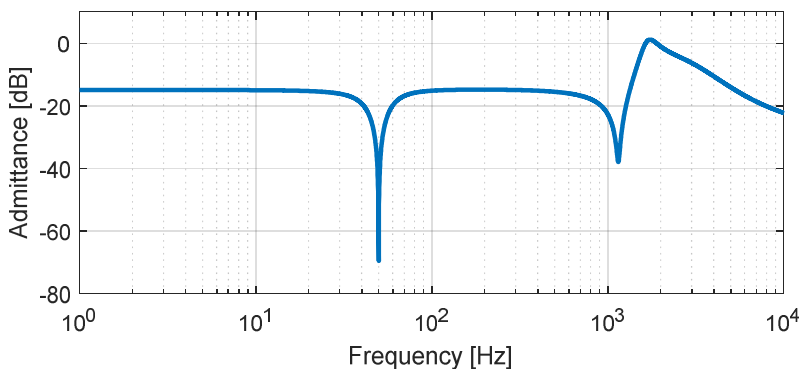
Figure 4-1 Converter output admittance delivered as a numerical table.

For some elements, obtaining the exact analytical equations for admittance/impedance is difficult. However, these characteristics can easily be obtained by measurements in either simulations or experiments. Figure 4-2 shows the advanced modelling of a sub marine cable which is done numerically for the double fundamental frequency. The asymmetrical current distribution is due to the skin and proximity effect of the cable, which is more severe in the low frequency range.
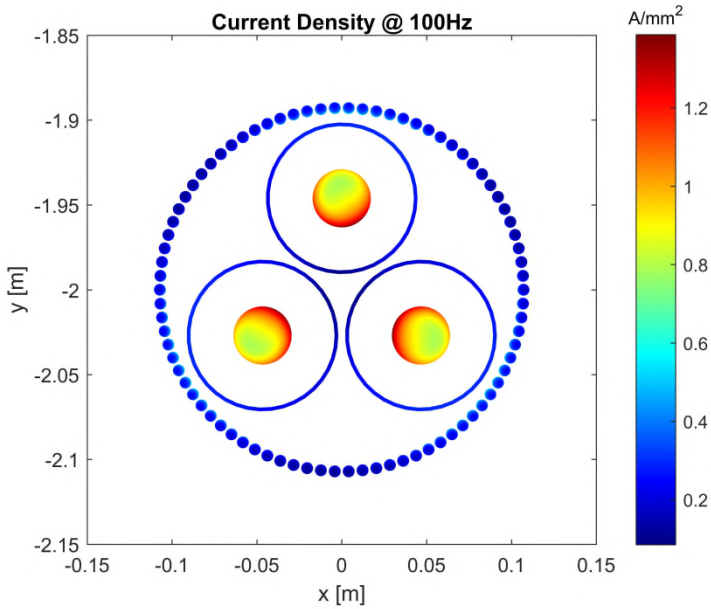
Figure 4-2 Current distribution in conductors of a sub marine cable due to the proximity and skin effect [16].

Furthermore, even though the analytical expressions are available for some systems, the numerical representation is advantageous due to the high complexity of the analytical equation. This is the case for representing the grid in harmonic studies. Modelling a grid as an inductive branch is a valid assumption at the fundamental frequency, however, in harmonic studies it must be modelled in detail due to the possible resonances at other frequencies inside the grid, which might affect harmonic emissions and stability of the system (see Figure 4-3).
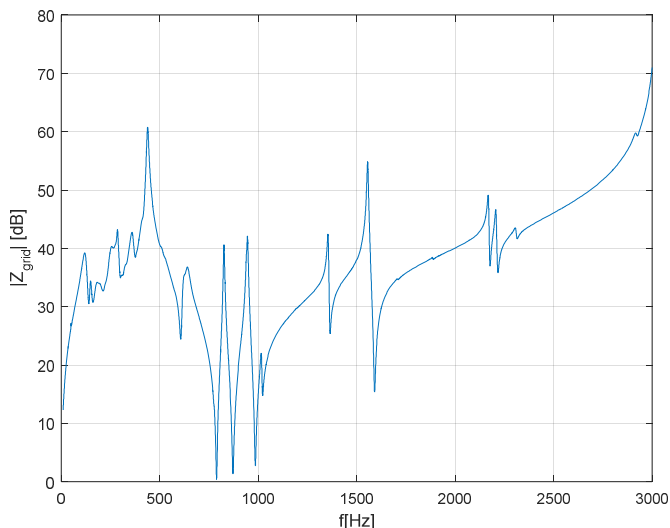
Figure 4-3 Grid impedance, where multiple resonances can be seen [16]

In this chapter, the use of numerical data for stability analysis of power-electronics-based power systems is discussed. First, the state of the art methods in analyzing the linear systems is discussed and then the numerical analysis of nonlinear systems and the associated challenges are discussed. Finally, an identification method is used to find state space models that are needed in the eigenvalue base stability analysis.

4.2. NUMERICAL DATA IN THE IMPEDANCE BASED STABILITY ANALYSIS METHOD

In this part, some methods for analyzing the stability using the numerical data based on the impedance-based stability analysis are presented. First a linear case is presented and then the method is expanded to nonlinear system, and some challenges such as the frequency couplings and the dependency on the operating point are addressed.

4.2.1. NUMERICAL ANALYSIS OF STABILITY IN A LINEAR SYSTEM

If it is assumed that all components behave almost linearly in the frequency range of interest, then as discussed in the previous chapter one can use the SISO representation for the admittance/impedance models. In other words, all elements can be defined by a numerical frequency response data, which describes the admittance/impedance at a specific frequency.

In the impedance based stability analysis, the driving point impedances are of interest. The circuit equations can be solved independently at each frequency due to the LTI assumptions. Therefore, the circuit elements can be replaced by complex numbers, which define the behavior at a given frequency. In the end, the Nyquist plot of the minor loop ratio, which is the ratio of the impedances, can be evaluated numerically.

4.2.1.1 Modelling different elements

Converter and black box models

If the frequency dependent admittance/impedance of a converter (or synchronous generators and loads) is known, then it can simply be modelled as a frequency dependent admittance/impedance in the power system software. Figure 4-4 shows the Norton equivalent of a power converter, where the electrical parameters must be updated at each frequency. Generators and loads can also be modelled in a similar way.
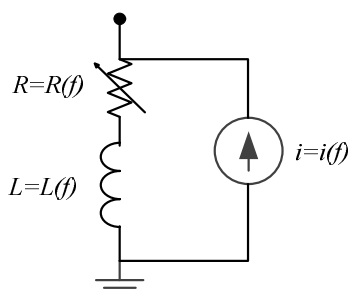
Figure 4-4 How to represent a converter in harmonic studies.

Line/Cable model

For harmonic studies it is very important to model the multiple resonances of a line/cable correctly. Therefore, a cable cannot be modelled accurately by the nominal π-model. Using multiple π-sections may increase the accuracy but at the other hand it increases the complexity. The accuracy near the resonance points is also not acceptable. The equivalent π-model, which is derived from the solution of the second order differential equations of the transmission lines (telegrapher's equation), can improve the accuracy significantly [7], [52]. The equivalent π-model parameters of the circuit shown in Figure 4-5 are

$$Z_S = Z_0 \sinh(\gamma l) \qquad (4\text{-}1)$$

$$Y_p = \frac{1}{Z_0} \tanh\left(\frac{\gamma l}{2}\right) \qquad (4\text{-}2)$$

where $Z_0 = \sqrt{Z'/Y'}$ is the characteristic impedance of the line, $\gamma = \sqrt{Z'Y'}$ is the propagation constant, l is the cable length, Z' is the per unit length series impedance of the cable and Y' is the per unit length shunt admittance of the cable.
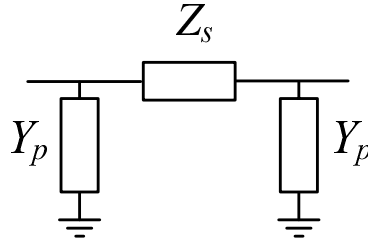
Figure 4-5 Equivalent π-model of a line/cable.

The skin and proximity effects can easily be incorporated into the equivalent π-model by

$$Z'(f) = R'(f) + j\omega L'(f) \tag{4-3}$$

It should be noted that in this thesis it has been assumed that these frequency dependencies are available from the suppliers either as analytic equations or numerical data.

For instance, for a 220 kV cable with the parameters listed in Table 4-1, the series and shunt elements of the equivalent π-model are shown in Figure 4-6 and Figure 4-7. The frequency dependency is only considered for the resistance as

$$R'(f) = 0.74 \left(0.267 + 1.073 \sqrt{\frac{f}{f_1}} \right) R'_1 \tag{4-4}$$

where f_1=50 Hz is the nominal frequency.

Table 4-1 Parameters of the considered cable.

Symbol	Description	Value
R'	Series resistance per unit length	0.03 Ω/km
L'	Series inductance per unit length	0.38 mH/km
C'	Shunt capacitance per unit length	0.19 μF/km
l	Length	100 km
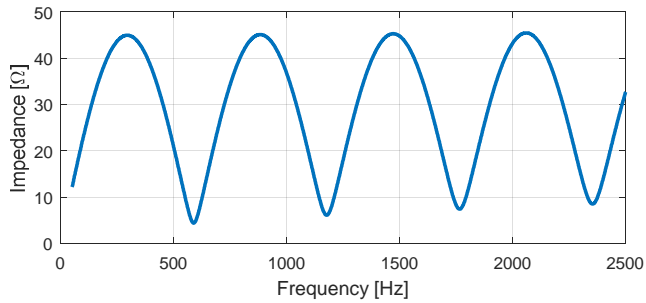
Figure 4-6 Series equivalent impedance Z_s as a function of frequency.
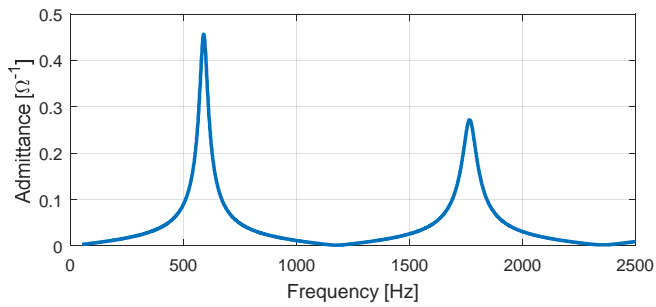
Figure 4-7 Shunt equivalent admittance Y_p as a function of frequency.

Transformer modelling

The transformer model in the frequency domain has previously shown in Figure 3-10. However, due to the skin effect and the proximity effect the leakage impedance significantly changes with the frequency. In the literature, this dependency is mainly considered for the leakage resistance while the leakage inductance is assumed to be constant [53]. The magnetizing resistance, which models the core losses such as hysteresis losses and eddy current losses, is also considered as constant. The effects of saturation and nonlinearities in the magnetizing inductance have also been neglected in this work, and the magnetizing inductance L_m is considered as constant. The frequency dependency of the leakage resistance is updated at each frequency in the analysis.
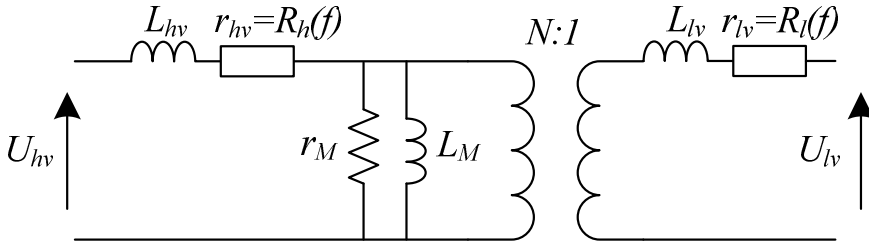
Figure 4-8 Two-winding transformer model in the frequency domain

Analysis methodology

Since it is assumed that the system is LTI, the electrical equations for each frequency can be solved independently. Each element is modelled by some complex numbers that describes the impedance/admittance at a given frequency. For stability studies as discussed in 0Chapter 2 the impedances are needed; however, for power quality studies the harmonic injections are also needed. In both cases the electrical quantities can be found by solving the nodal equation

$$[i(f)] = [Y(f)][v(f)] \tag{4-5}$$

The driving point impedance, which is important in the stability studies, can be found by injecting a current to the node under study and calculating the voltage from (4-5) or it can be calculated from the corresponding diagonal element of the Z-matrix (inverse of the Y-matrix). This impedance is needed for the impedance based stability analysis.

4.2.2. NUMERICAL ANALYSIS OF STABILITY IN NON-LTI SYSTEMS

As shown in Chapter 2, the outer control loops such as the dc link controller and the synchronization loop affect the admittance/impedance of a power converter in the low frequency range. For instance, if the frequency couplings in the modelling is neglected then it could result in a wrong evaluation of the stability of the system [34]. If the system is unbalanced (i.e. unequal tree-phase impedances that can happen in underground cables with a flat formation), then the situation is more complicated [54]. In [55] the closed loop impedance has been found by limiting the number of considered cross couplings; however, if there are unlimited number of couplings, obtaining the analytical expressions is almost impossible.

A numerical method is proposed, which is able to use black box models from suppliers considering the frequency couplings even in unbalanced systems [54], [56]. It is not necessary to know the structure and parameters of the converter and the terminal characteristics can be obtained from simulations or experiments.

In order to see why there are so many cross couplings in an unbalanced system, first this phenomenon is studied for balanced systems and then it is expanded to unbalanced systems.

4.2.2.1 Frequency couplings in a power converter

It has been shown in [55] that the negative sequence impedance is actually the complex conjugate of the positive sequence impedance at the negated frequency.

$$Z_{neg}(j\omega) = \left(Z_{pos}(-j\omega)\right)^*$$
(4-6)

Therefore, hereafter positive/negative frequencies stand for positive/negative sequence.

To see how a perturbation propagates in an electrical system, it is necessary to consider all elements such as the grid impedance together with the converter. Figure 4-9 shows the considered system, where an inductive filter is used. It should be noted any other types of filters can also be studied by simply changing the grid impedance.

It was shown in 0 that if the PLL is considered in the modelling, then, in response to a positive/negative sequence perturbation, the output current of the converter will have a positive/negative sequence component at the same frequency and a negative/positive sequence component at another frequency. It has been shown in [34] that neglecting these couplings may result in a wrong evaluation of stability. It also makes the analysis more complicated because the system cannot be analyzed at each frequency separately. Figure 4-10 shows how these frequency components interact with each other in a symmetrical system. A voltage perturbation in the grid with a frequency of f_p (highlighted in Figure 4-9) also appears at the PCC ($①→②$), and in response to this frequency component the converter generates two frequency components in the output current, one at the same frequency f_p ($②→③$), and another one at $-(f_p\text{-}2f_1)$ ($②→④$), where f_1 is the fundamental frequency. The grid impedance is symmetrical and passive, and therefore, it does not change the sequence or frequency and the PCC voltage will only have the mentioned frequencies ($③→⑤→②$ and $④→⑥→⑦$). Consequently, the converter response to the observed frequencies at the PCC voltage is at the same frequency f_p and $-(f_p\text{-}2f_1)$ ($②→③$ and $⑦→④$) and the coupling frequencies ($③→⑤→②$ and $④→⑥→⑦$). It can be seen that this is a closed loop and no more frequency components are generated.
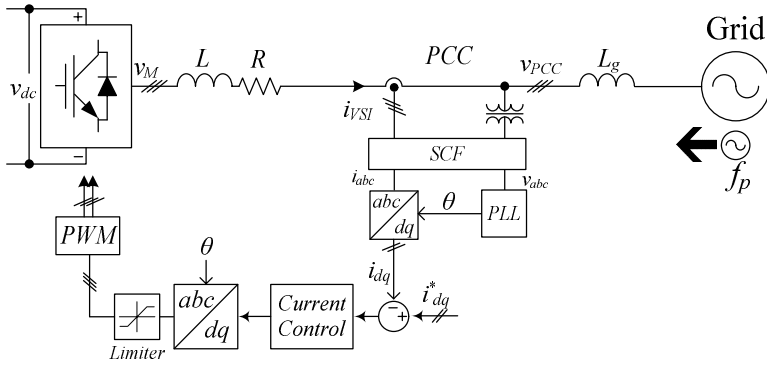
Figure 4-9 Considered power system, where a three- phase voltage source converter is connected to the grid [54].
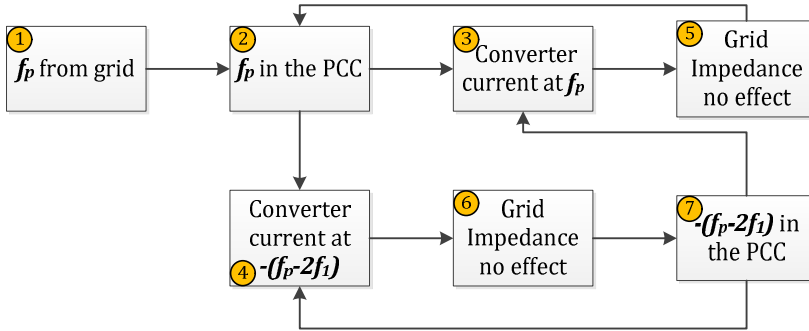
Figure 4-10 Perturbation propagation in a symmetrical power system [54].

If the grid impedance is asymmetrical (unequal impedances in phases), it couples the positive and negative sequences. In other words, in response to a positive sequence voltage it also generates some negative sequence voltage but at the same frequency. An asymmetrical inductive branch as shown in Figure 4-11, can be described in the sequence domain by

$$Z_{\pm} = \begin{bmatrix} Z_{pp} & Z_{pn} \\ Z_{np} & Z_{nn} \end{bmatrix} \tag{4-7}$$

where

$$Z_{pp} = Z_{nn} = \frac{1}{3}(Z_1 + Z_2 + Z_3) \tag{4-8}$$

$$Z_{pn} = (Z_{np})^* = \frac{1}{6}\left(2Z_1 - Z_2 - Z_3 - j\sqrt{3}(Z_2 - Z_3)\right) \tag{4-9}$$

and Z_i is the impedance of ith phase and Z_{seq} is the sequence domain impedance representation.
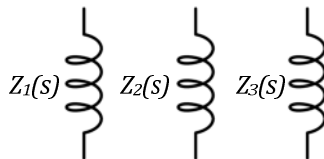
Figure 4-11 An asymmetrical three-phase inductive branch [54].

Figure 4-12 illustrates that an asymmetry leads to an unlimited number of frequency couplings and compared to a symmetric case it is more complicated to find a close form analytical equation for the impedance. It shows how a perturbation propagates and changes in a system, similar to Figure 4-11. The grid impedance is asymmetrical and it also creates a component at $(f_p\text{-}2f_1)$ in response to a current at $-(f_p\text{-}2f_1)$. The new frequency is observed by the power converter and it generates an additional component at $-(f_p\text{-}4f_1)$. More frequency components appear similarly and a closed form analytical equation cannot be found unless one makes some assumptions and neglect some components. However, it might lead to inaccurate results. Numerical techniques are useful here due to the simplicity that they offer [54].
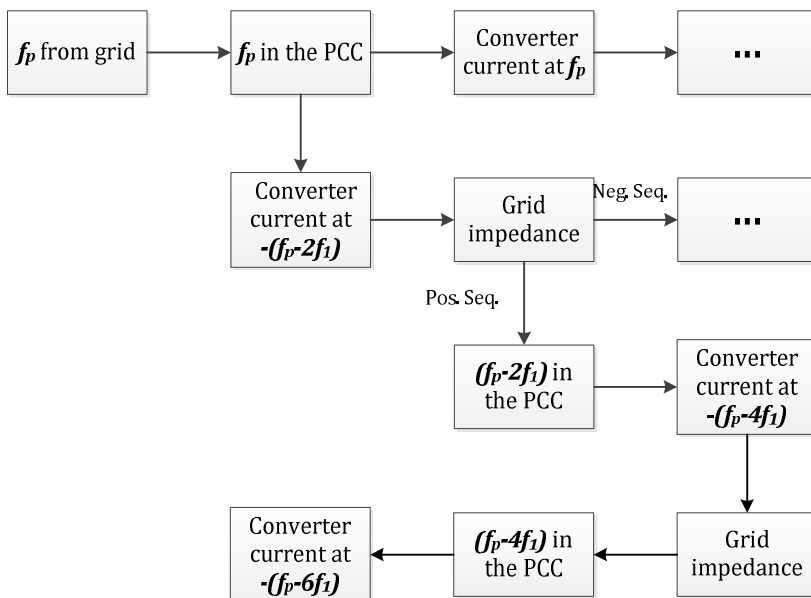
Figure 4-12 How a perturbation propagates in an asymmetrical system [54].

4.2.2.2 Matrix-Based Method

To deal with the abovementioned frequency couplings, the matrix frequency response method can be used [54], [56]. The response to a frequency perturbation includes some components: therefore, in order to model the system correctly, all the components of the response should be used instead of using only the dominant frequency component, which has the same frequency as the perturbation. Equation (4-10) shows the matrix frequency response in which each column is the frequency spectrum of the response to a single-tone (sinusoidal) perturbation. The matrix elements can be obtained by analytical equations, simulations or experiments [54], [56].

$$
\mathcal{H} = Response \begin{array}{c} \omega_1 \\ \omega_2 \\ \vdots \\ \omega_n \end{array} \underbrace{\left\{ \begin{bmatrix} H_{11}(j\omega_1) & H_{12}(j\omega_2) & \cdots & H_{1n}(j\omega_n) \\ H_{21}(j\omega_1) & H_{22}(j\omega_2) & \cdots & H_{2n}(j\omega_n) \\ \vdots & \vdots & \ddots & \vdots \\ H_{n1}(j\omega_1) & H_{n2}(j\omega_2) & \cdots & H_{nn}(j\omega_n) \end{bmatrix} \right.}_{\substack{\omega_1 \quad\quad \omega_2 \quad\quad \cdots \quad\quad \omega_n \\ Excitation}} \tag{4-10}
$$

"where H_{ij} is the frequency component of the output at $\omega=\omega_i$ to a sinusoidal input at $\omega=\omega_j$. It should be noted ω_1 in (4-10) is not the fundamental frequency. For a Linear Time-Invariant (LTI) system, only the diagonal elements are non-zero, because the input and output have the same frequency" [54].

The matrix frequency response is actually a different representation of the numerical Harmonic Transfer Function (HTF) concept in linear time periodic systems [57], [58]. In LTP systems the dynamics of the system are periodic similar to AC systems, where steady state quantities are at the system frequency. If the system is a black box (the main assumption of this chapter), then the Harmonic State Space equations cannot be utilized for analyzing these systems [59]. Similar to the LTI systems, (4-11) gives the relationship between the input and output signals.

$$
\mathcal{Y}(s) = \mathcal{H}(s)\mathcal{U}(s) \tag{4-11}
$$

where

$$
\mathcal{U}(s) = \begin{bmatrix} \vdots \\ U(s - j\omega_1) \\ U(s) \\ U(s + j\omega_1) \\ \vdots \end{bmatrix} \tag{4-12}
$$

and

$$\mathcal{Y}(s) = \begin{bmatrix} \vdots \\ Y(s - j\omega_1) \\ Y(s) \\ Y(s + j\omega_1) \\ \vdots \end{bmatrix} \tag{4-13}$$

are frequency components of the input and output respectively and

$$\mathcal{H}(s) = \begin{bmatrix} \ddots & \ddots & \ddots & \ddots & \ddots \\ \ddots & H_0(s - j\omega_1) & H_{-1}(s) & H_{-2}(s + j\omega_1) & \ddots \\ \ddots & H_1(s - j\omega_1) & H_0(s) & H_{-1}(s + j\omega_1) & \ddots \\ \ddots & H_2(s - j\omega_1) & H_1(s) & H_0(s + j\omega_1) & \ddots \\ \ddots & \ddots & \ddots & \ddots & \ddots \end{bmatrix} \tag{4-14}$$

is the HTF of the system. In the above equations ω_1 is the angular frequency of the system. "$H_m(s\text{-}jn\omega_1)$ shows the coupling between the input $U(s\text{-}jn\omega_1)$ and the output $Y(s\text{-}j[n\text{-}m]\omega_1)$" [54] .

For LTI systems the Nyquist diagram of the open loop transfer function can be used to analyze the stability. Similarly for an LTP system with an open loop harmonic transfer function of $\mathcal{G}(s)$, the generalized Nyquist criterion (GNC) can be used to evaluate the stability of the closed loop system. GNC is simply the plot of the collection of the eigenvalues of the open loop HTF $\mathcal{G}(s)$ by sweeping the frequency $s=j\omega$ in the interval $(-j\omega_1/2, +j\omega_1/2)$ [60]. This can also be done by considering the block diagonal matrix $\mathbb{G}$ in (4-15) due to the fact it has the same eigenvalues.

$$\mathbb{G} = \begin{bmatrix} \left[\mathcal{G}\left(-j\frac{\omega_1}{2}\right)\right] & 0 & \cdots & 0 \\ 0 & \left[\mathcal{G}\left(-j\frac{\omega_1}{2} + j\delta\omega\right)\right] & \ddots & \vdots \\ \vdots & \ddots & \ddots & 0 \\ 0 & \cdots & 0 & \left[\mathcal{G}\left(+j\frac{\omega_1}{2}\right)\right] \end{bmatrix} \tag{4-15}$$

where $\delta\omega$ is the desired frequency resolution of the GNC plot.

It should be noted $\mathcal{G}(s)$ cannot have unlimited number of elements as in (4-14) and must be truncated up to a certain harmonic M. Therefore,

$$[\mathcal{G}(s)] = \begin{bmatrix} G_0\left(s - j\frac{M}{2}\omega_1\right) & & & \\ & \ddots & G_{-1}(s) & \ddots & \\ & \ddots & G_0(s) & \ddots & \\ & \ddots & G_1(s) & \ddots & \\ & & & G_0\left(s + j\frac{M}{2}\omega_1\right) \end{bmatrix} \tag{4-16}$$

If the rows and columns of $\mathbb{G}$ are sorted based on the frequencies, then, (4-10) is obtained. It should be noted that the sorting does not change the eigenvalues.

Therefore (4-10) can be used for stability analysis using the GNC in a simpler manner compared to (4-15).

The matrix frequency response of the impedance model of a symmetrical and an asymmetrical inductive branch, which hereafter is called the impedance matrix, is shown in Figure 4-13. The perturbation (excitation) frequency is on the x-axis, the y-axis is the response frequency. This matrix is a complex matrix and the color intensity shows only the magnitude. The negative frequencies in the matrix mean the negative sequence. It can clearly be seen that there are some couplings between different frequencies and sequences.

Only diagonal elements of Figure 4-13 (a) are non-zero, which means that in response to a perturbation, there is only one frequency component in the response. For instance, in response to a +250 Hz (positive sequence) perturbation (red dashed line), the response has only one frequency at +250 Hz (blue dashed line). However, for the asymmetrical case shown in Figure 4-13 (b), the response has also an additional negative sequence component (green dashed line).
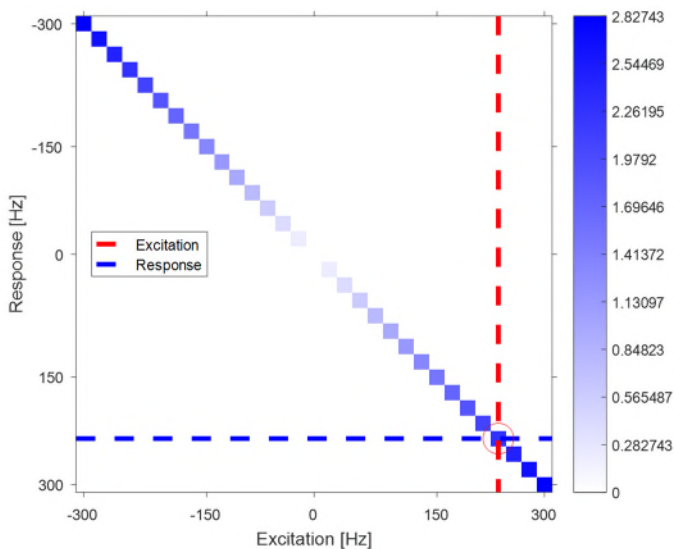
(a)
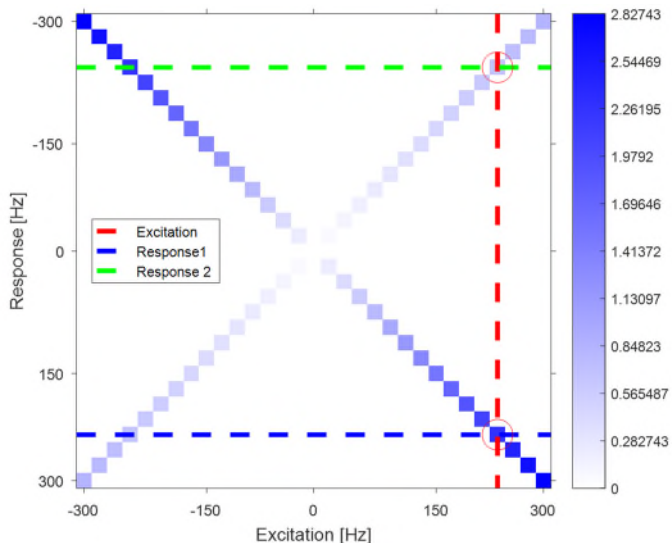
(b)

Figure 4-13 Impedance matrix of an inductive branch shown in Figure 4-11. (a) a balanced case (b) an unbalanced case [54].

To remove the adverse effects of the asymmetry on the conventional *dq* current controller, an unbalanced current controller is used [61]–[63]. A Sequence Extraction Block (SEB) as shown in Figure 4-14 separates the positive and negative sequence information. Then, the PLL can be synchronized with the positive sequence voltage (see Figure 4-14), and the positive- and negative-sequence currents can be controlled independently (see Figure 4-15). "T_{dq} is the dq transformation and

$$F = \frac{\omega_f}{s + \omega_f} \tag{4-17}$$

$$T_{dq^2}(\theta) = \begin{bmatrix} \cos 2\theta & \sin 2\theta \\ -\sin 2\theta & \cos 2\theta \end{bmatrix} \tag{4-18}$$

where θ is the phase angle of the positive sequence voltage (output of the PLL as shown in Figure 4-14) and $\omega_f=\omega_1/\sqrt{2}$ to have a good performance" [54].
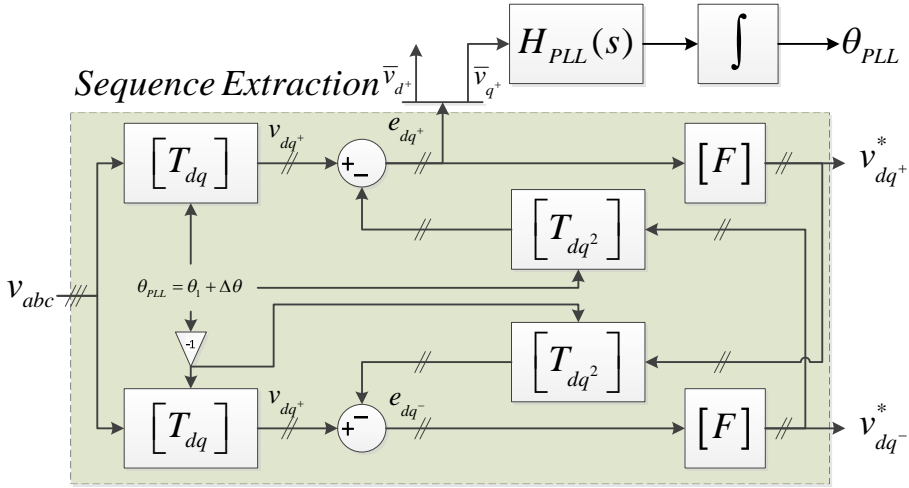
Figure 4-14 A Decoupled Double Synchronous Reference Frame PLL, where the Sequence Extraction Block is highlighted [54].

The current controller shown in Figure 4-15 simply uses PI regulators for both positive-/negative- sequence *dq* signals, where
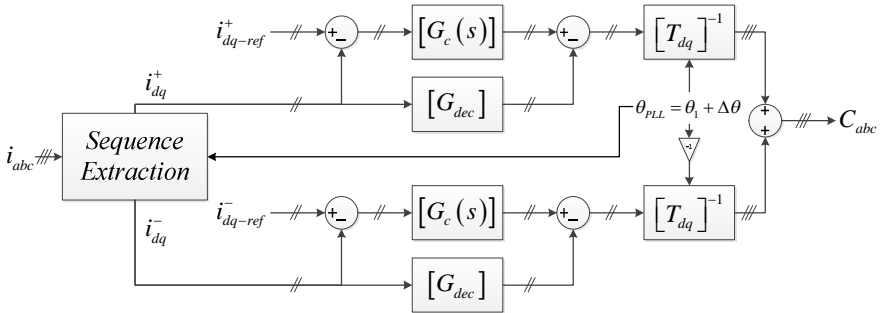
Figure 4-15 A Decoupled Double Synchronous Reference Frame current controller [54].

$$[G_c(s)] = \begin{bmatrix} H_i(s) & 0 \\ 0 & H_i(s) \end{bmatrix} \tag{4-19}$$

$$[G_{dec}] = \begin{bmatrix} 0 & K_d \\ -K_d & 0 \end{bmatrix} \tag{4-20}$$

and $H_i(s)=k_p+k_i/s$ is a PI regulator for current control. K_d is also for decoupling the *dq* signals.

A DDSRF current controller with the parameters listed in Table 4-2 (stable case) is considered in this part. The power converter is treated as a black box and its admittance matrix is obtained by only using simulations (no analytical equations are used). As mentioned before, for each frequency a small signal voltage with a defined frequency is applied at the converter terminals (assuming no grid impedance in Figure 4-9). A change in the terminal voltage affects the terminal current, which is defined as the terminal admittance. Therefore, one column of the admittance matrix (4-10) can be filled in by calculating the FFT of the output current when the terminal voltage is excited with the frequency related to that column. Figure 4-16 shows the admittance matrix, which is obtained from the simulations.

Table 4-2 Parameters of the Grid-Connected Inverter for Simulation [54].

Symbol	Description	Value
f_1	Grid frequency	50 Hz
L	Filter inductance	1.5 mH
R	Filter equivalent resistance	0.5 Ω
V_{dc}	Inverter dc voltage	600 V
K_p	Proportional gain of the current controller	0.01
K_i	Integrator gain of current controller	0.1
BW_{PLL}	Bandwidth of PLL	65 Hz
K_d	Decoupling term	0
V_g^+	Grid line-ground peak voltage (Pos. Seq.)	100 V
I_{dr}^+	Pos. seq. d channel current reference (stabe/unstable cases)	20/2 A
I_{qr}^+	Pos. seq. q channel current reference	0 A
I_{dr}	Neg. seq. d channel current reference	0 A
I_{qr}	Neg. seq. q channel current reference	0 A
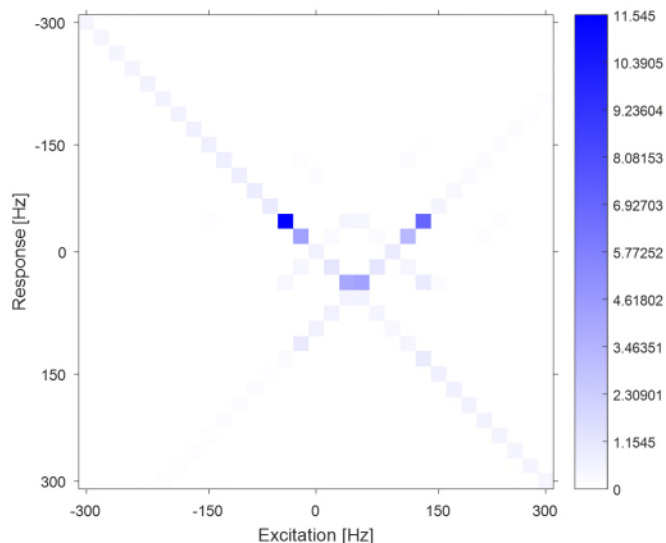
Figure 4-16 Admittance matrix of a DDSRF current controller [54].

The obtained admittance matrix is dependent on the operating point due to the nonlinearity and small signal linearization. Therefore, if the operating point (i.e. the output power) is changed, then the admittance matrix would be different. This is the case in a wind power plant, where the output power is dependent on the available wind. The whole identification process cannot be repeated for different cases because it is a time consuming process. In [54], it has been shown that the differential of the admittance can be calculated by having the partial derivatives as follows:

$$
\begin{aligned}
Y\big(V_{dq}^+ + \Delta V_{dq}^+,\ I_{dq}^+ + \Delta I_{dq}^+, V_{dq}^- &+ \Delta V_{dq}^-,\ I_{dq}^- + \Delta I_{dq}^-\big) \\
&\approx Y\big(V_{dq}^+,\ I_{dq}^+, V_{dq}^-,\ I_{dq}^-\big) + \frac{\partial Y}{\partial V_{dq}^+}\Delta V_{dq}^+ + \frac{\partial Y}{\partial I_{dq}^+}\Delta I_{dq}^+ + \frac{\partial Y}{\partial V_{dq}^-}\Delta V_{dq}^- \\
&+ \frac{\partial Y}{\partial I_{dq}^-}\Delta I_{dq}^-
\end{aligned}
\tag{4-21}
$$

The partial derivatives in (4-21) can be found by the procedure shown in Figure 4-17. For instance, by repeating the simulation for another positive sequence voltage reference, while all other quantities are kept constant (ΔV^-_{dq}=0, ΔI^+_{dq}=0, ΔI^-_{dq}=0), the partial derivative $\frac{\partial Y}{\partial V_{dq}^+}$ can be calculated.
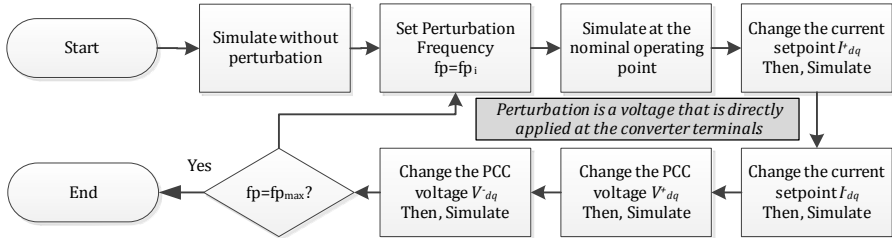
Figure 4-17 How to calculate the parameters that are needed for the matrix-based method [54].

Figure 4-18 shows the results of the abovementioned procedure for a perturbation at 110 Hz. It can be seen that all differentials are linear except for the positive sequence voltage. This is due to the nonlinearity of the PLL that is synchronized with the positive sequence voltage. However, it can be seen that if the voltage is kept inside the interval (0.95, 1.05), the differential is almost linear. In power systems the voltages of different nodes are kept near the nominal value by reactive power control otherwise possible over voltages may damage the insulators.
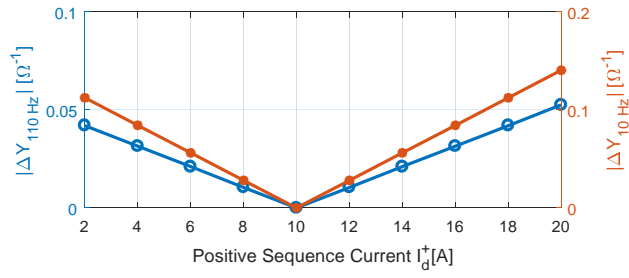
(a)
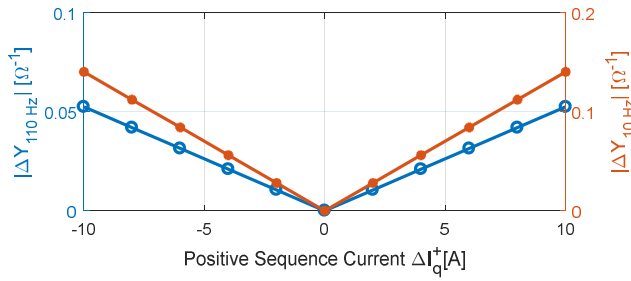
(b)
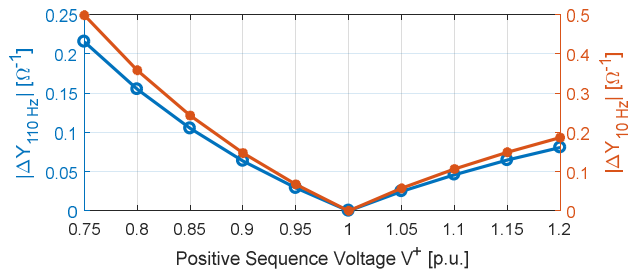
(c)
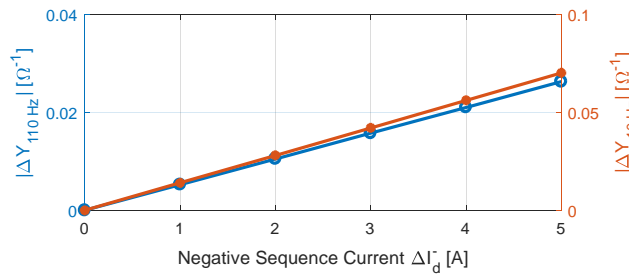
(d)
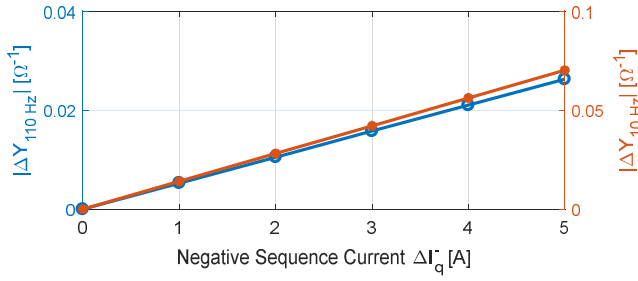
(e)
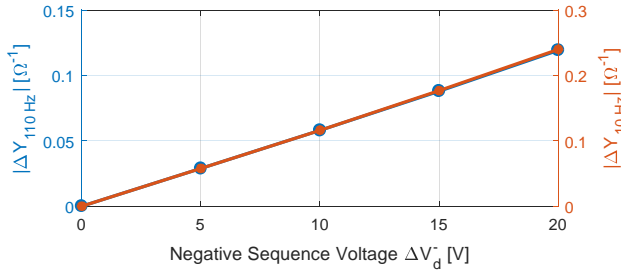
(f)
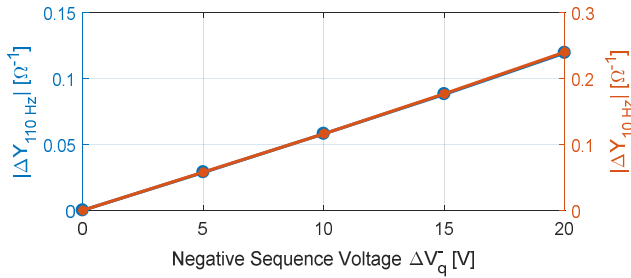
(g)

Figure 4-18 Admittance change versus: (a) positive sequence current reference d channel I_d^+ . (b) positive sequence current reference q channel I_q^+ . (c) positive sequence voltage at the PCC. (d) negative sequence current reference d channel I_d^-. (e) negative sequence current reference q channel I_q^-. (f) negative sequence voltage at the PCC d channel V_d^-. (g) negative sequence voltage at the PCC q channel V_q^- [54] for the system shown in Figure 4-9.

Time domain simulations of an unknown operating point (v_{dq}^+=95, I_{dq}^+=20+j5, V_{dq}^-=10+j5, I_{dq}^-=2+j2, f_p=110 Hz) can be used to verify (4-21). The results listed in Table 4-3 show a good agreement between the predicted quantities using (4-21) and the simulations.

Table 4-3 Comparing the predicted results using (4-29) with the simulations [54].

Frequency	110 Hz		10 Hz	
	Theory	Sim.	Theory	Sim.
$|I_a|$	0.0240	0.0244	0.1600	0.1614
$\angle I_a$	0.053	0.032	0.142	0.180
$|I_b|$	0.0282	0.0286	0.1534	0.1557
$\angle I_b$	-2.373	-2.407	2.336	2.369
$|I_c|$	0.0187	0.0187	0.1431	0.1455
$\angle I_c$	1.771	1.738	-1.9433	-1.902

4.2.2.3 Simulation Results

To calculate the admittance matrix of the converter using (4-21), the operating point quantities are necessary. The operating point can be found by running a load flow analysis assuming the power converter as a PQ source/load.

Two cases are reported in this section to show the capability of this method in stability analysis and power quality studies.

Case 1: Stability analysis of an unbalanced system

In this part the grid impedance is unbalanced as shown in Table 4-4. As shown in Table 4-2 the power converter only injects positive sequence current that is synchronized with the positive sequence voltage. The grid impedance and the power converter admittance are modelled as matrix impedances and admittances. To analyze the stability, the Generalized Nyquist Criterion should be used, which is the plot of the eigenvalues of the matrix minor loop (product of the grid impedance matrix and the converter admittance matrix).

Table 4-4 Parameters of the grid used for the study [54].

Symbol	Description	Value
V_g^+	Grid line-ground peak voltage (Pos. Seq.)	100 V
L_1	Grid inductance-phase A (unbalanced/balanced)	2.3 / 2.3 mH
L_2	Grid inductance-phase B (unbalanced/balanced)	1.1 / 2.3 mH
L_3	Grid inductance-phase C (unbalanced/balanced)	3.4 / 2.3 mH

Figure 4-19 indicates that the system is stable when the output current is 20 A, and it is unstable when the output current is 2 A. Time domain simulations as shown in Figure 4-20 and Figure 4-21 also verify this conclusion. The output current is heavily distorted for the unstable case; however, the converter is not saturated as shown in Figure 4-21 (c). This behavior can be explained by the theory of limit cycles in large signal analysis of nonlinear systems [64], [65], which states that even though a system is unstable the signals may be bounded (see Appendix C). The FFT of the output current and the PCC voltage shown in Figure 4-22 reveals that the

frequency of the instability is around 14 Hz, which perfectly matches with the cross over frequency of the GNC plot shown in Figure 4-19.
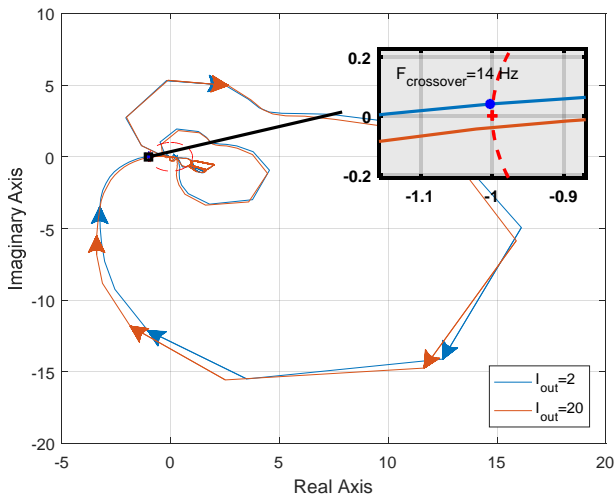
Figure 4-19 Generalized Nyquist Plot of the unbalanced system when the output current set-point is changed from 2 A to 20 A [54].
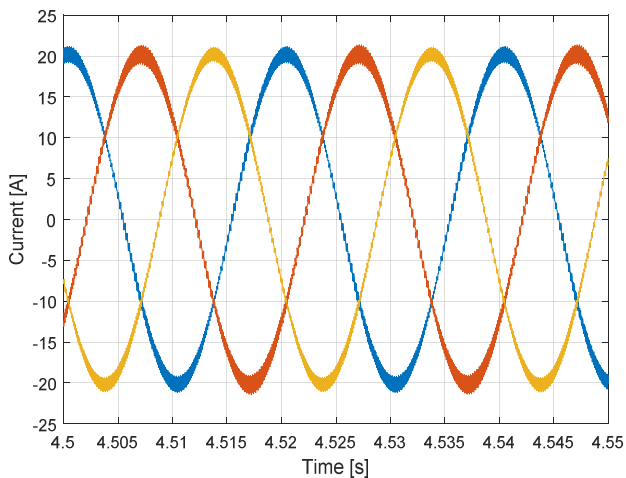
(a)
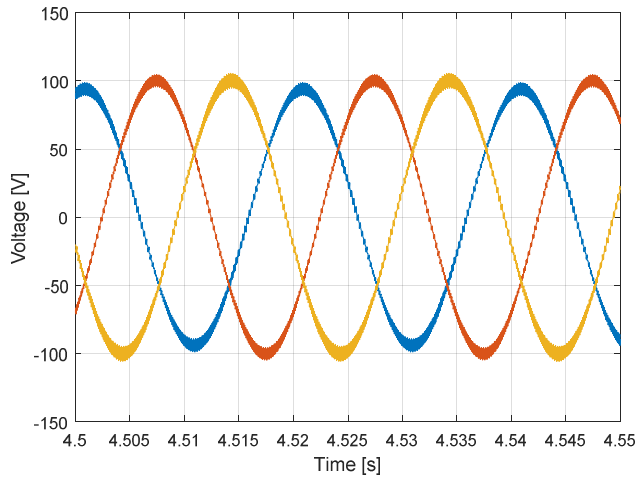
(b)
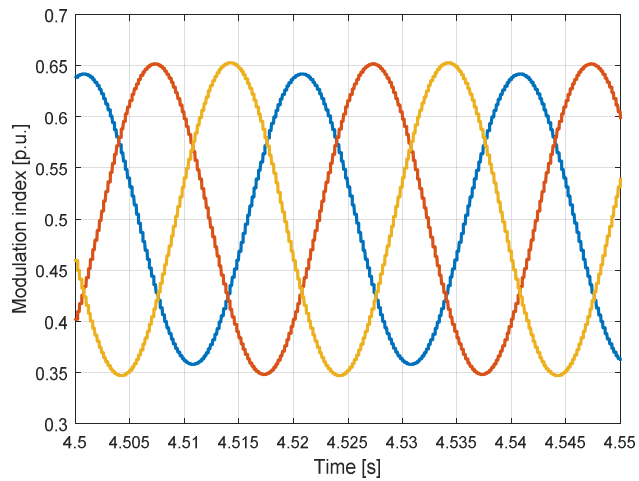
(c) Modulation index

Figure 4-20 Time domain simulations of the unbalanced system, when the output current set point is 20 A (a) the output current (b) the PCC voltage (c) the modulation indices [54].
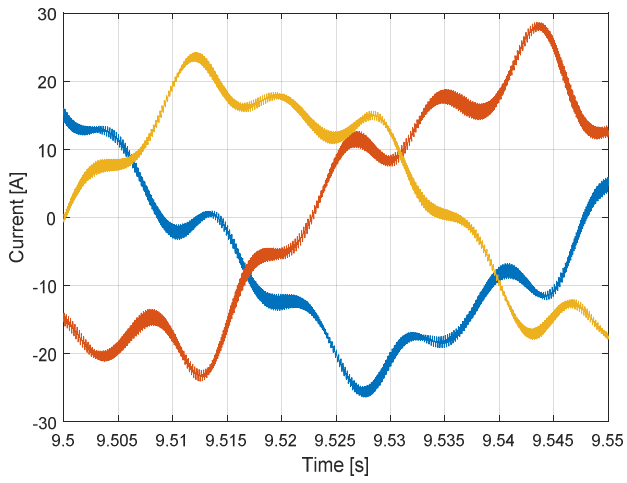
(a)
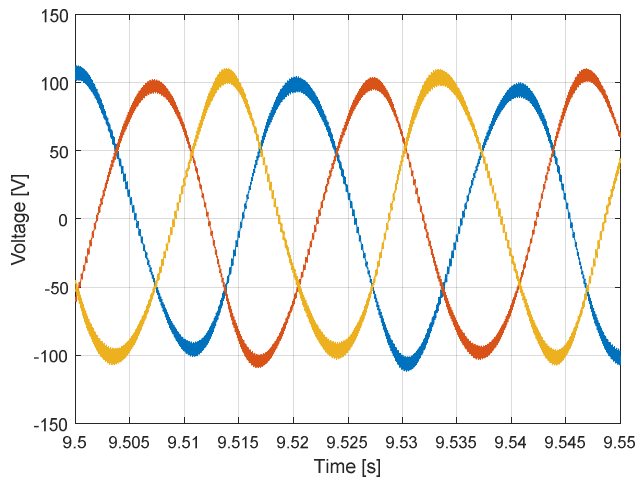
(b)
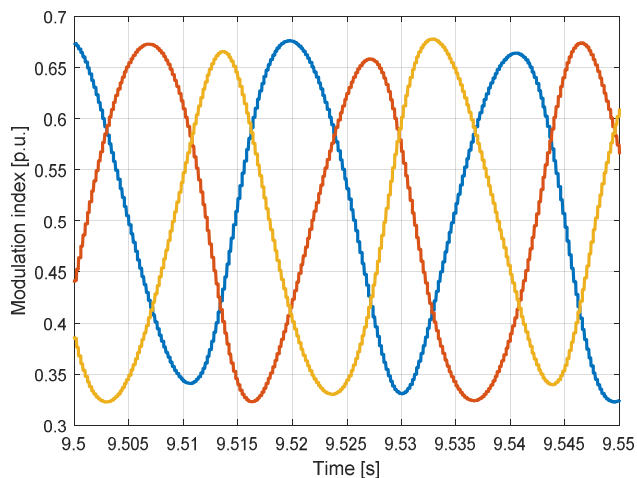
(c)

Figure 4-21 Time domain simulations of the unbalanced system, when the output current set point is 2 A (a) the output current (b) the PCC voltage (c) the modulation indices [54].
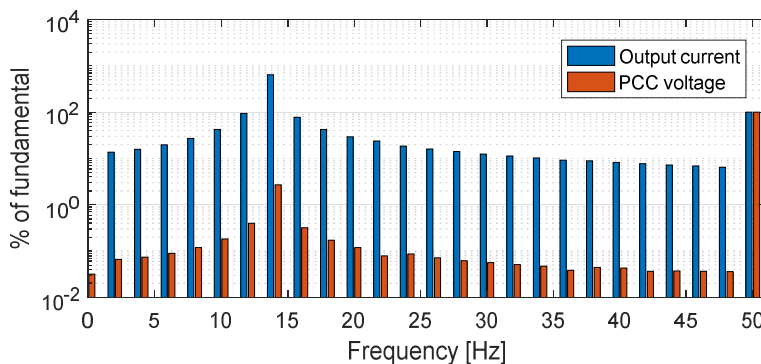
Figure 4-22 Frequency spectrum of the output current and the PCC voltage, when the output current set point is 2 A (the unstable case) [54].

It is worth repeating the analysis for the balanced impedances to see what the effect of imbalance is. The inductances are changed in a way that the cross couplings in the sequence domain are removed without altering the positive or negative sequence impedances.

The GNC plot and the time domain results shown in Figures 4-23 – 4-25 are well correlated. The results are similar to the unbalanced case, and it can even be said that the results of the balanced case are worse (the Nyquist plot is closer to the critical point).
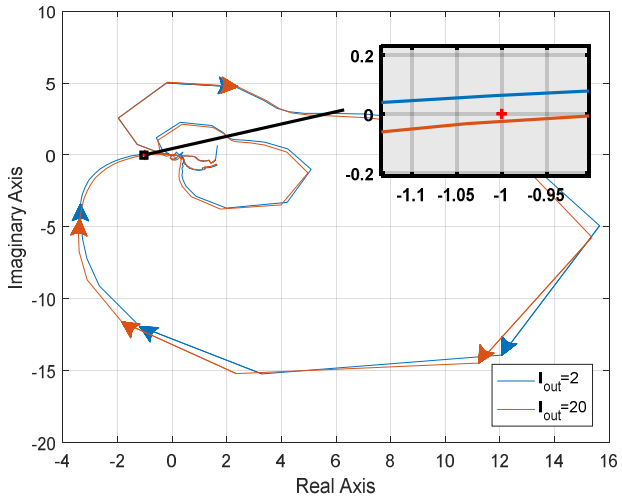
Figure 4-23 Generalized Nyquist Plot of the balanced system when the output current setpoint is changed from 2 A to 20 A [54].
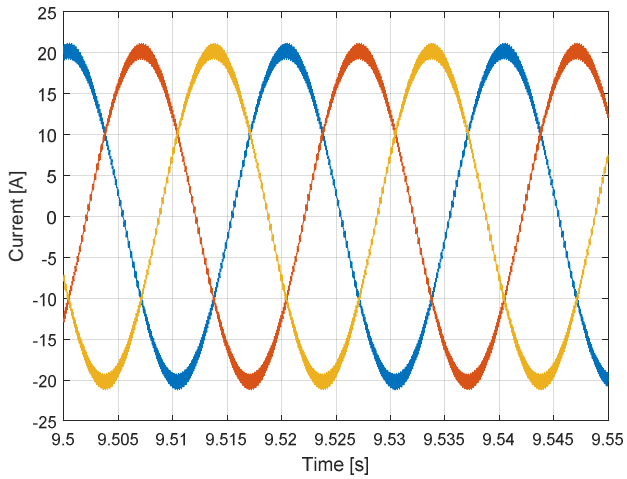
(a)
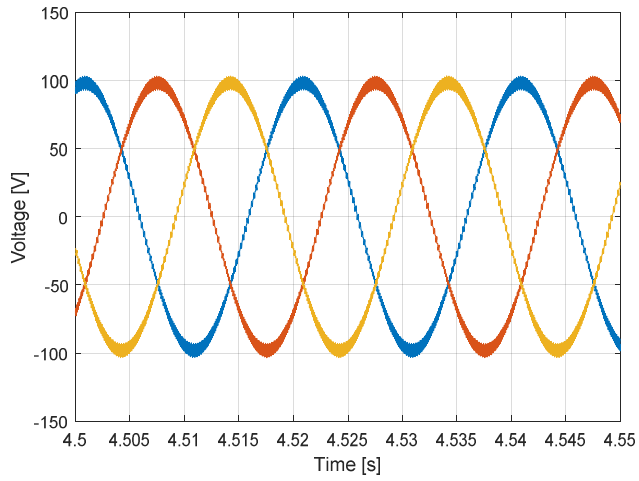
(b)
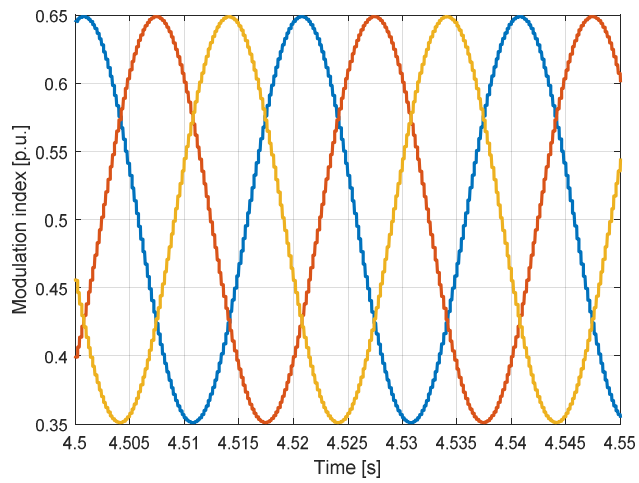
(c)

Figure 4-24 Time domain simulations of the balanced system, when the output current set point is 20 A (a) the output current (b) the PCC voltage (c) the modulation indices [54].
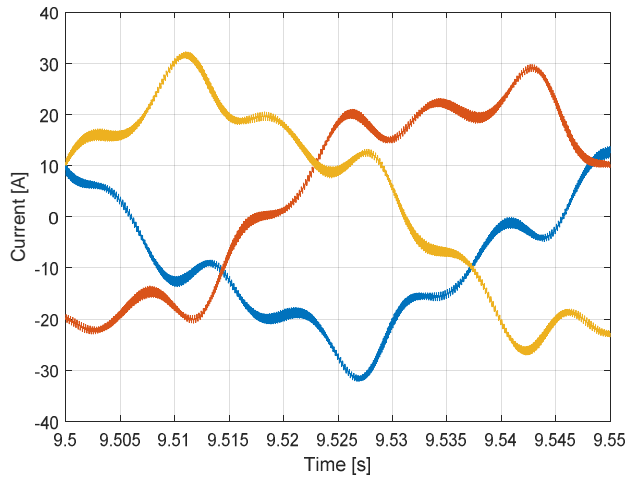
(a)
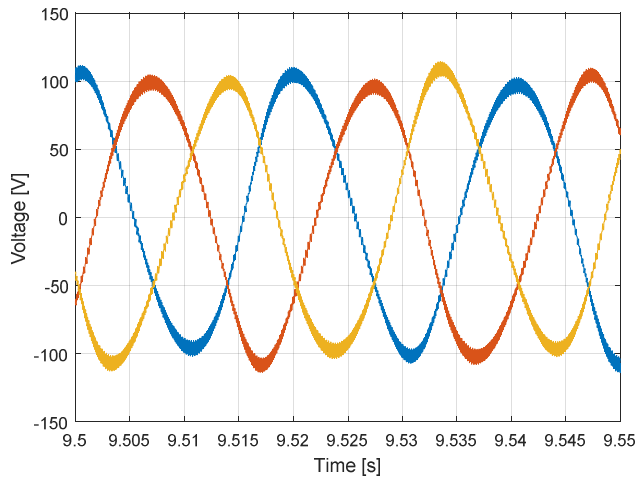
(b)
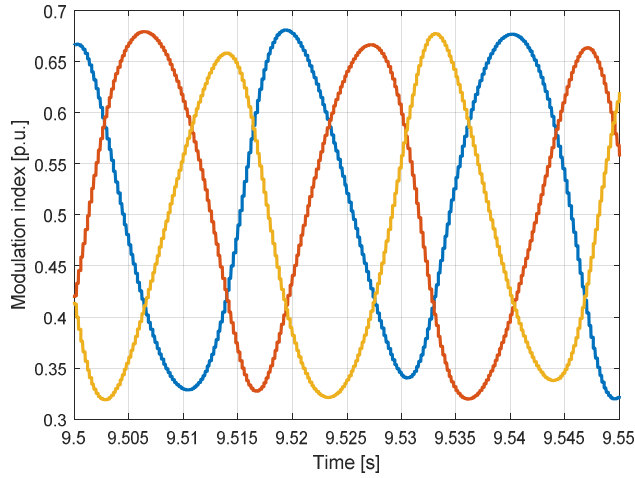
(c)

Figure 4-25 Time domain simulations of the balanced system, when the output current set point is 2 A (a) the output current (b) the PCC voltage (c) the modulation indices [54].

Case 2: Power quality studies

The previous case investigated the stability in a non-LTI and unbalanced system, where numerical models are used. The methodology was able to find the frequency of instability. However, the magnitudes of the oscillations in the system are also dependent on the background harmonics generated by elements. In other words, for small signal stability analysis only impedances are of importance and the excitations can be neglected. However, for power quality studies, the effects of harmonics from each element should be considered. The nodal equations of (4-3) are also valid for matrix components. If the harmonic sources are known as matrices then the harmonic analysis can be performed for the entire electrical network even with the cross couplings. For instance if the back-ground harmonics of the grid voltage in Figure 4-9 are given as a vector, then, the frequency components at the PCC voltage can easily be obtained by

$$[V_{PCC}] = [Z_c][Z_g + Z_c]^{-1}[V_g] \qquad (4-22)$$

where, $[Z_c]$ is the impedance matrix of the converter (inverse of the admittance matrix), $[Z_g]$ is the impedance matrix of the grid and $[V_g]$ is the present harmonics at the grid.

To show the effectiveness of the method, the converter also injects some negative sequence current into the unbalanced grid. Moreover, the grid has a positive sequence inter-harmonic at 90 Hz. Due to the frequency couplings mentioned in §4.2.2.1, in the phasor plot shown in Figure 4-26, another dominant frequency component can also be seen at 10 Hz ($-(f_p\text{-}2f1)$), which is even larger than the 90

Hz component for the output current. It can also be seen that the results of the matrix based method are closely correlated to the time domain simulation results.
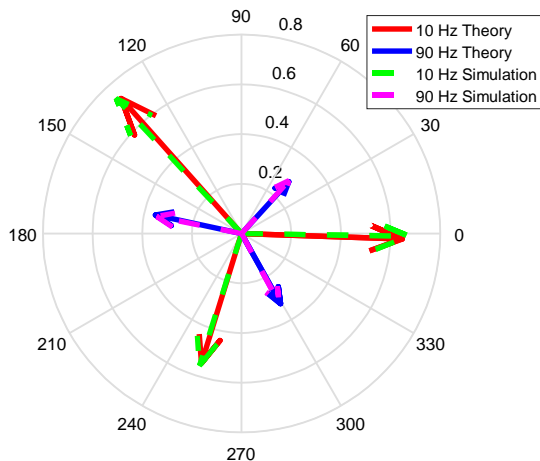
(a)
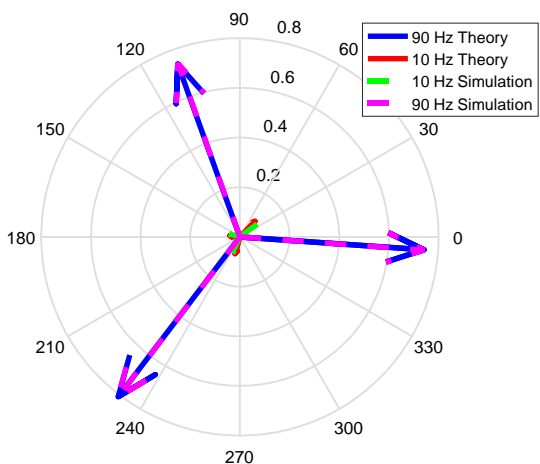
(b)

Figure 4-26 The phasor plot of (a) harmonic currents and (b) harmonic voltages at the PCC found by theory and simulations [54].

Table 4-5 Set points of the current controller and the parameters of the grid [54].

Symbol	Description	Value
I_{dr}^{+}	Pos. seq. d channel current reference (stabe/unstable cases)	20 A
I_{qr}^{+}	Pos. seq. q channel current reference	5 A
I_{dr}	Neg. seq. d channel current reference	2 A
I_{qr}	Neg. seq. q channel current reference	2 A

V_g^+	Grid line-ground peak voltage (Pos. Seq.)	100 V
L_1	Grid inductance-phase A	2.3 mH
L_2	Grid inductance-phase B	1.1 mH
L_3	Grid inductance-phase C	3.4 mH

4.3. NUMERICAL DATA IN EIGENVALUE BASED STABILITY ANALYSIS

In Chapter 2, the eigenvalue based stability was introduced and the advantages of using this method over the impedance based stability criterion were discussed. However, this method needs the state space models for all elements, and as pointed out in this chapter, the models are not always available. The proposed solution is to use an identification method like the vector fitting (VF) method to convert the frequency response data to proper state space models [66]–[69]. The application of VF in stability studies of power electronic based power systems was first introduced in [70]. In [70] the impedance is measured from a node in an electrical network and then by using the VF the eigenvalues are calculated. However, this method is very similar to the impedance based stability analysis, which is a local method, and suffers from the problems discussed in [38], [71]. It also considers the entire system as a black box and therefore it cannot use the advantages of the eigenvalue based method such as the participation factor analysis.

In this chapter, first the VF is used for unknown power converters and the challenges are discussed. Then the application of VF is extended for modelling other elements such as cables and transformers. In the end, the eigenvalue based analysis and the impedance based analysis are combined together using the VF.

4.3.1. THE PROPOSED METHOD FOR DEALING WITH BLACK BOX MODELS

In Chapters 2 and 3 methods were introduced for stability analysis if all analytical models are available. The VF can be used to find the state space models from the numerical terminal characteristics of unknown elements. The VF is an identification method, which makes an approximation of a given numerical frequency response.

$$f(s) \approx \sum_{m=1}^{N} \left(\frac{R_m}{s - P_m} \right) + D + sE \tag{4-23}$$

where $f(s)$ is the numerical frequency response (note it is a complex vector for a SISO system), N is the order of approximation (i.e. order of the transfer function). P_m is the mth pole and R_m is its corresponding residue. D is the feed-through matrix and E is to model improper transfer functions. It should be noted that the frequency response is obtained in a stable case; therefore, the identified model should not have any RHP poles. This can be achieved by activating the stability enforcement feature of the VF, which simply rejects the RHP poles at each iteration.

If $f(s)$ is the outcome of a measurement then for sure it contains some noise; there are some advanced methods to minimize the noise effect, which are out of the scope of this work. It should be noted that in order to have a good approximation and to cover the effects of different control loops properly, $f(s)$ should contain samples up to the Nyquist frequency (i.e. half of the sampling frequency).

4.3.2. SIMULATION RESULTS

In this section the application of vector fitting is explained by two cases. The first case is a linear case where the terminal characteristics of the power converters can be described by SISO frequency responses. The second case is a nonlinear case where linearized models in the dq domain are used for the analysis. In contrast to the linear case, the terminal characteristics of the power converters in this case are MIMO frequency responses, and therefore, matrix fitting (MF) should be used for identification [69].

4.3.2.1 A Linear Case study

The first case is the simplified Cigré benchmark system that has been introduced in §2.4.2. Figure 4-27 shows the structure and the parameters and the control structure can be found in §2.4.2. However, in this chapter it is assumed that no information about the converters is available and only the output admittances of the converters are available as shown in Figure 4-28.
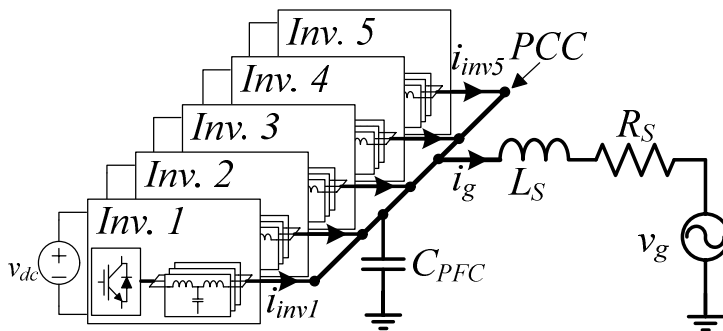
Figure 4-27 Considered power system, which is based on Cigré LV benchmark system [38].
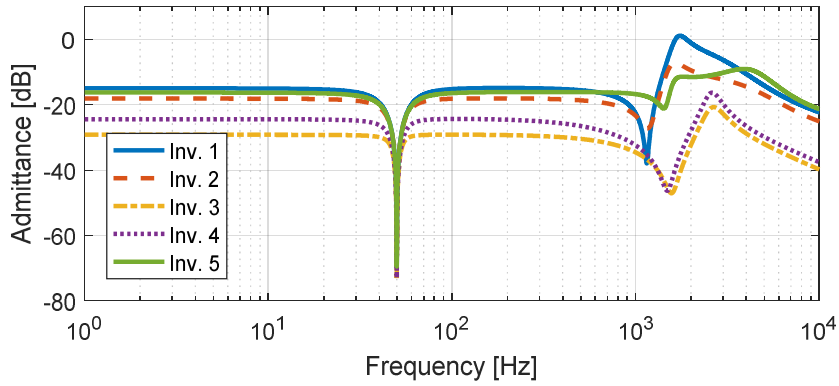
(a)
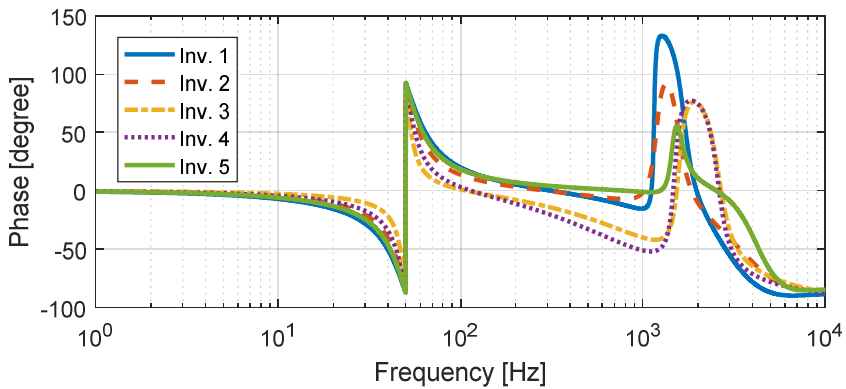
(b)

Figure 4-28 Output admittances of the considered converters. (a) Magnitude plot (b) phase plot [38].

The order of approximation in the VF should be chosen in a way that it meets the accuracy requirement (e.g. 1% difference between the original numerical data and the identified model). In this part to see how different orders affect the analysis, the study is conducted with 6th, 8th and 12th order models.
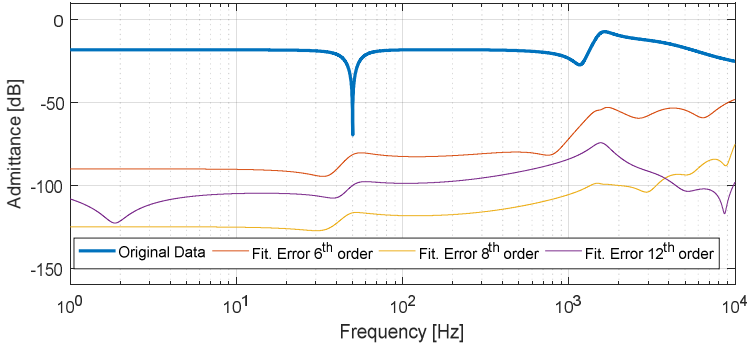
Figure 4-29 Fitting results of Inverter 2 using 6th, 8th and 12th order models [38].

Figure 4-29 shows the absolute error between the original data (the admittance of Inverter 2) and the identified models with the mentioned orders by the VF.

The known elements can be modelled by the approach described in §3.4. For instance, the grid can be modelled by

$$\dot{x} = A_{net}x + B_{net}u$$

$$= \begin{bmatrix} -\dfrac{R_s}{L_s} & \dfrac{1}{L_s} \\ \dfrac{-1}{C_{PFC}} & 0 \end{bmatrix} \begin{bmatrix} i_g \\ v_{pcc} \end{bmatrix}$$

$$+ \begin{bmatrix} -\dfrac{1}{L_s} & 0 & 0 & 0 & 0 & 0 \\ 0 & \dfrac{1}{C_{PFC}} & \dfrac{1}{C_{PFC}} & \dfrac{1}{C_{PFC}} & \dfrac{1}{C_{PFC}} & \dfrac{1}{C_{PFC}} \end{bmatrix} \begin{bmatrix} v_g \\ i_{inv1} \\ i_{inv2} \\ i_{inv3} \\ i_{inv4} \\ i_{inv5} \end{bmatrix} \qquad (4\text{-}24)$$

$$y = [v_{pcc}] = C_{net}x + D_{net}u = [0 \quad 1]x + [0 \quad 0 \quad 0 \quad 0 \quad 0 \quad 0]u$$

where the inputs are the currents of the inverters and the output is the PCC voltage as explained in the CCM in §3.3.2.

The CCM can be used to build up the overall state space model of the system. The eigenvalues/poles of the system, when Inverters 3 and 4 are disconnected, are plotted in Figure 4-30.
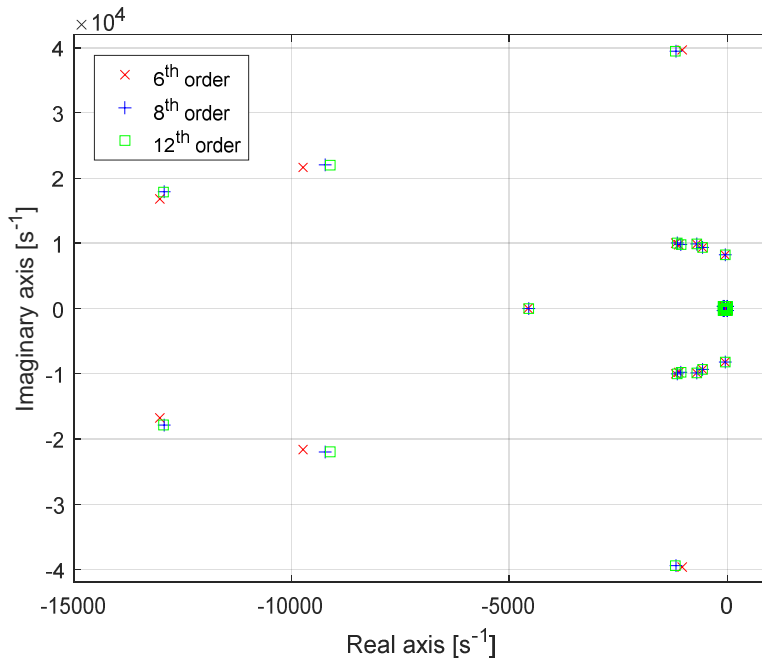
Figure 4-30 Poles of the system, when Inverters 3 and 4 are disconnected [38] *in the system in Figure 4-27.*

A challenge in using the VF is the limited data from the measurements. In other words, the measurements are done for a limited frequency range and the response to excitations beyond the trained range is unknown. For instance, Figure 4-31 shows the passivity of the converters beyond the trained frequency. It can be seen that the sixth order model behaves passive (i.e. positive real part or the phase of the impedance between -90° and +90°) but the eight order model is non-passive. Passivity is a sufficient condition for stability [72], [73]. In other words, a non-passive system could be stable or unstable. Therefore, it can be concluded that the eighth order model could be unstable if connected to another grid impedance, but the sixth order model will not create any problems. To avoid this problem, the VF tool is able to enforce the passivity [74], which means it can find a fully passive approximation for all frequencies even beyond the trained range by pushing the Hamiltonian matrix to have no imaginary eigenvalues [75]. However, this work around cannot be used for identifying the active elements such as power converters, because they could be non-passive at different frequencies depending on the control strategy [73].

The proposed solution in [38] is to limit the analysis within the confident frequency range. This can easily be done by rejecting the identified poles that are outside the circle of confidence (their magnitude is larger than the maximum trained frequency) as shown in Figure 4-32.

(a)

(b)
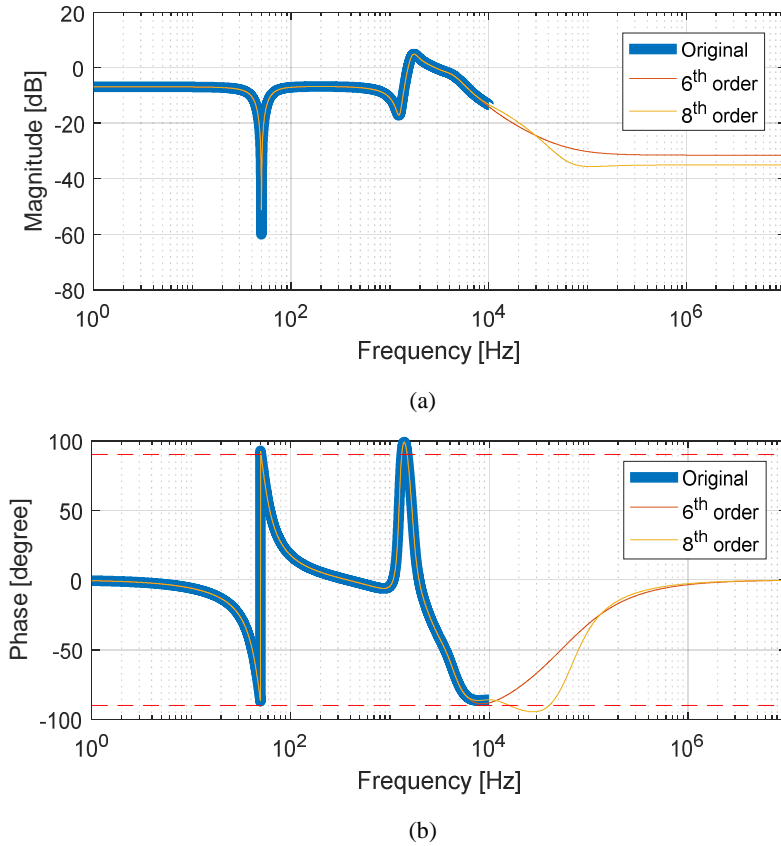
Figure 4-31 Aggregated admittance of the converters, when Inverters 3 and 4 are disconnected (a) magnitude plot (b) phase plot [38].
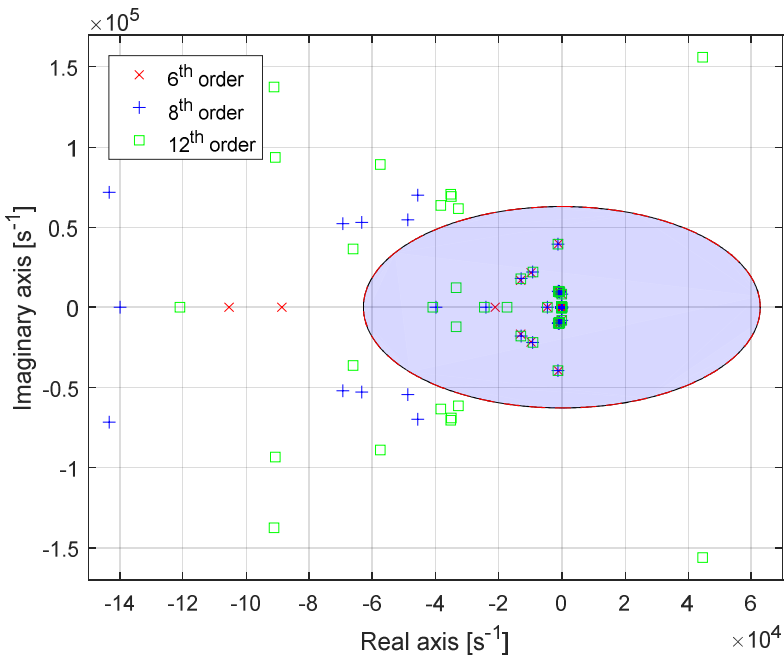
Figure 4-32 Poles outside the confidence circle must be disregarded (this is for a case, where Inverters 3 and 4 are disconnected) [38].

If Inverter 2 is disconnected, the system becomes unstable as shown in §2.4.2. Figure 4-33 shows the pole plot of the system using the numerical data, which is almost the same as the pole plot of the analytical models shown in Figure 2-32 (a). Similarly the participation factor analysis can be done for the unstable pole pair (229 ± 8180) rad/s to find which converter is mainly responsible for this. Table 4-6 shows the top five contributors to this instability. It also shows that different approximation orders have minor impact on the PF results. Inverter 1 has the most impact on the instability but since the models are considered as black boxes, no more information about the internal state variables can be obtained [38].
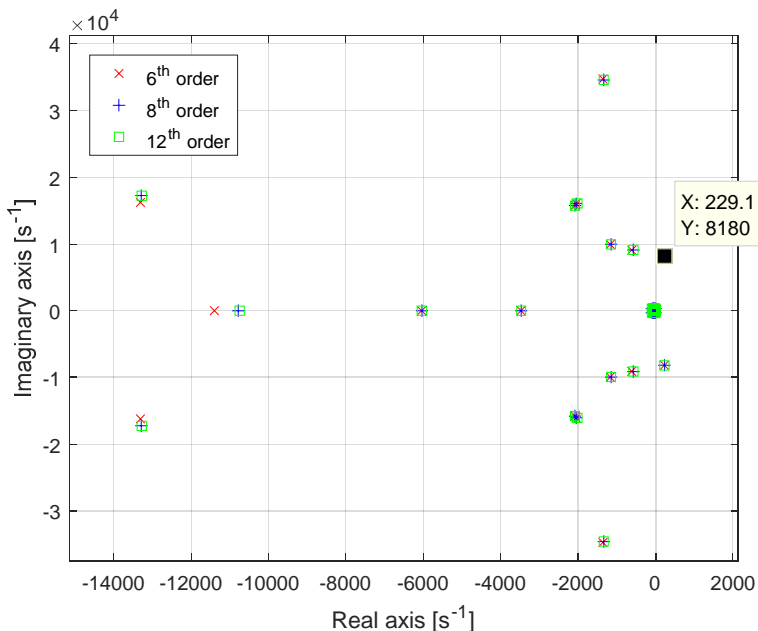
Figure 4-33 An unstable pole is highlighted for the case, where Inverter 2 is disconnected [38].

Table 4-6 Identifying how much the converters contribute to the instability in Case 2 [38].

sixth order		eighth order		twelfth order	
State Name	PF	State Name	PF	State Name	PF
INV1.State 3	0.296	INV1.State 4	0.294	INV1.State 5	0.295
INV1.State 4	0.302	INV1.State 5	0.300	INV1.State 6	0.300
INV2.State 3	0.167	INV2.State 3	0.167	INV2.State 7	0.167
INV2.State 4	0.169	INV2.State 4	0.169	INV2.State 7	0.169
Grid.State 1	0.112	Grid.State 1	0.112	Grid.State 1	0.112

4.3.2.2 A nonlinear case

As discussed in Chapter 2, *dq* domain models should be used for the analysis of converters with outer loop control. Therefore, the admittance/impedance characteristics are no longer SISO models and the MIMO VF (also known as matrix fitting) should be used. The original matrix fitting (MF) implementation [69] assumes that the transfer function matrix is symmetrical, but it is obviously not the case for *dq* domain models. The MF tool is changed slightly to be able to handle *dq* domain models (see Appendix E).

In this section, the system shown in Figure 4-34, which has previously been discussed in §2.4.3, is considered but it is now assumed that only numerical terminal characteristics are available. The small signal output admittances are operating point dependent and therefore it is necessary to use new linearized models for any new

operating point. In this section it is assumed that the small signal models for the given operating points are available.
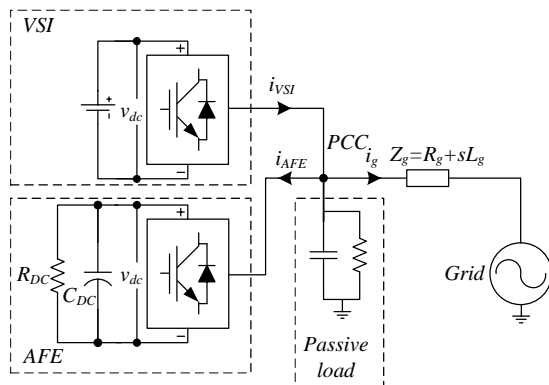
Figure 4-34 A nonlinear power system that is formed of a Voltage Source Inverter and an Active Front End [38].
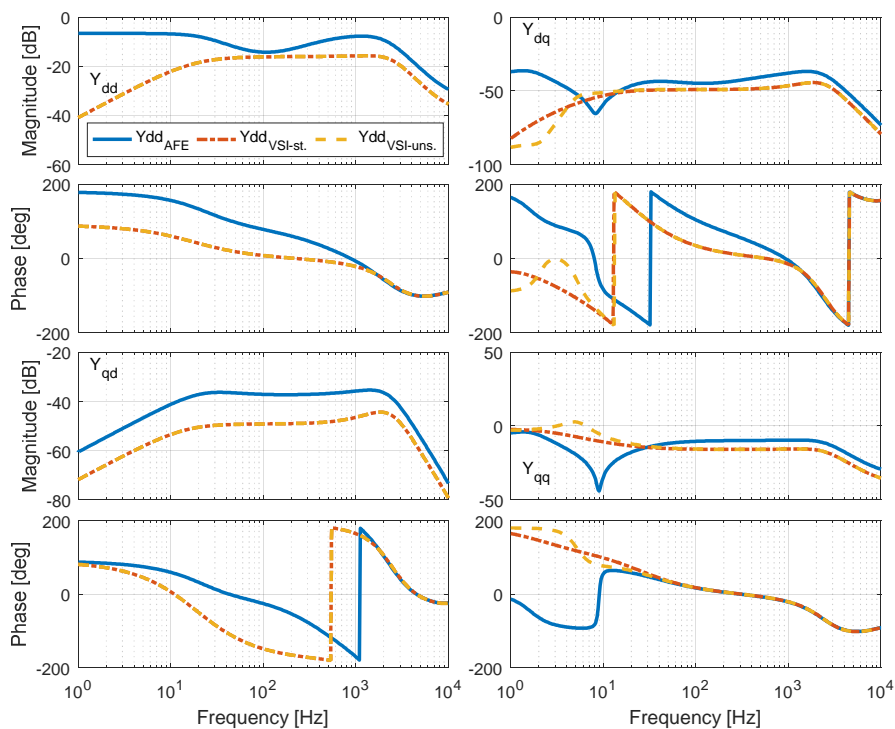
Figure 4-35 Admittance of the AFE and the VSI for the considered stable and unstable cases in the dq domain [38].

Figure 4-35 shows the admittances of the converters in the *dq* frame, where the parameters of VSI are intentionally changed to create an instability (this is highlighted in Figure 4-35 by subscripts VSI-st. and VSI-uns.). It can be seen the change happens in the low frequency range since it is due to a change in the PLL, which is a low frequency control loop.

The state space model of the grid in the positive sequence domain is

$$
\dot{x} = A_{net}x + B_{net}u = \begin{bmatrix} -\dfrac{R_g}{L_g} & -\dfrac{1}{L_g} \\ \dfrac{1}{C_L} & -\dfrac{1}{C_L R_L} \end{bmatrix}\begin{bmatrix} \Delta i_g \\ \Delta v_x \end{bmatrix} + \begin{bmatrix} \dfrac{1}{L_g} & 0 & 0 \\ 0 & \dfrac{1}{C_L} & \dfrac{1}{C_L} \end{bmatrix}\begin{bmatrix} \Delta v_g \\ \Delta i_1 \\ \Delta i_2 \end{bmatrix}
$$

$$
y = \begin{bmatrix} \Delta i_g \\ \Delta v_x \end{bmatrix} = C_{net}x + D_{net}u = \begin{bmatrix} 1 & 0 \\ 0 & 1 \end{bmatrix}x + \begin{bmatrix} 0 & 0 & 0 \\ 0 & 0 & 0 \end{bmatrix}u
$$

(4-25)

As shown in §3.4.1 the equations must be transformed to the *dq* frame by (3-59) in order for the CCM to be used. Figure 4-36 shows the eigenvalues of the two scenarios, which is almost the same as the results obtained in §2.4.3.
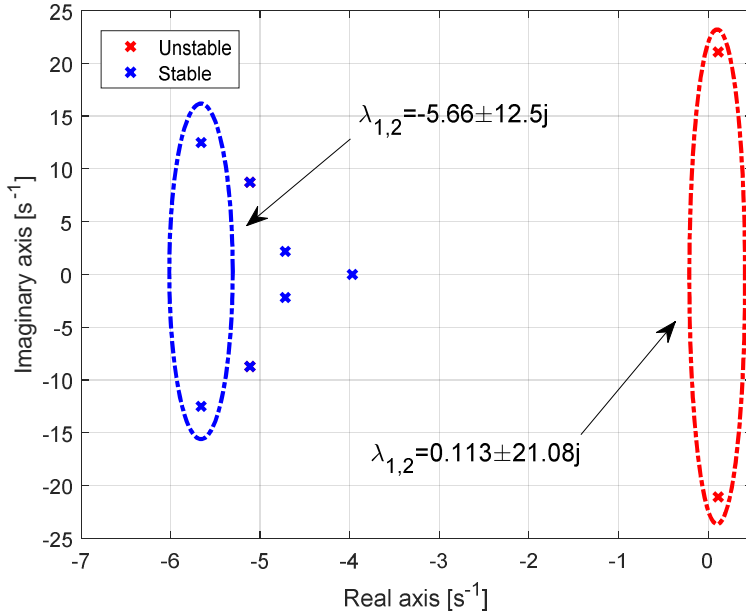
Figure 4-36 Low frequency poles of the entire system in Figure 4-34 for stable and unstable cases [38].

A participation factor analysis as shown in Table 4-7 indicates that the VSI is mainly responsible for this. This is as expected since the instability was created by increasing the PLL gain of the VSI.

Table 4-7 Participation factor analysis for the unstable case [38].

State Name	PF
VSI.State 15	0.44
VSI.State 16	0.35
AFE.State 17	0.19

4.3.3. USING THE VECTOR FITTING METHOD TO CREATE SUITABLE MODELS OF FREQUENCY DEPENDENT ELEMENTS IN THE STABILITY ANALYSIS PLATFORM

In Chapter 3 the stability analysis platform was introduced and it was discussed how to model different elements in the tool. The main assumption was that the models were analytically available. However, as shown in this chapter it is not always true. In this part, the VF is used to create suitable models for the stability platform.

4.3.3.1 Unknown converters

As it was shown in §4.3.2, the converter model can be identified by the vector fitting, and it can be combined by the models using the CCM. Therefore, no matter how a converter is modelled it can be connected to the rest of the system by the method explained in §3.4.4.

4.3.3.2 Shunt black box models (one-port elements)

Assume the frequency dependent admittance of an unknown component is available. Equation (4-26) shows the expanded form of the identified transfer function of the mentioned component. This equation can easily be realized by a number of parallel RL branches as shown in Figure 4-37, and the values of resistances and inductances can be found from (4-27). A capacitor and a resistor can also be put in parallel for improper admittance models. It should be noted that some poles are imaginary that may result in imaginary values for the equivalent resistance/inductances. However, this is not a problem in the developed stability platform because the tool can handle imaginary matrices.
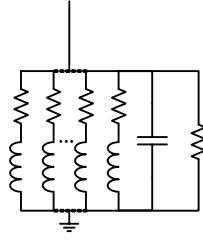
Figure 4-37 How to realize a transfer function with some circuit elements.

$$Y = \sum_{i=1}^{N} \frac{r_i}{s - p_i} + D + sE \Rightarrow \sum_{i=1}^{N} \frac{1}{L_i s + R_i} + \frac{1}{R_p} + C_p s \qquad (4\text{-}26)$$

$$L_i = \frac{1}{r_i}$$

$$R_i = \frac{-p_i}{r_i}$$

$$R_p = \frac{1}{D} \qquad (4\text{-}27)$$

$$C_p = E$$

4.3.3.3 Two port elements

If the admittance matrix of a two port element is available as

$$Y = \begin{bmatrix} Y_{11} & Y_{12} \\ Y_{12} & Y_{22} \end{bmatrix} \qquad (4\text{-}28)$$

Then, one can use the equivalent model as shown in Figure 4-38 to realize it based on (4-26) and (4-27). Equation (4-29) shows how to define the different elements of Figure 4-38 (assuming a reciprocal two port element $Y_{12}=Y_{21}$).

$$Y_{series} = -Y_{12}$$

$$Y_{shunt1} = Y_{11} + Y_{12} \qquad (4\text{-}29)$$

$$Y_{shunt1} = Y_{22} + Y_{12}$$
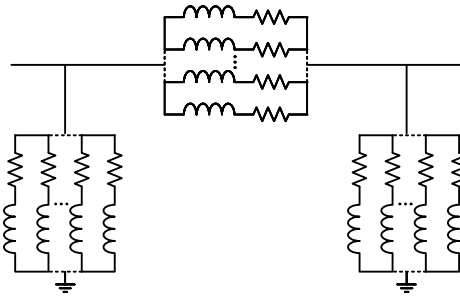
Figure 4-38 Realization of a frequency dependent two-port network.

4.3.3.4 Cable modelling

Equivalent π-model is chosen in this work based on the advantages mentioned in §4.2.1.1. The series impedance and the shunt admittance can be identified by the VF and realized by (4-26) and (4-27).
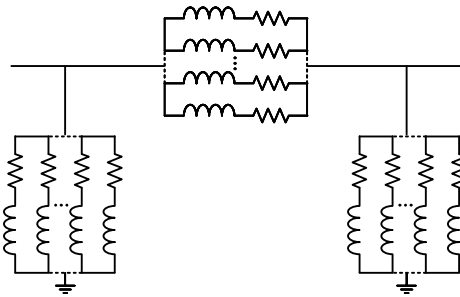
Figure 4-39 Frequency dependent cable model using constant parameters.

4.3.3.5 Transformer modelling

Only leakage impedance is considered as frequency dependent as discussed in §4.2.1.1. Therefore, the VF can be applied to find an equivalent circuit for the leakage impedances using (4-26) and (4-27) as shown in Figure 4-40.
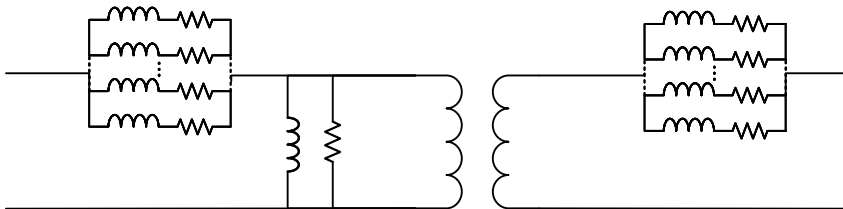
Figure 4-40 Frequency dependent transformer model using constant parameters.

4.3.3.6 Grid model

A grid can also be modelled as a frequency dependent shunt element similar to what presented in §4.3.3.2 since in the stability studies only small signal impedances are of interest.

4.3.3.7 Validation

The proposed method for modelling the black-box models in the stability analysis platform is done by an embedded Vector Fitting code entirely rewritten in Python. The 35-WT system in Appendix B is considered with the defined frequency dependent characteristics. Similar to §3.5.2 impedance frequency scans are used for validating the results using PowerFactory. The final model of this system includes 1585 RLC elements and 700 state variables. The impedance frequency scans as shown in Figure 4-41 reveal a good agreement except for the 220 kV onshore bus bar, where the error is amplified due to the resonance.
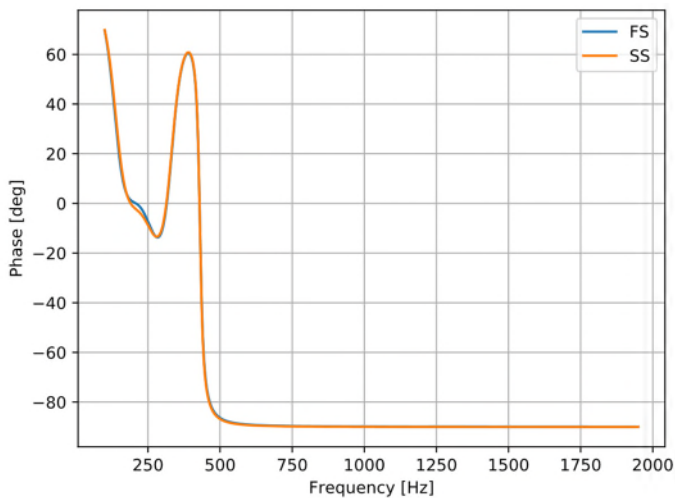
(a)
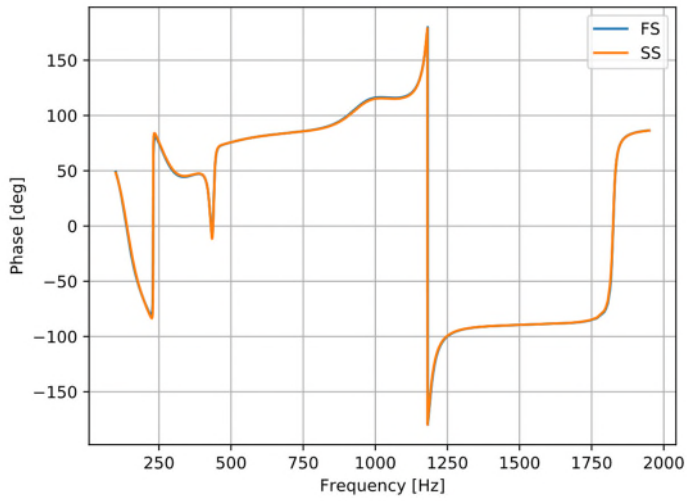
(b)
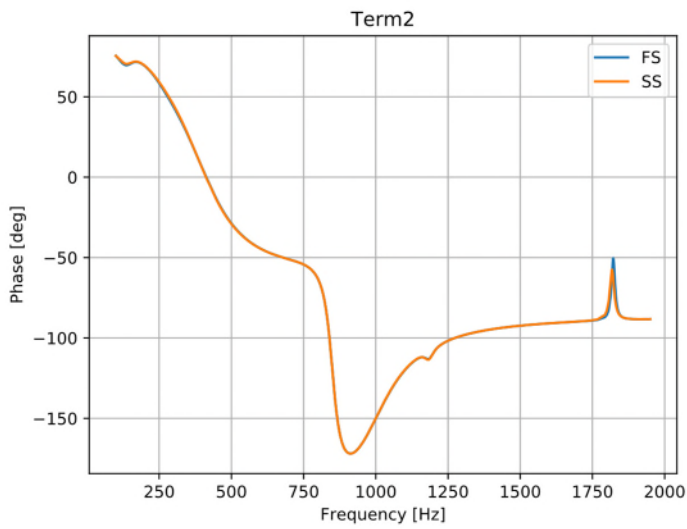
(c)
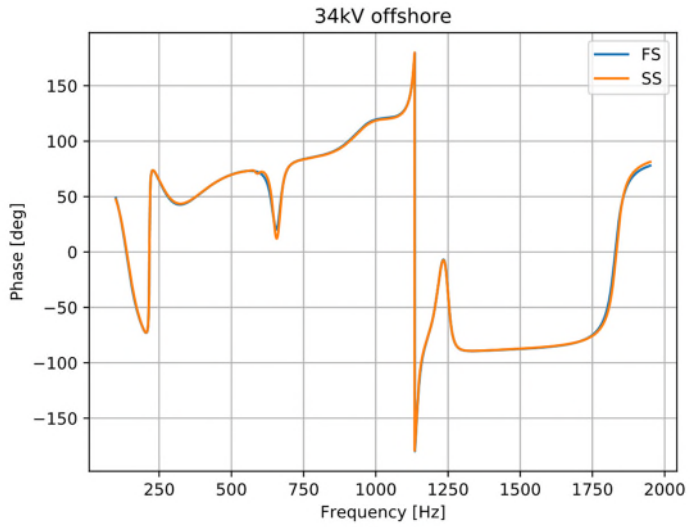
(d)
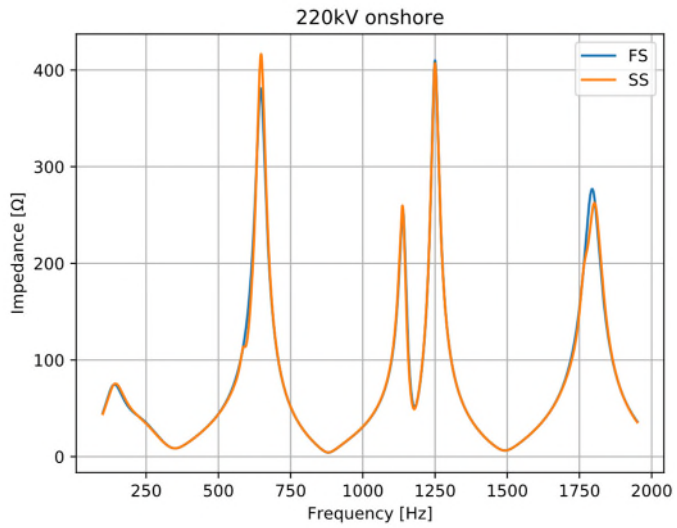
(e)
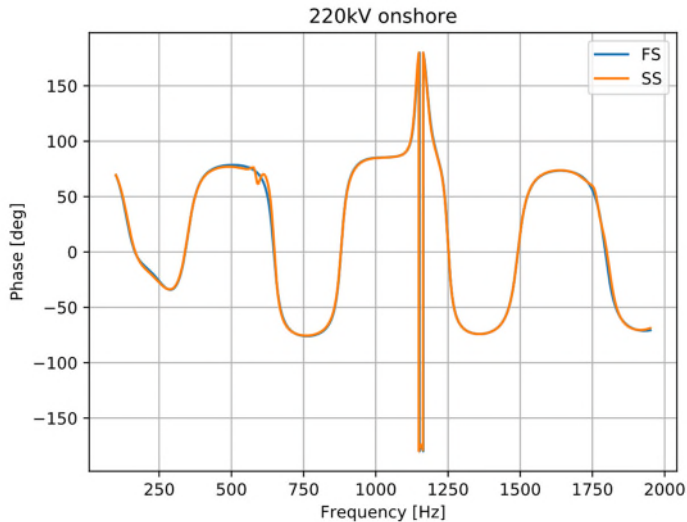
(f)

Figure 4-41 Comparing the impedance frequency scans calculated by PowerFactory (FS) and the tool (SS) for (a),(b) Wind turbine terminal (c),(d) 34 kV offshore bus bar (e),(f) 220 kV onshore bus bar.

4.4. IMPROVING THE IMPEDANCE BASED STABILITY CRITERION BY USING THE VECTOR FITTING METHOD

In impedance based stability analysis of a multi-converter system, one converter is considered as the source impedance and the other converters are grouped together with the grid as the load impedance [21]. Therefore, the second precondition of the IBSA, which assumes a stable load impedance, may not be satisfied [76]. If the load impedance becomes unstable, then, some right half plane (RHP) poles will appear in the minor loop gain L, since the poles of the load impedance are also the poles of the minor loop gain L. "Thus, the stability can simply not be evaluated by counting the number of encirclements due to the Nyquist Stability Criterion, which states the number of RHP poles of a closed loop system is equal to the number of times the Nyquist plot encircles the critical point (-1,0) **plus** the number of the RHP poles of the open loop gain [37]. In [77], [78] a step-by-step method is proposed to make sure that no RHP pole appears in the load impedance" [76]. For instance, for the test system shown in Figure 4-42, depending on how the source impedance is chosen, different Nyquist diagrams are obtained as shown in Figure 4-43, and surprisingly they give different conclusions.
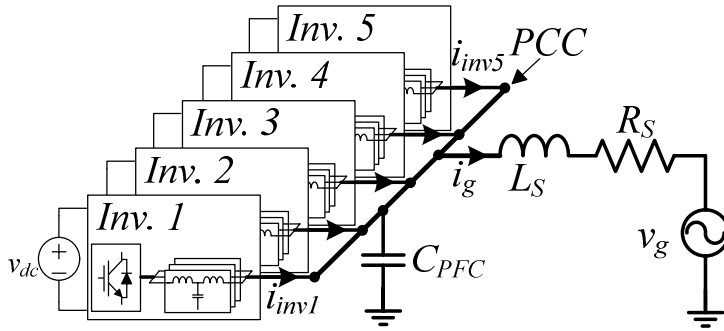
Figure 4-42 Test system that is used to validate the proposed method [38], [76] .
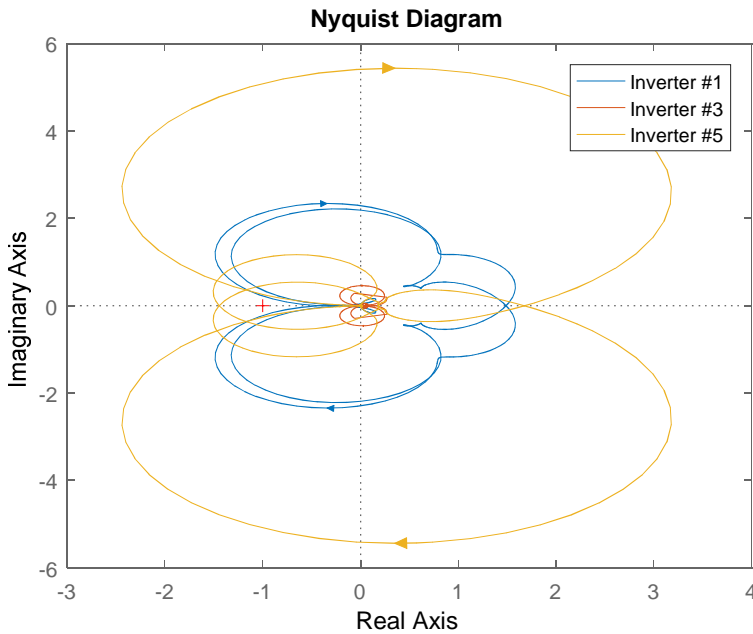
Figure 4-43 Impedance based stability analysis for different source impedances.

Another problem of the IBSA that can be seen in Figure 4-43 and has also been reported in [70], [79] is that relative stability indices such as phase margin (PM) and gain margin (GM) are dependent on how the source impedance is considered. However, the eigenvalues of the system are global variables and they are not different for different points [32], [70] (this means the damping of eigenvalues would not differ, however, some eigenvalues, which are not observable at the measurement point, may be concealed). "The eigenvalues can be obtained by an

analytical evaluation of the whole system [39] or by approximating the driving point impedance, which is indeed the equivalent impedance of that node as a frequency response, into state equations using the Vector Fitting method [32], [70]. However, the former leads to a very complicated study and it also needs analytical models of all components that might not be available due to the confidentiality or difficulty in the modeling [16], [38], [54]. The latter can also not identify the problematic subsystem because it only measures the driving point impedance. The method also assumes that the current configuration of the system is stable and uses some measurements either in simulations or in experiments. However, in the design phase the system designer might have some unstable cases, which cannot be predicted by this method"[76]. The method presented in §4.3 can also be used here, however, it is a full detailed analysis and it is time consuming and the resultant matrices are huge due to full modelling of every component. Moreover, if a system has many black boxes then multiple identifications must be used and at the end the uncertainty of each identification might be accumulated and affect the final results [76].

In this part a simplified method of the eigenvalue-based stability criterion is proposed to improve the IBSA. The method similar to [32], [70] analyzes the system from a point, therefore, no need exists to model every component even the unimportant ones. The other advantage is that only two transfer functions are identified, which minimizes the risk of error and uncertainty propagation. The drawback is that in the full analysis the exact component can be found but in this method the problematic subsystem is found. In §4.4.2.1 more information is obtained by repeating this process and rearranging the subsystems. The analysis is also a local analysis and it is only able to find the observable dynamics at the point under study (see §2.4.4). However, this is also a problem of the impedance based stability criterion and the idea of this part is to improve this method.

Advantages and differences to the methods in [32], [70] are

1) This method is able to find which subsystem is the problematic one. Since it decomposes the system into two subsystems compared to [32], [70] that only considers the driving point impedance.

2) In [32], [70] the stability enforcement is used in the identification process. In other words it ensures that the identified system is stable because the impedance measurement system does not work in the unstable system. However in this work, the stability enforcement in turned off. Therefore, it is able to work in unstable situations and find the problematic components. "It must be noted that this method is a design phase study, where the designers are very interested to see and mitigate problems before commissioning in order to minimize the risk and cost. Therefore, all components are known to the designer as detailed models or at least as frequency response data." [76].

4.4.1. THE PROPOSED ANALYSIS METHOD

In this method, the system is decomposed into an impedance system (current is the input and the voltage is the output) and an admittance system (voltage is the input and the current is the output). Figure 4-44 shows such a system, where Subsystem 1 is an impedance model and Subsystem 2 is an admittance model. The general state equations of the mentioned systems are [76]

$$\begin{cases} \dot{x}_1 = A_1 x_1 + B_1 i \\ v = C_1 x_1 + D_1 i + E_1 di/dt \end{cases} \tag{4-30}$$

$$\begin{cases} \dot{x}_2 = A_2 x_2 + B_2 v \\ i = C_2 x_2 + D_2 v + E_2 \dot{v} \end{cases} \tag{4-31}$$
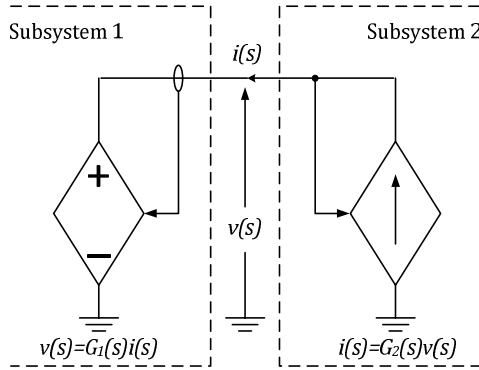
Figure 4-44 System is decomposed into two subsystems, one is represented by an impedance while the other one is modelled as an admittance [76].

The two subsystems are chosen arbitrarily, and then, they are identified by the VF allowing them to be improper (a nonzero E matrix). If both are improper (considerable E matrix) then the definitions of the subsystems must be inverted (admittance ↔ impedance).

It is first assumed that both transfer functions are proper (E_1 and E_2 matrices are Zero). Then, the two state equations can be combined into one dynamical system as

$$\begin{bmatrix} \dot{x}_1 \\ \dot{x}_2 \end{bmatrix} = \begin{bmatrix} A_1 & 0 \\ 0 & A_2 \end{bmatrix} \begin{bmatrix} x_1 \\ x_2 \end{bmatrix} + \begin{bmatrix} B_1 & 0 \\ 0 & B_2 \end{bmatrix} \begin{bmatrix} i \\ v \end{bmatrix} \tag{4-32}$$

Variables v and i can be eliminated from (4-32) and it can be expressed in terms of x_1 and x_2 as

$$\begin{bmatrix} \dot{x}_1 \\ \dot{x}_2 \end{bmatrix} = [A_T] \begin{bmatrix} x_1 \\ x_2 \end{bmatrix} = \begin{bmatrix} A_1 + B_1 \Gamma D_2 C_1 & B_1 \Gamma C_2 \\ B_2(C_1 + D_1 \Gamma D_2 C_1) & A_2 + B_2 D_1 \Gamma C_2 \end{bmatrix} \begin{bmatrix} x_1 \\ x_2 \end{bmatrix} \tag{4-33}$$

where, $\Gamma \overset{\text{def}}{=} (I - D_2 D_1)^{-1}$ and I is the identity matrix of the appropriate size.

If Subsystem 1 is improper ($E_1 <> 0$ and $E_2 == 0$) then two different cases exist:

1) If D_2 is a zero matrix, then

$$i = C_2 x_2 \overset{d/dt}{\Longrightarrow} di/dt = C_2 \dot{x}_2 = C_2(A_2 x_2 + B_2 v) \qquad (4\text{-}34)$$

The derivative of the current in (4-30) can be removed by using (4-34), and similar to the previous case the current and the voltage can be eliminated from the total state equations

$$A_T = \begin{bmatrix} A_1 & B_1 D_1 \\ B_2 \Phi C_1 & A_2 + B_2 \Phi(D_1 C_2 + E_1 C_2 A_2) \end{bmatrix} \qquad (4\text{-}35)$$

where, $\Phi \overset{\text{def}}{=} (I - E_1 C_2 B_2)^{-1}$.

2) If D_2 is a non-zero matrix, then the current should be considered as a new state variable. The derivative of the current can be found from (4-30) as follows

$$di/dt = E_1^{-1}(v - C_1 x_1 - D_1 i) \qquad (4\text{-}36)$$

v can easily be found in (4-31) and it can be replaced in (4-36). Therefore, the new state matrix is

$$A_T = \begin{bmatrix} A_1 & 0 & B_1 \\ 0 & A_2 - B_2 D_2^{-1} C_2 & B_2 D_2^{-1} \\ -E_1^{-1} C_1 & -E_1^{-1} D_2^{-1} C_2 & E_1^{-1} D_2^{-1} - E_1^{-1} D_1 \end{bmatrix} \qquad (4\text{-}37)$$

4.4.2. SIMULATION RESULTS

Figure 4-42 shows the considered power-electronics-based power system. More information of the system can be found in §2.4.2. The objective of this chapter is to use numerical data for everything. Therefore, the admittances are the same as Figure 4-28. It must be noted again that in this part linear converters (the impedance/admittance is in phase domain) are used for a better presentation. However, (4-30)−(4-37) can be used for a nonlinear converter model in the *dq* domain [32], [38].

4.4.2.1 Test Case 1 (Inverter 5 is disconnected)

Assuming Inverter 5 is disconnected, Subsystem 2 (admittance model) consists of the grid and Inverter 1 and the rest of the system is considered as Subsystem 1 (impedance model). Figure 4-45 shows the results of the VF for different orders,

where the maximum error between the original data and approximated model is set to 2% (the dashed line) [76].
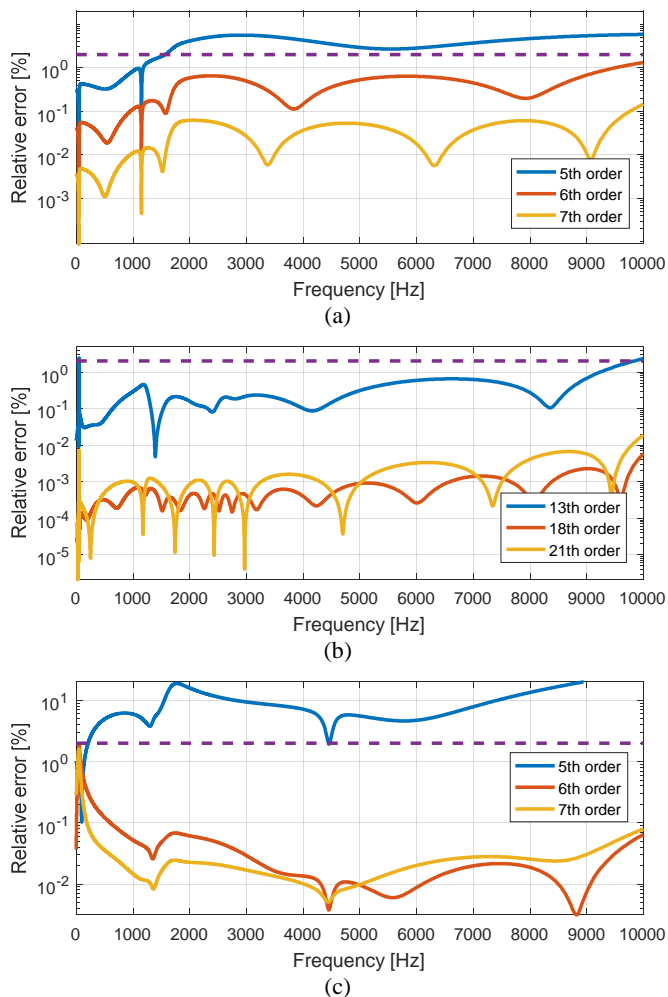
Figure 4-45 Results of the Vector Fitting for (a) Inverter 1 (b) Subsystem 1 and (c) Subsystem 2, with different orders for the system shown in Figure 4-42 [76].

"It must be noted that this method can also be considered as an order reduction technique. The unimportant dynamics have minimum impact on the frequency response. Therefore, by choosing a proper order for the fitting process, only the important dynamics are considered and it is not necessary to model the entire system, which otherwise leads to very large matrices. For instance, in this case an inverter should at least be modelled as a 6th order transfer function (3 orders for the LCL filter, 2 orders for the resonant controller and at least one order for the delay). This can be seen in Figure 4-45 (a). However, a 13th order model (instead of 3x6) is

enough for modelling Subsystem 1, which is formed of 3 inverters (Inv. 2, 3 and 4). The same is also true for Subsystem 2, where a 6th order model is enough" [76].

The Nyquist diagram of the minor loop gain (Considering the Subsystem 1 as the source) as shown in Figure 4-46 does not encircle the critical point. However, the time domain results as shown in Figure 2-33 (a) reveal that the system is unstable. As stated before, the RHP poles of the open loop system together with the number of encirclements show the stability of the closed loop system. Two RHP poles exist in the minor loop gain as shown in Figure 4-47 and the Nyquist plot does not encircle the critical point; therefore, two RHP poles are also present for the closed loop system. Figure 4-47 shows the identified poles of the minor loop gain using the VF. In other words, instead of using the sequential methods proposed in [77], [78] to avoid this wrong conclusion, the RHP poles can easily be detected by using the VF in one step [76].
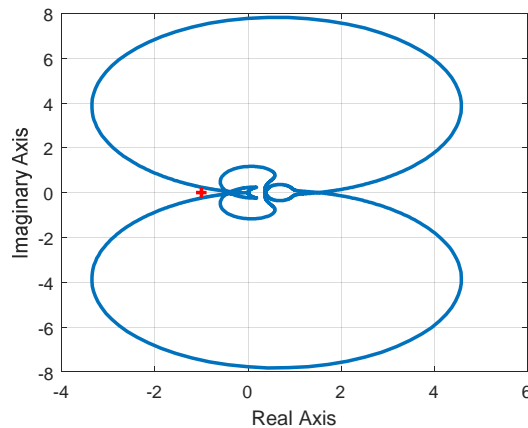
Figure 4-46 Nyquist plot of the minor loop gain for Case 1 for the system shown in Figure 4-42 [76] *.*
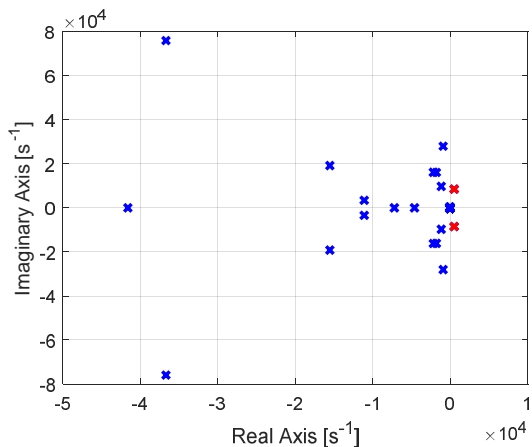
*Figure 4-47 Minor loop gain has two RHP poles in Case 1 for the system shown in Figure
4-42* [76]*.*

The eigenvalues of the overall system are obtained using the proposed methodology
and they are plotted in Figure 4-48, where it can be seen that the instability is
because of a pair of eigenvalues with positive real parts. The dominant eigenvalues
are the same as the poles found in Figure 2-32 (a) and validated by the time domain
simulations.
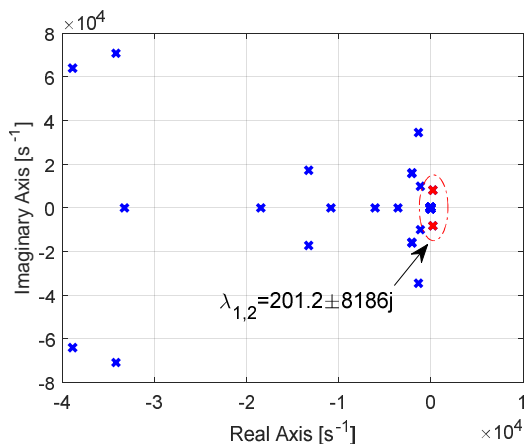
*Figure 4-48 Two unstable poles exist in the whole closed-loop system in Case 1 for the system
shown in Figure 4-42* [76]*.*

Furthermore, the PF analysis can be done using (2-100). Since the state variables are
unknown, the summations of participation factors for both subsystems are presented
in Table 4-8, which shows that the instability is mainly due to Subsystem 2 (Grid
and Inverter 1).

A different network partitioning scheme can be used to find the problematic component. For instance, only Inverter 1 is in Subsystem A and the rest of the system is grouped in Subsystem B. The Participation factor analysis as shown in Table 4-9 reveal that Inverter 1 is solely 51% responsible for this instability. Comparing results of Table 4-8 and Table 4-9 also indicates that 15% (65%-50%) contribution is now moved from Subsystem 2 to Subsystem B, which means the difference between the subsystems, i.e. the grid impedance, is 15% responsible. For more information on why sum of participation factors can be used refer to Appendix F.

Table 4-8 Participation factor analysis for the unstable pole of Case 1[76].

Participation Factor	Subsystem
35%	#1
65%	#2

Table 4-9 Participation factor analysis for the unstable pole of Case 1 with the new network decomposition [76].

Participation Factor	Subsystem
50.8%	A
49.2%	B

4.4.2.2 Test Case 2 (Inverter 3 is disconnected)

To analyze a stable system, Inverter 5 is reconnected and Inverter 3 is disconnected [22]. Figure 4-49 shows the eigenvalue plot of the system, where no unstable poles can be seen. Time domain results in Figure 2-33 (b) also verify that the system remains stable after a perturbation. The Prony Analysis of Figure 2-33 (b) can be used to evaluate how the dominant eigenvalues affect the transient response [40]. It can be seen that the dominant pole of Table 2-5 (for Case 4) is correctly identified by the eigenvalues in Table 4-10.
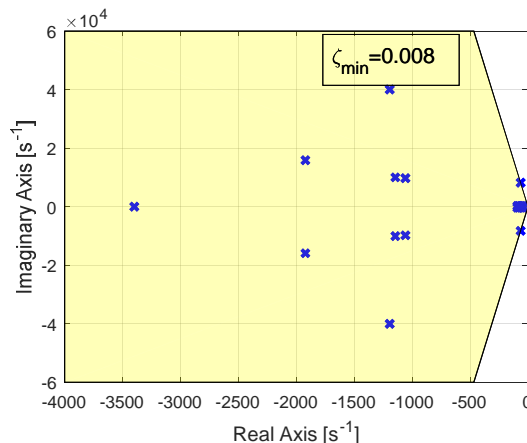
*Figure 4-49 Eigenvalues of Case 2 (Inverter 3 is disconnected). The minimum damping is
highlighted* [76].

Table 4-10 Critical eigenvalues of Case 2 with minimum damping [76].

Eigenvalue	Damping ratio
-6.441e+01 ± 8.254e+03j	0.007804
-1.194e+03 ± 4.003e+04j	0.029824
-1.058e+03 ± 9.785e+03j	0.107577

4.5. SUMMARY

In this chapter, different methods for harmonic analysis of systems containing
numerical and black box models are presented. First the state of the art methods in
analysis of the linear system are presented. Then, a numerical matrix-based method
for harmonic studies in unbalanced networks is proposed. The method is able to deal
with the possible frequency couplings between sequence impedances due to the
nonlinearities and asymmetries. Some concepts in the analysis of LTP systems are
used to prove the proposed method. Moreover, the dependency of the linearized
models to the operating point is discussed and a method is proposed to find the
linearized model at a new operating point without redoing all the time consuming
calculations. Time domain results verify the stability evaluation and the oscillations
of the considered cases.

The problem of having black box models in the eigenvalue based stability analysis is
also discussed and the vector fitting method is used to find the state space models.
Some challenges such as model order selection and the passivity are reported in this
approach. The participation factor analysis can also be used with the black box
models. Even though some state variables are unknown in this analysis, the results
are still valuable to find the problematic component. Further improvements can be
done by informing the manufacturer about the concerned dynamics. The identified
dynamics are verified by the time domain simulations and analytical derivation
reported in Chapter 2. Moreover, a nonlinear case is modelled in the *dq* domain and
the capability of the method in identification of 2×2 MIMO systems is also shown.

Finally, the eigenvalue based stability analysis and the impedance based analysis are
combined for the numerical analysis. This method solves some problems in the
impedance based stability analysis such as possible RHP poles in the minor loop
gain and the variable relative stability indices. The analysis compared to the full
detailed eigenvalue based analysis gives less information; however, it is simpler and
the orders of the resultant matrices are significantly less.

CHAPTER 5. MITIGATING THE HARMONIC AND STABILITY PROBLEMS

"A clever person solves a problem. A wise person avoids it."

Albert Einstein,

5.1. INTRODUCTION

In the previous chapters, challenges in the modelling of power-electronic-based power systems were discussed. In this chapter, the developed tools and methods are used to ensure the stable operation of a system. First, a useful add-on to the stability analysis platform for sensitivity analysis in large systems is presented. This tool enables the user to see how a change in the system can improve or worsen the stability. Then, after a brief review of origins of an instability, a large-scale system is presented and the mitigation methods (both software and hardware solutions) are applied both in the high frequency and the low frequency ranges.

5.2. SENSITIVITY ANALYSIS IN LARGE SYSTEMS

Figure 5-1 shows the time used by each phase of the stability analysis platform for a given case study. It can be seen that the electrical network modeling takes much more time than the other calculations. Therefore, in the sensitivity studies one can use this feature and accelerate the eigenvalue analysis significantly, if the network topology is unchanged and only the parameters are changed. In other words, if the network topology is unchanged then the connection matrices of the electrical system as obtained in (3-26)-(3-50) can be calculated once and be used for all the cases. However, the component connection method must be repeated for each case but it can be seen in Figure 5-1 that it does not take much time.
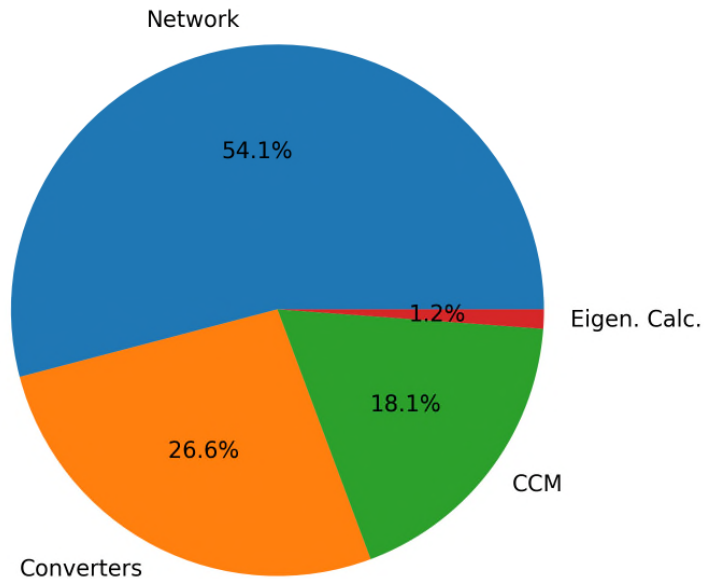
Figure 5-1 Time taken by different parts of the stability platform on a large scale power system.

The sensitivity of eigenvalues of a system to a specific parameter can be categorized into two types:

1) where a change in the parameter does not affect the steady state operating point. It is worth noting that in nonlinear systems, some parameters do not change the operating point. For instance, the controller gains of a power converter have no effect on the operating point since the power converter is represented as a PQ/PV load/generator in the load flow analysis (i.e. it is assumed that all the control objectives are fulfilled at the steady state).

2) where a change in the parameter affects the operating point. Parameters, which can affect the operating point, are the physical components (e.g. resistors, inductors, voltage sources, etc.) in the AC system since capacitors and inductors have no effect on a DC system (e.g. changing the DC link capacitor does not affect the operating point), and set points (e.g. active/reactive power set point, etc.).

Figure 5-2 shows the flowcharts of the two different types of the sensitivity analysis. In both cases the results of the stability analysis platform such as the network topology matrices and state space models of all converters are loaded. In the first type of the sensitivity analysis (operating-point-invariant), only the affected subsystems are recalculated and the entire state space matrices are generated using the CCM. However, in the second type of sensitivity study, the new operating point

must be calculated after changing the parameters. This can be done by running a load flow analysis on the updated model. Since, the operating point is changed; all nonlinear subsystems must be linearized around the new operating point. It is obvious that the second type sensitivity analysis is more time consuming than the first type. It should be noted that the sensitivity analysis of a linear system is placed in the first group.
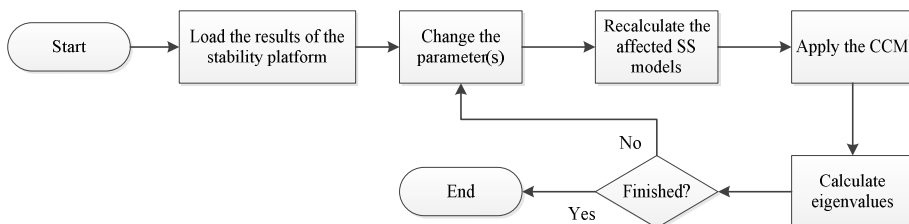
(a)
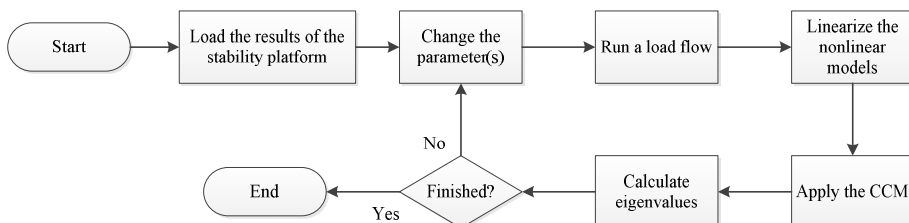
(b)

Figure 5-2 Flowchart of the sensitivity analysis in (a) operating-point-invariant (b) operating-point-variant systems.

It should be noted that the nonlinearity mainly affects the low frequency range, and therefore, if the aim of the sensitivity analysis is to see the effects of a parameter on a high frequency phenomenon, then, the linear sensitivity analysis can be conducted.

5.2.1. SENSITIVITY ANALYSIS IN AN OPERATING-POINT-INVARIANT STUDY

For the linear test case presented in §2.4.4, it was shown that the source of instability was an internal problem. In other words, the grid impedance should not have any effect on the unstable pole. This can easily be verified by evaluating the sensitivity of the eigenvalues of the system to the grid impedance. It is evident in Figure 5-3 that the unstable eigenvalues at $(470 \pm 9225j \pm 100j\pi)$ do not move by changing the grid inductance. However, another pole pair can be moved to the RHP.
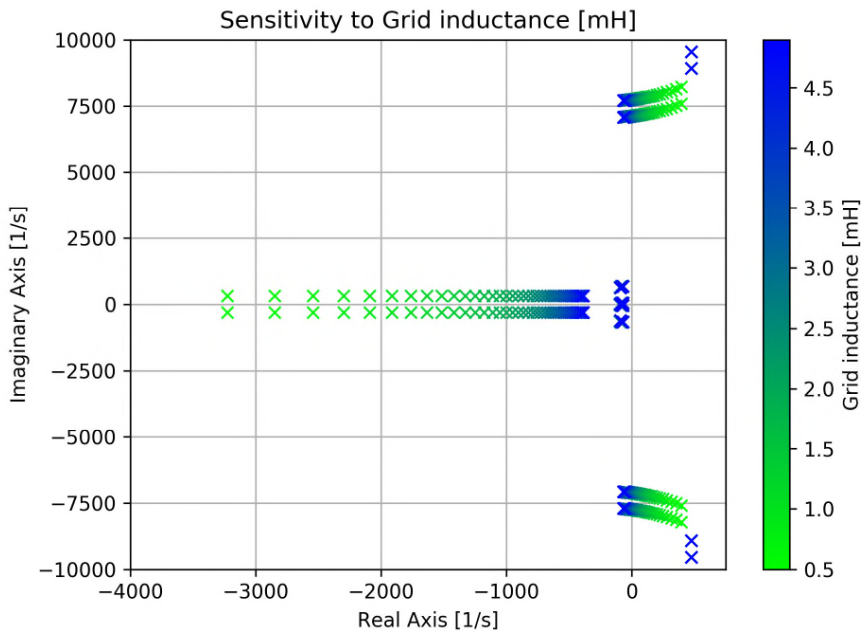
Figure 5-3 Sensitivity of the eigenvalues to the grid inductance in §2.4.4.

To verify the sensitivity analysis tool for the low frequency dynamics, the system in §2.4.3 is considered and the minimum amount of the dc link capacitance is found by the sensitivity analysis. Figure 5-4 shows that for C_{dc} = 7 µF the system is stable but it is not for C_{dc} = 5 µF. Figure 5-5 also shows the time domain simulations for different capacitor values, which is closely correlated with the sensitivity results. From Figure 5-5 it can easily be seen that the system for the dc link capacitor equal to 7 µF is closer to the instability than for 10 µF. This is also reflected in the time-domain simulations with higher steady-state harmonic distortion level, which is a clear indication that the system is very close to lose stability.
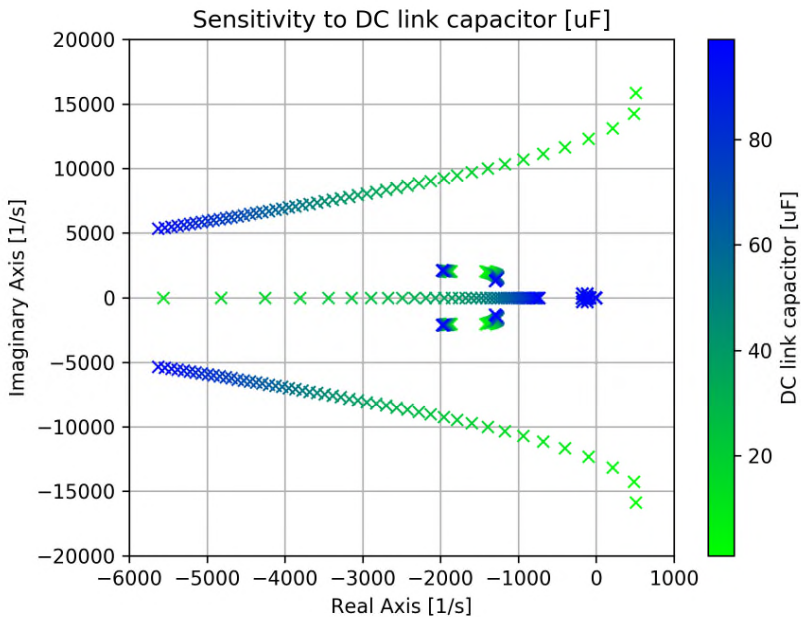
Figure 5-4 Sensitivity of the eigenvalues to the dc link capacitor in §2.4.3.
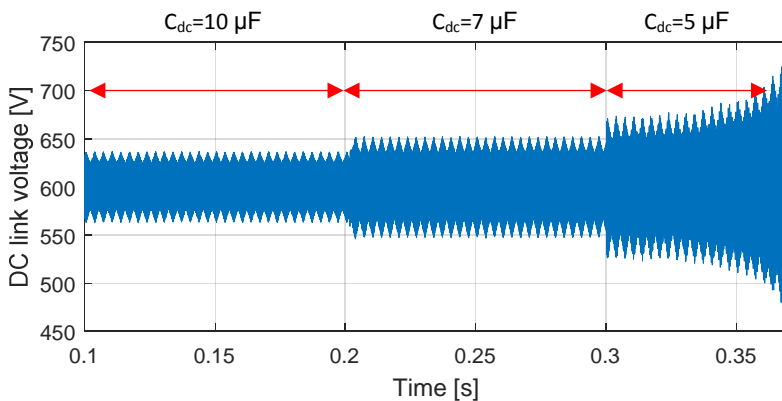
Figure 5-5 DC link voltage for different DC link capacitor values in §2.4.3.

Figure 5-6 also shows the sensitivity analysis for the PLL gains in the system shown in §2.4.3, and time domain simulation results for the stability boundary are shown in Figure 5-7.
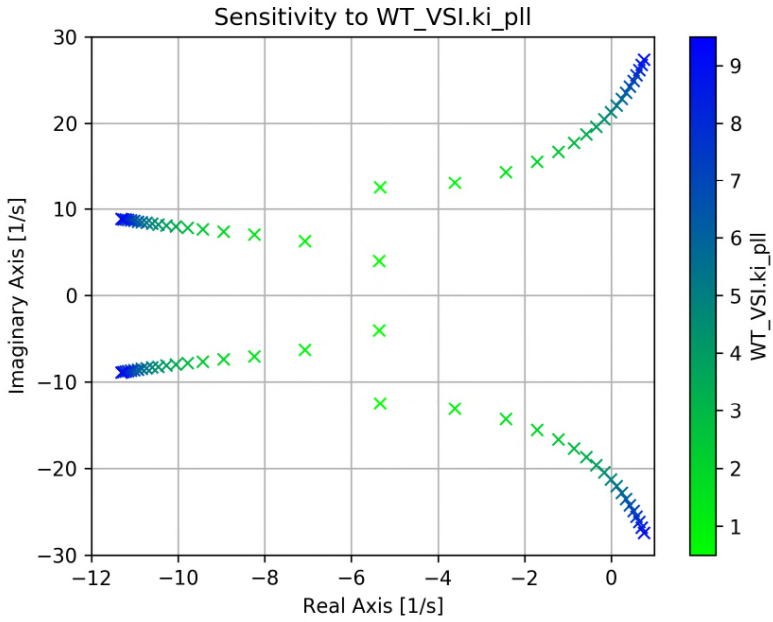
Figure 5-6 Sensitivity of the eigenvalues to the PLL gain in §2.4.3.
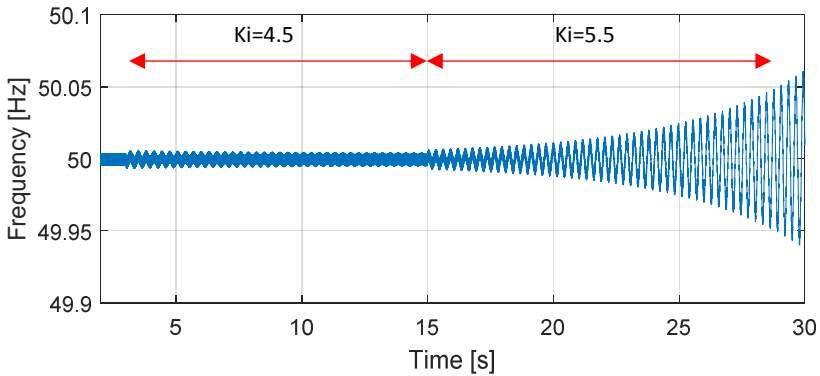
Figure 5-7 Frequency of the system for different PLL gains in §2.4.3.

5.2.2. SENSITIVTY ANALYSIS IN AN OPERATING-POINT-VARIANT STUDY

Figure 5-8 shows the sensitivity of the eigenvalues to the grid inductance for the system shown in §2.4.3. The system is nonlinear and by changing the grid inductance the operating point conditions, such as the PCC voltage (both magnitude

and angle), are changed. It is also worth to look at the participation factor results as listed in Table 5-1 to see which eigenvalue is mainly linked to the grid inductance. It can be seen that the grid inductance has the biggest contribution to a real pole, which is highlighted as black (both in Table 5-1 and Figure 5-8). The sensitivity of the black eigenvalue is also the most to the grid inductance.
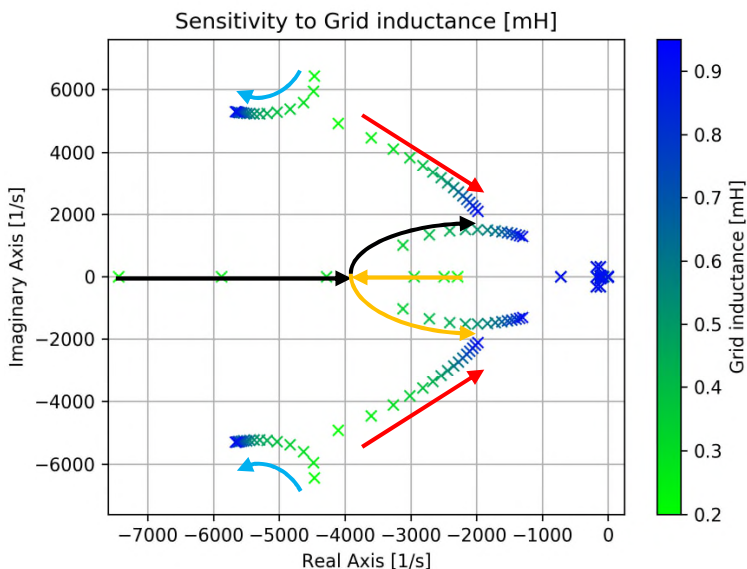
Figure 5-8 Sensitivity of the eigenvalues to the grid inductance in §2.4.3.

Table 5-1 Eigenvalues that are closely linked to the grid inductance.

State name / Eigenvalue	Grid inductance (d-axis)	Grid inductance (q-axis)
-4466.83±-6432.80	0.27	0.02
-4105.58± 4921.81	0.01	0.50
-2292.20	0.28	0.00
-7441.77	0.91	0.01

5.3. MITIGATION MEASURES

In this part, first to simplify the analysis, the frequency range is divided to the low and the high frequency range. Then, the high frequency stability problems in a power converter are briefly reviewed using a simplified high frequency model and some state-of-the-art methods for stabilizing the system are discussed. However, for

the studies of the large scale system, full detailed models are used both in the high frequency and the low frequency studies.

5.3.1. HIGH FREQUENCY PROBLEMS

It is not necessary to consider all the control loops in analyzing the high frequency behavior of power-electronic-based power systems. For instance, the synchronization or dc link control loops are much slower than the current control loop, and therefore, their effects are negligible at the high frequency range. The high frequency range is defined as a part of the current controller bandwidth, where the influence of lower frequency dynamics, e.g. dc link voltage controller and PLL, can be neglected. For instance, Figure 5-9 shows the output admittance of a converter with and without considering the PLL. It can be seen that this assumption does not influence the high frequency behavior.
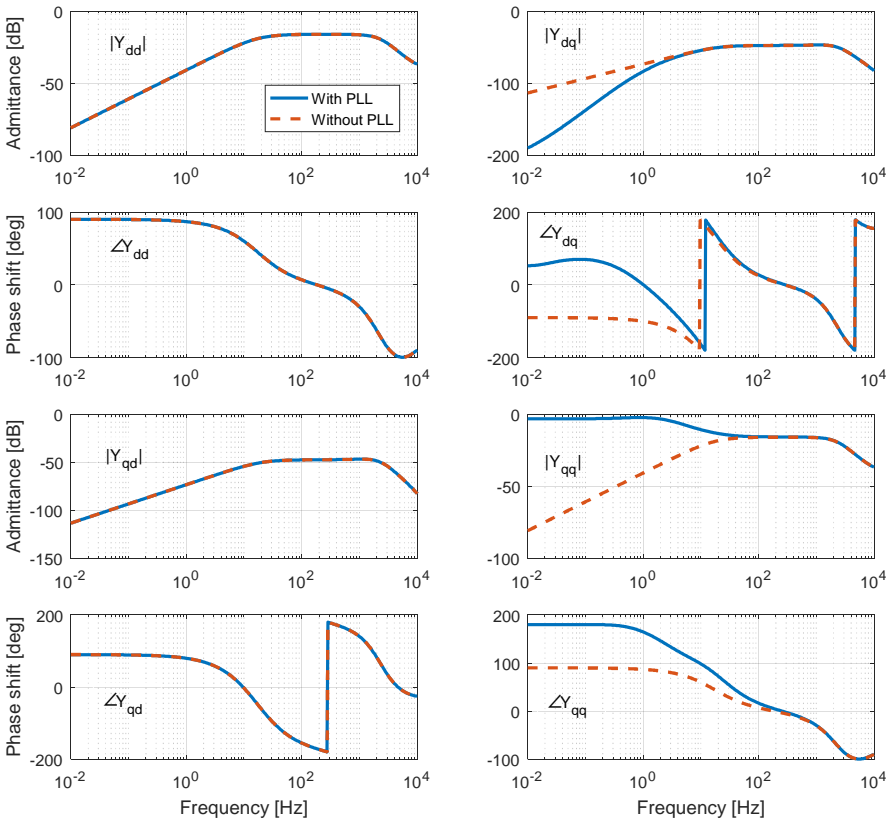
Figure 5-9 Output admittance of a converter with and without the PLL.

If the outer loops are neglected then the analysis can be done only for the current controller as shown in Figure 5-10. If one assumes that the analysis frequency range is much higher than the fundamental frequency then the off-diagonal elements of the *dq* admittance can be eliminated. This can also be concluded from Figure 5-9, where the off-diagonal elements are much smaller than the diagonal elements (note the y-axes are in dB). Eq. (2-14) further proves this, when the frequency is much higher than the fundamental the off-diagonal terms tend to zero since two similar values are subtracted. Figure 5-11 compares the single phase (if only the *dd* component of the *dq* matrix is considered) and *dq* representation of the open loop frequency response of the controller shown in Figure 5-10.
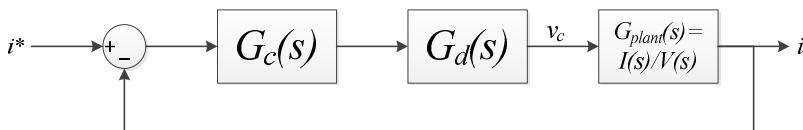
Figure 5-10 High frequency analysis when considering only the current control loop.
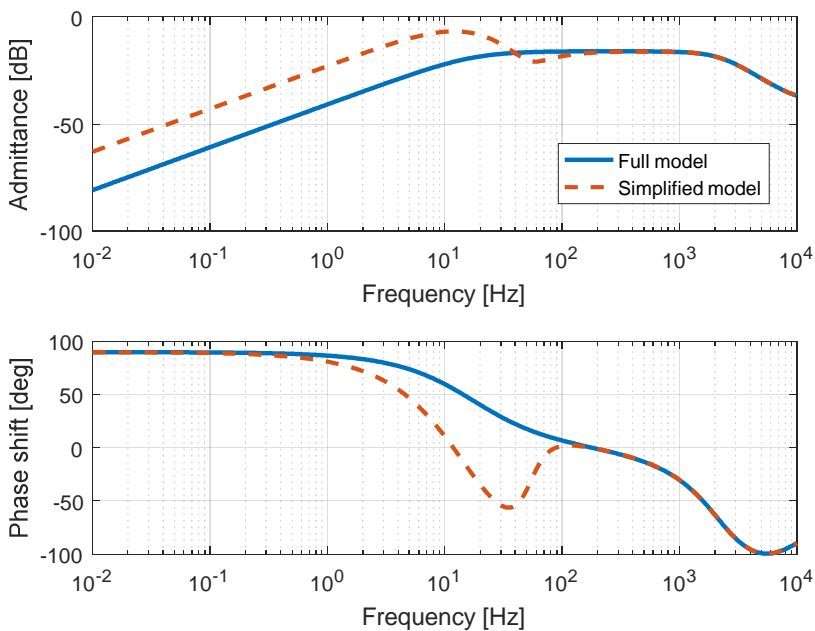
Figure 5-11 dq models (full model) can be simplified to single phase models (simplified model) at higher frequencies.

5.3.1.1 Stability regions of a current controller with an LCL filter

The time delay due to the discrete behavior of digital controllers is the main reason of creating instabilities within the high frequency range, and if it is neglected the system is always stable no matter how gains are selected [80]. The time delay directly appears in the open loop transfer function as shown in Figure 5-10, and it can be considered as 1.5 times the sampling period (one sampling period for the sampling and the computation and 0.5 sampling period for the PWM process). In the Laplace domain it can be represented as (5-1) and by replacing $s=j\omega$ the frequency domain equivalent is obtained as (5-2).

$$G_d(s) = e^{-1.5sT_s} \tag{5-1}$$

$$G_d(j\omega) = e^{-1.5j\omega T_s} = \cos(1.5\omega T_s) - j\sin(1.5\omega T_s) \tag{5-2}$$

It can be seen that at the critical frequency $\omega_c=2\pi/6T_s=\omega_s/6$, the delay has a phase angle of -90°, and if the passive system has also -90° phase angle (e.g. the admittance of an inductor), the phase of the open loop gain will hit -180°, and if the magnitude at this frequency is greater than one, the closed loop system will be unstable (the system will have a negative gain margin) [81].

Figure 5-10 shows a general current control strategy, where the open loop transfer function can be written as

$$G_{ol}(s) = G_c(s)G_d(s)G_{plant}(s) \tag{5-3}$$

where $G_c(s)=k_p+k_i/s$ is the current controller transfer function and $G_{plant}(s)$ is the transfer function from the output current to the modulated voltage v_c at the converter terminals. It is worth noting that at higher frequencies the integral part of the controller can be neglected and the characteristics is mainly defined by the proportional gain k_p [80], [81]. For the grid current control strategy, the plant transfer function, according to Figure 5-12 (the damping resistor R_d will be discussed later), can be written as

$$G_{plant}(s) = \frac{i_g(s)}{v_c(s)} = \frac{1}{L_f L_g C_f s(s^2 + \omega_r^2)} \tag{5-4}$$

where $\omega_r = \sqrt{\frac{L_f+L_g}{L_f L_g C_f}}$ is the resonance frequency. An example of the open loop gain with this plant is shown in Figure 5-13. If the resonance frequency ω_r is less than the critical frequency $\omega_s/6$, the system has a negative gain margin at the phase cross over frequency. This is highlighted as a red area in Figure 5-13.
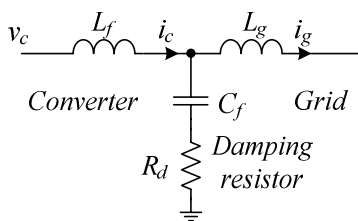
Figure 5-12 Currents and voltages in an LCL filter used in a voltage source converter.
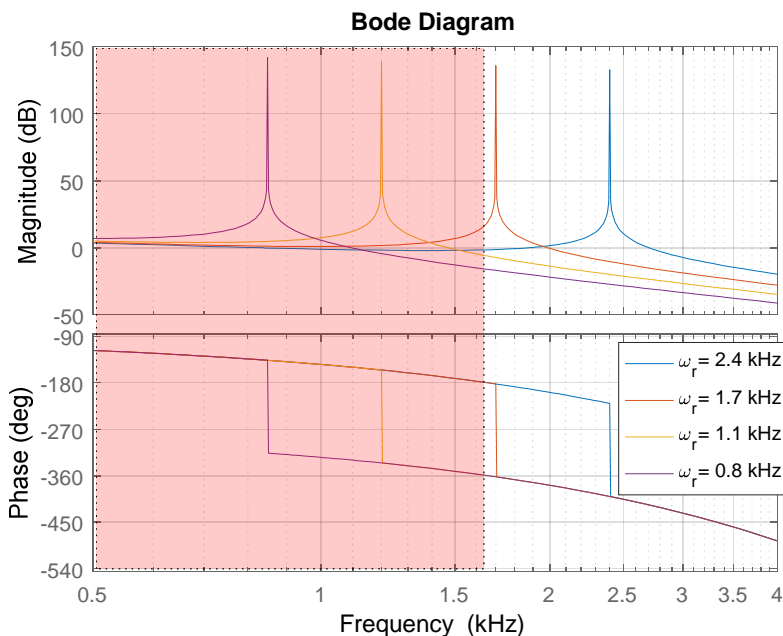
Figure 5-13 Open loop frequency response of a grid current controlled converter, where the negative margin happens when the resonance frequency of the filter is below the critical frequency (1/6 of the sampling frequency).

The plant for the converter current control is

$$G_{plant}(s) = \frac{i_c(s)}{v_c(s)} = \frac{s^2 + \omega_z^2}{L_f s(s^2 + \omega_r^2)} \tag{5-5}$$

where $\omega_r = \sqrt{\frac{L_f + L_g}{L_f L_g C_f}}$ and $\omega_z = \sqrt{\frac{1}{L_g C_f}}$. Figure 5-14 also shows an example of this strategy, where it is evident that the negative gain margin happens for the cases, where the critical frequency ω_c is larger than the filter resonance frequency ω_r.
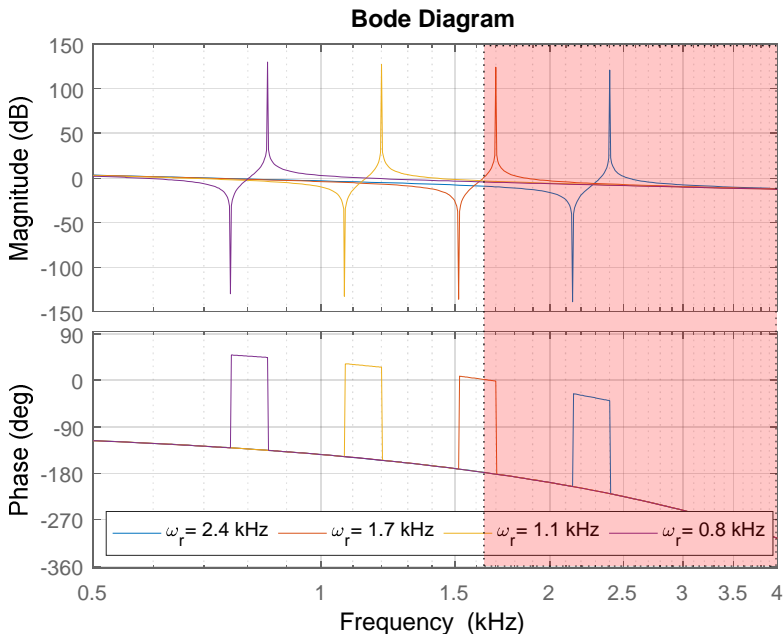
Figure 5-14 Open loop frequency response of a converter current controlled converter, where the negative gain margin happens when the resonance frequency of the filter is above the critical frequency (1/6 of the sampling frequency).

The converter current control strategy is considered in this thesis because no more sensors are needed for the overcurrent protection of the converter, it is more modular, i.e. the customer can use different filters, and it has an inherent damping [82].

5.3.1.2 Damping the high frequency resonances

By changing the proportional gain of the current controller k_p, one can shift the magnitude plot vertically. This is justified by the fact that the open loop transfer function is directly proportional to k_p as shown in (5-3). Hence, a change in the gain is translated to a vertical movement in the gain plot in the logarithmic scale. Similarly, the phase plot is not affected. However, it can be seen in Figure 5-13 and Figure 5-14, if the resonance has no damping the system always has a negative gain margin no matter which gain is chosen. Therefore, the mitigation measure in the unstable cases should be either to change the filter resonance frequency or to increase the damping of the filter actively or passively.

Passive damping

The plant transfer functions for both current control strategies by considering a damping resistor in series with the filter capacitor [83]–[85] are

$$G_{plant}(s) = \frac{i_g(s)}{v_c(s)} = \frac{1}{(L_1 + L_2)s} \left(\frac{\frac{Q_r}{\omega_r}s + 1}{\frac{s^2}{\omega_r^2} + \frac{Q_r}{\omega_r}s + 1} \right) \tag{5-6}$$

$$G_{plant}(s) = \frac{i_c(s)}{v_c(s)} = \frac{1}{(L_1 + L_2)s} \left(\frac{\frac{s^2}{\omega_z^2} + \frac{Q_z}{\omega_z}s + 1}{\frac{s^2}{\omega_r^2} + \frac{Q_r}{\omega_r}s + 1} \right) \tag{5-7}$$

where $Q_r = R_d \sqrt{C\left(L_f + L_g\right)/\left(L_f L_g\right)}$ and $Q_z = R_d \sqrt{1/\left(L_g C\right)}$.

Figure 5-15 shows the impact of a resistor in series with the capacitor on the characteristics of an LCL filter. It can be seen that increasing the damping resistance causes resonance damping, and consequently improves the stability. However, on the other hand, it increases the losses and reduces the filtering performance of the LCL filter for higher frequencies.

(a)
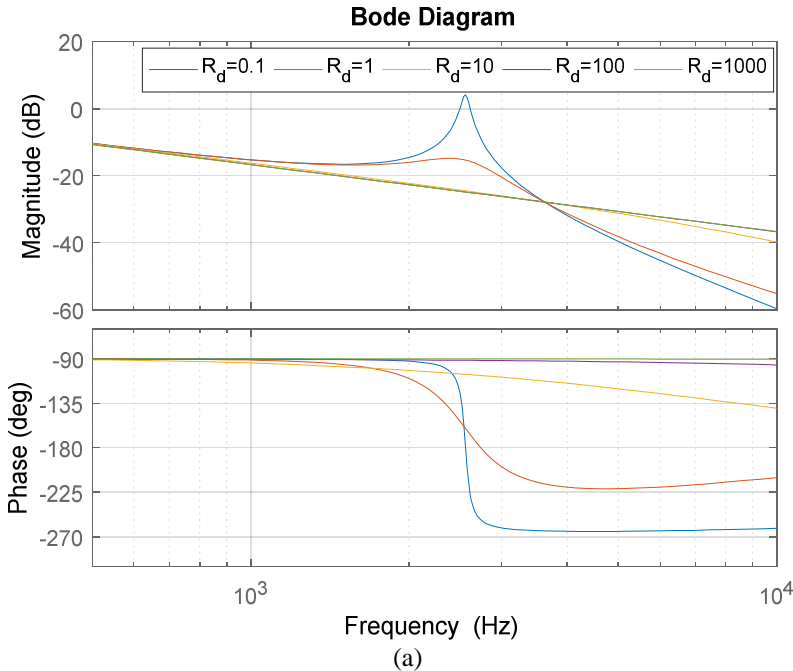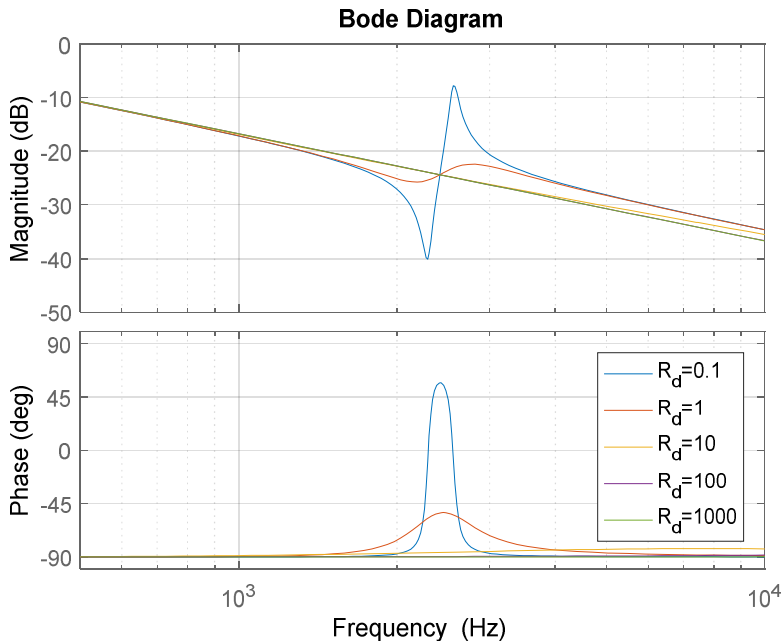
(b)

Figure 5-15 Frequency response of an LCL filter as a function of a damping resistor (a) grid current control strategy (b) converter current control strategy.

Active damping with Virtual impedances

If the damping resistor is instead emulated in the controller it can increase the damping without additional losses [81], [86]. Figure 5-16 shows that by adding a feedback loop inside the controller some impedances can virtually be added to the LCL filter. If the current of the converter side inductance is fed back to the controller (the blue path), it can create a virtual impedance in series with the converter inductance, and if the current of the capacitor is fed back to the controller (the red path), an impedance is emulated in parallel with the capacitance. However, it must be noted that the controller delay also appears in the virtual impedances [86].

(a)

(b)   (c)
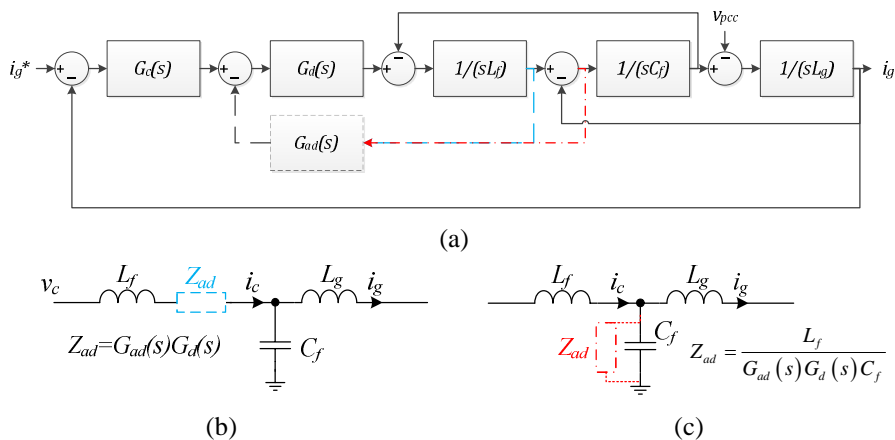
Figure 5-16 Emulating an impedance (a) the controller block diagram (b) a feedback of the converter inductance can emulate a series impedance with the inductance (c) a feedback of the capacitor voltage can emulate a shunt impedance [86] *.*

Figure 5-17 shows the effects of active damping by feeding back the capacitor current to the modulation by a constant gain ($G_{ad}=K$), which creates a virtual resistance.
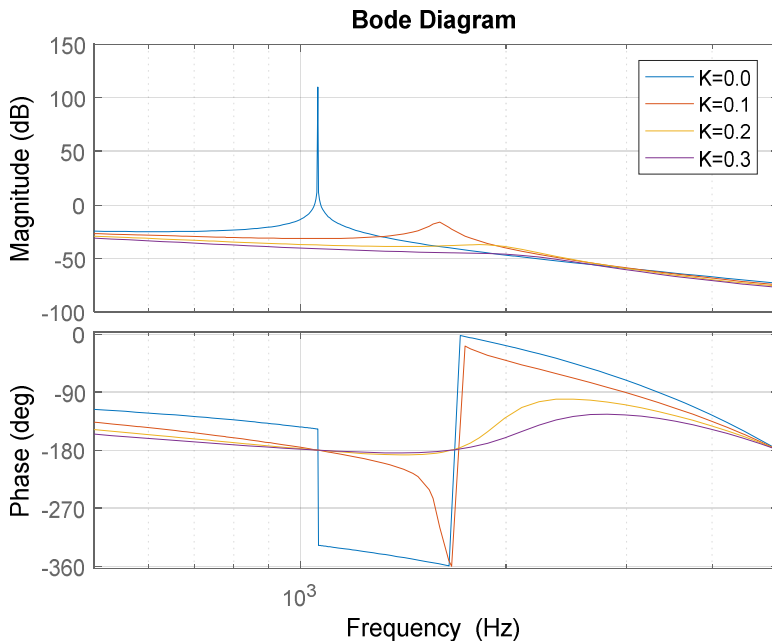
Figure 5-17 Effects of the virtual resistance on the open loop frequency response using capacitor current feedback for different active damping gains.

Active damping with Digital Notch filters

Additional sensors are needed for implementation of virtual impedance-based active damping (e.g. sensing the current of the filter capacitor), which increases the cost of an industrial product and may affect the reliability. Therefore, sensorless solutions are more appealing [87]–[89]. If a notch (band stop) filter is inserted in the open loop transfer function, and is tuned at the exact resonance frequency, it can effectively remove the resonance peak without affecting the controller performance.
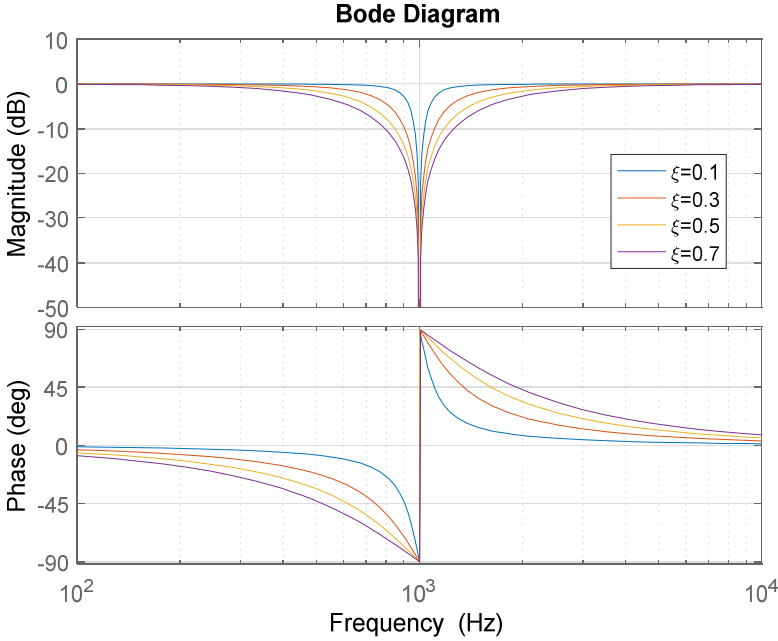
Figure 5-18 Frequency response of a notch filter with different bandwidths.

The transfer function of a second order notch filter is

$$G_{Notch}(s) = \frac{s^2 + \omega_n^2}{s^2 + 2\xi\omega_n s + \omega_n^2} \tag{5-8}$$

where ω_n is the tuned attenuation frequency and ξ defines the width of the stop band as shown in Figure 5-18. Figure 5-19 compares different discretizing techniques and it can be seen that the Tustin method with prewarping as given in (5-9) [88], [90], [91] has the highest accuracy around ω_n.

$$G_{Notch}(z) = \frac{1}{2}\frac{(1 + a_2)z^2 - 2a_1 z + 1 + a_2}{z^2 - a_1 z + a_2} \tag{5-9}$$

where

$$a_1 = 2\frac{k^2 - \omega_n^2}{k^2 + \omega_n^2 + 2k\xi\omega_n}$$

$$a_2 = \frac{k^2 + \omega_n^2 - 2k\xi\omega_n}{k^2 + \omega_n^2 + 2k\xi\omega_n} \qquad (5\text{-}10)$$

$$k = \frac{\omega_n}{\tan(\omega_n T_s/2)}$$

The main issue in designing the notch filter is the resonance frequency of the plant, which is not constant and varies over the time. The drift in the resonance frequency could be due to changes in the grid or the aging of the filter components. In [88], it has been shown that by setting the attenuation frequency different from the resonance frequency, the phase lag or lead of the notch filter can still stabilize the system, resulting in a more robust design.
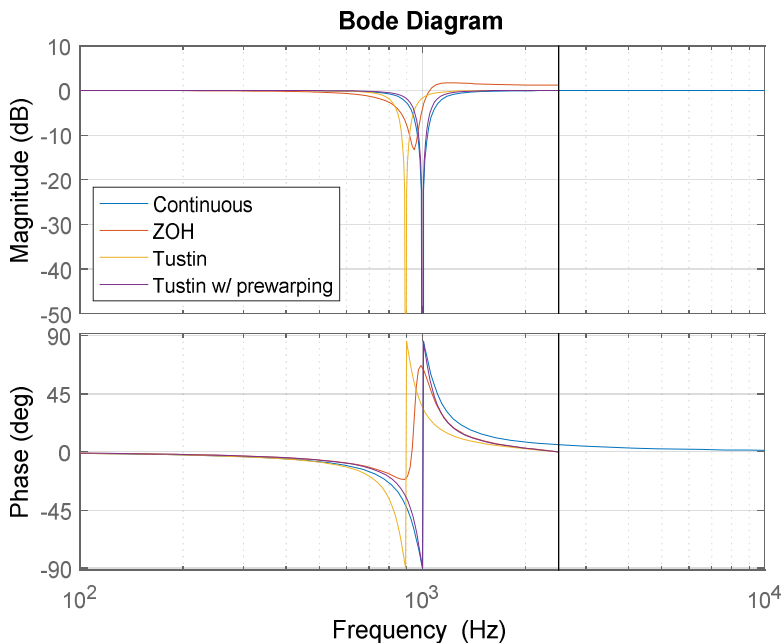
Figure 5-19 Different methods to discretize a notch filter (Ts= 5 kHz).

5.3.1.3 Guidelines for selection of mitigation measures

Some of the high frequency stability problems are not caused by the resonance of the passive filter. For instance, the instability could be due to the wrong settings of the controllers (e.g. high gains). Therefore, it is crucial to identify the root cause of the instability before taking any actions. Figure 5-20 shows an AFE connected to a grid, which is very similar to a converter-side current control with an LCL filter, and the parameters are listed in Table 5-2.
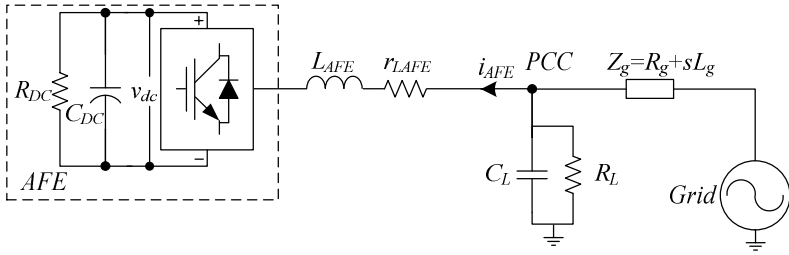
Figure 5-20 Considered system for stability analysis, where an AFE is connected to a grid.

Table 5-2 Parameters of the considered system for stability analysis.

Symbol	Description	Value	
		Case 1	**Case 2**
V_g	Grid voltage (phase voltage rms) [V]	120	
f_g	Grid frequency [Hz]	50	
R_L	Resistance of local passive load [Ω]	10	400
C_L	Capacitance of local passive load [μF]	250	5
L_g	Grid inductance [mH]	0.2	
R_g	Grid resistance [Ω]	0.1	
L_{AFE}	Inductance of the AFE [mH]	0.5	
r_{LAFE}	Self-resistance of L_{AFE} [mΩ]	90	
C_{dcAFE}	Dc link capacitor [μF]	100	
R_{dc}	Dc load resistance [Ω]	13.825	
V^*_{dc}	DC link voltage reference [V]	600	
$i^*_{q\text{-}vsi}$	q channel current reference [A]	0	
k_{piAFE}	Proportional gain of current controller	0.0208	0.0052
k_{iiAFE}	Integrator gain of current controller	1.152	
f_{sw}	Switching/sampling frequency [kHz]	20	
T_{del}	Time delay due to the digital control and PWM	$1.5/f_{sw}$	

Case 1

The system is unstable as shown in Figure 5-21 and Figure 5-22. It is expected that by putting a notch filter tuned at the unstable pole (the resonance frequency), the problem can be mitigated.
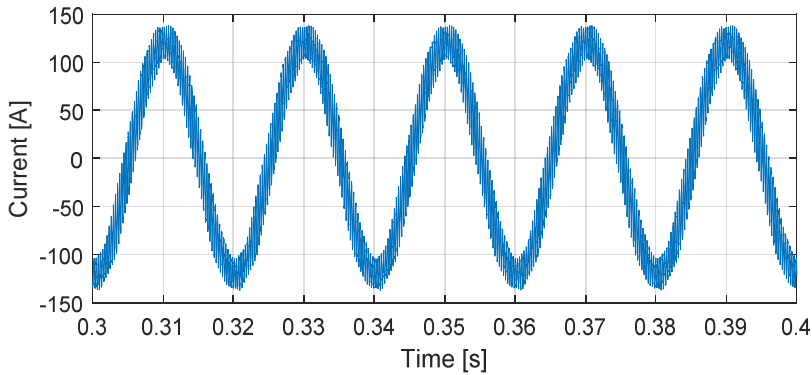
Figure 5-21 Output current of the AFE in Case 1, where high frequency oscillations are clear.
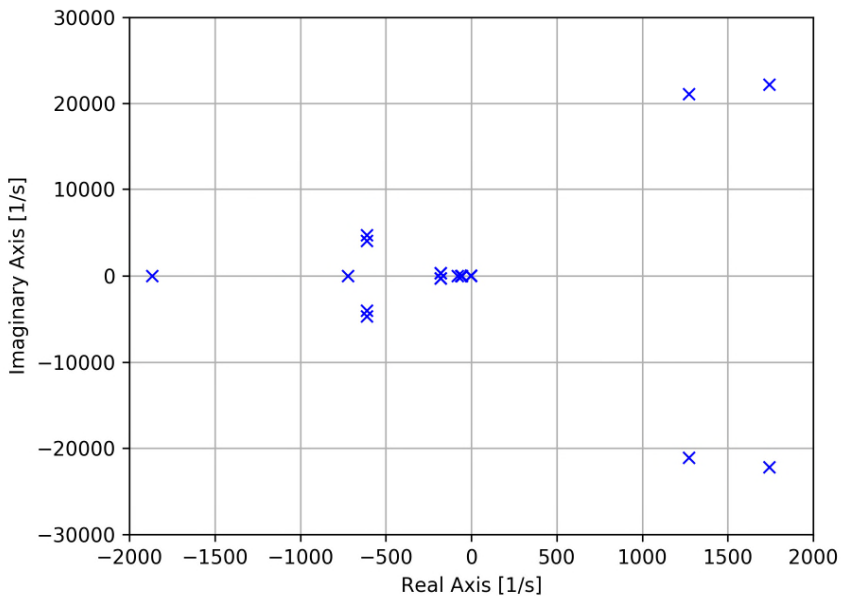
Figure 5-22 Eigenvalues of the system in Case 1, where unstable poles are present.

However, it is evident from Figure 5-23 and Figure 5-24 that this measure does not help the situation and the instability is shifted to another frequency. Figure 5-25 shows the Bode plot of the open loop transfer function, where it is clear that the instability is due to the high proportional gain (note the negative gain margin in both cases) of the converter not a resonance. Figure 5-25 also shows that even though the

notch filter effectively reduces the magnitude at the desired frequency, the phase cross over frequency is shifted to a lower frequency due to phase introduced by the notch filter, which again has a negative gain margin. This means that the active damping measures should be used when the problem is due to a resonance in the passive system, otherwise it cannot help the situation.
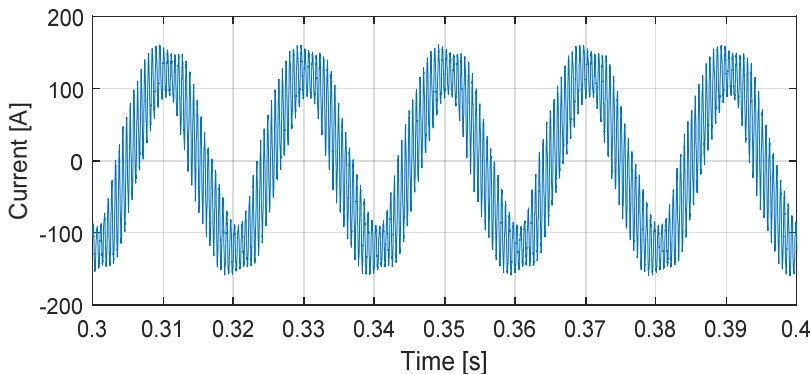
Figure 5-23 Output current of the AFE in Case 1 after applying a notch filter.
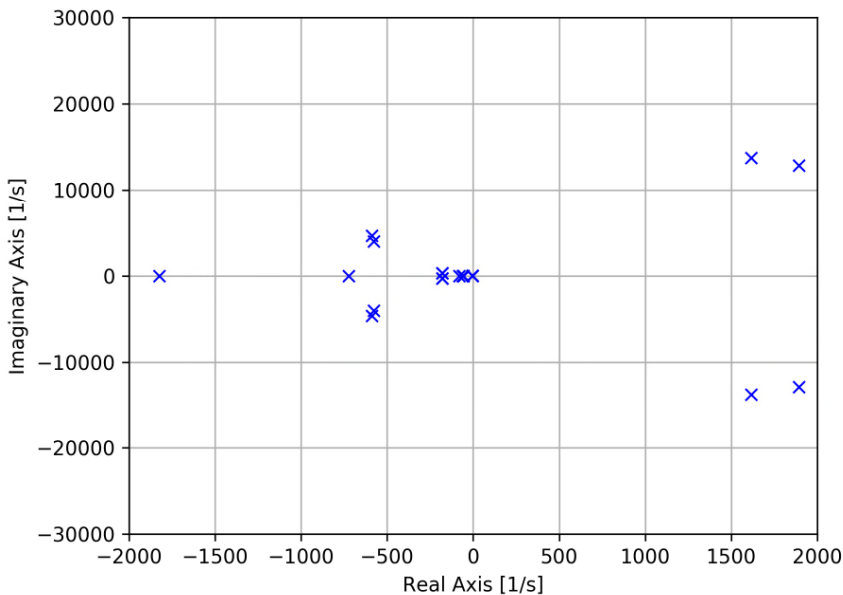
Figure 5-24 Eigenvalues of the system in Case 1 after applying a notch filter.
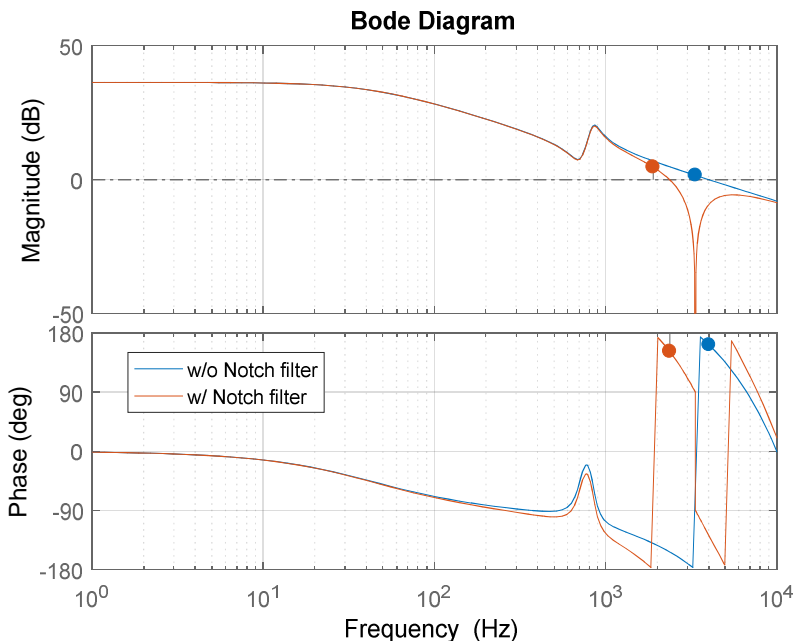
Figure 5-25 Bode plot of the open loop gain of the AFE in Case 1 with and without a notch filter.

Case 2

Figure 5-26 shows that by changing the filter parameters, the resonance frequency of the filter is increased and is placed at the unstable region (marked in red in Figure 5-14). A notch filter can significantly damp the resonance and stabilize the system, which is also verified by time domain simulations in Figure 5-27.

Table 5-3 shows the contribution of the filter to the instability in both cases by means of participation factor analysis. It can be seen that for the first case the capacitor has no influence on the instability, and therefore, to solve the problem either the gain or the switching frequency (this affects the delay) of the current controller should be changed. Changing the gain shifts the magnitude plot of Bode diagram vertically without changing the phase, and therefore, the gain can be changed to a negative value at the phase cross-over frequency. For the second case, the contribution of the filter is significant, which means that to solve the instability either a damping method should be used or the filter must be redesigned.
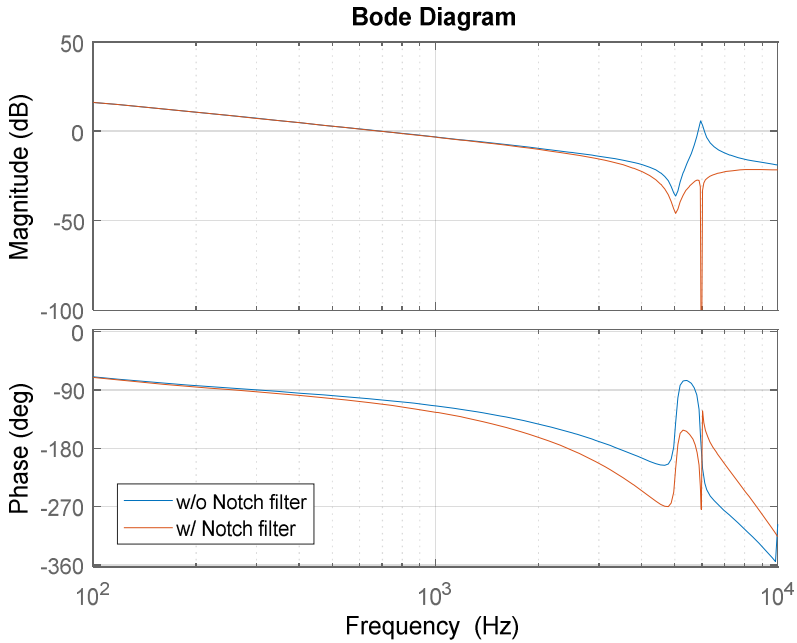
Figure 5-26 Bode plot of the open loop gain of the AFE in Case 2 with and without a notch filter. A notch filter can significantly attenuate the resonance.
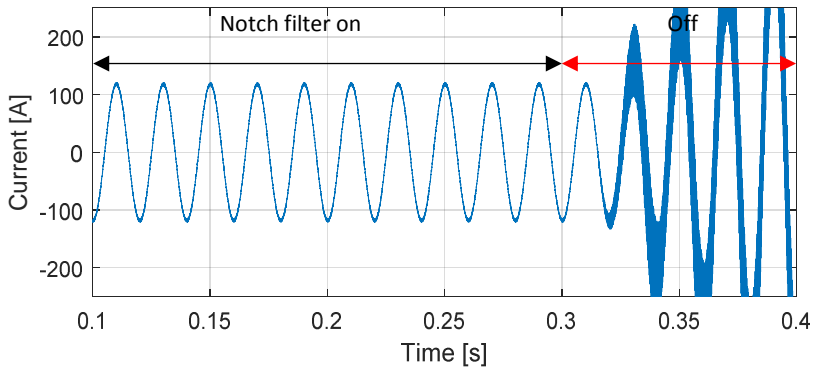
Figure 5-27 Output current of the AFE in Case 2 with and without a notch filter.

Table 5-3 Contribution of the LCL filter capacitor to the instabilities in Case 1 and Case 2.

	Eigenvalue	Contribution of C_f
First case	1743±22224j	0.00
	1273±21120j	0.00
Second case	394±37267j	0.46
	395±37895j	0.46

The studies performed in this part show the effectiveness of the participation factor analysis in identifying the source of the instability and consequently choosing the most efficient counter measure to mitigate the problem.

5.3.1.4 Large scale studies with PF analysis

In multi-converter systems, it is difficult to evaluate the system by interpreting the Bode plot, because the system is now a compicated MIMO system. Therefore, in this section only the eigenvalue based analysis is used.

Figure 5-28 shows the test system given in Appendix B, which has 35 6-MW WTs. In this chapter to investigate the effects of having variable number of WTs in operation the WTs are connected and disconnected based on a numerical order as highlighted in Figure 5-28.
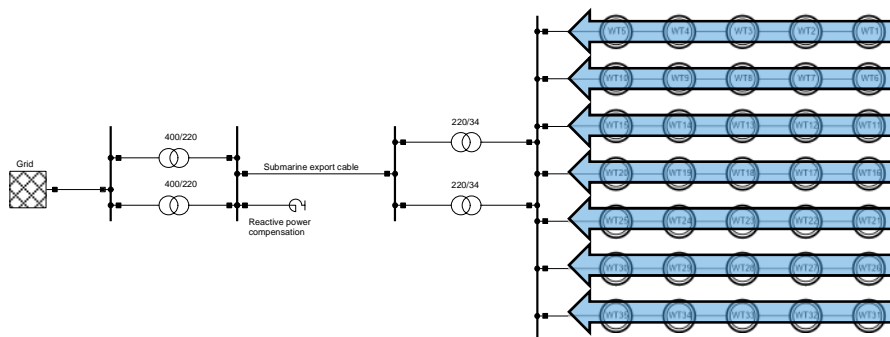
Figure 5-28 Considered offshore Wind power plant with 35 6-MW WTs (the arrows show how the number of WTs in operation is changed).

Figure 5-29 shows the eigenvalues of the system obtained by the stability analysis platform discussed in Chapter 3. It should be noted at this stage no additional damping (active or passive) is considered in the system and the system suffers from instability. The diagonal red lines are indicators of the desired 10% damping ratio in the system [92]. Three groups of eigenvalues are highlighted in Figure 5-29, where the red and the yellow group are sensitive to the number of WTs. However, the black group does not change a lot. Participation factor analysis as shown in Table

5-4 reveals that the black group is an internal instability between the passive filter
and the current controller delay, and the array cables are important in the red and the
orange groups. It can also be seen that the worst case is for all WTs in operation.
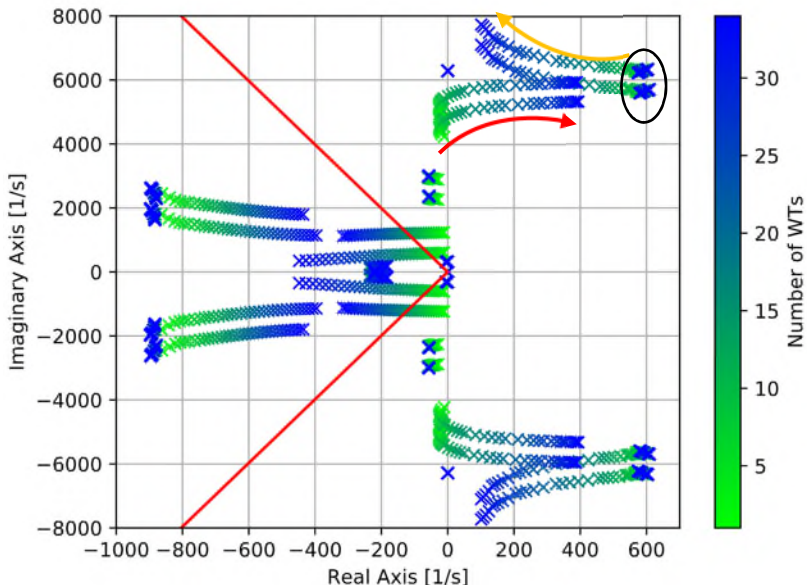
*Figure 5-29 How the dynamics of the system is affected by changing the number of WTs in
operation.*

Table 5-4 Contributors to the highlighted unstable poles in Figure 5-29.

Component name	Contribution on [%]		
	Black group	Yellow group	Red group
Export cable	0	0.5	0.3
400/220 kV Tr. (Onshore)	0	0	0
220/34 kV Tr. (Offshore)	0	12	3.7
34/1 kV Tr. (WT)	4.3	30.6	1.2
Array cables	0	38.4	7.3
WT Filter cap.	16.8	8.5	7.5
WT's reactor	35	4.6	34
PLL	0	0	0
Controller delay	43.1	5.3	45
Current controller	0.8	0.1	1

The filter is important in all unstable poles, therefore as the first action; a damping
resistor is placed in series with the filter capacitors of all WTs (see Figure 5-12).

Figure 5-30 shows the dynamics of the system as a function of the damping resistor value, when all WTs are connected. It can be seen that it improves the stability; however, there are still some unstable poles.
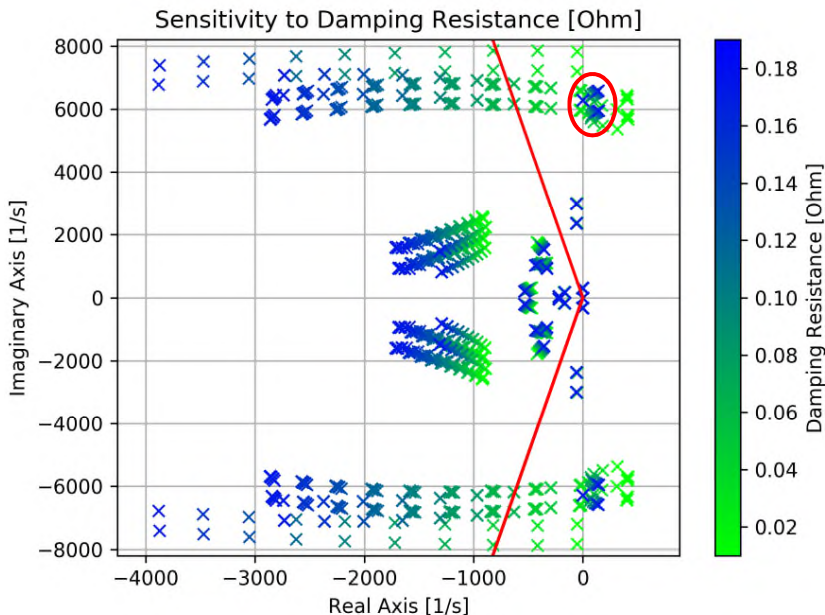
Figure 5-30 How the dynamics of the system is affected by changing the damping resistor in the LCL filter (All WTs are active).

The damping resistors increase the losses in the system (e.g. R_d=0.1 Ω dissipates 100 kW in a 6-MW WT), and there are still instabilities in the system. Therefore, notch filters are investigated in this part to see if the instability can be mitigated and keep the losses low.

A notch filter has two degrees of freedom, one is the notch frequency and another one is the bandwidth. Therefore, a two-variable optimization is needed to find the optimal settings. However, for the sake of simplicity, first, the optimum notch frequency is found by assuming a fixed bandwidth (ξ=0.5). Afterwards, the bandwidth is optimized by using the optimum notch frequency found in the previous step.

Figure 5-31(a) shows how the eigenvalues of the system are moved when the notch frequency is changed from 400 Hz to 650 Hz. A rough compromise to have more eigenvalues with enough damping is to set the notch frequency at 500 Hz, which is highlighted as red crosses in Figure 5-31 (a). Figure 5-31(b) shows that ξ=0.4 is a

relatively good choice as the bandwidth. However, it is evident that there are some unstable poles that cannot be stabilized by using active or passive damping.
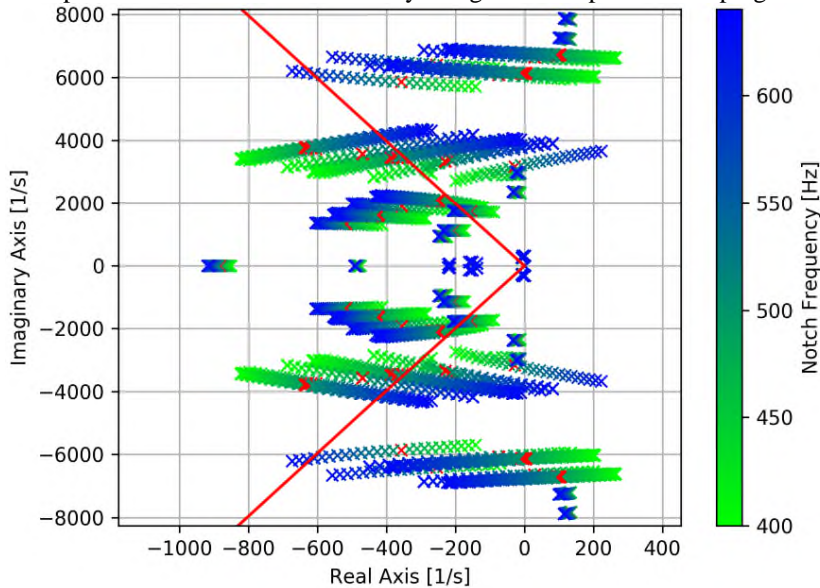
(a)
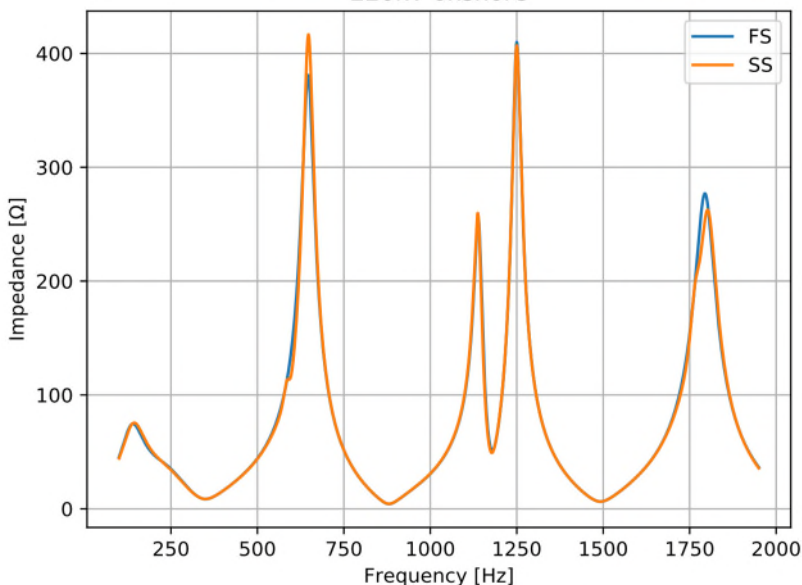
(b)

Figure 5-31 How the dynamics of the system is affected by changing (a) the notch frequency ($\xi=0.5$) (b) the bandwidth ($f_{notch}=500$ Hz) - All WTs are active.

Table 5-5 shows the contribution of different elements to the unstable poles where it is clear why the damping cannot improve the situation. The problem is actually due to a strong resonance between the array cables and offshore and WT transformers, and the non-passivity of the delay destabilizes this resonance. An impedance frequency scan at the offshore platform, as shown in Figure 5-32, identifies a resonance around the frequency of the instability.

Table 5-5 Contributors to the highlighted unstable poles in Figure 5-30.

Component name	Contribution on (95±7850j & 85±7250j) [%]
Export cable	0.4
400/220 kV Tr. (Onshore)	0
220/34 kV Tr. (Offshore)	10.1
34/1 kV Tr. (WT)	27.7
Array cables	33.1
Filter cap.	10
WT's reactor	7.4
PLL	0
Controller delay	9.4
Current controller	0.1
Notch filter	1.8
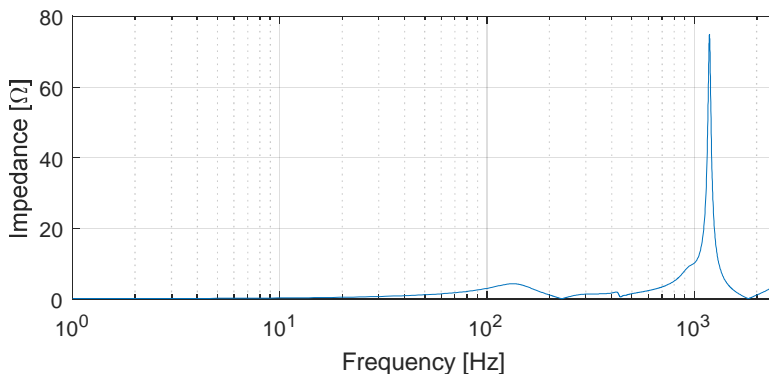
Figure 5-32 Driving point impedance measured from the MV-side of the offshore platform.

One way to smoothen this sharp resonance is to use a passive power filter in the MV-side of the offshore platform. In this part a C-Type filter as shown in Figure 5-33 is used. L and C_2 are designed in a way to resonate at the fundamental frequency; therefore, the filter is just a capacitor C_1 injecting some reactive power to the system without any losses. R_s mainly models the losses in the capacitors and inductor, and R_p defines the damping of the filter [93]. Figure 5-34 shows the driving point impedance at the offshore platform with different damping resistors of the C-Type filter, which is tuned at 1200 Hz to attenuate the resonance shown in

Figure 5-32 and its parameters are listed in Table 5-6. It can be seen that the filter removes the resonance; however, it creates two other smoother resonances. R_p=10 Ω is used for the rest of simulations, since the new resonance is below the critical frequency of the controller ($\omega_s/6$).
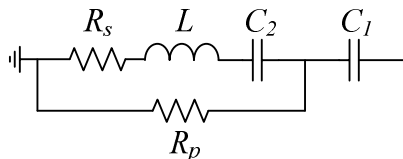
Figure 5-33 C-Type filter placed at the offshore 34 kV busbar.

Table 5-6 Parameters of the installed C-Type filter.

Parameter	Value
Rs [Ω]	0.016
L [mH]	0.43
C_1 [mF]	41.3
C_2[μF]	23.75
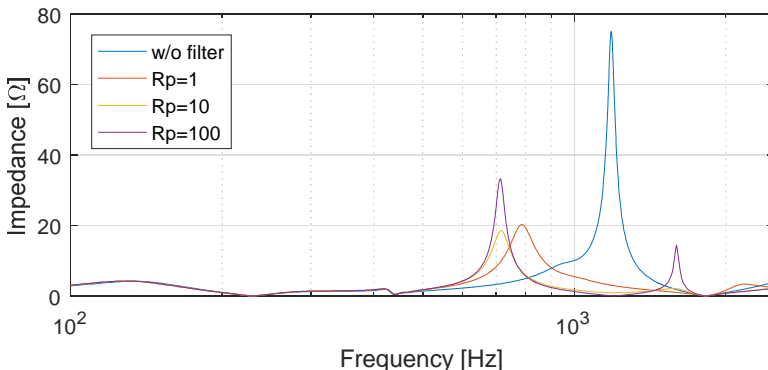
Figure 5-34 Driving point impedance of the MV side of the offshore platform after installing a C-Type filter.

To see how the passive filter improves the stability of the system, the passive and active damping solutions are repeated. Figure 5-35 shows that the passive damping by increasing the damping resistor in the WT filter improves the stability. Figure 5-36 also shows that a notch filter (active damping) tuned at 400 Hz with ξ=0.5 stabilizes the system (note that in both cases a C-Type filter at the MV terminal with the specified parameters is in place).
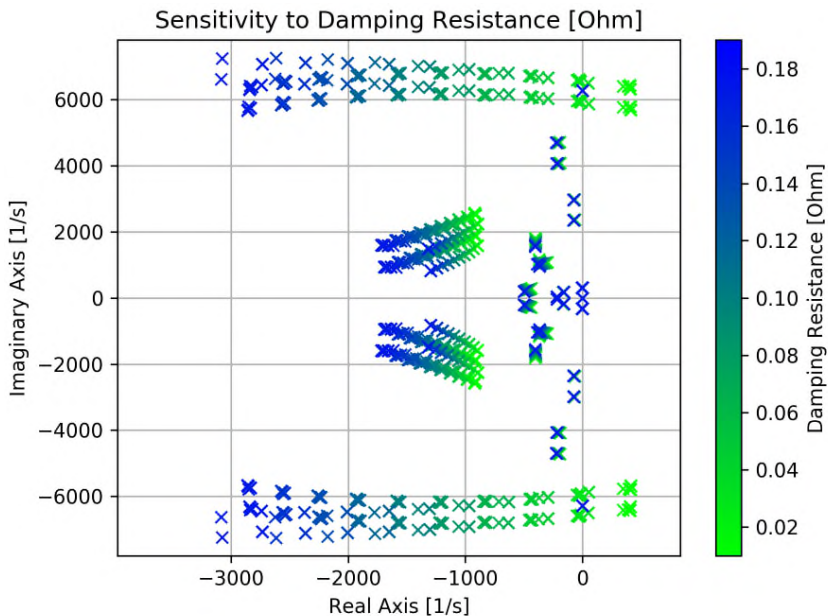
Figure 5-35 How the dynamics of the system are affected by changing the damping resistor in the WT filter (All WTs are active and a C-Type filter is used).

(a)

(b)
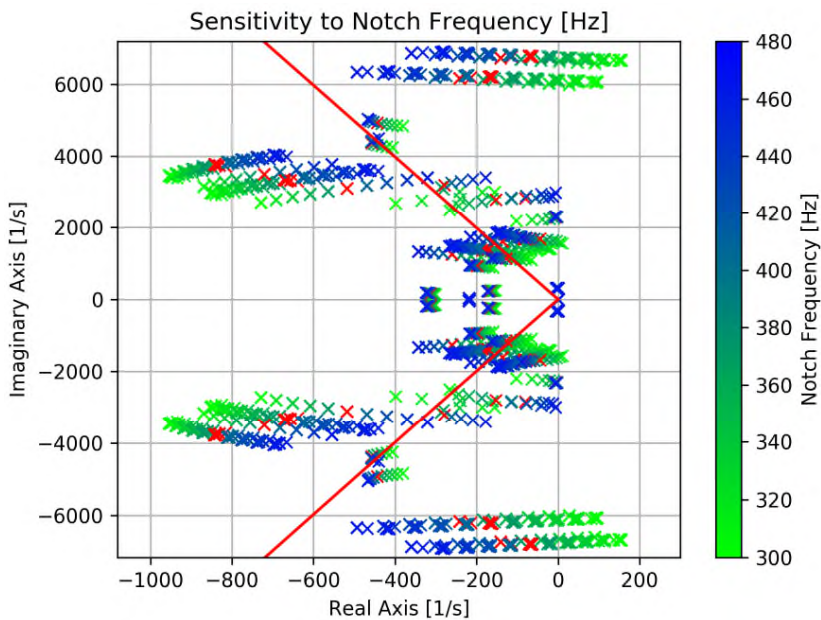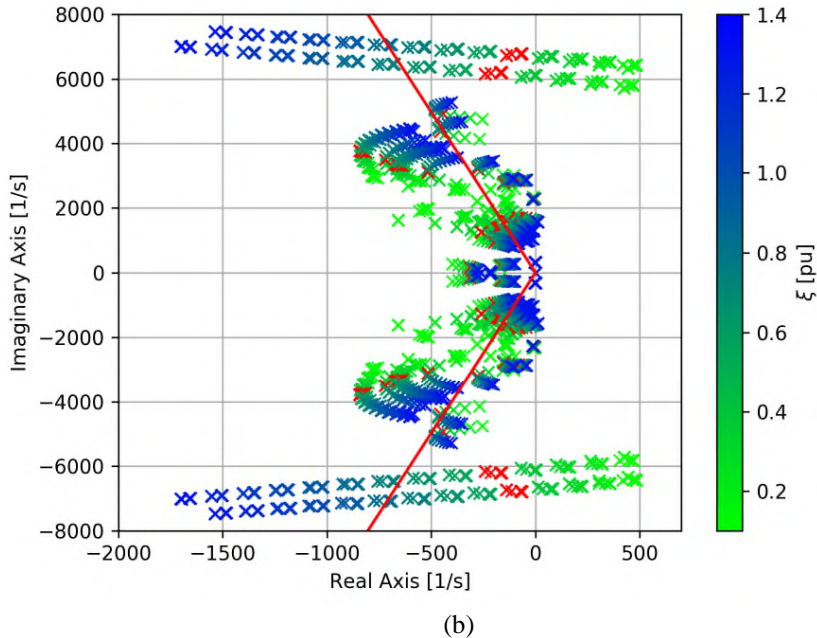
*Figure 5-36 How the dynamics of the system are affected by changing (a) the notch frequency
(ξ=0.5) (b) the bandwidth (f_{notch}=400 Hz) -All WTs are active and a C-Type filter is used.*

It can be concluded from the simulation results that

1) The passive damping generally improves the stability of the system, but it is not an attractive solution due to the losses.
2) The active damping can mitigate the high frequency problems but it may create other problems at the same time.
3) Sometimes the most effective way is to optimize the electrical infrastructure (i.e. installing a hardware filter).

5.3.2. LOW FREQUENCY PROBLEMS

In [94], [95], it has been shown that the PLL may cause instability if a converter is connected to a weak grid. In this part, the sensitivity analysis tool is utilized to find how the PLL may interact with the transmission system in an OWPP connected via a long cable.

Figure 5-37 shows that the worst case in the low frequency range is also when all WTs are connected. There is only one pole pair that indicates this is a global

problem and not an internal problem. Otherwise, there would have been more poles. Therefore, the analysis is conducted for all WTs in operation.

In Figure 5-38, the cable length is fixed at 100 km and the PLL bandwidth of all WTs is changed from 10 Hz to 110 Hz, which shows an unstable system for PLLs with a bandwidth higher than 50 Hz. It should be noted that the results are in the *dq* domain; therefore, an oscillatory mode is shifted by ±50 Hz when transformed into the *abc* domain.

The effects of the length of the export cable are shown in Figure 5-39, where for cables longer than 100 km, the system is unstable (the PLL bandwidth is fixed at 50 Hz).
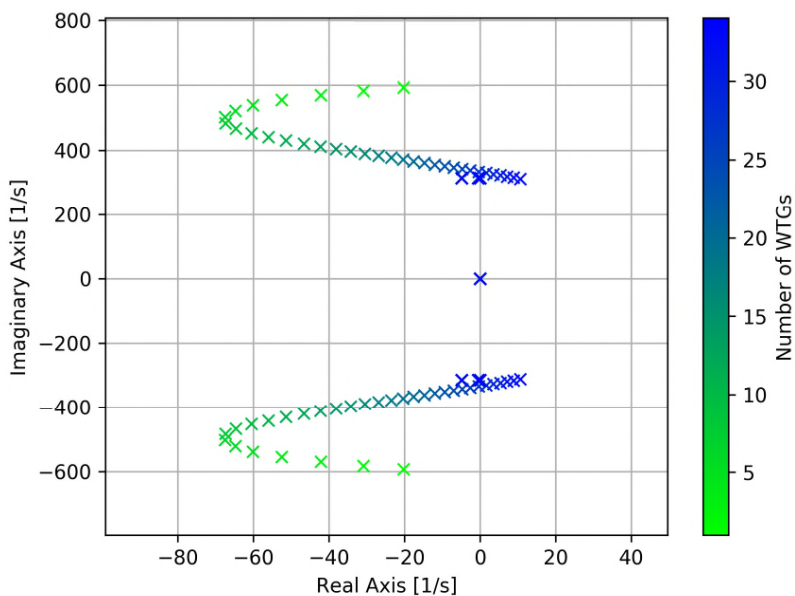
Figure 5-37 Low frequency eigenvalues of the system for different number of WTs in operation (PLL bandwidth=50 Hz).
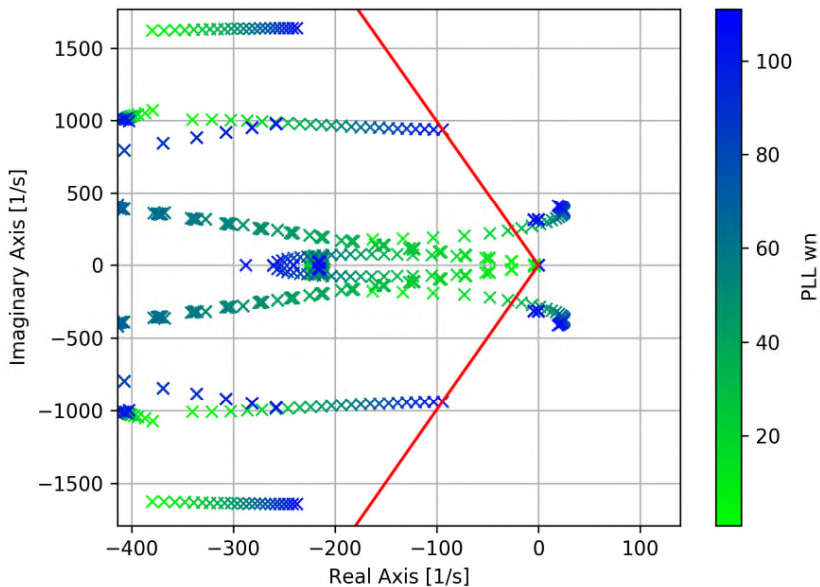
Figure 5-38 Eigenvalues of the system as a function of PLL bandwidth.
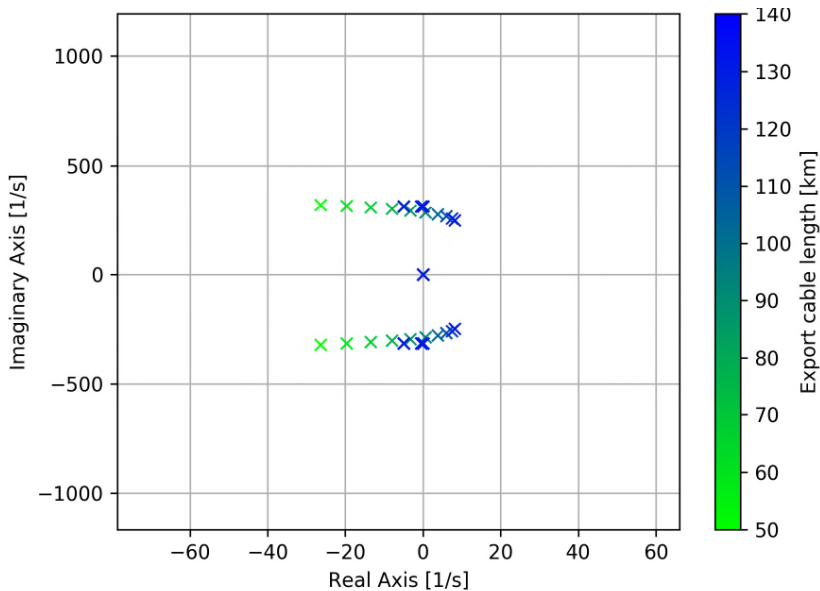
Figure 5-39 Eigenvalues of the system as a function of the cable length (PLL bandwidth=40 Hz).

The extreme case of Figure 5-39 is used as a case study to investigate the stabilizing measures. The first step as the high frequency studies is to find the contributors to

this instability by the participation factor analysis as shown in Table 5-7. The export system and the onshore transformers interact with the PLL, the current controller and the WT's coupling reactor. Therefore, it is concluded that a change in the PLL or the WT's reactor has a significant influence on the instability.

Table 5-7 Contributors to the highlighted unstable poles in Figure 5-39 when the cable length is 140 km.

Component name	Contribution on (15±265j) [%]
Export cable	21.5
400/220 kV Tr. (Onshore)	11.8
220/34 kV Tr. (Offshore)	3
34/1 kV Tr. (WT)	2.2
Array cables	1.6
Filter cap.	3.3
WT's reactor	24.7
PLL	18.1
Controller delay	1.9
Current controller	10.9

Figure 5-40 (a) shows that if a PLL with a bandwidth lower than 20 Hz is used, then enough damping (10%) in the system is guaranteed. Figure 5-40 (b) also verifies the results in Table 5-7, where it was concluded that WT's reactors are important contributors to this instability. The system can be stabilized by increasing the reactor size. This increases the voltage drop over the reactor and therefore, the power converter has to provide more voltage, which could lead to larger dc link voltages. A larger reactor is also more expensive and takes more space, which is problem in an offshore WT; therefore, it may be interesting to investigate this proposal using virtual impedances in series with the reactor as shown in Figure 5-16 (b) as a future work.
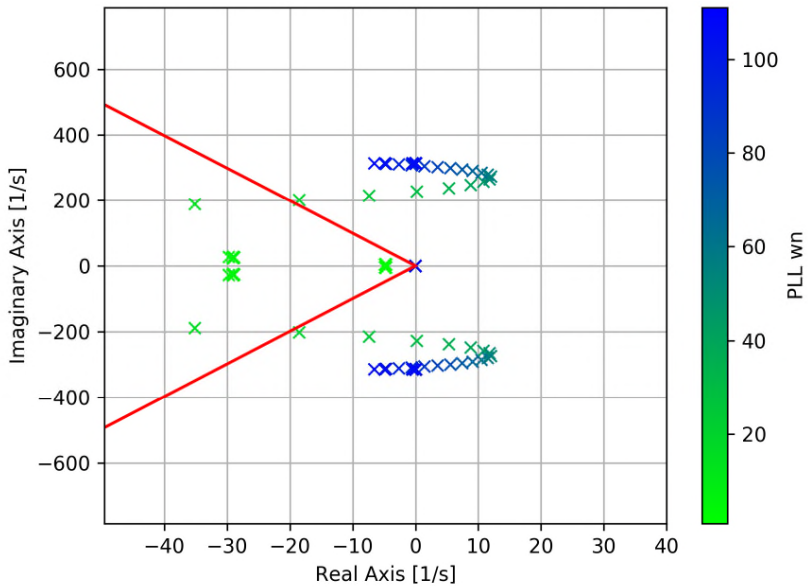
(a)
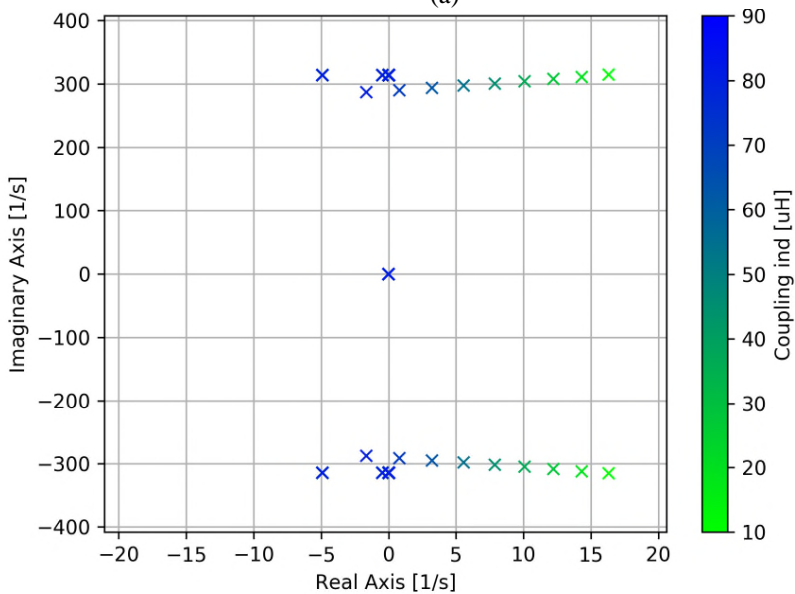
(b)

Figure 5-40 Mitigating the low frequency instability by (a) reducing the PLL bandwidth (b) increasing the reactor size.

5.4. SUMMARY

In this chapter it was shown that it is necessary to identify the root cause of a stability problem before taking any actions as there are many contributors to instabilities. Therefore, the first step is to look into the results from participation factor analysis, which identifies the largest contributors to a certain dynamic behavior. Afterwards, a sensitivity analysis tool can be used to see how a parameter affects the dynamics in a wide range of changes. It is also possible to find the optimum values for the parameters using the sensitivity analysis.

The resonances in the system can cause instability or poorly damped dynamics. This situation can be improved by using software solutions like active damping techniques in the controller or hardware solutions like power filters and damping resistors.

It was also shown that the PLL and the long cable can interact and create instability. According to the results of the participation factor analysis, this problem can be mitigated by reducing the bandwidth of the PLL or by increasing the reactor size.

CHAPTER 6. SUMMARY

"If you want a happy ending that depends, of course, on where you stop your story."

Orson Welles

6.1. SUMMARY

In this work, the correct modelling in the low frequency range is identified as one of the main challenges in the harmonic analysis of an OWPP connected via long cables. The developed tools and models in this thesis enable the user not only to perform the power quality and stability studies, but also to find the root cause of a problem. Based on the origin of a problem, the most effective action can be taken.

It should also be noted that even though this thesis mainly discusses the stability analysis in an OWPP, the models can also be used for the power quality studies. It should be noted that more detailed models are needed to investigate the power quality problem in the low frequency range.

In Chapter 1, the background, motivation and the objectives of this study are discussed.

In Chapter 2, different modelling methods are used to evaluate the stability of a power electronic based power system. As discussed in Chapter 1, the main concern in this project is the possible interaction of the long cables and active elements in the low frequency range due to the low frequency resonances in the system. It is shown that in the low frequency range, the PLL creates some frequency couplings, which are very important in power quality studies (harmonic emissions) and also in the stability studies. Furthermore, the *dq* domain models are also presented, which are advantageous to sequence domain models due to the fact no frequency coupling is present in the *dq* domain (as long as the system is balanced). Eigenvalue based stability analysis is a useful tool to analyze the system. However, the method is more complex. The methods are used to evaluate the stability of a few test cases, which are used in different chapters.

In Chapter 3, a systematic approach is proposed to obtain the state space model of a large WPP. A tool is developed in a power system software to extract the parameters of the system and also the steady state operating points which are necessary to linearize the system. The tool is developed in a modular way; therefore, additional elements can easily be added. The tool is also validated by different methods.

In Chapter 4, a practical challenge in analysis of real WPPs, which is the lack of analytical models for components, is discussed. The numerical data can easily be

used in the impedance based stability analysis for linear system. However, for nonlinear and coupled systems, matrix form should be used. A matrix-based method is used for evaluating the stability and power quality. The numerical data cannot be used in the eigenvalue based stability analysis, since it needs the analytical models. An identification method is used to obtain an approximate state space model of converters, cables and transformers. Furthermore, the impedance based stability analysis is improved by the vector fitting and the eigenvalue based stability analysis.

In Chapter 5, the instability in power electronic based power systems is reviewed from a different perspective and the state of the art methods for mitigating the stability are discussed. A relatively large wind power plant is considered and high frequency and low frequency instabilities are shown and discussed. The effects of passive and active damping, passive power filters, and PLL bandwidth are studied in this chapter. It is concluded that the participation factor analysis is a strong method to identify the root cause of the problem and to find a solution.

6.2. MAIN CONTRIBUTIONS

The contributions of this study can be summarized as follows:

1. Developing models of power electronic converters for stability studies with a focus on the low frequency range:
   The frequency and sequence couplings are highlighted in this thesis and its importance in the stability studies has been shown. In the *dq* domain modelling, the models from the literature were improved.
2. Large Scale stability analysis
3. Using the numerical and black box models in stability studies:
   The stability analysis using the numerical frequency responses for a nonlinear and unbalanced system is studied. A matrix-based method is proposed to consider all the frequency couplings. The vector fitting method is also utilized to obtain the state space models of power converters, transformers, cables, etc.
4. A tool is developed, which enables the user to perform stability analysis in large scale systems:
   The tool uses the vector fitting to find the best approximation of frequency dependent models of cables and transformers. The eigenvalue based stability analysis is used in the tool, by which the user can benefit from the participation factor analysis to identify which component are contributing to a specific problem. A high-speed sensitivity analysis is also proposed based on the stability analysis platform. This useful add-on shows the sensitivity of the eigenvalues of the system to a change in the system.
5. Investigating the stability problems in the high and low frequency ranges:
   The origins of the high and low frequency problems are investigated in a large scale system using the developed tool.

6.3. FUTURE WORK

As the systems are very complicated a number of open questions that are still not answered in this thesis:

- How does the uncertainty of the identification (i.e. vector fitting) propagate in the system?
- The effects of the dc link and the generator side converter can be considered in the large scale stability evaluation.
- The high speed sensitivity analysis tool can be used to find the optimal controller gains. An objective function should be defined and this tool accelerates the whole optimization.
- STATCOMs can also be modelled similarly. It is interesting to study the effects of the STATCOM since they typically are located onshore.
- The current analysis tool is able to model a synchronous generator with relevant controllers. It is interesting to see how the WPP interacts with the nearby synchronous machines in conventional power plants.
- It is proposed that by increasing the reactor size, the instability caused by a long cable and the PLL can be mitigated. It is interesting to investigate the advantages and disadvantages of this solution from different perspectives. The reactor size can also be increased virtually, which is desirable in offshore applications due to the limited space.
- Experimental verification of the results of this study for a relatively complicated system.

REFERENCES

[1]   Ł. H. Kocewiak, "Harmonics in Large Offshore Wind Farms," Ph.D. dissertation, Aalborg University, 2012.

[2]   "The World Wind Energy Association- 2014 Half-year Report." [Online]. Available: http://www.wwindea.org/webimages/WWEA_half_year_report_2014.pdf. [Accessed: 01-Mar-2018].

[3]   "Wind Power Capacity reaches 539 GW, 52.6 GW added in 2017." [Online]. Available: http://www.wwindea.org/2017-statistics/. [Accessed: 01-Mar-2018].

[4]   M. Mohseni and S. M. Islam, "Comparing technical connection requirements for large wind power plants," in *Proc. IEEE PES General Meeting*, 2011, pp. 1–8.

[5]   A. D. Hansen, "Generators and Power Electronics for Wind Turbines," in *Wind Power in Power Systems*, John Wiley & Sons, 2012, pp. 73–103.

[6]   Ł. Kocewiak, S. Chaudhary, and B. Hesselbæk, "Harmonic Mitigation Methods in Large Offshore Wind Power Plants," in *Proc. 12th Wind Integration Workshop*, 2013, pp. 443–448.

[7]   J. Arrillaga and N. R. Watson, *Power System Harmonics*. John Wiley & Sons, 2003.

[8]   J. H. R. Enslin and P. J. M. Heskes, "Harmonic Interaction Between a Large Number of Distributed Power Inverters and the Distribution Network," *IEEE Trans. Power Electron.*, vol. 19, no. 6, pp. 1586–1593, Nov. 2004.

[9]   P. Brogan, "The stability of multiple, high power, active front end voltage sourced converters when connected to wind farm collector systems," in *Proc. EPE 2010*, 2010, pp. 1–6.

[10]   Z. Shuai, D. Liu, J. Shen, C. Tu, Y. Cheng, and A. Luo, "Series and Parallel Resonance Problem of Wideband Frequency Harmonic and Its Elimination Strategy," *IEEE Trans. Power Electron.*, vol. 29, no. 4, pp. 1941–1952, Apr. 2014.

[11]   M. Larsson, "Harmonic Resonance and Control Interoperability Analysis for HVDC Connected Wind Farms," presented at IEEE eT&D 2017, Aalborg University, Denmark, 2017.

[12]   "'Dirty electricity' probe at BorWin1." [Online]. Available: http://renews.biz/68145/dirty-electricity-probe-at-borwin1/. [Accessed: 01-Mar-2018].

[13]   R. D. D. Middlebrook, "Input filter consideration in design and application of switching regulators," *IEEE Ind. Appl. Soc. Annu. Meet.*, pp. 366–382, 1976.

[14]   Y. Wang, X. Wang, F. Blaabjerg, and Z. Chen, "Eigenvalue-based harmonic stability analysis method in inverter-fed power systems," in *IECON 2015 - 41st Annual Conference of the IEEE Industrial Electronics Society*, 2015, pp. 003277–003282.

[15]   Prabha Kundur, *Power System Stability and Control*. McGraw-Hill, 1994.

[16]   M. K. Bakhshizadeh, F. Blaabjerg, C. L. Bak, F. Faria da Silva, J. Hjerrild, K. Lukasz, B. Hesselbaek, and T. Sørensen, "Harmonic Modelling, Propagation and Mitigation for Large Wind Power Plants Connected via Long HVAC Cables: Review and Outlook of Current Research," in *Proc. IEEE ENERGYCON 2016*, 2016, pp. 1–5.

[17]   X. Wang and F. Blaabjerg, "Harmonic Stability in Power Electronic Based Power Systems: Concept, Modeling, and Analysis," *IEEE Trans. Smart Grid*, to be published.

[18]   Ł. Kocewiak, B. Gustavsen, and A. Holdyk, "Wind Power Plant Transmission System Modelling for Harmonic Propagation and Small-signal Stability Analysis," in *Proc. 16th Wind Integration Workshop*, 2017, pp. 1–6.

[19]   Ł. H. Kocewiak, J. Hjerrild, and C. L. Bak, "Wind turbine converter control interaction with complex wind farm systems," *IET Renew. Power Gener.*, vol. 7, no. 4, pp. 380–389, Jul. 2013.

[20]   B. Wen, D. Boroyevich, R. Burgos, P. Mattavelli, and Z. Shen, "Analysis of D-Q Small-Signal Impedance of Grid-Tied Inverters," *IEEE Trans. Power Electron.*, vol. 31, no. 1, pp. 675–687, Jan. 2016.

[21]   X. Wang, F. Blaabjerg, and W. Wu, "Modeling and analysis of harmonic stability in an AC power-electronics- based power system," *IEEE Trans.*

Power Electron., vol. 29, no. 12, pp. 6421–6432, 2014.

[22]   C. Yoon, H. Bai, R. N. Beres, X. Wang, C. L. Bak, and F. Blaabjerg, "Harmonic Stability Assessment for Multiparalleled, Grid-Connected Inverters," *IEEE Trans. Sustain. Energy*, vol. 7, no. 4, pp. 1388–1397, Oct. 2016.

[23]   J. B. Glasdam, "Harmonics in Offshore Wind Power Plants Employing Power Electronic Devices in the Transmission System," Ph.D. dissertation, Aalborg University, 2015.

[24]   J. Sun, "Impedance-based stability criterion for grid-connected inverters," *IEEE Trans. Power Electron.*, vol. 26, no. 11, pp. 3075–3078, Apr. 2011.

[25]   S. Buso and P. Mattavelli, *Digital Control in Power Electronics*. Morgen & Claypool Publishers, 2006.

[26]   J. Sun, "Small-Signal Methods for AC Distributed Power Systems–A Review," *IEEE Trans. Power Electron.*, vol. 24, no. 11, pp. 2545–2554, Nov. 2009.

[27]   P. C. Krause, O. Wasynczuk, and S. D. Sudhoff, *Analysis of Electric Machinery and Drive Systems*. John Wiley & Sons, 2002.

[28]   D. N. Zmood, D. G. Holmes, and G. H. Bode, "Frequency-domain analysis of three-phase linear current regulators," *IEEE Trans. Ind. Appl.*, vol. 37, no. 2, pp. 601–610, 2001.

[29]   B. Wen, D. Dong, D. Boroyevich, R. Burgos, P. Mattavelli, and Z. Shen, "Impedance-Based Analysis of Grid-Synchronization Stability for Three-Phase Paralleled Converters," *IEEE Trans. Power Electron.*, vol. 31, no. 1, pp. 26–38, Jan. 2016.

[30]   "PLECS, The Simulation Platform for Power Electronic Systems." [Online]. Available: https://www.plexim.com/plecs.

[31]   G. Francis, R. Burgos, D. Boroyevich, F. Wang, and K. Karimi, "An algorithm and implementation system for measuring impedance in the D-Q domain," in *Proc. IEEE Energy Conversion Congress and Exposition*, 2011, pp. 3221–3228.

[32]   A. Rygg and M. Molinas, "Apparent Impedance Analysis: A Small-Signal Method for Stability Analysis of Power Electronic-Based Systems," *IEEE J. Emerg. Sel. Top. Power Electron.*, vol. 5, no. 4, pp. 1474–1486, 2017.

[33]   M. Cespedes, "Impedance Modeling and Analysis of Grid-Connected
        Voltage-Source Converters," *IEEE Trans. Power Electron.*, vol. 29, no. 3,
        pp. 1254–1261, Mar. 2014.

[34]   M. K. Bakhshizadeh, X. Wang, F. Blaabjerg, J. Hjerrild, L. Kocewiak, C. L.
        Bak, and B. Hesselbek, "Couplings in Phase Domain Impedance Modelling
        of Grid-Connected Converters," *IEEE Trans. Power Electron.*, vol. 31, no.
        10, pp. 6792–6796, 2016.

[35]   K. R. Padiyar, *Analysis of Subsynchronous Resonance in Power Systems*.
        Springer Science & Business Media, 1999.

[36]   H. K. Khalil, *Nonlinear Systems*. Prentice Hall, 2002.

[37]   K. Ogata, *Modern control engineering*. Prentice Hall, 2002.

[38]   M. K. Bakhshizadeh, C. Yoon, J. Hjerrild, C. L. Bak, L. H. Kocewiak, F.
        Blaabjerg, and B. Hesselbaek, "The Application of Vector Fitting to
        Eigenvalue-Based Harmonic Stability Analysis," *IEEE J. Emerg. Sel. Top.
        Power Electron.*, vol. 5, no. 4, pp. 1487–1498, Dec. 2017.

[39]   Y. Wang, X. Wang, F. Blaabjerg, and Z. Chen, "Harmonic instability
        assessment using state-space modeling and participation analysis in inverter-
        fed power systems," *IEEE Trans. Ind. Electron.*, vol. 64, no. 1, pp. 806–816,
        2017.

[40]   J. F. Hauer, "Application of Prony analysis to the determination of modal
        content and equivalent models for measured power system response," *IEEE
        Trans. Power Syst.*, vol. 6, no. 3, pp. 1062–1068, 1991.

[41]   L. Harnefors, "Modeling of Three-Phase Dynamic Systems Using Complex
        Transfer Functions and Transfer Matrices," *IEEE Trans. Ind. Electron.*, vol.
        54, no. 4, pp. 2239–2248, Aug. 2007.

[42]   M. K. Bakhshizadeh, J. Hjerrild, L. Kocewiak, F. Blaabjerg, and C. L. Bak,
        "On Aggregation Requirements for Harmonic Stability Analysis in Wind
        Power Plants," in *Proc. 16th Wind Integration Workshop*, 2017, pp. 424–
        427.

[43]   "MATLAB   -   Mathworks."   [Online].   Available:
        https://www.mathworks.com/products/matlab.html.

[44]   "PowerFactory   -   DIgSILENT."   [Online].   Available:
        https://www.digsilent.de/en/powerfactory.html.

[45]   "Python." [Online]. Available: https://www.python.org/.

[46]   "NumPy, the fundamental package for scientific computing with Python." [Online]. Available: http://www.numpy.org/.

[47]   "SciPy , a Python-based ecosystem of open-source software for mathematics, science, and engineering." [Online]. Available: https://www.scipy.org/.

[48]   Y. Wang, X. Wang, F. Blaabjerg, and Z. Chen, "Harmonic stability analysis of inverter-fed power systems using Component Connection Method," in *Proc. IEEE 8th Int. Power Electron. Motion Control Conf. (IPEMC-ECCE Asia)*, 2016, pp. 2667–2674.

[49]   N. Balabanian and T. A. Bickart, *Electrical network theory*. Wiley, 1969.

[50]   J. B. Kruskal, "On the Shortest Spanning Subtree of a Graph and the Traveling Salesman Problem," *Proc. Am. Math. Soc.*, vol. 7, no. 1, p. 48, 1956.

[51]   P. M. Anderson, B. L. Agrawal, and J. E. Van Ness, "The Generator Model," in *Subsynchronous Resonance in Power Systems*, Wiley-IEEE Press, 2009, pp. 31–91.

[52]   G. J. Wakileh, *Power Systems Harmonics: Fundamentals, Analysis, and Filter Design*, vol. I. Springer, 2001.

[53]   W. Dugui and X. Zheng, "Harmonic model of power transformer," in *Proc. Power Syst. Technol. (POWERCON'98) Conf*, 1998, vol. 2, pp. 1045–1049.

[54]   M. K. Bakhshizadeh, F. Blaabjerg, J. Hjerrild, X. Wang, L. Kocewiak, and C. L. Bak, "A Numerical Matrix-Based Method for Stability and Power Quality Studies Based on Harmonic Transfer Functions," *IEEE J. Emerg. Sel. Top. Power Electron.*, vol. 5, no. 4, pp. 1542–1552, Dec. 2017.

[55]   M. K. Bakhshizadeh, J. Hjerrild, L. Kocewiak, B. Hesselbaek, X. Wang, F. Blaabjerg, and C. L. Bak, "Small-signal model of a decoupled double synchronous reference frame current controller," in *Proc. IEEE 17th Workshop on Control and Modeling for Power Electronics (COMPEL)*, 2016, pp. 1–6.

[56]   M. K. Bakhshizadeh, J. Hjerrild, Ł. H. Kocewiak, F. Blaabjerg, C. L. Bak, X. Wang, F. M. F. da Silva, and B. Hesselbæk, "A Numerical Matrix-Based method in Harmonic Studies in Wind Power Plants," in *Proc. 15th Wind*

Integration Workshop, 2016, pp. 335–339.

[57]   E. Möllerstedt, "Dynamic analysis of harmonics in electrical systems," Ph.D. dissertation, Lund Institute of Technology (LTH), 2000.

[58]   N. M. Wereley, "Analysis and control of linear periodically time varying systems," Ph.D. dissertation, Massachusetts Institute of Technology, 1990.

[59]   J. B. Kwon, X. Wang, F. Blaabjerg, C. L. Bak, A. R. Wood, and N. R. Watson, "Harmonic Instability Analysis of a Single-Phase Grid-Connected Converter Using a Harmonic State-Space Modeling Method," *IEEE Trans. Ind. Appl.*, vol. 52, no. 5, pp. 4188–4200, 2016.

[60]   S. R. Hall and N. M. Wereley, "Generalized Nyquist Stability Criterion for Linear Time Periodic Systems," in *Proc. American Control Conference*, 1990, pp. 1518–1525.

[61]   P. Rodriguez, J. Pou, J. Bergas, J. I. Candela, R. P. Burgos, and D. Boroyevich, "Decoupled Double Synchronous Reference Frame PLL for Power Converters Control," *IEEE Trans. Power Electron.*, vol. 22, no. 2, pp. 584–592, Mar. 2007.

[62]   R. Teodorescu, M. Liserre, and P. Rodríguez, *Grid Converters for Photovoltaic and Wind Power Systems*. IEEE-Wiley, 2011.

[63]   M. Reyes, P. Rodriguez, S. Vazquez, A. Luna, J. M. Carrasco, and R. Teodorescu, "Decoupled Double Synchronous Reference Frame current controller for unbalanced grid voltage conditions," in *Proc. IEEE Energy Conversion Congress and Exposition (ECCE)*, 2012, pp. 4676–4682.

[64]   L. Kocewiak, C. L. Bak, and S. Munk-Nielsen, "Bifurcation and Chaos in a Pulse Width modulation controlled Buck Converter," in *Proc. 6th Eurosim Congress on Modelling and Simulation*, 2007, pp. 1–6.

[65]   P. Blanchard, R. L. Devaney, and G. R. Hall, *Differential equations*. Thomson Brooks/Cole, 2006.

[66]   B. Gustavsen and A. Semlyen, "Rational approximation of frequency domain responses by vector fitting," *IEEE Trans. Power Deliv.*, vol. 14, no. 3, pp. 1052–1061, Jul. 1999.

[67]   D. Deschrijver, M. Mrozowski, T. Dhaene, and D. De Zutter, "Macromodeling of Multiport Systems Using a Fast Implementation of the Vector Fitting Method," *IEEE Microw. Wirel. Components Lett.*, vol. 18, no.

6, pp. 383–385, Jun. 2008.

[68]   B. Gustavsen, "Improving the Pole Relocating Properties of Vector Fitting," *IEEE Trans. Power Deliv.*, vol. 21, no. 3, pp. 1587–1592, Jul. 2006.

[69]   "The Vector Fitting Web Site." [Online]. Available: https://www.sintef.no/projectweb/vectfit/.

[70]   A. Rygg, M. Amin, M. Molinas, and B. Gustavsen, "Apparent impedance analysis: A new method for power system stability analysis," in *Proc. IEEE COMPEL*, 2016, pp. 1–7.

[71]   J. L. Agorreta and M. Borrega, "Modeling and Control of N -Paralleled Grid- Connected Inverters With LCL Filter Coupled Due to Grid Impedance in PV Plants," vol. 26, no. 3, pp. 770–785, 2011.

[72]   L. Harnefors, L. Zhang, and M. Bongiorno, "Frequency-domain passivity-based current controller design," *IET Power Electron.*, vol. 1, no. 4, pp. 455–465, 2008.

[73]   L. Harnefors, X. Wang, A. G. Yepes, and F. Blaabjerg, "Passivity-Based Stability Assessment of Grid-Connected VSCs—An Overview," *IEEE J. Emerg. Sel. Top. Power Electron.*, vol. 4, no. 1, pp. 116–125, Mar. 2016.

[74]   B. Gustavsen and A. Semlyen, "Enforcing passivity for admittance matrices approximated by rational functions," *IEEE Trans. Power Syst.*, vol. 16, no. 1, pp. 97–104, 2001.

[75]   P. K. Goh, "Broadband Macromodeling via A Fast Implementation of Vector Fitting with Passivity Enforcement," Ph.D. dissertation, University of Illinois at Urbana-Champaign, 2007.

[76]   M. K. Bakhshizadeh, F. Blaabjerg, J. Hjerrild, Ł. Kocewiak, and C. Leth Bak, "Improving the Impedance Based Stability Criterion by Using the Vector Fitting Method," *IEEE Trans. Energy Convers.,* to be published.

[77]   C. Yoon, H. Bai, X. Wang, C. L. Bak, and F. Blaabjerg, "Regional modeling approach for analyzing harmonic stability in radial power electronics based power system," in *Proc. IEEE PEDG 2015*, 2015, pp. 1–5.

[78]   W. Cao, X. Zhang, Y. Ma, and F. Wang, "Stability criterion and controller parameter design of radial-line renewable systems with multiple inverters," in *Proc. IEEE Applied Power Electronics Conference and Exposition*, 2016, pp. 2229–2236.

[79]   C. Buchhagen, M. Greve, A. Menze, and J. Jung, "Harmonic Stability –
        Practical Experience of a TSO," in *Proc. 15th Wind Integration Workshop*,
        2016, pp. 1–6.

[80]   D. G. Holmes, T. A. Lipo, B. P. McGrath, and W. Y. Kong, "Optimized
        Design of Stationary Frame Three Phase AC Current Regulators," *IEEE
        Trans. Power Electron.*, vol. 24, no. 11, pp. 2417–2426, Nov. 2009.

[81]   S. G. Parker, B. P. McGrath, and D. G. Holmes, "Regions of Active
        Damping Control for LCL Filters," *IEEE Trans. Ind. Appl.*, vol. 50, no. 1,
        pp. 424–432, Jan. 2014.

[82]   Z. Xin, P. Mattavelli, W. Yao, Y. Yang, F. Blaabjerg, and P. C. Loh,
        "Mitigation of Grid Current Distortion for LCL-Filtered Voltage Source
        Inverter with Inverter Current Feedback Control," *IEEE Trans. Power
        Electron.*, vol. 33, no. 7, pp. 6248–6261, Jul. 2017.

[83]   R. Peña-Alzola, M. Liserre, F. Blaabjerg, R. Sebastián, J. Dannehl, and F.
        W. Fuchs, "Analysis of the Passive Damping Losses in LCL-Filter-Based
        Grid Converters," *IEEE Trans. Power Electron.*, vol. 28, no. 6, pp. 2642–
        2646, Jun. 2013.

[84]   R. N. Beres, X. Wang, M. Liserre, F. Blaabjerg, and C. L. Bak, "A Review
        of Passive Power Filters for Three-Phase Grid-Connected Voltage-Source
        Converters," *IEEE J. Emerg. Sel. Top. Power Electron.*, vol. 4, no. 1, pp.
        54–69, Mar. 2016.

[85]   R. N. Beres, "Optimal design of passive power filters for gridconnected
        voltage-source converters," Ph.D. dissertation, Aalborg University, 2016.

[86]   X. Wang, Y. W. Li, F. Blaabjerg, and P. C. Loh, "Virtual-Impedance-Based
        Control for Voltage-Source and Current-Source Converters," *IEEE Trans.
        Power Electron.*, vol. 30, no. 12, pp. 7019–7037, Dec. 2015.

[87]   J. Dannehl, M. Liserre, and F. W. Fuchs, "Filter-Based Active Damping of
        Voltage Source Converters With LCL Filter," *IEEE Trans. Ind. Electron.*,
        vol. 58, no. 8, pp. 3623–3633, Aug. 2011.

[88]   W. Yao, Y. Yang, X. Zhang, F. Blaabjerg, and P. C. Loh, "Design and
        Analysis of Robust Active Damping for LCL Filters Using Digital Notch
        Filters," *IEEE Trans. Power Electron.*, vol. 32, no. 3, pp. 2360–2375, Mar.
        2017.

[89]   M. Liserre, A. Dell'Aquila, and F. Blaabjerg, "Genetic algorithm based

design of the active damping for a LCL-filter three-phase active rectifier," in *Proc. IEEE Applied Power Electronics Conference and Exposition,* 2003, vol. 1, pp. 234–240.

[90]   K. Hirano, S. Nishimura, and S. Mitra, "Design of digital notch filters," *IEEE Trans. Circuits Syst.*, vol. 21, no. 4, pp. 540–546, Jul. 1974.

[91]   K. J. Astrom and B. Wittenmark, *Computer-Controlled Systems Theory and Design*. Tsinghua University Press, 1997.

[92]   M. Liserre, A. Dell'Aquila, and F. Blaabjerg, "Stability improvements of an LCL-filter based three-phase active rectifier," in *Proc. IEEE PESC*, 2002, vol. 3, pp. 1195–1201.

[93]   Y. Xiao, J. Zhao, and S. Mao, "Theory for the design of C-type filter," in *Proc. 11th IEEE ICHQP*, 2004, pp. 11–15.

[94]   J. Z. Zhou, H. Ding, S. Fan, Y. Zhang, and A. M. Gole, "Impact of Short-Circuit Ratio and Phase-Locked-Loop Parameters on the Small-Signal Behavior of a VSC-HVDC Converter," *IEEE Trans. Power Deliv.*, vol. 29, no. 5, pp. 2287–2296, Oct. 2014.

[95]   M. J. Korytowski, "Effects of the Phase Locked Loop on the Stability of a Voltage Source Converter in a Weak Grid Environment," Ph.D. dissertation, University of Pittsburgh, 2014.

[96]   D. A. Frickey, "Conversions between S, Z, Y, H, ABCD, and T parameters which are valid for complex source and load impedances," *IEEE Trans. Microw. Theory Tech.*, vol. 42, no. 2, pp. 205–211, 1994.

[97]   ABB, "XLPE Submarine Cable Systems." [Online]. Available: http://new.abb.com/docs/default-source/ewea-doc/xlpe-submarine-cable-systems-2gm5007.pdf.

[98]   Nexans, "6-36kV Medium Voltage Underground Power Cables." [Online]. Available: http://www.nexans.co.uk/UK/files/Underground Power Cables Catalogue 03-2010.pdf.

[99]   G. Funk and T. Hantel, "Frequenzabhängigkeit der Betriebsmittel von Drehstromnetzen," *etz-Archiv*, vol. 9, no. 11, pp. 349–356, 1987.

APPENDICES

Appendix A. Two-port networks

The terminal characteristics of a two-port network as shown in Figure A-1 can be described by the Admittance-, Impedance- or ABCD- parameters as shown in (A-1)-(A-3), respectively [96].
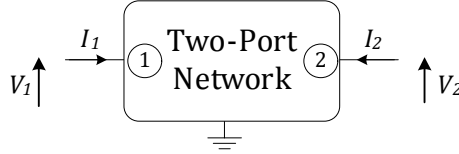

Figure A-1 A two-port network.

$$\begin{bmatrix} V_1 \\ V_2 \end{bmatrix} = \begin{bmatrix} z_{11} & z_{12} \\ z_{21} & z_{22} \end{bmatrix} \begin{bmatrix} I_1 \\ I_2 \end{bmatrix} \tag{A-1}$$

$$\begin{bmatrix} I_1 \\ I_2 \end{bmatrix} = \begin{bmatrix} y_{11} & y_{12} \\ y_{21} & y_{22} \end{bmatrix} \begin{bmatrix} V_1 \\ V_2 \end{bmatrix} \tag{A-2}$$

$$\begin{bmatrix} V_1 \\ I_1 \end{bmatrix} = \begin{bmatrix} A & B \\ C & D \end{bmatrix} \begin{bmatrix} V_2 \\ -I_2 \end{bmatrix} \tag{A-3}$$

The relationship between different parameters is given in Table A-1.

Table A-1 Transformation between different parameters.

	z	y	a
z		$\dfrac{1}{\Delta[\mathbf{y}]}\begin{bmatrix} y_{22} & -y_{12} \\ -y_{21} & y_{11} \end{bmatrix}$	$\dfrac{1}{a_{21}}\begin{bmatrix} a_{11} & \Delta[\mathbf{a}] \\ 1 & a_{22} \end{bmatrix}$
y	$\dfrac{1}{\Delta[\mathbf{z}]}\begin{bmatrix} z_{22} & -z_{12} \\ -z_{21} & z_{11} \end{bmatrix}$		$\dfrac{1}{a_{12}}\begin{bmatrix} a_{22} & -\Delta[\mathbf{a}] \\ -1 & a_{11} \end{bmatrix}$
a	$\dfrac{1}{z_{21}}\begin{bmatrix} z_{22} & -\Delta[\mathbf{z}] \\ -1 & z_{11} \end{bmatrix}$	$\dfrac{1}{y_{12}}\begin{bmatrix} -y_{11} & 1 \\ \Delta[\mathbf{y}] & -y_{22} \end{bmatrix}$	

where $\Delta[x]$ means the determinant of matrix $[x]$.

ABCD parameters are useful when two-port networks are put in a cascaded connection, due to the fact the final ABCD matrix is the matrix product of the two sub-networks (see Figure A-2).

$$[a]=[a]_1\times[a]_2$$
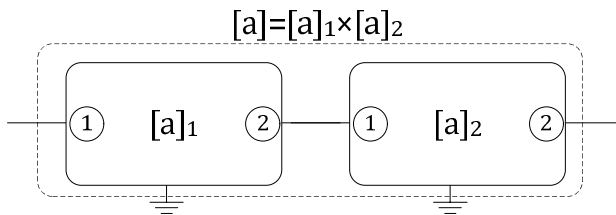
Figure A-2 Cascaded connection of two-port networks.

Admittance parameters are useful when two port networks are connected in parallel as shown in Figure A-3. Therefore, the final admittance matrix is the sum of the sub-matrices. Also, when a shunt element is added to a network the change can be inserted in the admittance by adding the new admittance to the corresponding diagonal element of the admittance matrix.
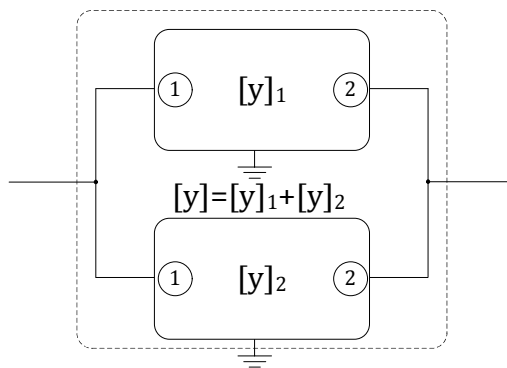
Figure A-3 Parallel connection of two-port networks.

Finally, impedance matrix is useful for calculating the driving point impedance of a given node, since the diagonal elements of the impedance matrix show the driving point impedance of those nodes.

Appendix B. Parameters of the test system

The proposed methods have been used for stability studies of a real OWPP at Ørsted Wind Power; however for commercial reasons the real model and parameters cannot be published. Therefore, in this part a simplified wind power plant is presented. As shown in Figure B-1 the WPP is formed of 35 WTs rated as 6 MW. Two transformers are used in parallel in each substation to increase availability.

The cable parameters are chosen from the online datasheets that are publicly available [97], [98]. The frequency dependent characteristics are only considered for the resistance (inductance is assumed as constant) and it is based on the equations from [7]. For 220 kV cables

$$R(f) = 0.74R_1 \left(0.267 + 1.073 \sqrt{\frac{f}{f_{nom}}} \right) \qquad \text{(B-1)}$$

and for 34 kV cables

$$R(f) = R_1 \left(0.187 + 0.532 \sqrt{\frac{f}{f_{nom}}} \right) \qquad \text{(B-2)}$$

where R_1 is the AC resistance at the fundamental frequency f_{nom}.

Table B-1 Information of the cables.

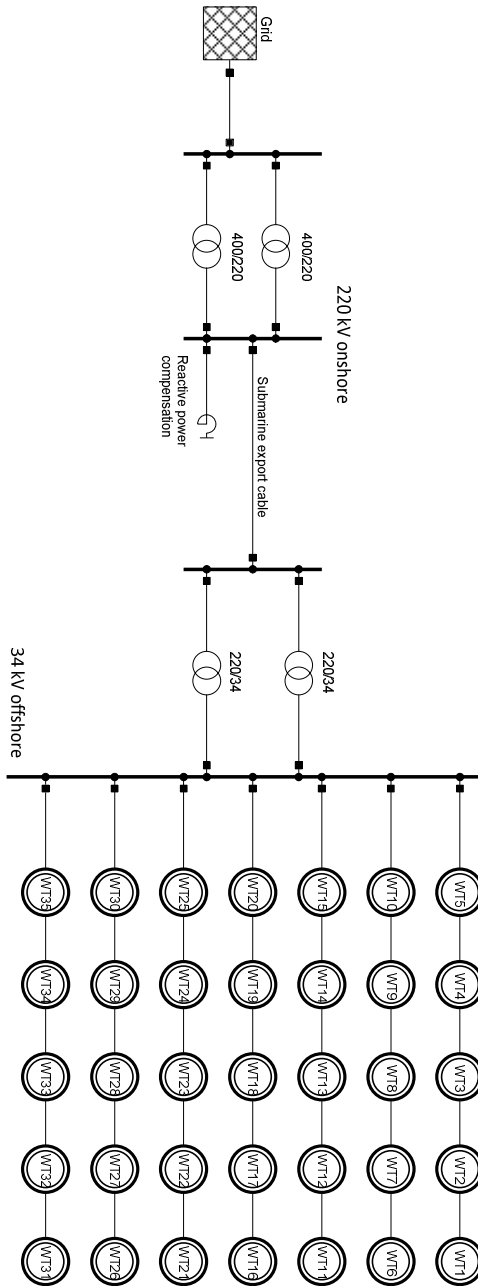| Parameter	Export Cable (ABB)	Array Cable (Nexans)
Nominal voltage [kV]	220	34
Cross section [mm^2]	1000	630
AC-Resistance [Ω/km]	0.03	0.042
Inductance [mH/km]	0.38	0.31
Capacitance [μF/km]	0.19	0.32
Length [km]	100	3 (each section)

Figure B-1 Considered Offshore WPP for simulations with 35 6-MW wind turbines.

The transformer parameters as shown in Table B-2 are chosen arbitrary by the author to reflect system resonance behavior relevant for studies.

Table B-2 Information of the transformers.

| Parameter	Voltage ratio		
	400/220	**220/34**	**34/1**
Rated Power [MVA]	200	200	9
Leakage impedance [pu]	0.12	0.14	0.09
Copper Losses [kW]	375	300	35
A_r	0.2	0.2	0.2
B_r	1.6	1.6	1.4
A_L	1.0	1.0	1
B_L	0.0	0.0	-0.02

where A_r, B_r, A_L and B_L define the frequency dependent characteristics of the transformers [99] as (B-3) and (B-4).

$$R(f) = R_1 \left(1 + A_r \left(\frac{f}{f_{nom}} - 1 \right)^{B_r} \right) \tag{B-3}$$

$$L(f) = L_1 A_L \left(\frac{f}{f_{nom}} \right)^{B_L} \tag{B-4}$$

This test system is used in different chapters and in each chapter to some extent some simplifications are made. Here is a list of the main assumptions:

In §2.5 the system is considered for harmonic stability studies using numerical models. Different frequency responses are used for the grid as shown in Figure 2-46. The cables are modelled by the equivalent π-models and the frequency dependent characteristics as given in (B-1) and (B-2) are used. The wind turbines are modelled as frequency dependent impedances as shown in Figure B-2. This converter is obtained by simply paralleling 20 Inverters, which are the same as Inverter 2 in §2.4.2.
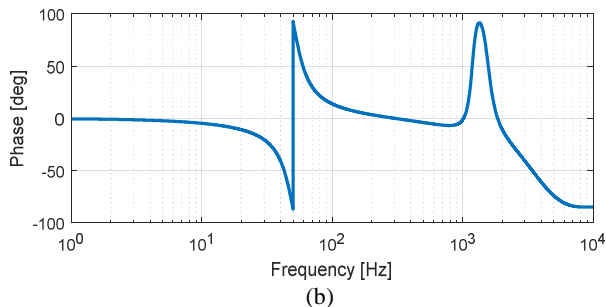

(a)

(b)
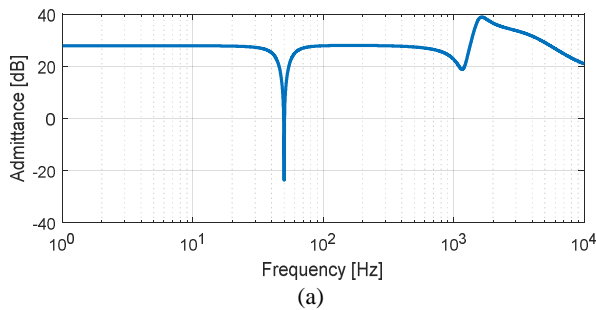
Figure B-2 Output admittance of the considered power converter. (a) Magnitude plot (b) Phase plot

Figure B-3 shows how the converter is modeled in Chapter 5, where only the PLL and current controller in the *dq* domain are considered. The frequency dependency in cables are neglected to be able to run sensitivity analysis. The parameters are listed in Table B-3.
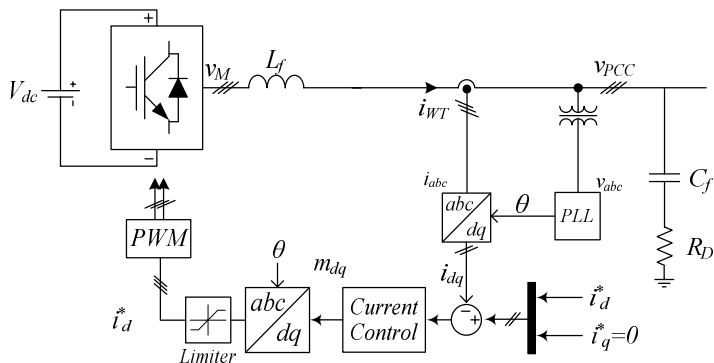
Figure B-3 Internal circuit of the considered wind turbine.

Table B-3 Parameters of the wind turbine.

Symbol	Description	Value
f_1	Nominal frequency	50 Hz
V_{dc}	DC link voltage	2000 V
K_p	Proportional gain of the current controller	0.00007
K_i	Integrator gain of the current controller	0.014
P_{ref}	Active power set point	6 MW
C_f	Filter capacitance	3.3 mF
L_f	Coupling reactor	30 µH
f_s	Sampling frequency	5 kHz
f_{sw}	Switching frequency	2.5 kHz

The damping resistor R_D is 1mΩ unless otherwise specified.

According to (2-28), the PLL can be considered as a second order system. Therefore, the PLL gains are dependent on the bandwidth as

$$k_{p_{pll}} = \frac{2\xi\omega_n}{V_d^0} \tag{B-5}$$

$$k_{i_{pll}} = \frac{\omega_n^2}{V_d^0} \tag{B-6}$$

where V_d^0 is the steady state value of the PCC voltage (peak of the phase to ground voltage), ω_n is the PLL bandwidth and ξ=0.707 is the damping.

In §3.5.2, the frequency dependent characteristics in cables, transformers and grid are neglected. The converters are modelled as frequency dependent impedances, where only the current controller is considered. The converter side current controller strategy as shown in Figure B-3 is used, and therefore, the converter impedance can be written as

$$Z_{conv}(s) = \left(k_p + \frac{k_i}{s}\right)V_{dc}e^{-1.5sT_s} + L_f s \tag{B-7}$$

In §4.3.3.7, the converter is modelled similar to §3.5.2, however, the frequency dependent models are used for cables and transformers as given in (B-1)-(B-4).

Appendix C. Limit Cycles

It can be concluded from Figure 4-21(c) that the modulation signals are not saturated, which is not as expected. The system is unstable, and therefore it should go to infinity and the converter must be saturated. The reason behind this is that in this thesis small signal linearized models are used. Therefore, the evaluations are valid in a small signal region. A nonlinear system could leave the equilibrium point after a perturbation and get trapped in a limit cycle. However, the small signal stability criterion ensures that this operating point is not reachable, and uncontrolled currents and harmonics will appear.

This is discussed more in here by a simple example. Van der Pole equation [65] is a nonlinear differential equation that is widely used for demonstrating a nonlinear system as given by

$$
\begin{aligned}
\frac{dx}{dt} &= f_1(t,x,y) = y \\
\frac{dy}{dt} &= f_2(t,x,y) = -x + (1-x^2)y
\end{aligned}
\tag{C-1}
$$

Therefore, the small signal model can be found around an operating point (X_0, Y_0) as

$$
\frac{d}{dt}\begin{bmatrix} x \\ y \end{bmatrix} = \begin{bmatrix} \dfrac{\partial f_1}{\partial x} & \dfrac{\partial f_1}{\partial y} \\ \dfrac{\partial f_2}{\partial x} & \dfrac{\partial f_2}{\partial y} \end{bmatrix}_{|(x,y)=(X_0,Y_0)} = \begin{bmatrix} 0 & 1 \\ -1-2X_0Y_0 & (1-X_0^2) \end{bmatrix}
\tag{C-2}
$$

One equilibrium point is $(X_0, Y_0)=(0,0)$, which pushes the derivatives to zero. Therefore, the eigenvalues are

$$
\lambda_{1,2} = \frac{1 \pm j\sqrt{3}}{2}
\tag{C-3}
$$

It is expected that due to the positive real parts of the eigenvalues, the response should go to infinity after a perturbation. However, as it can be seen in Figure C-1 the system oscillates and the state variables remain bounded (blue curve). As expected the linear system goes to infinity (orange curve).
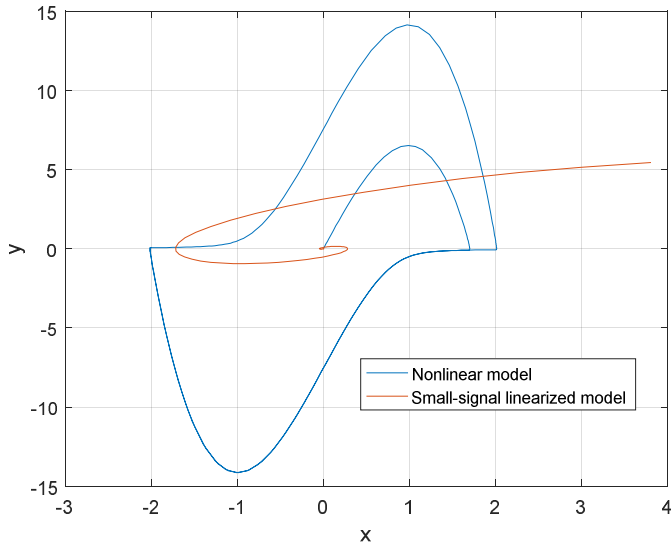
Figure C-1 XY plot of the state variables of van der Pole equation.

It must be noted that the aim of this project is to ensure the stable operation, and if the converter cannot work in the requested condition, even though the response is bounded it generates harmonics. The calculation of the large signal response is outside of this study.

Appendix D. Stability margins

The definition of different stability margins are given in the Nyquist diagram shown in Figure D-1. The phase margin is the additional phase that can be added to the open loop transfer function until the closed loop system becomes unstable. The gain margin is the gain that can be added to the open loop transfer function until the closed loop system becomes unstable. The Vector Gain Margin (VGM) shows how close a Nyquist diagram is to the critical point (-1,0). It can be seen that sometimes a system has enough phase and gain margins; however, it is close to instability. The VGM considers the PM and GM together.
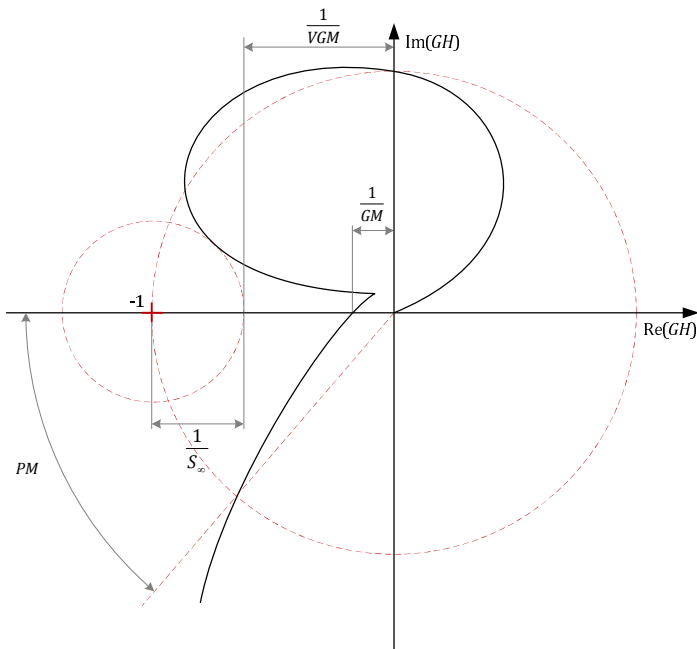

Figure D-1 Various stability indices such as gain margin (GM), vector gain margin (VGM) and phase margin (PM) are used in order to indicate the controller sensitivity to the plant changes.

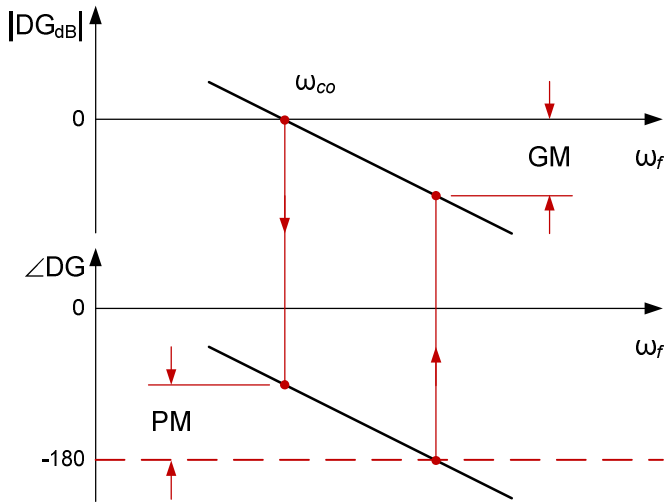The PM and GM can also be obtained from a Bode plot as shown in Figure D-2.

Figure D-2 Illustration of the gain margin and phase margin in a Bode plot.

Appendix E. Matrix Fitting

The Matrix fitting toolbox developed by Dr. Gustavsen [69] assumes the transfer function matrix is symmetrical, which is the case for modelling of the multi-terminal passive networks. However, in the *dq* domain if the low frequency loops such as PLL, dc link and power control are modelled, the matrix is no longer symmetrical. There is no option for disabling this assumption in the current toolbox; hence the problem has simply been solved by changing a few lines in the source code of the matrix fitting toolbox, which is publicly available.

Figure E-1 shows this problem, where the results of the original Matrix Fitting are plotted. It can be seen that in Figure E-1 the error in Y_{dq} is more than 200% but in Figure E-2, which shows the results of the modified matrix fitting, the error is less than 0.01%.
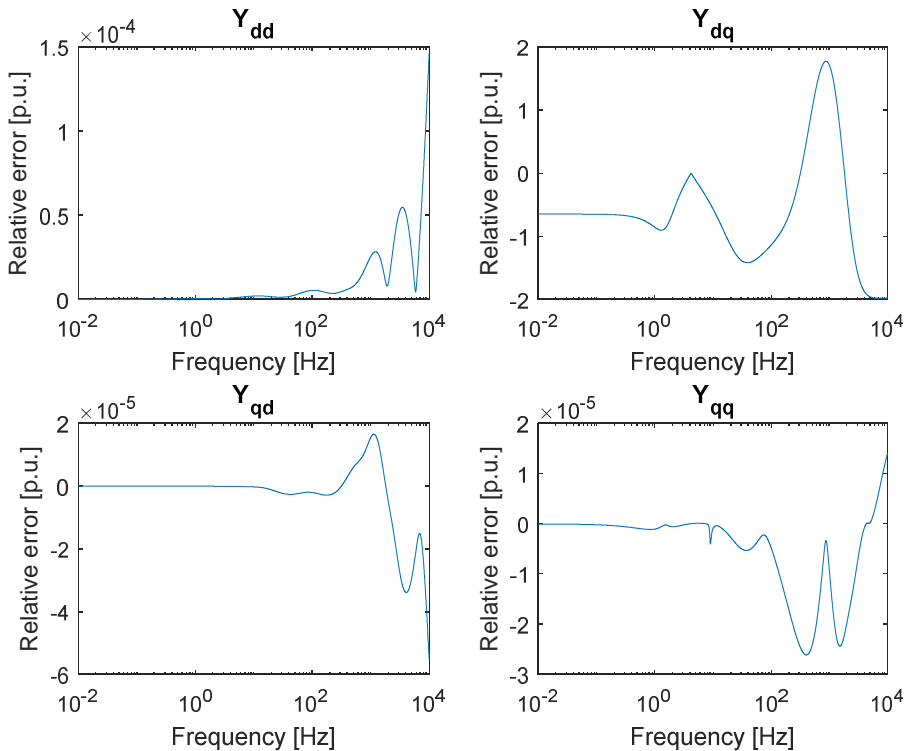

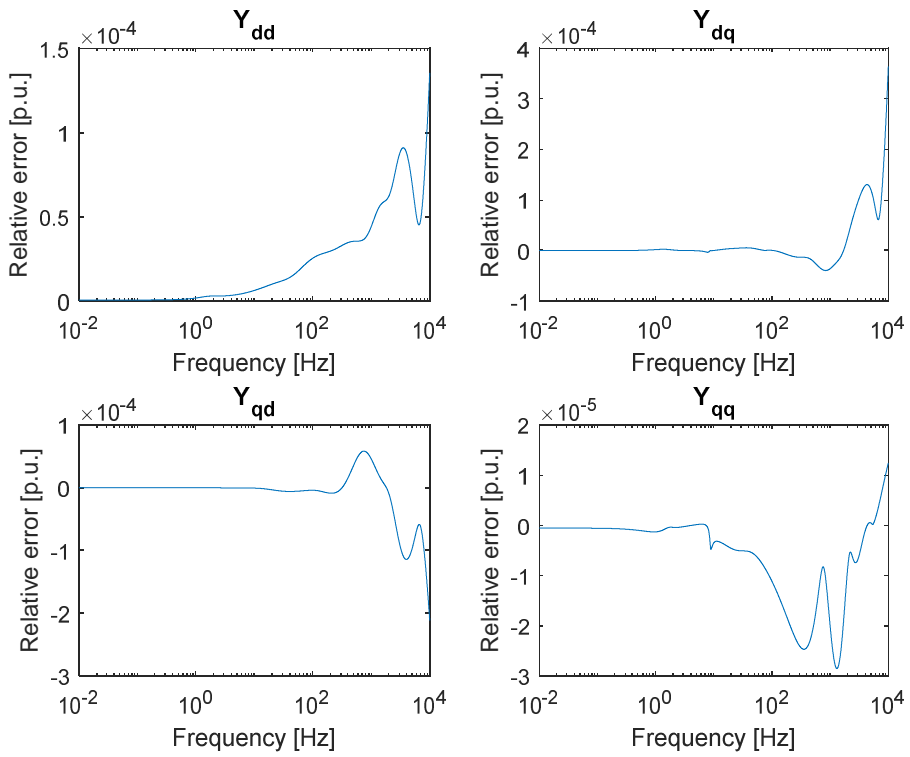*Figure E-1 Relative error of the original Matrix Fitting code.*

Figure E-2 Relative error of the modified Matrix Fitting code.

Appendix F. Participation factor analysis in black-box models

A dynamical system can be described by unlimited state space realization. In other words, the state variable can be chosen differently and hence, the state equations could be different.

$$\frac{dx}{dt} = Ax + Bu$$
$$y = Cx + Du$$

(F-1)

Assume an invertible matrix P. Substituting $x = P\tilde{x}$ gives

$$P\frac{d\tilde{x}}{dt} = AP\tilde{x} + Bu$$
$$y = CP\tilde{x} + Du$$

(F-2)

Pre-multiplying the derivative term of (F-2) by P^{-1} gives

$$\frac{d\tilde{x}}{dt} = P^{-1}AP\tilde{x} + P^{-1}Bu$$
$$y = CP\tilde{x} + Du$$

(F-3)

It can be seen that (F-3) is a new state space definition with a set of new state variables, which are linear combinations of old state variables. The new state space matrices are

$$\tilde{A} = P^{-1}AP$$
$$\tilde{B} = P^{-1}B$$
$$\tilde{C} = CP$$
$$\tilde{D} = D$$

(F-4)

It is also worth seeing what happens to the eigenvalues and eigenvectors. The original state matrix A can be rewritten as

$$A = P\tilde{A}P^{-1}$$

(F-5)

If Φ is the right eigenvector of A corresponding to the eigenvalue λ, then

$$A\Phi = \lambda\Phi \Rightarrow P\tilde{A}P^{-1}\Phi = \lambda\Phi$$

(F-6)

Pre-multiplying (F-6) by P^{-1} gives

$$\tilde{A}P^{-1}\Phi = \lambda P^{-1}\Phi$$

(F-7)

that can be rewritten as

$$\tilde{A}\tilde{\Phi} = \lambda\tilde{\Phi} \tag{F-8}$$

where $\tilde{\Phi} = P^{-1}\Phi$. In other words, the eigenvalue is unchanged and the right eigenvector is pre-multiplied by P^{-1}. Similarly it can be shown that the left eigenvector is post-multiplied by P. Therefore, the results of the participation factor analysis, which is the product of the left and right eigenvectors, could be different for different cases. This is as expected since a participation factor shows the contribution of a state variable on an eigenvalue. If the state variables are mixed together (using a linear operator) then the participation factor results would also be mixed. Sometimes the results could also be misleading. For instance, there could be two large contributors inside a subsystem but this might be for an unrealistic state variable (note a participation factor is a complex number).

The freedom in defining the state variables is an important topic in identification of black-box models as discussed in §4.4. It means that special care should be taken when evaluating the contribution of unknown state variables on a specific eigenvalue. As it was shown by simply rerunning the identification, another state space model might be obtained, and therefore, the contributions could be different. To further clarify this matter the case presented in §4.4.1 is investigated with this uncertainty. Figure F-1 shows the considered system which consists of two black box models. For the sake of the simplicity it is assumed that both subsystems are strictly proper.
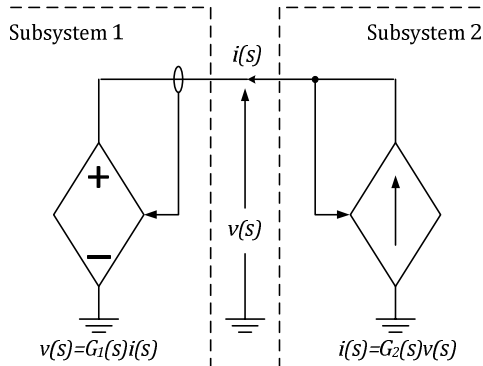

Figure F-1 System is formed of two black-box subsystems.

A similarity operator can be considered for both state space models to see what happens to the participation factors.

$$\begin{cases} \dot{\tilde{x}}_1 = P_1^{-1}A_1P_1\tilde{x}_1 + P_1^{-1}B_1 i \\ v = C_1P_1\tilde{x}_1 \end{cases} \tag{F-9}$$

$$\begin{cases} \dot{\tilde{x}}_2 = P_2^{-1}A_2P_2\tilde{x}_2 + P_2^{-1}B_2 v \\ i = C_2P_2\tilde{x}_2 \end{cases} \tag{F-10}$$

The overall state space model of the system, as obtained in (4-33), can be expressed as

$$\begin{bmatrix} \dot{x}_1 \\ \dot{x}_2 \end{bmatrix} = [A_T]\begin{bmatrix} x_1 \\ x_2 \end{bmatrix} = \begin{bmatrix} P_1^{-1}A_1P_1 & P_1^{-1}B_1C_2P_2 \\ P_2^{-1}B_2C_1P_1 & P_2^{-1}A_2P_2 \end{bmatrix}\begin{bmatrix} x_1 \\ x_2 \end{bmatrix} \tag{F-11}$$

A^T can be further simplified to

$$[\tilde{A}_T] = \begin{bmatrix} P_1^{-1} & 0 \\ 0 & P_2^{-1} \end{bmatrix}\begin{bmatrix} A_1 & B_1C_2 \\ B_2C_1 & A_2 \end{bmatrix}\begin{bmatrix} P_1 & 0 \\ 0 & P_2 \end{bmatrix} = \mathbb{P}^{-1}A_T\mathbb{P} \tag{F-12}$$

It is interesting to see that the final state matrix is indeed a similarity transformation of the original one.

As mentioned above the participation index of a specific state variable on a specific eigenvalue is uncertain due to the uncertainty in state variable definition. However, **sum of the participation indices is constant for each subsystem.** This is a good indicator that shows how much a subsystem contributes to the instability. The following is the proof of this statement. Suppose x_1 and x_2 have n_1 and N-n_1 elements (N is the number of state variables of the total system), respectively. The sum of participation indices for state variables in x_1 can be calculated by the dot product of the relevant portions of the transformed left and right eigenvectors.

$$\sum_{i=1..n_1} PF_i = \Psi\mathbb{P} \times \begin{bmatrix} I_{n_1 \times n_1} \\ [0]_{(N-\ _1)\times n_1} \end{bmatrix} \times [I_{n_1 \times n_1} \quad [0]_{n_1 \times (N-n_1)}] \times \mathbb{P}^{-1}\Phi$$
$$= \Psi\begin{bmatrix} I_{n_1 \times n_1} & 0 \\ 0 & 0 \end{bmatrix}_{N \times N} \Phi \tag{F-13}$$

It can be seen that no matter how the state variables are defined the total contribution of each subsystem is constant. This conclusion is used in §4.4.2.1.